The Physics and Chemistry of Marine Aerosols

Thesis by
Lynn M. Russell

In Partial Fulfillment of the Requirements
for the Degree of
Doctor of Philosophy

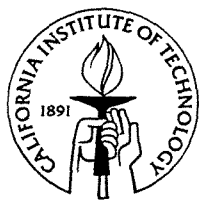

California Institute of Technology
Pasadena, California

1996
(Submitted October 4, 1995)

Acknowledgements

My graduate education has provided me the opportunity to explore the field of atmospheric chemistry. For encouraging me to tackle a broad range of subjects, but continually focusing my studies on the most intriguing (if slightly frustrating) issues in the field, I am indebted to my advisor, John Seinfeld. His trust and patience were the foundation for all of my achievements during the past four years. The indefatiguable enthusiasm with which he strives to understand science has provided an inspiring example for me for the years to come.

I would like to thank the National Science Foundation for supporting me as a Fellow through three years of my graduate work. The Chemical Engineering Department has provided a wealth of resources and support for my education, including the Landau Fellowship, which supported my fourth year of study.

I have had the fortune to work with several experts in a variety of fields as part of my work. All of the work on aerosol instrumentation has been completed in collaboration with Richard Flagan. His helpful suggestions and eagerness to try different appoaches have been an endless source of new ideas.

The modeling work on a simplified marine aerosol system was guided largely by the wisdom of Spyros Pandis. Helpful comments by M. O. Andreae are also gratefully appreciated.

My participation in the Atlantic Stratocumulus Transition Experiment and Marine Aerosol Gas Exchange was an amazing introduction into atmospheric chemistry. By organizing a valiant effort to collect a Lagrangian set of atmospheric chemistry data, Barry Huebert provided the insight to the challenges of field sampling that hooked my interest. He has continued to be a valued mentor and a witty colleague, for both of which I am grateful. I also wish to thank Byron Blomquist, Brigitte Noone, Richard Benner, Antony Clarke, and the crew of the R/V *Oceanus* for their generous assistance in the field. I am grateful to Chris Bretherton for his calculation of back-trajectories for the air masses studied. This work was supported in part by National Science Foundation grant ATM-9307603 and by Office of Naval Research grant N00014-93-1-0555.

The development of the Radially Classified Aerosol Detector provided me the opportunity to implement a new instrument design for aircraft aerosol sampling. This development effort was primarily supported by the Office of Naval Research Ship Tracks Initiative under grant N00014-93-1-0872. I am grateful for the help of the University of Washington Cloud and Aerosol research group for their assistance in integrating the RCAD and the filter collection apparatus into the C131a with special thanks to Dean Hegg, Ron Ferek, Peter Hobbs, Jack Russell, and Don Spurgeon. Access to the laboratories of TSI, Inc., and the support of Rob Caldow, Fred Quant, Rick Holm, Maynard Havlicek, and Gil Sem were indispensable in constructing and cali-

brating the modified CPC. I owe thanks to Mark Stolzenburg and Shou-Hua Zhang, who have been generous in giving their time to teach me the tricks of mechanical and electrical design.

Sampling of aerosol size distributions and organic compounds was also supported by the Office of Naval Research as part of the Monterey Area Ship Tracks Experiment. For designing and coordinating the MAST Experiment, I appreciate the tireless efforts of Robert Bluth, Phil Durkee and Kevin Noone. In collecting and interpreting these data, I owe gratitude to Patrick Chuang, Carlos Maldonado, Rob Pockalny, Rebecca Green, Kurt Nielsen, and Doug Johnson.

In analyzing the organic samples, I was aided by the state-of-the-art instrumentation of the Bank of America Environmental Analysis Center at C.I.T., as well as the extensive experience of several people in the Atmospheric Aerosol Group. Glen Cass, Lynn Hildemann, Jean Andino, Matt Fraser, and Peter Green provided helpful suggestions in designing the sampling and analysis method I developed for the MAST Experiment.

For getting me through all of the impossible challenges of everyday graduate work, I would like to thank my research group and dear friends at C.I.T., especially Jean Andino, Melissa Lunden, Paul Drayton, Donald Dabdub, Alison McCurdy, Micah Altman, Sarah Ngola, and Susan Rubin.

Without the support of numerous inspiring educators over the past twenty years, I could not have succeeeded here. Rosamond Naylor, Paul Roberts, and Bud Homsy have advised me since my undergraduate work at Stanford and have provided sound advice in my decisions in graduate school. I am indebted especially to Alice Gast for continuing to inspire and guide me in

my work in Chemical Engineering.

To my brother, Noel, and my good friends in scattered locations, I owe many thanks for keeping me in touch with life on the outside. For giving me the strength to take challenges and for supporting my stubborn pursuit of them, I am grateful to my parents, Donna and Paul, for their love and respect. This work is dedicated to them, and to the memory of Aranka Feldstein Russell.

Abstract

Understanding the physics and chemistry of the marine atmosphere requires both predicting the evolution of its gas and aerosol phases and making observations that reflect the processes in that evolution. This work presents a model of the most fundamental physical and chemical processes important in the marine atmosphere, and discusses the current uncertainties in our theoretical understanding of those processes. Backing up these predictions with observations requires improved instrumentation for field measurements of aerosol. One important advance in this instrumentation is described for accelerating the speed of size distribution measurements. Observations of aerosols in the marine boundary layer during the Atlantic Stratocumulus Transition Experiment (ASTEX) provide an illustration of the impact of cloud processing in marine stratus. More advanced measurements aboard aircraft were enabled by redesigning the design of the system for separating particles by differential mobility and counting them by condensational growth. With this instrumentation, observations made during the Monterey Area Ship Tracks (MAST) Experiment have illustrated the role of aerosol emissions of ships in forming tracks in clouds. High-resolution gas chro-

matography and mass spectrometry was used with samples extracted by supercritical fluid extraction in order to identify the role of combustion organics in forming ship tracks. The results illustrate the need both for more sophisticated models incorporating organic species in cloud activation and for more extensive boundary layer observations.

Contents

1 Introduction 1

2 Aerosol Production and Growth in the Marine Boundary Layer 7

2.1 Modeling the Dimethyl Sulfide-Cloud Condensation Nuclei System 14

2.1.1 Gas Phase Chemistry 16

2.1.2 Aerosol Growth 18

2.1.3 Non-Precipitating Clouds 23

2.1.4 Precipitating Clouds 24

2.2 Predicting the DMS-CCN Link 25

2.3 Model Sensitivity to Prescribed Conditions and Parameters . . 34

2.3.1 Cloud Diel Cycle 34

2.3.2 Cloud Frequency and Duration 38

2.3.3 OH Concentration 42

2.3.4 Aerosol and Gas-Phase Parameters 45

2.3.5 Aerosol Distribution Description 49

2.4 Comparison With Other Models 52
2.5 Regimes of Model Behavior 54
2.6 Discussion 55

3 Asymmetric Instrument Response Resulting from Mixing Effects in Accelerated DMA-CPC Measurements 69

3.1 Kernel Function for Scanning Mobility Measurements 74
3.2 Instrument Response Characterization 79
3.2.1 History-Dependent Transfer Function 83
3.2.2 Measurement Channel Response 91
3.3 Data Inversion 97
3.4 Simulations 99
3.4.1 Distortion of Kernel Function with Mixing Time 100
3.4.2 Predicted Asymmetry of Increasing and Decreasing Scans 105
3.5 Conclusions 105

4 Characterization of Submicron Aerosol Size Distributions from Time-Resolved Measurements in ASTEX/MAGE 112

4.1 Characterizing Atmospheric Aerosols in Situ 116
4.2 Accelerated Aerosol Mobility Measurements 118
4.3 Time-Resolved Aerosol Measurements in ASTEX/MAGE . . . 123
4.4 Implications for Aerosol Processing Over the Ocean 136

5 Radially-Classified Aerosol Detector for Aircraft-Based Submicron Aerosol Measurements 144

5.1 Aircraft-based Aerosol Measurements 146

5.2 Instrument Design 150
5.2.1 Alternating Double-Bag Sampler 153
5.2.2 Neutralizer 155
5.2.3 Flow Control 157
5.2.4 Radial DMA 159
5.2.5 Voltage Ramp 160
5.2.6 Turbo CPC 162
5.2.7 RCAD Software 164
5.3 Characterization of Instrument Components 165
5.3.1 Particle Losses in Tubing and Sampling Chamber . . . 165
5.3.2 Classifier Resolution 169
5.3.3 Particle Counting Efficiency 170
5.3.4 Kernel Function for RCAD Operation 173
5.4 In-flight Performance 178
5.4.1 Temperature and Humidity 180
5.4.2 Pressure and Flow Rates 182

6 Submicron Aerosol Size Distribution Measurements in Ship Tracks During the MAST Experiment **191**

6.1 June 11 (JDT 162) 194
6.2 June 27 (JDT 178) 196
6.3 June 28 (JDT 179) 201
6.4 June 29 (JDT 180) 206
6.5 June 30 (JDT 181) 211

7 Combustion Organic Aerosol as Cloud Condensation Nuclei in Ship Tracks **227**

7.1 Airborne Sampling of Interstitial and Cloud Droplet Residual Aerosol 235

7.1.1 Sample Collection Protocol 236

7.1.2 Extraction and Identification Procedure 238

7.2 Organic Species in Marine Stratus 241

7.2.1 Variability of Background Conditions 247

7.2.2 Ship Track and Plume Characteristics 250

7.2.3 Case Studies from MAST 253

7.3 Partitioning of PAHs Between Cloud Droplets and Interstitial Aerosol 257

8 Conclusions **273**

A The Relationship Between DMS Flux and CCN Concentrations in Remote Marine Regions **277**

B Detailed Method for Online SFE/GC-MS Analysis **291**

B.1 Connecting SFE. 292

B.2 In-line SFE-GC extraction. 293

B.3 GC/MS Method. 295

B.3.1 HP-5MS column method 5mscryramp320by2.m. 296

B.3.2 DB-1701 column method 1701cryramp280hi2.m. 301

B.4 Disconnecting SFE. 308

C Organic Analysis Logs, Standards, and MAST Experiment Data 310

List of Tables

2.1 Base case model parameters. 26
2.2 Variation of parameters in dynamic DMS/CCN model. 47

5.1 Comparison of instrumentation for measuring size-classified submicron aerosol particles. 148
5.2 Dimensions of six differential mobility analyzer (DMA) designs. 151

7.1 Previous measurements of PAHs, PAQs and PAKs. 229
7.2 Characterization of detection limits by SFE/GC-MS for PAH, PAQ and PAK standards. 240
7.3 Summary of samples analyzed. 244
7.4 Water solubilities for PAHs. 260

B.1 SFE Procedure. 295

C.1 Aerosol interstitial and out-of-cloud filter samples analysis log. 311
C.2 Residual cloud droplet samples analysis log. 312
C.3 Primary standards and their retention times. 313

C.4 Compound concentrations in all samples and blanks collected for MAST Experiment. 314

List of Figures

2.1 A modeling perspective of the DMS-CCN system. 15
2.2 Predicted variation of the dimethyl sulfide (DMS) and SO_2. . 28
2.3 Predicted variation of the $H_2SO_{4(g)}$. 29
2.4 Predicted variation of the nuclei and accumulation mode (CCN) aerosol number concentration. 31
2.5 Predicted value of nuclei and CCN concentrations for DMS fluxes. 33
2.6 Predicted CCN variation with the cloud occurring from 2300 to 000. 36
2.7 Predicted CCN variation with the cloud occurring from 1100 to 1200. 37
2.8 Average CCN predicted for one cloud occurring per day. . . . 39
2.9 Average CCN predicted for two clouds occurring per day. . . . 40
2.10 Average CCN predicted for four clouds occurring per day. . . . 41
2.11 Comparison of "ensemble-average" of predicted CCN for cloud frequencies of 1, 2, and 4 d^{-1}. 43

2.12 Predicted nuclei and CCN concentrations as functions of the maximum OH concentration. 44
2.13 Predicted CCN concentrations for various functional forms of diurnal OH variations. 46
2.14 Average CCN for values of the nucleation scaling factor (k_n) and the sulfuric acid accommodation coefficient (a_e). 56

3.1 Experimental data from scanning measurements. 73
3.2 Step change response of commercial CPCs. 84
3.3 The system transfer function for several values of θ_s. 90
3.4 The maximum value of the transfer function. 92
3.5 Isopleths of ζ/ζ^*. 93
3.6 Kernel functions for SEMSu channel 10. 101
3.7 Kernel functions for SEMSd channel 20. 102
3.8 Predicted raw SEMSu measurements for a bimodal distribution. 103
3.9 Predicted raw SEMSd measurements for a bimodal distribution. 104
3.10 Inverted bimodal SEMSu size distribution. 106
3.11 Inverted bimodal SEMSd size distribution. 107
3.12 Four channels of the SEMSu and SEMSd kernel functions. . . 108

4.1 Schematic diagram of the SEMS-DMA. 119
4.2 Kernel functions illustrating the SEMS operation. 122
4.3 Back-trajectories for the position of the R/V *Oceanus* at JDT 160.5 and 164.5 124
4.4 Summary of total particle concentrations for JDT 160 and 161 (June 8 and 9). 125

4.5 Aerosol size distributions from 2032 to 2048 on June 8. . . . 128
4.6 Aerosol size distributions measured with SEMSu from 0724 to 0742 on June 9. . . . 130
4.7 Summary of total particle concentrations from JDT 163.5 to 165.5 (June 11 to 13). . . . 131
4.8 Aerosol size distributions from 0322 to 0336 on June 12. . . . 133
4.9 Summary of total particle concentrations from JDT 163.78 to 164.00 (June 12). . . . 135
4.10 Comparison of the aerosol size distributions presented in this work with other measurements made in the marine boundary layer. . . . 138

5.1 Components and configuration of the Radial Classified Aerosol Detector (RCAD). . . . 152
5.2 Grab sampling apparatus. . . . 154
5.3 Design of the housing for a bipolar charger. . . . 155
5.4 Particle charging efficiency in the bipolar neutralizer. . . . 156
5.5 Exponential Ramp Circuit (ERC). . . . 161
5.6 Particle transmission efficiency through the RCAD. . . . 167
5.7 Performance of the exponential ramp circuit. . . . 171
5.8 Apparatus for calibration of modified condensation particle counter. . . . 172
5.9 Particle counting efficiency for the modified CPC. . . . 174
5.10 Response of the RCAD to a step change in concentration. . . . 177
5.11 Kernel function of the RCAD system. . . . 179

5.12 Illustration of temperature variation in flight. 181
5.13 Performance of the flow control system in flight. 183

6.1 RCAD Aerosol Size Distributions, June 11, 1994: Flight 1641.1.197
6.2 RCAD Aerosol Size Distributions, June 11, 1994: Flight 1641.2.198
6.3 RCAD Aerosol Size Distributions, June 11, 1994: Flight 1641.3.199
6.4 RCAD Aerosol Size Distributions, June 11, 1994: Flight 1641.4.200
6.5 RCAD Aerosol Size Distributions, June 27, 1994: Flight 1646.1.202
6.6 RCAD Aerosol Size Distributions, June 27, 1994: Flight 1646.2.203
6.7 RCAD Aerosol Size Distributions, June 27, 1994: Flight 1646.3.204
6.8 RCAD Aerosol Size Distributions, June 27, 1994: Flight 1646.4.205
6.9 RCAD Aerosol Size Distributions, June 28, 1994: Flight 1647.1.207
6.10 RCAD Aerosol Size Distributions, June 28, 1994: Flight 1647.2.208
6.11 RCAD Aerosol Size Distributions, June 28, 1994: Flight 1647.3.209
6.12 RCAD Aerosol Size Distributions, June 28, 1994: Flight 1647.4.210
6.13 RCAD Aerosol Size Distributions, June 29, 1994: Flight 1648.1.212
6.14 RCAD Aerosol Size Distributions, June 29, 1994: Flight 1648.2.213
6.15 RCAD Aerosol Size Distributions, June 29, 1994: Flight 1648.3.214
6.16 RCAD Aerosol Size Distributions, June 29, 1994: Flight 1648.4.215
6.17 RCAD Aerosol Size Distributions, June 29, 1994: Flight 1648.5.216
6.18 RCAD Aerosol Size Distributions, June 30, 1994: Flight 1649.1.218
6.19 RCAD Aerosol Size Distributions, June 30, 1994: Flight 1649.2.219
6.20 RCAD Aerosol Size Distributions, June 30, 1994: Flight 1649.3.220
6.21 RCAD Aerosol Size Distributions, June 30, 1994: Flight 1649.4.221
6.22 RCAD Aerosol Size Distributions, June 30, 1994: Flight 1649.5.222

6.23 RCAD Aerosol Size Distributions, June 30, 1994: Flight 1649.6.223

7.1 Distribution of compounds detected for all samples (PAHs, PAQs, and PAKs) by class. 245
7.2 Ambient variability in and averages of PAH concentrations. . . 248
7.3 Plume and track variability in and average concentrations of PAHs. 251
7.4 Case study for MAST study day 163. 255
7.5 Case study for MAST study day 178. 258
7.6 Comparison of calculated activation indices and water solubilities. 262

B.1 Total ion chromatogram for HP5MS column method. 302
B.2 Total ion chromatogram for DB1701 column method. 307

Chapter 1

Introduction

Submicron aerosol particles can affect the radiative properties of the Earth's atmosphere both through direct light scattering and by serving as cloud condensation nuclei (CCN). Since marine clouds cover large areas of the Earth's oceans, the resulting alterations in the global radiation balance could result in regional climate changes. In the stratus cloud layer, the absorption and scattering of light that would otherwise be reflected directly at ocean surfaces can cause cooling in the boundary layer. The optical scattering properties of the aerosol are determined primarily by the physical distribution of particles with size but are also a function of particle composition, as the chemical makeup of a droplet will determine its refractive index. The indirect consequences of aerosols also vary with both the physical and chemical properties of marine aerosols.

Many fundamental questions about the processes controlling the evolution of marine aerosols remain unanswered. From what marine source are

new particles in the atmosphere generated? What are the mechanisms by which, in the absence of continental influence, such particles grow to sizes sufficient to activate to cloud droplets? Which mechanisms govern the formation and persistence of the characteristic features of the marine aerosol size distributions? And, how do continental influences impact both the structure of the size distribution and the relative number of CCN that are formed? How closely are the CCN concentrations in the boundary layer related to the droplet concentrations of the clouds produced when this aerosol is activated?

Aerosol particles are the cynosure of these questions governing the chemistry of the marine boundary layer. Marine boundary layer aerosol reflects the history of the air mass through its number concentrations and size distribution. Over the ocean, an aerosol signature of continental emissions may persist for several days. Eventually, drizzle events result in wet scavenging leading to an aerosol that is characteristic of that in the unperturbed marine boundary layer. Models of marine aerosol processes have provided several alternative frameworks for addressing the questions posed above.

The dependence of cloud condensation nuclei (CCN) production on the marine dimethylsulfide (DMS) flux has been modelled with a dynamic description of the gas-, aerosol- and aqueous-phase processes in a closed air parcel. The results support the conclusion that an approximately linear dependence exists between CCN concentration and DMS flux under typical remote marine conditions. This linearity does not hold for low DMS fluxes (the threshold is typically near 2.5 μmole m^{-2} d^{-1}) because the sea-salt particles heterogeneously convert the available SO_2 to sulfate inhibiting the creation of new particles. Chapter 2 describes a series of sensitivity stud-

ies used to investigate the conditions under which this linear relationship holds. The study focuses particular attention on the impact of the timing and frequency of cloud events. The regimes of the model's semiempirical parameters were probed, showing that the uncertainty associated with two such parameters, namely the nucleation rate scaling factor and the sulfuric acid accommodation coefficient, is sufficient to change the predicted CCN production due to DMS from over 300 cm^{-3} d^{-1} to none. This sensitivity accounts for most of the range of results predicted by previous models of the DMS-CCN system.

Resolving the questions posed by the uncertainties in model descriptions requires improved measurements of atmospheric properties in the marine boundary layer. As part of the Atlantic Stratocumulus Transition Experiment and Marine Aerosol Gas Exchange (ASTEX/MAGE), ship-based aerosol size distribution measurements were collected with a scanning electrical mobility spectrometer (SEMS) aboard the R/V *Oceanus*. Employing this method required developing a description of the instrument kernel function which would take the non-ideal flow profiles within the instrument into account. The derivation of this kernel function is discussed in Chapter 3.

The resulting fast time resolution attainable with these measurements illustrates some of the short time scale variability of both the marine background aerosol and of the anthropogenically-influenced continental air masses. The aerosol size distributions provide characteristic signatures for different atmospheric conditions, showing low-concentration bimodal distributions in cleaner air masses and higher-concentration single-mode distributions in air masses with apparent recent continental influence. These results

are illustrated in Chapter 4 and are compared to previous measurements of marine aerosol size distributions.

The appearance and persistence of anomalous lines in cloud structures visible in satellite imagery, commonly attributed as ship tracks, provide an opportunity to study cloud processing through a surrogate. Measurements of aerosol in ship tracks enhance both our picture of marine boundary layer chemistry and of the nature of its interaction with anthropogenic aerosols. Understanding the stages in the particle evolution of a ship track requires identifying the mechanisms of the perturbation imposed on the marine boundary layer aerosol. However, in order to take advantage of this atmospheric-scale experiment, instruments with resolution higher and faster than commercial designs are required.

As part of the MAST Experiment, instrumentation for fast characterization of fine particle size distributions was designed, implementing both a radially-designed aerosol classifier and a high-flow, high-effiency condensation nuclei counter. The heating and cooling elements in a commercially available CNC (TSI Model 3010) were modified in order to make the condensation of ultrafine particles more efficient by increasing the difference in temperatures in the saturator and the condenser. The resulting instrument utilizes feedback control of flows for airborne adjustments and is described in detail in Chapter 5.

This instrumentation has provided detailed physical descriptions of the precursors of cloud condensation nuclei both in and near ship tracks. The evidence from ship track measurements we have collected indicates that combustion emissions in pristine air masses can effect observable increases in local

cloud reflectivity by their flux of small particles, providing additional nucleation sites for condensible gas-phase species and shifting the cloud droplet distribution to smaller sizes. This connection suggests an important link between cloud droplet concentrations and the boundary layer aerosol. This link is illustrated in the size distribution data collected with the RCAD aboard the University of Washington C131 research aircraft as part of MAST. These data are summarized in Chapter 6.

The chemistry of ship tracks also provides important clues to the activation process by which some nuclei grow to droplets in cloud. For this reason, specially-constructed filters have been employed to characterize in detail the chemical composition of ship tracks. These filters maximize sample collection by utilizing high flow rates, while conforming to the constraints of aircraft measurements, so that the detection capabilities of high-resolution Gas Chromatography and Mass Spectrometry (GC-MS) could be used to identify trace organics. Polycyclic aromatic hydrocarbons (PAHs) have been sampled in marine stratus conditions to identify the role of anthropogenic combustion emissions in activation of aerosol to form droplets in cloud. The MAST Experiment provided an opportunity to acquire data on the role of organic compounds in clouds that could be correlated to distinct satellite-observed radiative signatures. The identification of PAHs in cloud droplet residual samples indicate that several PAHs are present in cloud condensation nuclei in anthropogenically influenced air, and do result in activated droplets in cloud. These results establish the presence of combustion products, such as PAHs, in submicron aerosols in anthropogenically-influenced marine air, with enhanced concentrations in air polluted by ship effluent. The presence

of PAHs in droplet residuals indicates that some fraction of those combustion products is present in CCN that activate in cloud. In addition, the correlation of the probability that a compound will be found in cloud droplets rather than in the unactivated interstitial aerosol to the compound's water solubility has been investigated. These results are discussed in Chapter 7.

Finally, Chapter 8 assesses the impact of these contributions and their implications for future advances toward reconciling the atmospheric measurements collected to date with our theoretical understanding of the processes which control the evolution of aerosol in the marine environment.

Chapter 2

Aerosol Production and Growth in the Marine Boundary Layer

Published in the *Journal of Geophysical Research*, 1994 (99: 20,989 - 21003).

Lynn M. Russell[1], Spyros N. Pandis[2], and John H. Seinfeld[1]

[1]Department of Chemical Engineering, California Institute of Technology, Pasadena, CA

[2]Departments of Chemical Engineering and Engineering and Public Policy, Carnegie Mellon University, Pittsburgh, PA

Aerosols, solid or liquid particles in the 0.001 to 10 μm size range, play a potentially important role in the Earth's climate system because of their direct and indirect interaction with solar and terrestrial radiation [Coakley et al., 1983; Charlson et al., 1992a; Fouquart and Isaka, 1992]. These particles scatter and absorb radiation in the solar and thermal infrared spectral ranges and modify the radiation budget of the planet. Aerosols also serve as the condensation nuclei on which cloud droplets form. Consequently, the aerosol concentration, size, and water solubility have an immediate influence on the concentration and size of cloud droplets and hence on the radiative properties of clouds. The direct and indirect aerosol effects on the Earth's radiation budget have been estimated as possibly comparable in magnitude, but opposite in sign, to those caused by greenhouse forcing [Wigley, 1989; Charlson et al., 1987, 1990, 1991, 1992b].

A significant fraction of the tropospheric aerosol mass in the submicron-size particles is estimated to be derived from homogeneous and in-cloud oxidation of gaseous sulfur compounds [Langner et al., 1992] which are both of anthropogenic (mainly SO_2) and biogenic origin. The aqueous phase reactions of SO_2 with $H_2O_{2(aq)}$, $O_{3(aq)}$ and other oxidants are expected to dominate the overall SO_2 to sulfate conversion [Langner et al., 1992]. Natural emissions of sulfur are estimated to represent a significant part of the total flux of gaseous sulfur to the atmosphere [Andreae, 1985].

Most species of phytoplankton excrete dimethylsulfide (DMS) which escapes to the air as dimethylsulfide vapor and reacts to form non-sea-salt sulfate aerosol. This non-sea-salt sulfate aerosol is abundant in the marine boundary layer (MBL) and contributes to the cloud condensation nuclei

(CCN) in the marine atmosphere [Charlson et al., 1987]. In the unpolluted MBL the concentration of particles capable of being CCN varies from about 30 to 200 cm^{-3} [Pruppacher and Klett, 1980].

Shaw [1983] first suggested that the aerosol produced during the atmospheric oxidation of biogenic sulfur gases may affect climate. Charlson et al. [1987] and Meszaros [1988] proposed that DMS is the major source of aerosol sulfate in the remote marine atmosphere and, in turn, of cloud CCN. They hypothesized that an increase in marine DMS emissions would increase the number density of sulfate aerosol and, consequently, the number density of the cloud droplets, thus enhancing cloud albedo [Twomey, 1974; Coakley et al., 1983; Scorer, 1987; Radke et al., 1989]. This enhancement would act as a negative forcing on global temperature. Lower temperatures would then result in reduced marine productivity and DMS emission fluxes. The effect of aerosols on cloud properties has been inferred indirectly from satellite studies of ship tracks in marine stratocumulus clouds that are consistently brighter in visible wavelengths [Coakley et al., 1983; Radke et al., 1989]. The increase in brightness is postulated to result not directly from particles from the ship smoke but rather from elevated CCN concentrations that enhance the cloud visible optical depth.

From a climatic perspective, low-level stratiform clouds are of the most interest because of their large spatial and temporal extent and high albedo. Marine boundary layer clouds contribute about a third of the Earth's albedo [Charlson et al., 1987]. For constant cloud liquid water content, somewhere between a 40 and a 100% increase in the number concentration of cloud droplets has been estimated to be sufficient to counterbalance the CO_2 dou-

bling effect [Charlson et al., 1987; Slingo, 1990]. CCN variations are also expected to result in changes of the total cloud liquid water content. Drizzle is frequently observed in marine stratocumulus [Brost et al., 1982; Albrecht et al., 1985; Albrecht, 1989]. Albrecht [1989] suggested that an increase of CCN that decreases mean droplet size reduces drizzle production, resulting in larger cloud liquid water and fractional cloudiness. Thus an increase of the CCN concentration may lead to droplet size reduction and an increased cloud albedo both directly via optical thickness enhancements at constant cloud liquid water content and indirectly through increased cloud water and increased low-level cloud amounts.

Several components of the so-called CLAW hypothesis [Charlson et al., 1987] for the complicated DMS-CCN link have already been verified by field measurements. The warmest, most saline, and most intensely illuminated regions of the oceans have indeed the highest rate of DMS emission to the atmosphere [Bates et al., 1992]. The largest DMS flux comes from the tropical and equatorial oceans. Although there are large parts of the oceans that are influenced by anthropogenic sulfur emissions (e.g., western Pacific, parts of Atlantic Ocean), there are vast remote ocean regions (e.g., mid latitude North Pacific) where natural sulfur emissions account for essentially all the atmospheric non-sea-salt sulfate [Savoie and Prospero, 1989]. The number concentration measurements of sulfate particles in the remote MBL suggest that sulfate is the dominant and probably the limiting species for cloud condensation nuclei in remote oceans [Clarke et al., 1987]. New particle concentrations are inversely related to available aerosol surface area and their volatility suggests a sulfuric acid composition [Clarke, 1992]. Clarke et

al. [1987] found that in remote marine areas the mass concentration of submicron particles increases over biologically active parts of the ocean, with the highest concentrations being observed in summer [Bigg et al., 1984]. Ayers et al. [1991] observed a high correlation between DMS fluxes across the sea surface and concentrations of aerosol particles.

Several physical and biological aspects of the CLAW hypothesis have yet to be quantified. A complete evaluation of the importance of the DMS-CCN feedback mechanism requires quantitative understanding of the relationships between (a) the meteorological conditions (temperature, sunlight intensity, and wind speed) and the DMS flux; (b) the DMS flux and the CCN number concentration; (c) the CCN number concentration and the cloud properties (cloud droplet concentrations, liquid water content, and cloud lifetime); (d) the cloud properties and the cloud albedo; and (e) the cloud albedo and the meteorological conditions. In this study, the second step of this sequence, namely the link between the DMS and the CCN number concentration, is investigated in detail.

The large number of the DMS-CCN system variables, their spatial and temporal variability, and the highly variable time constants involved have made it difficult to quantify through field campaigns the relationship between DMS fluxes and cloud albedo. A complementary approach is to probe the theoretical basis for the link between DMS flux and CCN by developing a model incorporating all of the appropriate chemical and physical processes and using it together with the available field data.

As a first approximation, this gas-to-particle link could be investigated using a time-dependent nucleation and condensation model. Kreidenweis

and Seinfeld [1988] proposed a framework for such a model using a three-variable aerosol parameterization and focusing on the kinetics of the H_2SO_4 and MSA formation. Hegg et al. [1990, 1991] and Hegg and Hobbs [1992] have adapted this model to study conditions in the remote troposphere that might foster nucleation and growth of aerosol. Raes and Van Dingenen [1992] demonstrated, using a multi-sectional aerosol model, that current uncertainty about condensation and nucleation rates can influence the outcome of theoretical predictions. The same model has also been used to simulate the effect of boundary layer-free troposphere interaction on CCN levels [Raes et al., 1992b].

Lin et al. [1992] and Lin and Chameides [1993] evaluated the competing mechanisms involved in the process of CCN formation by comparing their characteristic times and estimated that heterogeneous SO_2 conversion is not important as a growth mechanism of small sulfate particles to CCN. However, Chameides and Stelson [1992] have shown, using an aqueous phase chemistry model, that heterogeneous conversion of SO_2 is a significant sink when sea-salt particles are present. Fitzgerald [1992] used a model describing aerosol dynamics and gas phase chemistry in a well-mixed MBL over the remote ocean to show that in fair weather the nucleation rate of new sulfate particles is not high enough to maintain the population of small particles against depletion due to coagulation and growth to larger sizes.

However, including meteorological perturbations to the system such as periodic reduction in accumulation and coarse-mode particles due to precipitation scavenging increases sulfuric acid vapor concentrations and results in nucleation rates that can restore the population of small particles, thus

allowing a different interpretation of such model results. Despite the improvements of our understanding of the DMS-CCN system as a result of the above studies, the source and growth mechanisms of new particles up to sizes effective as CCN in remote regions remain uncertain.

In this study we propose a dynamic model which reproduces the essential features of the evolution of sulfate aerosol to CCN in the marine atmosphere. The model used in the present study is the dynamic version of the Pandis et al. [1994] steady-state model. The same process parameterizations and model variables are used, with the three exceptions mentioned below (OH concentration variation, cloud process variation, coagulation).

The model under a set of typical marine conditions is first presented and then used as the base case for sensitivity studies. We consider extensively the effects of varying both the initial conditions and the empirical parameters used in our model, to identify the range of values for which the conclusions reached here might be applicable. We focus particular attention on the model response to variations in cloud occurrences. This type of sensitivity is better reflected in terms of regimes of behavior of the model. Those regimes for two of the poorly known parameters, the accommodation coefficient and the nucleation scaling factor, are investigated.

2.1 Modeling the Dimethyl Sulfide-Cloud Condensation Nuclei System

The present model incorporates the primary sulfur cycle in the marine boundary layer, from the emission of DMS to the atmosphere to the fate of particulate sulfate. We presuppose a well-mixed boundary layer, topped with intermittent stratus clouds, as illustrated in Figure 2.1. In the gas phase, the processes considered are homogeneous oxidation of biogenic-derived sulfur species to products which may then be transferred to the particulate phase. Mass transfer from the gas phase is generally the rate-limiting step in particulate growth for heterogeneous reactions, but homogeneous nucleation can also produce particulate sulfate. Aqueous phase chemistry in both cloud droplets and sea-salt aerosol provides additional oxidation pathways. Processing of the air parcel through nonprecipitating stratus clouds results in additional transfer of SO_2 to activated cloud droplets, followed by evaporation, resulting in particles with higher sulfate content. Precipitating clouds are the main means for removal of particulate sulfate from the air parcel.

The development of the equations describing processes in the marine boundary layer is summarized here, focusing on distinctions from the steady state system described previously [Pandis et al., 1994]. The modeling framework proposed by Pandis et al. [1994] has been used to follow the variation of the key reactants, the DMS gas phase concentration, $(DMS)_g$, the SO_2 gas phase concentration, $(SO_2)_g$, the H_2SO_4 gas phase concentration, $(H_2SO_4)_g$, the nucleation mode number concentration, N_1, and the CCN number con-

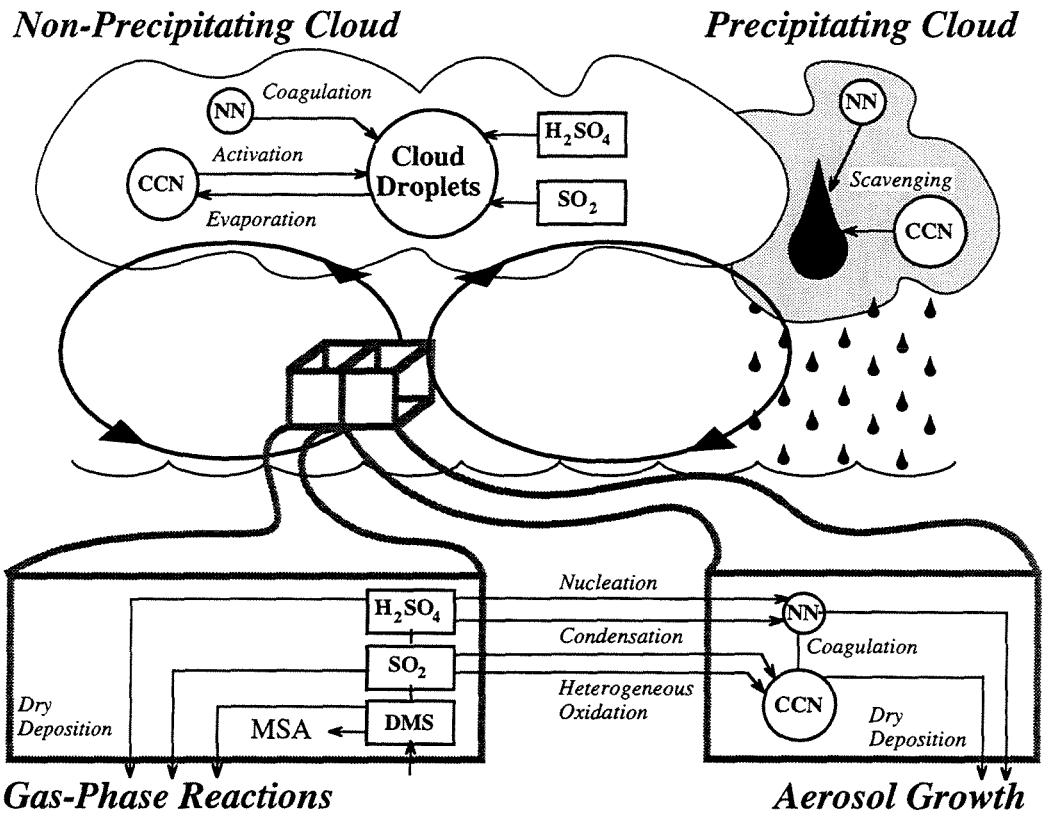

Figure 2.1: A modeling perspective of the DMS-CCN system. The figure illustrates the interaction between the physical and the chemical processes incorporated in the model. NN refers to nucleation-mode nuclei, and CCN are cloud condensation nuclei.

centration, N_2. To implement the diurnal effects of the MBL in our model, we have specified the OH concentration as a sinusoidal diel cycle and have introduced clouds as intermittent, finite-duration events during which cloud processing influences the aerosol distribution evolution.

2.1.1 Gas Phase Chemistry

In the gas phase, the primary oxidant is the OH radical. The concentration of OH in the atmosphere, $(\mathrm{OH})_g$, is governed by photochemical reactions and, consequently, is a function of the amount of UV light that reaches the MBL. The fraction of light reaching the MBL will vary with the solar zenith angle, local cloud cover, and non-MBL atmospheric composition (including volcanic sulfate aerosol and stratospheric ozone distribution). Since predicting the consequent variations of OH would require a multi dimensional tropospheric model which accounts for differences in both location and season, we have prescribed as our base case a diurnal cycle consisting of a sinusoidal variation that peaks at 1200. This choice is constructed to emulate a lower to mid latitude day with only partial cloud cover. The effects of this choice on the model predictions will be investigated in detail in section 2.3.2.

This diel cycle, in turn, governs the atmospheric $(\mathrm{DMS})_g$ as the equation describing the rate of change of $(\mathrm{DMS})_g$ is

$$\frac{(\mathrm{DMS})_g}{dt} = F_{DMS} - k_{DMS}(\mathrm{OH})_g(\mathrm{DMS})_g \tag{2.1}$$

where F_{DMS} is the net flux and k_{DMS} is the rate constant for DMS oxidation

by OH.

Sulfur dioxide is produced by this reaction, with an empirically determined fractional yield, which is designated as y_{SO_2}. Additional products of DMS oxidation, in particular MSA, were shown by Pandis et al. [1994] to affect particle size by less than 6% for ranges of F_{DMS} and consistent with field measurements [Quinn et al., 1993; Fitzgerald, 1991]. The fates of those products have, consequently, been neglected here. Considerable uncertainty still surrounds the DMS oxidation pathways and products. Berresheim et al. [1993] suggested that the dominant oxidation product of DMS may be dimethylsulfone ($DMSO_2$). Bandy et al. [1992] proposed that the major pathway for the oxidation of DMS to H_2SO_4 is via SO_3 and not SO_2 , and Lin and Chameides [1993] showed that such a mechanism is compatible with the MSA/non-sea-sulfate ratios measured in remote marine air. The implications of these alternative reaction pathways for the modeled DMS/CCN system have been briefly discussed by Pandis et al. [1994].

Gas phase SO_2 is removed by several pathways including deposition, oxidation, and heterogeneous reaction with aerosol and cloud,

$$\begin{aligned}\frac{d(\mathrm{SO_2})_g}{dt} &= y_{\mathrm{SO_2}} k_{DMS} (\mathrm{OH})_g (\mathrm{DMS})_g - K_{dep}^{\mathrm{SO_2}} (\mathrm{SO_2})_g \\ &\quad - k_{\mathrm{SO_2}} (\mathrm{OH})_g (\mathrm{SO_2})_g - R_{aeros} - R_{cloud}^{\mathrm{SO_2}} \end{aligned} \tag{2.2}$$

The deposition rate constant of $(SO_2)_g$, $K_{dep}^{SO_2}$, for a well- mixed boundary layer can be defined as the ratio of the SO_2 deposition velocity, taken to be 0.5 cm s^{-1}, to the mixing height of the boundary layer, H_{mix}. The rate constant $k_{SO_2} = 10^{-12}$ cm^3 $molecule^{-1}$ s^{-1} [Atkinson and Lloyd, 1984].

Sulfuric acid has a very low vapor pressure, so almost all of the $(H_2SO_4)_g$ produced from the SO_2 oxidation is transferred to the aerosol or cloud phases. Loss by deposition is analogous to the $(SO_2)_g$ calculation. The $(H_2SO_4)_g$ balance is

$$\frac{d(H_2SO_4)_g}{dt} = k_{SO_2}(OH)_g(SO_2)_g - L_{nucl} - R_{cloud}^{H_2SO_4} - (K_{mt}^1 N_1 + K_{mt}^2 N_2)(H_2SO_4)_g - K_{dep}^{H_2SO_4}(H_2SO_4)_g \quad (2.3)$$

where K_{mt}^i is the sectional mass transfer coefficient for section i [Pandis et al., 1994].

2.1.2 Aerosol Growth

Most of the aerosol particles in the MBL are in the submicron regime. We have chosen our description of the submicron particle size distribution based on a series of measurements that all indicate the presence of a temporally stable bimodal distribution in the pristine marine boundary layer [Quinn et al., 1993; Hoppel et al., 1989]. Consequently, we represent the distributions as two sections as follows:

$$\begin{aligned} n(x) &= 0, && x < log_{10}(D_1) \\ n(x) &= n_1, && log_{10}(D_1) < x < log_{10}(D_a) \\ n(x) &= n_2, && log_{10}(D_a) < x < log_{10}(D_2) \\ n(x) &= 0, && log_{10}(D_2) < x \end{aligned}$$

where D_1, D_a, and D_2 are the particle diameter boundaries for the two sections. The aerosol number concentrations of these two sections, then, are given by N_1, and N_2, where

$$\begin{aligned} N_1 &= n_1(\log_{10}(D_a) - \log_{10}(D_1)) \\ N_2 &= n_2(\log_{10}(D_2) - \log_{10}(D_a)) \end{aligned}$$

This simplified representation of the marine aerosol distribution (two fixed sections) is adopted in an attempt both to capture the essential features of the DMS/CCN system and to keep the computational requirements of the model at a reasonable level. This approximation of the aerosol distribution may introduce numerical errors that are discussed in detail in the sensitivity analysis and in the model intercomparison sections.

Particles in the aerosol phase are produced primarily by two mechanisms: homogeneous nucleation of $(H_2SO_4)_g$ and evaporation of sea spray. We have parameterized the process of binary homogeneous nucleation based on the theoretical results of Jaecker-Voirol and Mirabel [1989] and have scaled those predictions by a semi empirical nucleation multiplying factor as proposed by Raes et al. [1992]. The resulting expression for the nucleation rate for a temperature of 298 K is

$$\begin{aligned} \log_{10}(J_{\text{nucl}}) &= \log_{10}(k_n)) - (64.24 + 4.7\text{RH}) \\ &\quad +(6.13 + 1.95\text{RH})\log_{10}(\text{H}_2\text{SO}_4)_g \end{aligned} \tag{2.4}$$

where J_{nucl} (cm^{-3} s^{-1}) is the number of new particles (N_1) produced, RH is

the relative humidity (from 0.0 to 1.0), $(H_2SO_4)_g$ is the sulfuric acid concentration in molecules cm^{-3}, and k_n is an empirical scaling coefficient for nucleation analogous to the "nucleation tuner" of Raes and Van Dingenen [1992]. The inability of classical nucleation theory to reproduce experimentally measured nucleation rate values has been documented by several investigators [Raes et al., 1992; Wyslouzil et al., 1991a, b]. The mathematical expression (equation (2.4)) used to describe the nucleation rate in the H_2SO_4/H_2O system should therefore be viewed as a fit of the available experimental values using a functional form suggested by theory and one free variable, namely the nucleation factor. This choice of a non-unity nucleation factor indicates our belief that the experimental data, even if they are highly uncertain, are probably more reliable than the available nucleation theory at this stage.

Nucleation-mode (N_1) particles are depleted by deposition, coagulation, and growth to accumulation-mode (N_2) particles:

$$\frac{dN_1}{dt} = J_{\text{nucl}} - K^1_{\text{dep}} N_1 - J_{\text{growth}} - K_{11} N_1 N_1 - K_{12} N_1 N_2 - K_{cloud} N_1 N_2. \quad (2.5)$$

The deposition velocity of particles is calculated based on Hummelshoj et al. [1992] to be 0.04 cm s^{-1} for nucleation-mode particles, assuming a wind speed of 8 m s^{-1}. Loss of these small particles by in-cloud coagulation with large droplets is significant, and after a burst of nucleation, coagulation between small particles is also rapid. For collisions between particles in the nucleation mode and cloud droplets, the appropriate coagulation coefficients, K_{11}, K_{12}, and K_{cloud} are 1.1x10^{-5} cm^3 h^{-1}, 2.7x10^{-5} cm^3 h^{-1}, and 1x10^{-3}

cm^3 h^{-1} [Seinfeld, 1986], respectively. The above coagulation coefficients have been calculated following the method described by Seinfeld [1986] and assuming diameters of 0.06, 0.3, and 20 μm for the nucleation mode aerosol, CCN, and cloud droplets, respectively. The sensitivity of the model to these values will be discussed in a subsequent section.

The condensation rate of H_2SO_4 to the aerosol particles is described using the modified form of the Fuchs-Sutugin equation [Hegg, 1990; Kreidenweis et al., 1991]. The condensation rate J to a particle of diameter D_p is given by

$$J = 2\pi D D_p F(Kn) A (P - P_o)$$

where D is the diffusivity of sulfuric acid in air (set to 0.1 cm^2 s^{-1}), Kn is the Knudsen number (that is the ratio of the air mean free path to the particle radius), $F(Kn)$ is a coefficient correcting for free molecular effects,

$$F(Kn) = \frac{1 + Kn}{1 + 1.71Kn + 1.33Kn^2}$$

and A is a coefficient correcting for the interfacial mass transport limitations described by the accommodation coefficient a_e,

$$A = [1 + 1.33KnF(Kn)(\frac{1}{a_e} - 1)]^{-1}.$$

Finally, P is the bulk $H_2SO_{4(g)}$ partial pressure and P_o is its partial pressure at the particle surface. An accommodation coefficient of 0.02 for the condensation of H_2SO_4 on the aerosol particles is assumed as the base case

value [Van Dingenen and Raes, 1991]; the sensitivity of the model predictions to this parameter is examined below. The vapor pressure of H_2SO_4 at the aerosol surface can be estimated from the data of Bolsaitis and Elliot [1990]. A value of approximately 10^{-5} ppt is obtained for a relative humidity of 90% and a temperature of 293 K, and therefore the surface vapor pressure of H_2SO_4 in the mass transfer calculation can be assumed to be zero.

When a volume dV of condensate (sulfuric acid and water) is added to the particles in the first section, it causes growth of dN particles to the second section. The diameter of these particles increases from D_p ($D_1 < D_p < D_a$) to D_a. The growth rate calculated by Pandis et al. [1994], as suggested by Warren and Seinfeld [1985], using conservation of aerosol number and mass is

$$J_{\text{growth}} = 0.12 N_1 (H_2SO_4)_g$$

where J_{growth} is given in particles cm^{-3} d^{-1} for N_1, in particles cm^{-3} and $(H_4SO_4)_g$ in ppt. This is the instantaneous growth rate of the available nuclei mode particles, assumed to be always evenly distributed between D_1 and D_a to CCN. For N_1 equal to zero, there are no particles to grow and the rate is zero. For large N, there are many particles that are just a little smaller than the activation diameter and therefore the growth rate remains proportional to N_1. Higher concentrations of H_2SO_4 lead to higher condensation rates and higher growth rates. This growth rate, as a product of two independent variables, introduces nonlinearity in the system of the differential equations describing the DMS/CCN system.

Nucleation-mode particles that grow above D_a result in accumulation-mode (N_2) particles, or CCN. Particles in this size range are also generated by evaporation of sea spray. The emission rate of sea-salt aerosol has been calculated here based on the measurements of Monahan et al. [1983]. The flux of sea-salt particles is

$$J_{\text{salt}} = \frac{2.5U^{3.41}}{H_{\text{mix}}}$$

where U is the wind speed and H_{mix} is the boundary layer height. This mode of particles is primarily processed in clouds but is also lost by deposition at a velocity estimated to be 0.06 cm s^{-1} for 8 m s^{-1} wind speed. The number concentration of the accumulation mode particles is thus governed by

$$\frac{dN_2}{dt} = J_{\text{salt}} + J_{\text{growth}} - K_{\text{dep}}^2 N_2 - f_{\text{precip}} e_p N_2 \tag{2.6}$$

where the rainout efficiency is e_p.

2.1.3 Non-Precipitating Clouds

During processing in stratus clouds, accumulation-mode particles are assumed to activate to form cloud droplets, which serve as a sink for $(SO_2)_g$ and $(H_2SO_4)_g$. This assumption is based on a lower activation diameter cutoff of 0.1 mm for typical marine cloud supersaturations of 0.1% [Baker and Charlson, 1990]. Dissolved SO_2 may be oxidized in cloud by H_2O_2, O_3 or O_2 [Pandis and Seinfeld, 1989]. The reported levels of H_2O_2 in marine environments (0.5 - 1.5 ppb) [Ray et al., 1990] are sufficient to oxidize all

SO_2 during the average residence time of an air parcel inside a cloud. The aqueous phase oxidation of SO_2 by H_2O_2 has therefore been parameterized as a first order process with a timescale $\tau_{H_2O_2} = 4$ hours and

$$R_{\text{cloud}}^{SO_2} = \frac{1}{\tau_{H_2O_2}} (SO_2)_g.$$

This timescale selection is consistent with the measured H_2O_2 concentrations and cloud liquid water contents, and also results in depletion of SO_2 after an hour of cloud processing. The H_2O_2 concentrations, the cloud's liquid water content, and the in-cloud residence times of air parcels vary widely and the above parametrization does not attempt to capture this variability. The choice of the above expression combined with the average residence time in clouds tends to deplete the air parcel of SO_2 every time it is processed by a cloud. This complete loss of SO_2 without any growth of new CCN is expected to result in an underprediction of CCN concentrations. Similarly, the large increase in particulate surface area which accompanies droplet activation provides a considerable sink for $(H_2SO_4)_g$. We assume that all the available H_2SO_4 is transferred to the cloud droplets during processing of the air parcel by clouds.

2.1.4 Precipitating Clouds

Rainout events are the main sink of accumulation-mode particles, which we approximate by the frequency of precipitating cloud cycling f_{precip} and a rainout efficiency e_p. For the base case, we have chosen a rainout frequency of 0.1 d^{-1} and a rainout efficiency equal to unity, as representative values for

the MBL [Raes, 1993; Hamrud and Rodhe, 1986]. The sensitivity to these values is discussed in a subsequent paragraph. The frequency of rainout is critical in determining the relevant time scale for aerosol evolution in the MBL.

2.2 Predicting the DMS-CCN Link

The set of parameters and initial conditions used in the base case simulation is presented in Table 2.1. For each run of the model, we calculate the evolution of species concentrations for a sufficiently long period so that a steady state cycle is reached. The duration of this cycle is governed by the rain/drizzle events that are incorporated into the model. The results during this ten-day cycle are independent of the initial atmospheric concentrations we specified. Our analysis will mainly focus on this steady state cyclic behavior. However, as the times necessary to reach a steady state cycle are different for the various species, in order to evaluate the point at which the system might be said to be in a steady state, we will initially consider the transient response of the system.

At the beginning of this cycle (Figures 2.2-2.4), from 0000 to 0100 of the first day, rain/drizzle depletes the MBL of CCN. The available surface area of the nucleation-mode particles is not sufficient to serve as a sink for the sulfuric acid produced by DMS oxidation after sunrise, and at 1200 of the first day a nucleation event, lasting three hours and producing almost 3000 cm^{-3} new particles, is predicted to occur. At 1500 the surface area of the aerosol (both in the accumulation and in the nucleation modes) has increased

Table 2.1: Base case model parameters.

Parameter	Symbol	Base Case Value
Temperature	T	298
Relative Humidity	R.H.	0.8
Mixing Height (m)	H_{mix}	1000
Wind Speed (m s^{-1})	U	8
Cloud Frequency (d^{-1})	f_{cloud}	1
Rain Frequency (d^{-1})	f_{rain}	0.1
DMS Flux (μmole $m^{-2}d^{-1}$)	F_{DMS}	5.0
H_2SO_4 Mass Accommodation Coefficient	a_e	0.02
H_2SO_4 Molecular Diffusivity (cm^2 s^{-1})	D	0.1
Lower Diameter (μm)	D_1	0.02
Activation Diameter (μm)	D_a	0.1
Upper Diameter (μm)	D_2	0.6
SO_2 Deposition Velocity (cm s^{-1})	v_{SO_2}	0.5
H_2SO_4 Deposition Velocity (cm s^{-1})	$v_{H_2SO_4}$	1.0
Nuclei Deposition Velocity (cm s^{-1})	v_{N_1}	0.04
CCN Deposition Velocity (cm s^{-1})	v_{N_2}	0.06
Nuclei-Nuclei Coagulation Coefficient (cm^3 hr^{-1})	K_{11}	1.1×10^{-5}
Nuclei-CCN Coagulation Coefficient (cm^3 hr^{-1})	K_{12}	2.7×10^{-5}
Nuclei-Droplet Coagulation Coefficient (cm^3 hr^{-1})	K_{cloud}	1.0×10^{-3}
Nucleation Rate Scaling Factor	k_n	10^7
OH Maximum Concentration (molec cm^{-3})	$(OH)_g$	5×10^6
SO_2 Yield for DMS Oxidation	y_{SO_2}	0.9
Initial DMS Mixing Ratio (ppt)	$(DMS)_g$	50
Initial SO_2 Mixing Ratio (ppt)	$(SO_2)_g$	0
Initial H_2SO_4 Mixing Ratio (ppt)	$(H_2SO_4)_g$	0
Initial Nuclei Concentration (cm^{-3})	N_1	100
Initial CCN Concentration (cm^{-3})	N_2	0
Reaction Constant (DMS+OH) (cm^3 molec s^{-1})	k_{DMS}	8.0×10^{-12}
Reaction Constant (SO_2+OH) (cm^3 molec s^{-1})	k_{SO_2}	1.0×10^{-12}

sufficiently that the nucleation of new particles ceases. Coagulation between the newly created particles is rapid, and 10 hours later their concentration has dropped to 1800 cm^{-3}.

The $DMS_{(g)}$ concentration reaches a steady state diurnal cycle during the fourth day after the beginning of the simulation (Figure 2.2). Following the initial transition period, the $DMS_{(g)}$ concentration is predicted to follow a simple diurnal pattern determined by its constant source rate and its diurnally varying sink rate. $DMS_{(g)}$ reaches a maximum mixing ratio of 150 ppt at 700 and a minimum mixing ratio of 82 ppt at 1600. The predicted average mixing ratio of $DMS_{(g)}$ is 115 ppt. Sulfur dioxide also reaches a constant diurnal cycle in the fourth simulation day. $SO_{2(g)}$ is depleted by in-cloud oxidation during the processing of the air parcel by clouds from 000 to 100 and its concentration remains zero for the rest of the night. $SO_{2(g)}$ is formed after sunrise as OH builds up and reaches a maximum mixing ratio of 85 ppt at 1700. From 1700 to 2300 its concentration decreases to 72 ppt as a result of losses by heterogeneous reactions on sea-salt aerosol and deposition. Its diurnal average mixing ratio is 44 ppt.

The gas phase concentration of H_2SO_4 exhibits both a one-day cycle and a ten-day cycle (Figure 2.3). Sulfuric acid starts building up in the MBL at sunrise and reaches a maximum at 1500 each day. This maximum is predicted to be 3.1 ppt the first day resulting in the major nucleation event and around 1.5 ppt the other nine days. The maximum value becomes 3.5 ppt during the steady state cycle reached after the first ten-day period. After 1500 the mixing ratio of H_2SO_4 decreases due to its condensation on the available aerosol and reaches a low of 0.1 ppt at midnight. At this time the

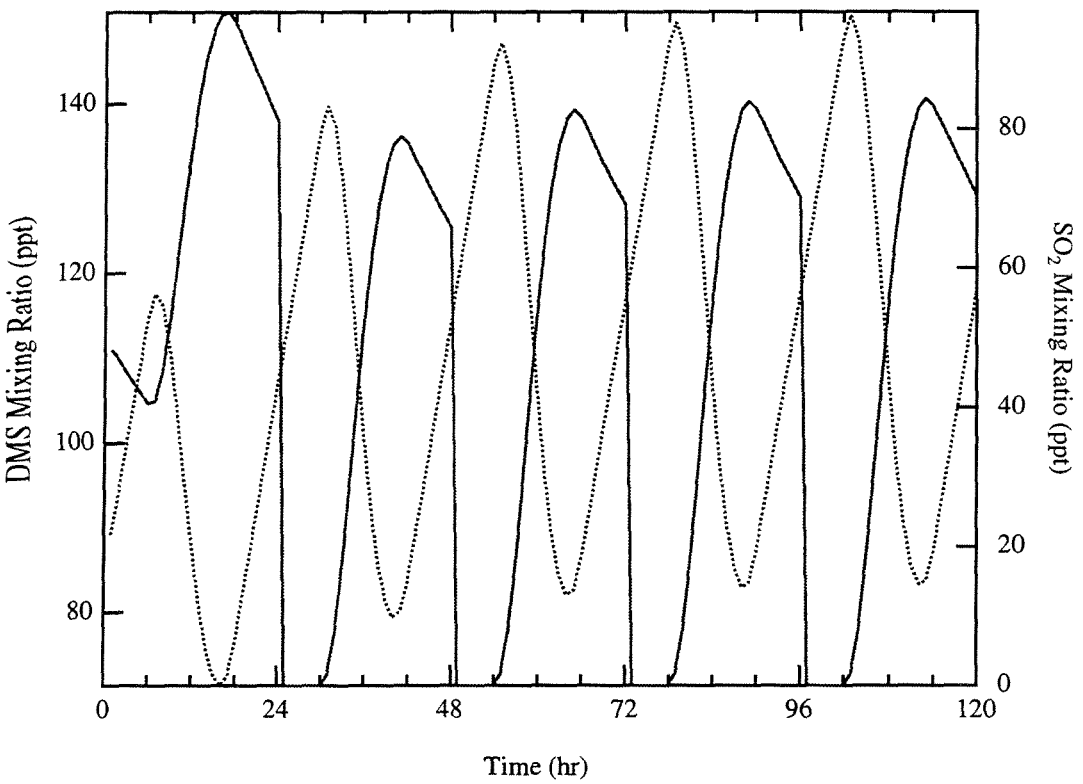

Figure 2.2: Predicted variation of the dimethyl sulfide (DMS) and SO_2 gas phase concentrations for five simulation days for the base case conditions. A steady state diurnal cycle is reached by both compounds during the fourth day.

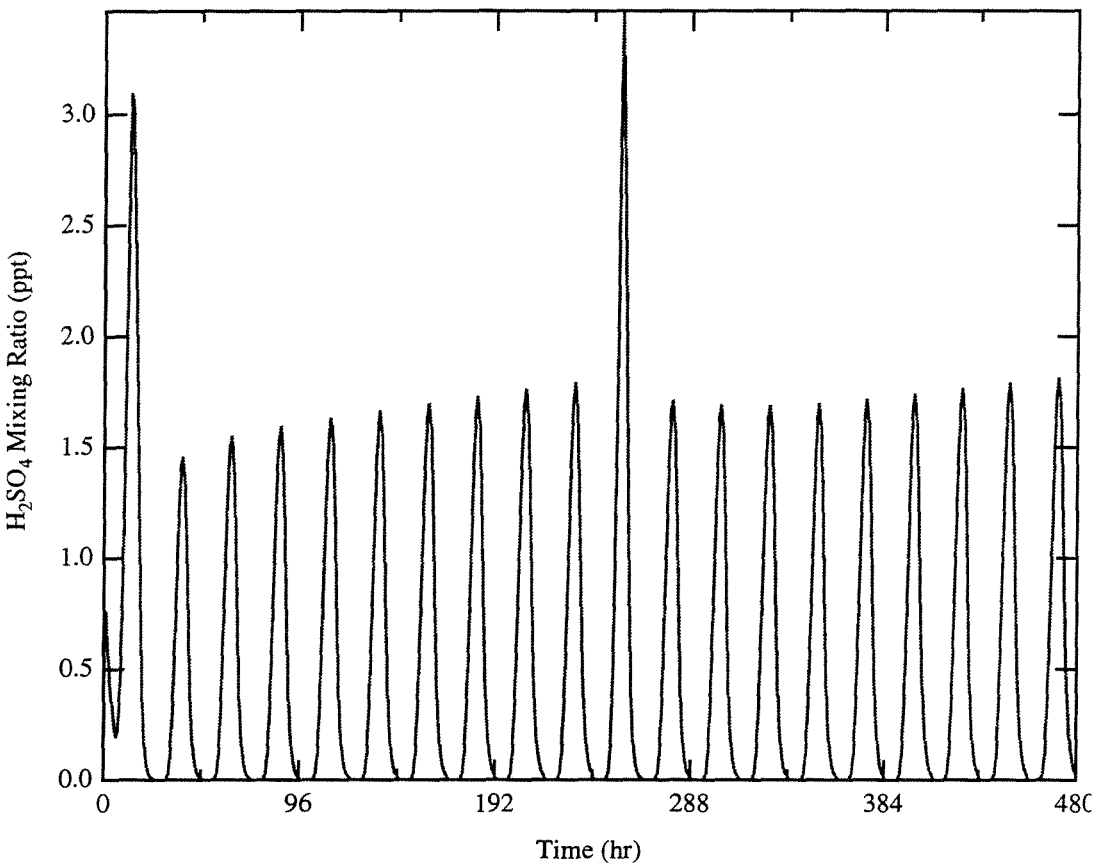

Figure 2.3: Predicted variation of the $H_2SO_{4(g)}$ concentration for 20 simulation days for the base case conditions. A steady state ten-day cycle is reached at the eleventh day.

air parcel is assumed to be processed by a cloud and this remaining sulfuric acid dissolves in the cloud droplets, depleting the parcel of H_2SO_4. The average H_2SO_4 mixing ratio during this ten-day period is predicted to be 0.5 ppt.

Beginning with day 11, the full system enters a ten-day steady state cycle. This cycle is qualitatively similar to the first ten-day cycle, with only a few minor differences (Figure 2.4). After the first day nucleation event the nucleation-mode concentration decays rapidly due to coagulation and by the end of the second day it has reached 1200 cm^{-3}. At noon of the fourth day of the cycle (day 14 of the simulation) the aerosol surface area has decreased sufficiently that a minor nucleation event creating around 5 particles cm^{-3} is predicted. This minor nucleation event is repeated every noon creating increasingly more particles each day, reaching a maximum of 50 particles cm^{-3} during day 10. These minor nucleation events are predicted to last 2 to 3 hours and prevent the nuclei mode concentration from declining any further. During the last six days of the cycle the nuclei mode aerosol concentration remains around 200 cm^{-3}, showing small variation. The major growth of new CCN occurs during the first day after the rain/drizzle event with the creation of 150 CCN cm^{-3} (Figure 2.4). Another 50 and 30 CCN cm^{-3} grow during the second and third day, respectively. After this point, and for the other seven days of the ten-day cycle, the CCN concentration remains practically constant, as the sources and sinks are in approximate balance. The model predicts, in agreement with available observations [Hegg and Hobbs, 1992], that the aerosol size distribution can remain constant for extended periods of time. DMS-CCN Relationship

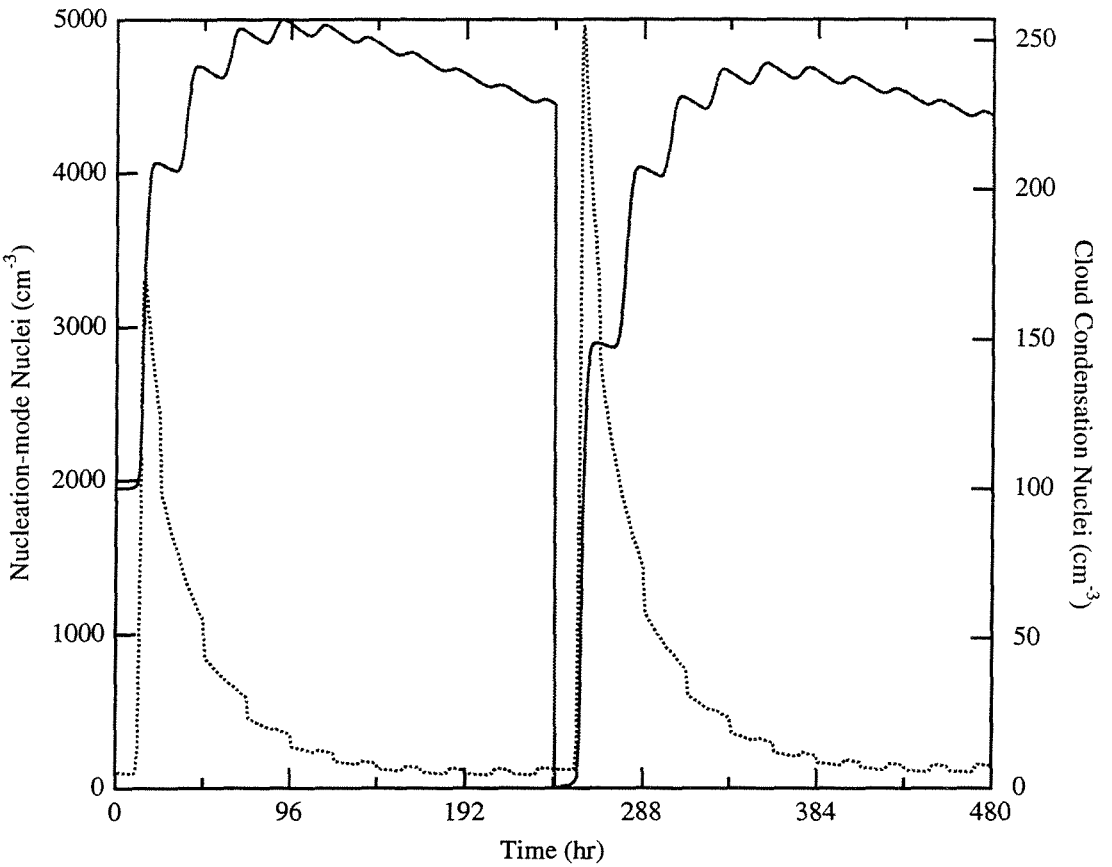

Figure 2.4: Predicted variation of the nuclei and accumulation mode (CCN) aerosol number concentration for 20 simulation days for the base case conditions. The aerosol distribution reaches a steady state ten-day cycle at the eleventh day.

Bates et al. [1987] compared summer and winter condensation nuclei (CN) data for three southern latitudes with DMS flux data for corresponding seasons and northern latitudes and found a linear correlation between the DMS flux and the aerosol number concentration. Lawrence [1993] used the same method and proposed that the data support equally well a linear or a nonlinear relationship. Lawrence [1993] also argued that dependence of the DMS chemistry on temperature, the variability of ambient conditions, the sea-salt oxidation of SO_2 , and the nonlinearity of the nucleation rate could result in a nonlinear DMS/CCN relationship. Using a steady state model of the DMS/CCN cycle, Pandis et al. [1994] presented the first theoretical evidence favoring a linear relationship. The above authors argued that neither the sea-salt oxidation of SO_2 nor the nonlinear nucleation rate alters this linear dependence. The dynamic model predicts also a practically linear relationship between the DMS flux and the CCN number concentration. Figure 2.5 illustrates this linearity for the base case with DMS fluxes ranging from 1 to 15 μmol m^{-2} d^{-1}.

The predicted CCN levels are approximately a factor of 2 higher than the predictions of Pandis et al. [1994]. The reasons for this discrepancy are discussed below.

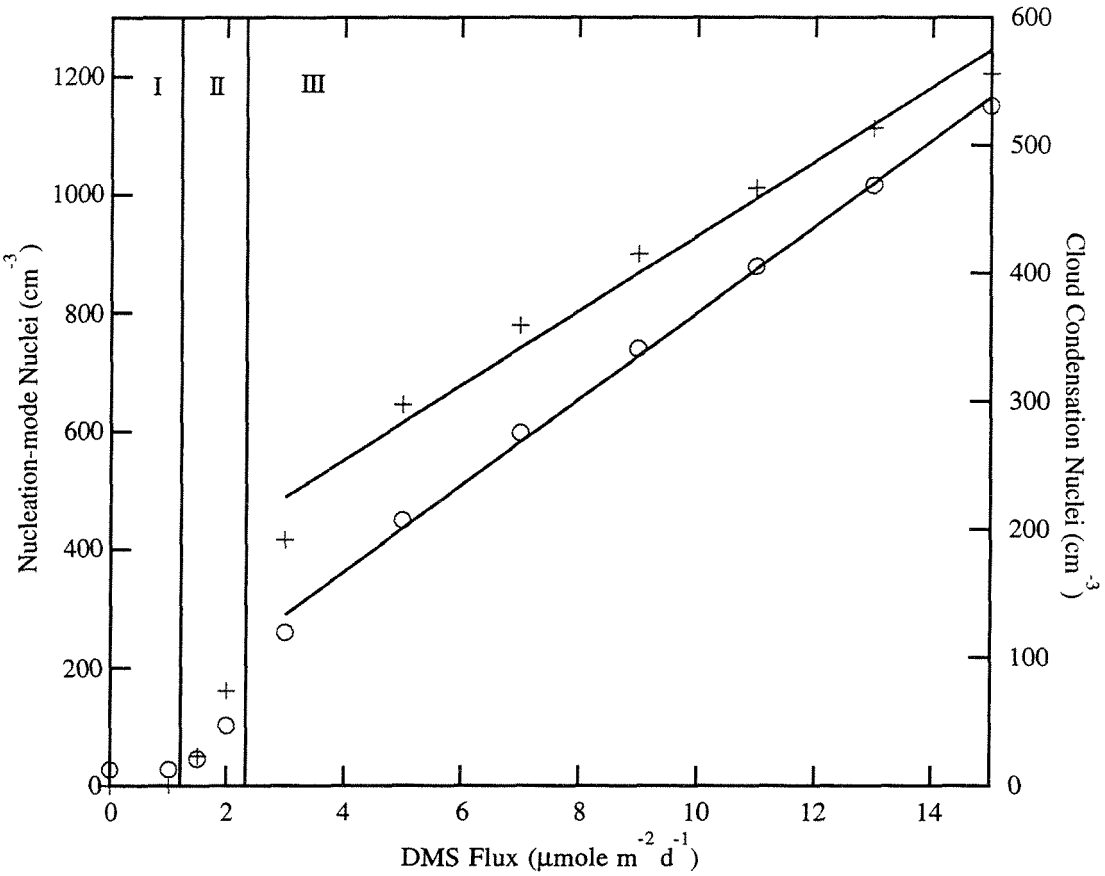

Figure 2.5: Predicted average value of nuclei and CCN concentrations over a ten-day period for the base case model for a range of DMS fluxes. Averages are calculated after the model has reached steady state cycle. Region I indicates the range of DMS values for which the predicted CCN concentration is essentially constant as all of the SO_2 produced is oxidized in CCN particles; in region II a large fraction of SO_2 is still heterogeneously converted in CCN, but the residual sulfate produced can form new CCN so that there is a small increase in CCN concentration with DMS emission rate; and region III bounds those DMS values for which the production of CCN can be expected to be nearly linear with DMS emissions.

2.3 Model Sensitivity to Prescribed Conditions and Parameters

Since this model incorporates the effects of clouds as well as winds, relative humidity, and species flux rates, it is critical to determine to what extent the observed response of the model is governed by specific sets of conditions. In addition, as some of the descriptions of microphysical processes (most notoriously binary homogeneous nucleation) rely on semi empirical parameters to scale the theoretically predicted values to conform with experimental results, it is important to determine how both the magnitude of the predicted result and the trend in the predicted behavior are influenced by these values. To assess the sensitivity of the model to variations in these values, we have run the model numerous times, varying one parameter at a time from its base case value. To compare the results of these runs, we examine a one-day cycle after the model has reached a steady state, that is, at the point where consecutive ten-day cycles yield identical predictions. In almost all cases, this steady state is achieved by the second ten-day cycle (days 11 through 20).

2.3.1 Cloud Diel Cycle

For a dynamic simulation of the MBL, both the period of cloud processing of an air parcel and the timing of that cloud event relative to the prescribed diel cycle of OH significantly affect the predicted CCN concentration. Since the OH radical governs the appearance of $H_2SO_{4(g)}$, cloud processing will have a much greater impact on CCN production if the cloud event coincides with a

relative maximum of OH. Such coincidence results in more sulfate adding to existing CCN while in cloud, so that fewer CCN may be produced by growth of smaller particles. This distinction is illustrated by a comparison of the ten-day time series for one-hour cloud events at 2300 and 1100 in Figures 2.6 and 2.7, respectively.

The case of a cloud at 2300 is almost identical to the base case with a burst of nucleation creating over 5000 particles cm^{-3}. These particles then coagulate and grow during the remainder of the 10 day period, resulting in predicted CCN concentrations of over 200 particles cm^{-3}. However, for the cloud at 1100, there are significant changes in the predicted behavior of the system. First, considerably fewer new particles are created, primarily because at the time of the peak expected sulfuric acid concentrations (corresponding to the peak in the OH), the cloud occurs and provides a sink for all of the available SO_2 . The result is that the initial burst of nucleation is much smaller (100 particles cm^{-3} instead of 5000 particles cm^{-3}), and hence nucleation is not quenched immediately. In fact, in this case nucleation events continue to occur throughout the ten-day cycle. However, as in the base case, new CCN are produced from the nucleated particles but at much lower concentrations (60 particles cm^{-3}).

For a one-hour cloud the maximum average CCN concentration predicted is 207 cm^{-3}, which results from clouds during OH-free nighttime hours, from 2300 to 0000. The minimum value is 36, corresponding to a cloud from 1100 to 1200. If we suppose that a series of air parcels will each cycle through the cloud at different times, then the appropriate ten-day average would be the mean of cloud events for all 24 hours, namely 162 cm^{-3} d^{-1}. This

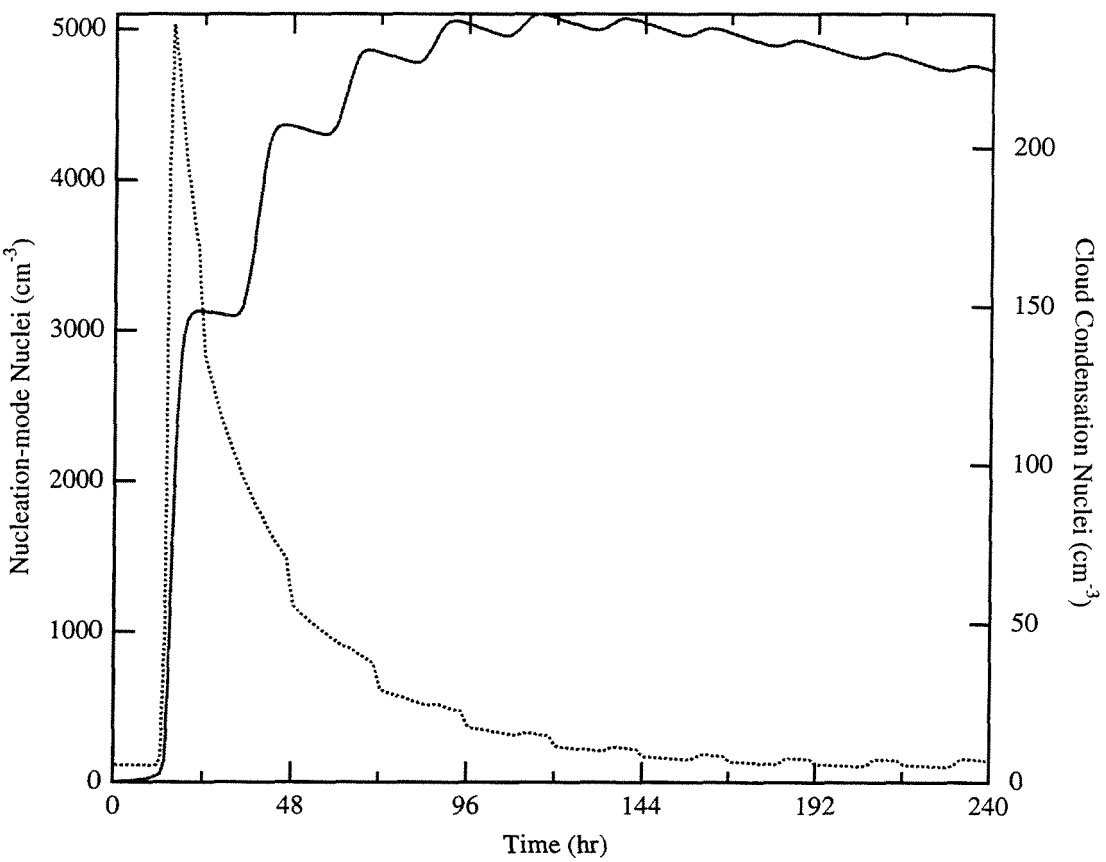

Figure 2.6: Predicted variation of the nuclei and accumulation mode (CCN) aerosol number concentration for ten simulation days (beginning after the model has reached steady state) for the base case conditions but with the cloud occurring from 2300 to 000.

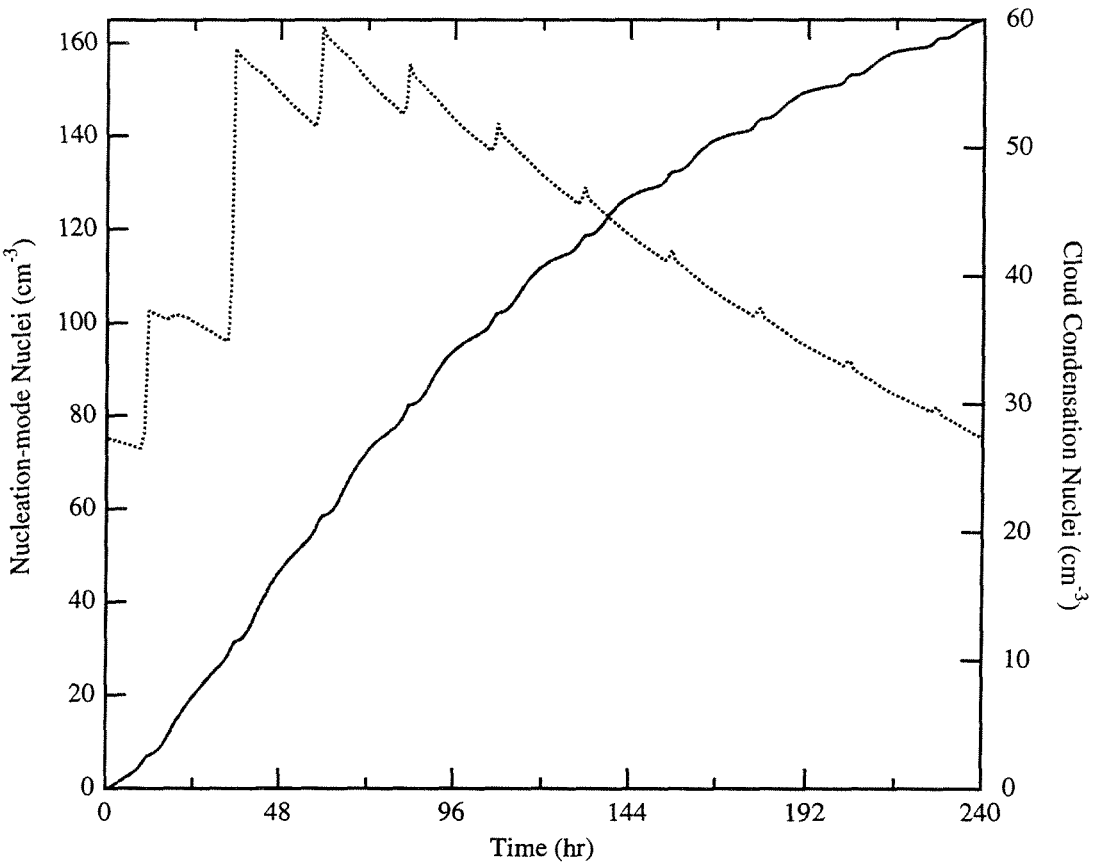

Figure 2.7: Predicted variation of the nuclei and accumulation mode (CCN) aerosol number concentration for ten simulation days (beginning after the model has reached steady state) for the base case conditions but with the cloud occurring from 1100 to 1200.

value reflects a difference of 40% from the base case, but still results in a linear relationship between DMS and CCN for DMS fluxes exceeding 2 μmol m^{-2} d^{-1}, as illustrated in Figure 2.8. The trends for the maxima and minima of predicted CCN in general follow the base case results; the maximum predicted CCN corresponds to a nighttime cloud, and the mimimum corresponds to a cloud at mid-day. Another important point is that although the model is highly sensitive to the time of occurrence of the cloud for a DMS flux of 5 μmol m^{-2} d^{-1}, the range of values predicted at 2 μmol m^{-2} d^{-1} is significantly smaller.

2.3.2 Cloud Frequency and Duration

In addition to the time of the cloud event, the frequency of cloud processing also significantly affects the number of CCN produced, as the greater the frequency, the more often $H_2SO_{4(g)}$ is depleted. This effect is illustrated by the range of results shown in Figures 2.8, 2.9, and 2.10. The range of CCN produced with clouds occurring at different times throughout the day for 1 d^{-1} is not much larger than that for 2 d^{-1}. This result would suggest that from the perspective of an isolated air parcel, it would be difficult to distinguish the effects of 1 d^{-1} from 2 d^{-1} processing.

However, if we adopt the perspective of an "ensemble-type" average of air parcels, each of which is processed through a cloud at a different point in the day and assuming that each evolves independently without mixing with other parcels, then we can define a mean predicted CCN concentration that allows us to compare the effects of cloud frequency. This comparison is shown

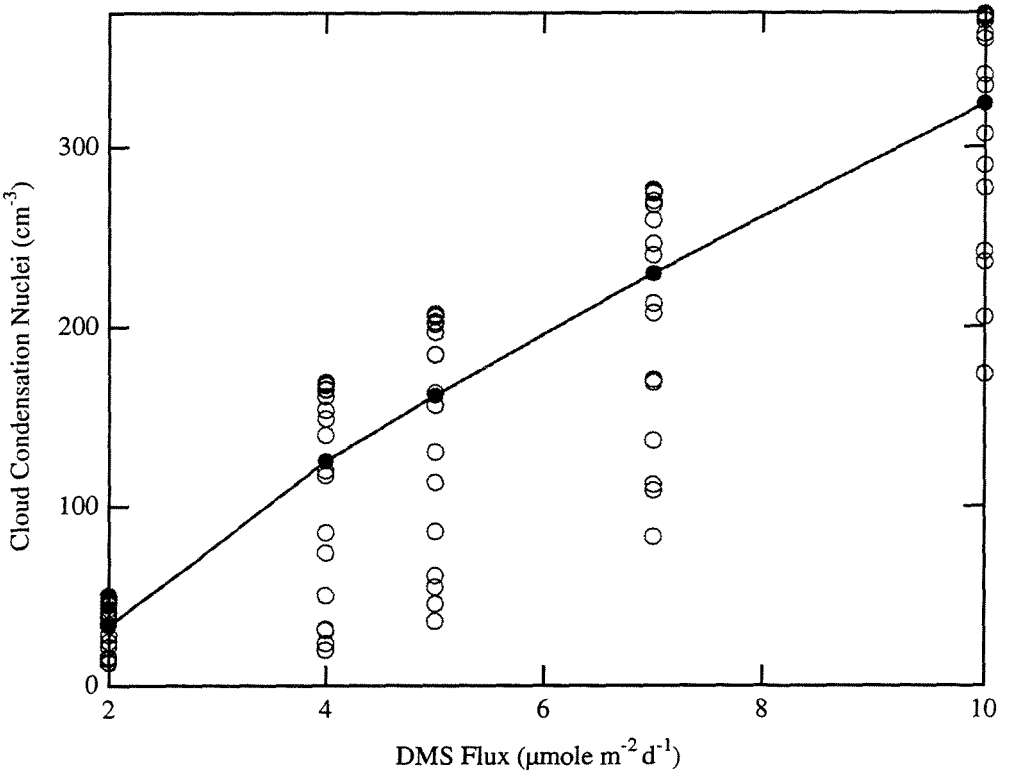

Figure 2.8: Average CCN predicted for one cloud occurring per day. The data points represent predictions for a one-hour cloud each day at 000, 100, etc., through 2300. The maximum for each DMS flux rate corresponds to nighttime clouds, and the minimum corresponds to midday clouds. The line is drawn through the "ensemble-average" values for a cloud frequency of 1 d^{-1}.

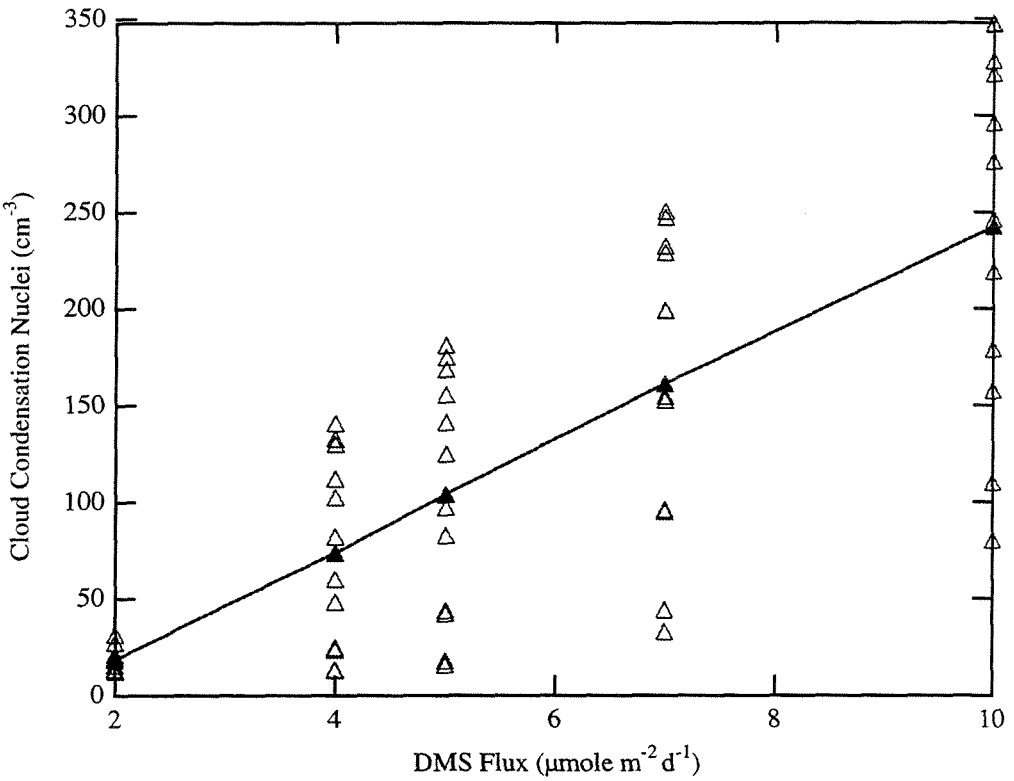

Figure 2.9: Average CCN predicted for two clouds occurring per day. The data points represent predictions for one-hour clouds every 12 hours starting with the first cloud from 0000 to 0100, from 100 to 200, etc., through 1100. The maximum for each DMS flux rate corresponds to both clouds occurring at night. The line is drawn through the "ensemble-average" values for a cloud frequency of 2 d^{-1}.

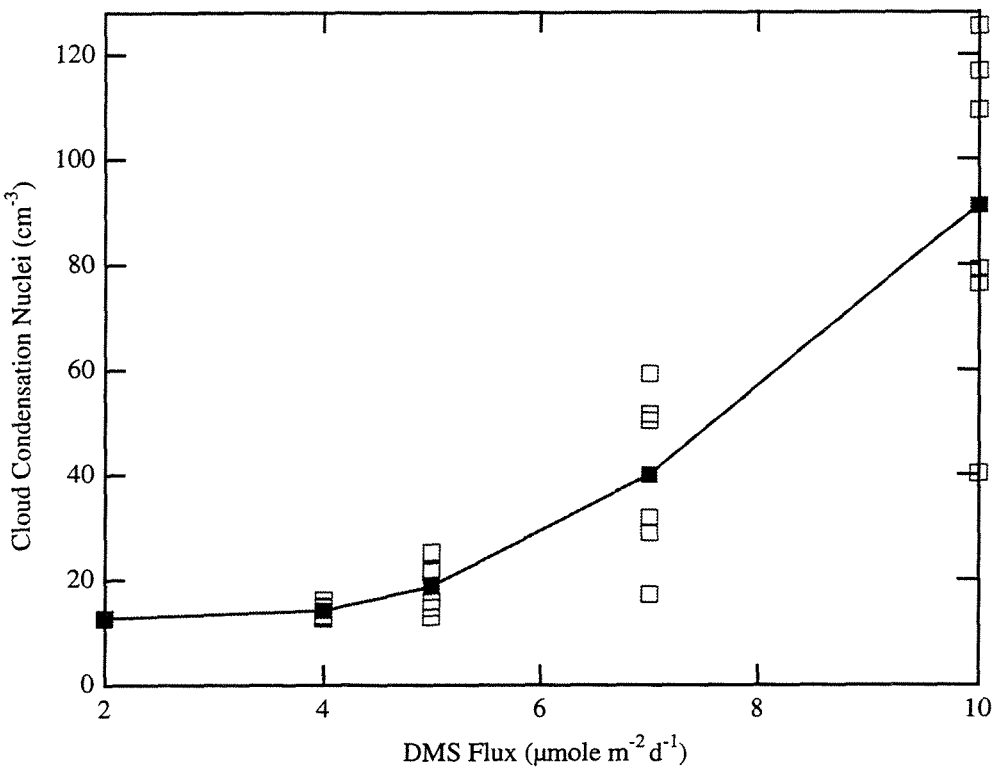

Figure 2.10: Average CCN predicted for four clouds occurring per day. The data points represent predictions for one-hour clouds every 6 hours starting with the first cloud at 000, 100, etc., through 500. The line represents the "ensemble-average" values for a cloud frequency of 4 d^{-1}.

in Figure 2.11. Both 1 d^{-1} and 2 d^{-1} exhibit a linear dependence of CCN concentration on DMS flux, but the number of CCN predicted for a cloud frequency of 2 d^{-1} is significantly less than for 1 d^{-1}. However, for a cloud frequency of 4 d^{-1}, not only are the levels of CCN predicted significantly less than for the base case, but their dependence on DMS flux appears to be linear only for DMS emissions greater than 5 μmol m^{-2} d^{-1}.

2.3.3 OH Concentration

Pandis et al. [1994] suggested that the CCN concentration levels are very sensitive to the assumed OH concentration with a 50% reduction of the OH concentration resulting in a 50% decrease of the predicted CCN. The sensitivity of the present model results to the assumed OH concentration was investigated by scaling the OH concentration (Figure 2.12).

The semisinusoidal OH variation assumed in the base case was also used for all these simulations. The predicted CCN concentration varies linearly with the OH concentration, while the nuclei concentration is a nonlinear function of assumed OH (Figure 2.12). A 50% decrease in OH throughout the day results in a 55% reduction of the predicted ten-day average CCN concentration. If the maximum daily OH concentration is less than 1 x 10^6 molecules cm^{-3}, no CCN are created from DMS and the only available CCN are the sea-salt particles.

The effect of the assumed OH variation with time was also investigated. A set of five simulations was performed where different diurnal profiles were used, all with the same diurnal average OH of 1 x 10^6 cm^{-3} (Figure 2.13).

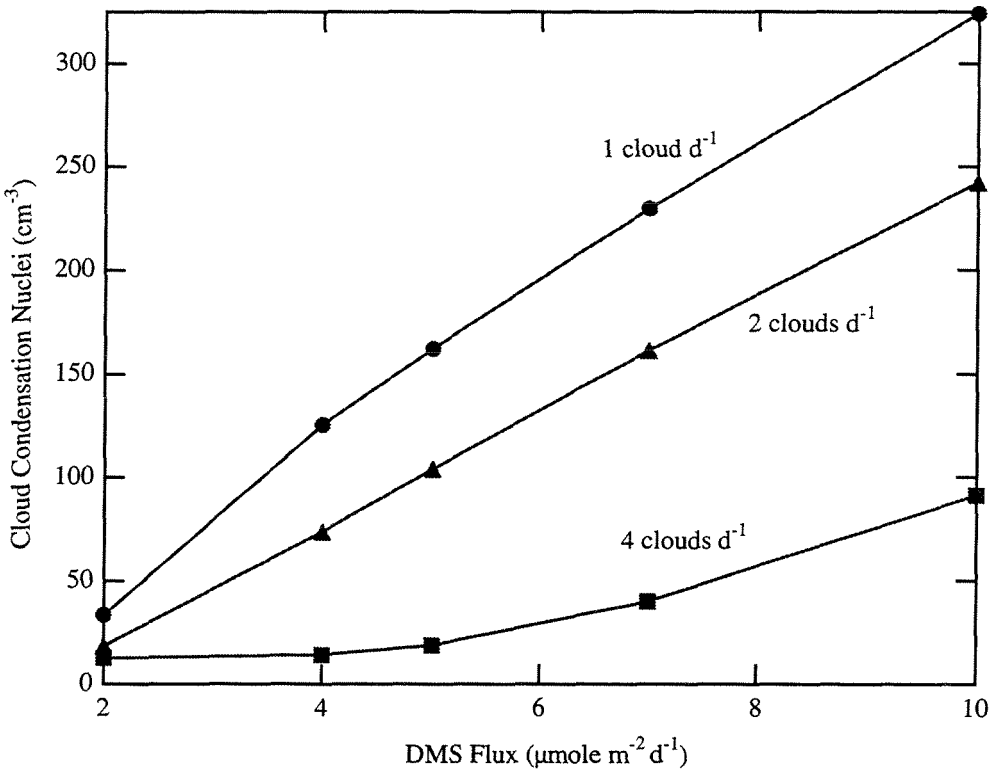

Figure 2.11: Comparison of "ensemble-average" of predicted CCN for cloud frequencies of 1, 2, and 4 d^{-1}. For one and two clouds per day there is a strong linear dependence of predicted CCN on DMS flux; however, for four clouds per day there is almost no dependence of predicted CCN on DMS flux for DMS fluxes smaller than about 6 μmol m^{-2} d^{-1}.

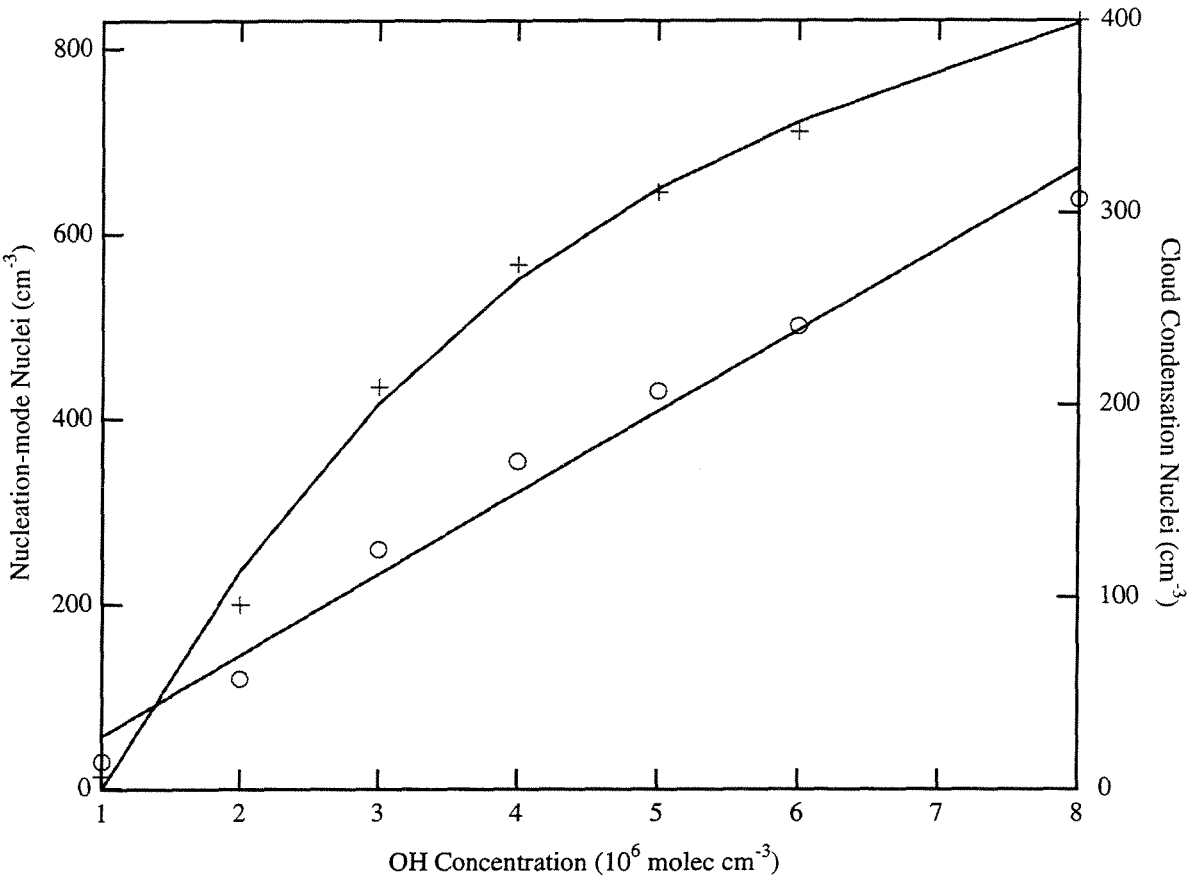

Figure 2.12: Predicted nuclei and CCN concentrations as functions of the maximum OH concentration. A semisinusoidal OH variation is assumed.

The predicted ten-day average CCN concentration increased by a factor of 2 from the constant OH value of the first case (24 hours of 1.6 x 10^6) to the spike like variation of the last case (6 hours of 6.3 x 10^6). Periods of high OH concentrations result in high H_2SO_4 production rates that cannot be balanced by condensation and cause high nucleation rates and subsequent growth of new CCN. The dependence of the CCN on the OH diurnal variation is the major cause for the discrepancy between the results of the present study and the steady state model of Pandis et al. [1994], where a constant OH concentration had to be assumed.

2.3.4 Aerosol and Gas-Phase Parameters

The model's responses to the remaining parameters, including prescribed meteorological conditions, have been investigated by varying the parameters listed from their base case values, as specified in Table 2.2. For each value tested, the model was run for 100 days, and the average predicted CCN concentration for a single, steady state cycle was compared to the base case prediction of 207 cm^{-3}. A range of values for meteorological conditions, aerosol distribution boundaries, deposition velocities, coagulation constants, and oxidation product yields were used in the model, resulting in differences in the predicted CCN concentration ranging from a decrease of 30% for a doubling of the upper diameter cutoff to a 117% increase for a 30% decrease of the assumed activation diameter.

A decrease in relative humidity of 10% resulted in a decrease of 21% in the CCN concentration predicted. This change is the net effect of a decrease

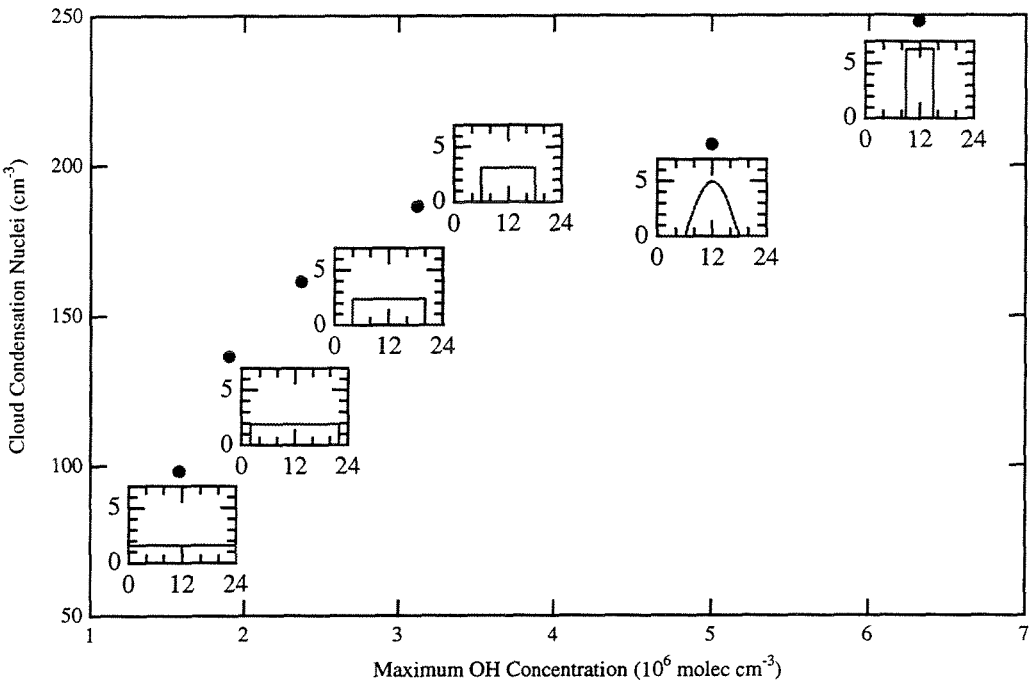

Figure 2.13: Predicted CCN concentrations for various functional forms of diurnal OH variations, including the semisinusoidal case. The inset graphs illustrate the functional form assumed in each case. For each inset graph, the left axis represents OH concentration in units of 10^6 molecules cm^{-3}, and the bottom axis represents time units of hours. In all cases the average OH concentration is the same, equal to 1 x 10^6 molecules cm^{-3}. The semisinusoidal curve represents the base case used for this study.

Table 2.2: Predicted change in ten-day average CCN concentration for variation of parameters in dynamic DMS/CCN model of the MBL.

Parameter	Base Case	Test Values	Change in CCN (%)
Meteorological Conditions			
Relative Humidity	0.8	0.7	-21
		0.9	+35
Mixing Height (m)	1000	500	+48
		1500	-23
Wind Speed (m s^{-1})	8	4	+2
		12	-6
Rain Frequency (d^{-1})	0.1	0.05	+1
		0.20	-13
Aerosol Size Distribution Boundaries			
Lower Diameter (μm)	0.02	0.001	-29
Activation Diameter (μm)	0.1	0.05	+151
Upper Diameter (μm)	0.6	1.2	-36
Deposition Parameters			
SO_2 Deposition Velocity (cm s^{-1})	0.5	0.25	+2
		1.00	-4
H_2SO_4 Deposition Velocity (cm s^{-1})	1.0	0.5	+3
		1.5	-3
Nuclei Deposition Velocity (cm s^{-1})	0.04	0.02	+1
		0.06	-1
CCN Deposition Velocity (cm s^{-1})	0.06	0.1	-9
Coagulation Constants			
Nuclei-Nuclei Coagulation Coefficient (cm^3 hr^{-1})	1.1×10^{-5}	5.5×10^{-6}	+10
		2.2×10^{-5}	-9
Nuclei-CCN Coagulation Coefficient (cm^3 hr^{-1})	2.7×10^{-5}	1.3×10^{-5}	+2
		5.4×10^{-5}	-3
Nuclei-Droplet Coagulation Coefficient (cm^3 hr^{-1})	1.0×10^{-3}	5.0×10^{-4}	+4
		2.0×10^{-3}	-5
Oxidation Product Yield			
SO_2 Yield for DMS Oxidation	0.9	0.7	-20

of the nucleation rate, a decrease of the particle growth rate, and an increase due to a lower activation diameter. The impact of decreasing the boundary layer depth to 500 m effectively decreases the column height into which marine emissions are mixed, thus the increasing average local concentrations of sulfate, so that the predicted CCN concentrations increase by 48% over the base case. Increasing the boundary layer depth to 1500 m results in a 23% decrease in predicted CCN. This almost proportional response of the system to boundary layer depth is consistent with the predicted linearity with DMS emission flux.

Changing the upper and the lower limits of the overall aerosol size distribution effects relatively small decreases in the predicted CCN concentration. Extending either the lower or the upper diameter cutoff does not significantly change the results, as the critical aerosol dynamics are described sufficiently by the two sections in the base case. A decrease of 50% in the activation diameter, however, increases the predicted CCN concentration by 151%. This response illustrates the model sensitivity to the definition of the cutoff for activation of CCN.

The model shows smaller than 10% variation in the predicted CCN concentration for all tested values of deposition velocities of gas and aerosol species. Similar results were obtained for the range of coagulation coefficients used. The yield of SO_2 from oxidation of DMS, however, results in an almost proportional response in the predicted CCN concentration.

2.3.5 Aerosol Distribution Description

The simplified mathematical form of the aerosol distribution used in our model introduces further uncertainties in the predicted CCN concentration. When a group of particles are created by nucleation, the model automatically distributes them evenly over the first section (20 - 100 nm) and artificially 'diffuses' them. This numerical artifact allows faster growth of aerosol to the second section and results in a tendency by the model to overpredict the CCN concentration. When a similar group of particles grows to the second section (100 - 600 nm), the same numerical smearing occurs. In this case, this numerical error results in an increased surface area of the CCN mode and increased condensation of the available $H_2SO_{4(g)}$ in this section, and it slows down the CCN growth. Therefore, the same numerical error from the one side accelerates and from the other decelerates the CCN growth. The target of the model is the prediction of the CCN number concentration, and therefore the magnitude of the error in the predicted CCN concentration introduced by our approximation is estimated below. The magnitude of this error can be quantified both by comparing the predicted timescales for growth of fresh particles to CCN and by direct comparisons of predicted CCN with models that describe explicitly the full aerosol distribution.

The model results presented in Figure 2.6 may be used for a calculation of the CCN growth timescale. At the morning of the first day of the cycle the predicted aerosol distribution consists of 120 particles cm^{-3} evenly distributed between 20 and 100 nm and no CCN. The nucleation event lasts 4 hours with the $H_2SO_{4(g)}$ concentration reaching 3.5 ppt. During this period

of rapid condensation (and the next 4 hours) around 150 particles cm^{-3} grow to the CCN mode. Note that most of these particles preexisted and only 20% of the CCN are particles that were just created. The 120 preexisting particles cm^{-3} were created during the previous nucleation event, and therefore it has taken them several days to grow to CCN in agreement with previous studies [Lin et al., 1992; Raes and Van Dingenen, 1992]. Summarizing, the model predicts that the timescale for the growth of nuclei to CCN is around 8 hours for 13% of the CCN, 1 day for 22%, 2 days for 13%, and several days for the remainining 52%. The results of multimodal models for similar conditions (e.g., no large particles) indicate timescales of roughly one [Lin et al., 1992] or two days [Raes and Van Dingenen, 1992]. For example, Raes and Van Dingenen suggested that the characteristic time (equal to the time required to grow half of the maximum CCN) for growth of CCN at 2% supersaturation is 50 hours (in their Figure 5a). Employing their conditions the present model predicts a characteristic time of 45 hours. The model, in general, tends to slightly undepredict the growth timescale, but the magnitude of the error appears small. This overall agreement in the predicted timescales of the present model with multimodal models is a first indication that the numerical diffusion errors are, to a large extent, canceling each other out.

In an effort to quantify the error or bias that may be introduced by our bimodal aerosol distribution, our model results are compared with the published results of multimodal models (see also the following section about comparison with other models). In these tests the only difference is the treatment of the aerosol distribution (the variable values and other conditions used by the other groups are also adopted in the present modeling framework).

Five different comparisons with three different models are performed and agreement within 50% (based on the results of the more rigorous models) is observed. As an additional comparison we have simulated the scenario 2c of Lin et al. [1992] (presented in their Table 3). At t=12 hours the Lin et al. model predicts 9 CCN cm^{-3}, ours 25. At t=24 hours the Lin et al. model predicts 37 versus 45 in ours. At t=48 hours our model underpredicts the CCN concentration (94 versus 60), and at t=72 hours both models reach their almost steady state values of 122 and 70. The effects of our simplification are interesting. During the first 24 hours when there are very few CCN present, our model overpredicts the CCN concentration by 50% or less. During the remaining 2 days this initial overprediction leads to an increased CCN surface area and an underprediction of further CCN growth. The result of this complex interplay is that the results of our simplified model remain close to the predictions of the much more complicated models.

The effect of this aerosol distribution parameterization on the reported DMS/CCN linearity is more difficult to quantify. The simplified description of the CCN growth process tends to partially dampen the overall nonlinearity of the system. Considering the above discussed magnitude of this effect, one may conclude that the DMS/CCN relationship is approximately linear. This uncertainty in the linearity of the DMS/CCN system will be quantified in future work employing a detailed description of the aerosol distribution.

2.4 Comparison With Other Models

Several models have been proposed simulating the production of CCN in the MBL using different parameterizations of the aerosol distribution and of the various physicochemical MBL processes. There has been significant discussion about the similarities and differences of these models [Lin et al., 1993a,b, Hegg, 1993ab], and a comparison of our model with the previous studies provides valuable insights into the existing uncertainties about the MBL processes.

Lin et al. [1992] argue that growth of nucleation mode particles to CCN can take place only when the concentration of the preexisting CCN is less than 1 cm^{-3}. In an effort to compare our work with their study we used our base case set of parameters with the following changes: (1) Replacing the first two differential equations with a constant SO_2 mixing ratio of 30 ppt. A DMS emission flux of 3.5 μmoles m^{-2} d^{-1} is required by our model for a daily average SO_2 mixing ratio of 30 ppt; (2) assuming no clouds or drizzle occur during the three simulation days; (3) initial conditions of zero $(H_2SO_4)_g$, zero nucleation mode particles, and 40 cm^{-3} CCN; (4) an RH value of 85%; (5) zero emission of sea-salt particles; (6) an accommodation coefficient value of unity.

Under these conditions we predict, in agreement with the results of Lin et al. [1992], virtually no nucleation of new particles (less than 1 cm^{-3}) and consequently no growth of new CCN. The diurnal variation of H_2SO_4 agreed exactly with that in Figure 2 of Lin et al. [1992]. Using our base case value for the accommodation coefficient of 0.02 resulted in a CCN concentration

of 350 cm^{-3}, and using the value of 0.3 used by Hegg [1990] resulted again in no particle formation. Therefore, our model is in agreement with that of Lin et al. [1992] if the same parameters are used, but the importance of the accommodation coefficient for H_2SO_4 is evident and will be discussed below. For the case of only 1 CCN cm^{-3} our model predicts the growth of 34 cm^{-3} after 72 hours in essential agreement with the 23 cm^{-3} predicted by Lin et al. [1992].

Hegg [1990] assumed a constant OH concentration of 5 x 10^6 molecules cm^{-3} and an initial SO_2 mixing ratio of 100 ppt. He also selected an accommodation coefficient value of 0.3 and used the same nucleation theory as in the present paper but without any multiplicative nucleation factor. For these conditions both his and the present model predict no CCN growth for 14 hours of simulation. For our base case parameter values ($a_e = 0.02$ and $k_n = 10^7$) our model predicts the growth of 330 cm^{-3} CCN particles during this period.

We have also employed the initial conditions and parameters of Raes and Van Dingenen [1992]. For a constant SO_2 concentration of 15 ppt, no particle production is predicted. For $(SO_2)g = 30$ ppt, $a_e = 0.04$, and $k_n = 10^4$, the present model predicts a CN concentration of 90 cm^{-3} after five simulation days, somewhat lower than the 200 cm^{-3} predicted by Raes and Van Dingenen.

2.5 Regimes of Model Behavior

The above results indicate that if the initial conditions and parameter values of previous studies are used, the present model essentially reproduces the results in these previous studies. The above comparison also shows that a detailed investigation of the model sensitivity to the values of the nucleation rate and sulfuric acid accommodation coefficient is required.

The uncertainty in the nucleation rate used can be probed by changing the nucleation scaling factor. This parameter, k_n, lacks a theoretical basis and could potentially span several orders of magnitude; the values extant in the empirical literature for this value range from 10^{-12} [Wyslouzil et al., 1991a, b] to 10^{7} [Raes et al., 1992]. Our choice for a base case value of this parameter, on the other hand, has been based on the measurements of Raes et al. [1992]. Therefore, the nucleation rate used in this study is for all practical purposes a fit of experimental results using an expression suggested by theory and one free variable (the nucleation scaling factor). The sulfuric acid accommodation coefficient (a_e) is also based on experimental results which have yielded contradictory results, from the value proposed by Raes and Van Dingenen [1992] of 0.04 to that used by Hegg [1990] of 0.3.

To probe the relationship between model prediction and the variation of accommodation coefficient and nucleation rate, we have investigated the model's behavior in a two-dimensional cross section of parameter space. These results should be viewed as an investigation of the existing uncertainty in the H_2SO_4/H_2O nucleation rate and not on the scaling factor per se. Figure 2.14 illustrates this cross section and summarizes the results pre-

dicted by the model for several regimes of values of the nucleation scaling factor and the sulfuric acid accommodation coefficient. These results indicate that for parameter values spanning those presented in the literature, the daily average flux of CCN which the model predicts ranges from 15 cm^{-3} (which is strictly the background flux due to mechanical generation of sea salt particles) to over 300 cm^{-3}. Consequently, for all other factors identical and at $k_n = 10^5$, the model would predict vastly differing roles for sulfate in the formation of CCN for the two extreme values of the accommodation coefficient; for $a_e = 1.0$, the predicted average CCN concentration is less than 50 cm^{-3}; whereas for $a_e = 0.02$, it is over 150 cm^{-3}.

As discussed above, the choice of these parameters accounts for several of the discrepancies among existing models of the MBL [Hegg, 1990; Lin et al., 1992; Raes and Van Dingenen, 1992]. To make predictions for specific initial conditions for the DMS-CCN system, it will be necessary to identify more precisely appropriate values of the nucleation rate and the sulfuric acid accommodation coefficient.

2.6 Discussion

Although the ten-day average CCN concentrations predicted by the current dynamic model are lower than those of the steady state model presented in an earlier work [Pandis et al., 1994] specifically because of the assumption of a constant OH radical level in that work, the linear dependence of CCN concentration on DMS flux in pristine marine conditions is predicted for DMS fluxes greater than about 2.5 μmol m^{-2} d^{-1}, in agreement with

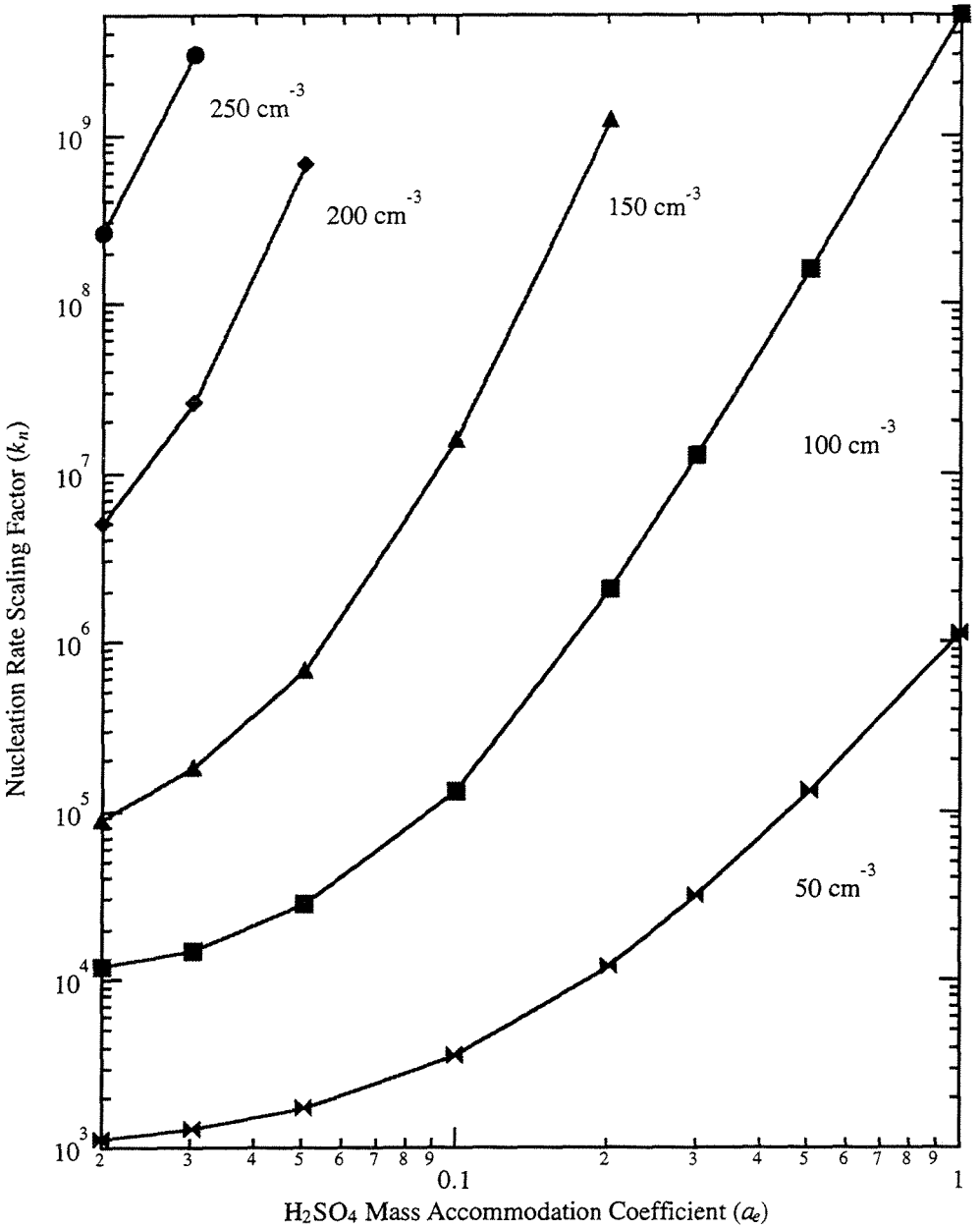

Figure 2.14: Average CCN predicted for a range of values of the nucleation scaling factor (k_n) and the sulfuric acid accommodation coefficient (a_e). Predicted CCN concentrations were averaged for one complete, ten-day, steady state cycle. Isopleths are drawn for CCN values of 50, 100, 150, 200, and 250 cm^{-3} day^{-1} . These isopleths delineate the regimes of behavior which can be expected from the model.

the conclusions of Pandis et al. [1994]. The present dynamic modeling results verify numerically the timescale estimates presented by Pandis et al. [1994]. The pseudo steady state model predicts the rainout cycle average concentrations of DMS, H_2SO_4, SO_2, nuclei, and CCN and provides useful insights in the interplay among the various processes. These concentrations are equivalent to the rainout cycle average concentrations predicted by the present model. The pseudo steady state framework requires the averaging of the effects of discrete periodic time events (rainout, cloud processing) over their corresponding period. The inability of the pseudo steady state model to account for diurnal variation of fluxes, meteorology, and other processes renders the present dynamic model as the preferred choice for incorporation in a three-dimensional global chemistry modeling framework.

Our present results have been based on constant meteorological conditions (temperature, wind speed, relative humidity, and depth of the boundary layer), independent, noninteracting air parcels, constant marine emission rates of DMS and sea-salt particles, and a well-mixed but closed boundary layer. No attempt was made to quantify the effects of the diurnal variation of the DMS flux and of the meteorological conditions. The importance of the OH concentration variation is indicative of the possible significance of these variations for the predicted CCN concentration. Even if a detailed investigation of the effects of the phase lag of the various cycles (e.g., DMS flux cycle versus cloud cycle versus relative humidity) was beyond the scope of the present study, it should be the subject of future work, coupled with a comprehensive set of field measurements. Certain phenomena proposed in other work [Raes et al., 1992b; Hegg et al., 1990], including transport

of particles from the free troposphere and radiation-enhanced cloud-related particle production, are not considered.

A simplified description of the aerosol distribution (two step functions) has been adopted. This representation of the aerosol distribution decreases significantly the computational cost of the model but also introduces further uncertainties in the predicted CCN concentration. Comparison of the present results with other models with more detailed descriptions of the aerosol distribution suggested that the corresponding uncertainty in the predicted CCN is of the order of 50% or lower. This uncertainty is significant but still much smaller than the uncertainties introduced by our lack of knowledge of the sulfuric acid nucleation and condensation rates.

Given the above assumptions of the current model, the DMS- CCN system exhibits linearity, at most combinations of cloud frequency and duration considered here. The threshold for this DMS/CCN linearity was found to depend on the cloud frequency. The SO_2-depleting effects of cycling through non precipitating clouds and rainout, with a sufficiently high frequency of cloud events, can effectively dampen nucleation of new particles and growth of new CCN to the point where a linear relationship between DMS and CCN no longer holds for the DMS flux range of interest. Since the key variable in this processing is cloud cycling which is governed by local meteorology, in order to evaluate actual data, CCN formation should be modeled specifically for the measurement conditions for which accurate data on the boundary layer structure are available. The uncertainty introduced by the simplified aerosol distribution used in the present model and its effects on the linearity of the DMS/CCN relationship will be further investigated in future work.

The present modeling exercise indicates that the major obstacle in theoretically verifying the DMS/CCN link is the lack of knowledge of the values of the atmospheric H_2SO_4 nucleation rates and the H_2SO_4 accommodation coefficient. Depending on the choice of these parameters, models can support or oppose the existence of such a link. The existing uncertainty in these values also prevents us from interpreting the rough agreement of this study (or similar ones) with observed values as anything else than supporting evidence for the DMS/CCN link based on a reasonable but imperfect model using reasonable but highly uncertain parameters. The present study can also be used as a guide on the mathematical form of the relationship that can be used to fit the available DMS/CCN data [Lawrence, 1993] and to obtain estimates of the importance of the potential DMS feedback mechanism.

References

Albrecht, B. A., Aerosols, cloud microphysics and fractional cloudiness, *Science*, 245, 1227-1230, 1989.

Albrecht, B. A., R. S. Penc, and W. H. Schubert, An observational study of cloud-topped mixed layers, *J. Atmos. Sci.*, 42, 800-822, 1985.

Andreae, M. O., The emission of sulfur to the remote atmosphere, in *Biogeochemical Cycles of Sulfur and Nitrogen in the Remote Atmosphere*, edited by N. J. Galloway et al., pp. 5-25, D. Reidel, Hingham, Mass., 1985.

Atkinson, R., and A. C. Lloyd, Evaluation of kinetic and mechanistic data for modeling of photochemical smog, *J. Phys. Chem. Ref. Data*, 13, 315-444, 1984.

Ayers, G. P., and J. L. Gras, Seasonal relationship between cloud condensation nuclei and aerosol methanesulfonate in marine air, *Nature*, 353, 834-835, 1991.

Baker, M. B., and R. J. Charlson, Bistability of CCN concentrations and thermodynamics in the cloud-topped boundary layer, *Nature*, 345, 142-145, 1990.

Bandy, A. R., D. L. Scott, B. W. Blomquist, S. M. Chen, and D. C. Thornton, Low yields of SO_2 from dimethyl sulfide oxidation in the marine boundary layer, *Geophys. Res. Lett.*, 19, 1125-1127, 1992.

Bates, T. S., R. J. Charlson, and R. H. Gammon, Evidence for the climatic role of marine biogenic sulfur, *Nature*, 329, 319-321, 1987.

Bates, T. S., B. L. Lamb, A. Guenther, J. Dignon, and R. E. Stoiber, Sulfur emissions to the atmosphere by natural sources, *J. Atmos. Chem.*, 14, 315-337, 1992.

Berresheim, H., F. L. Eisele, D. J. Tanner, L. M. McInnes, and D. C. Ramseybell, Atmospheric sulfur chemistry and cloud condensation nuclei (CCN) concentrations over the northeastern Pacific coast, *J. Geophys. Res.*, 98, 12,701-12,711, 1993.

Bigg, E. K., J. L. Gras, and C. Evans, Origin of Aitken particles in remote regions of the southern hemisphere, *J. Atmos. Chem.*, 1, 203-214,1984.

Bolsaitis, P., and J. F. Elliott, Thermodynamic activities and equilibrium partial pressures for aqueous sulfuric-acid-solutions, *J. Chem. Eng. Data*, 35, 69, 1990.

Brost, R. A., D. H. Lenschow, and J. C. Wyngaard, Marine stratocumulus layers, Part I, Mean conditions, *J. Atmos. Sci.*, 39, 800- 817, 1982.

Chameides, W. L., and A. W. Stelson, Aqueous-phase chemical processes in deliquescent sea-salt aerosols: A mechanism that couples the atmospheric cycles of S and sea salt, *J. Geophys. Res.*, 97, 20,565-20,580, 1992.

Charlson, R. J., J. Langner, and H. Rodhe, Sulphate aerosol and climate, *Nature*, 348, 22, 1990.

Charlson, R. J., J. Langner, H. Rodhe, C. B. Leovy, and S. G. Warren, Perturbation of the northern hemisphere radiative balance by backscattering from anthropogenic sulfate aerosols, *Tellus*, 43, 152- 163, 1991.

Charlson, R. J., J. E. Lovelock, M. O. Andreae, and S. G. Warren, Oceanic phytoplankton, atmospheric sulfur, cloud albedo and climate, *Nature*, 326, 655-661, 1987.

Charlson, R. J., S. E. Schwartz, J. M. Hales, R. D. Cess, J. A. Coakley, Jr., J. E. Hansen, and D. J. Hofmann, Climate forcing by anthropogenic aerosols, *Science*, 255, 423-430, 1992b.

Clarke, A. D., Atmospheric nuclei in the remote troposphere, *J. Atmos. Chem.*, 14, 479-488, 1992.

Clarke, A. D., N. C. Alquist, and D. S. Covert, The Pacific marine aerosol: Evidence for natural acid sulfates, *J. Geophys. Res.*, 92,4179-4190, 1987.

Coakley, J. A., Jr., R. D. Cess, and F. B. Yurevich, The effect of troposheric aerosols on the earth's radiation budget: A parametrization for climate models, *J. Atmos. Sci.*, 40, 116-138, 1983.

Fitzgerald, J. W., Marine aerosols: A review, *Atmos. Environ.*, 25(A), 533-545, 1991.

Fitzgerald, J. W., Numerical simulation of the evolution of the aerosol size distribution in a remote marine boundary layer, in *Nucleation and Atmospheric Aerosols*, edited by N. Fukuta and P. E. Wagner, pp. 157-160, Deepak, Hampton, VA, 1992.

Fouquart, Y., and H. Isaka, Sulfur emission, CCN, clouds and climate: A review, *Ann. Geophys.*, 10, 462-471, 1992.

Hamrud, M., and H. Rodhe, Lagrangian timescales connected with clouds and precipitation, *J. Geophys. Res.*, 91, 14,377-14,383, 1986.

Hegg, D. A., Heterogeneous production of cloud condensation nuclei in the marine atmosphere, *Geophys. Res. Lett.*, 17, 2165-2168, 1990.

Hegg, D. A., Comment on "A model study of the formation of cloud condensation nuclei in remote marine areas" by Lin et al., *J. Geophys. Res.*, 98, 7127-7128, 1993a.

Hegg, D. A., Comment on "A model study of the formation of cloud condensation nuclei in remote marine areas" by Lin et al., *J. Geophys. Res.*, 98, 20,813-20,814, 1993b.

Hegg, D. A., and P. V. Hobbs, Cloud condensation nuclei in the marine atmosphere: A review, in *Nucleation and Atmospheric Aerosols*, edited by N. Fukuta and P. E. Wagner, pp. 181-192, A. Deepak, Hampton, VA, 1992.

Hegg, D. A., L. F. Radke, and P. V. Hobbs, Particle production associated with marine clouds, *J. Geophys. Res.*, 96, 13,917-13.926, 1990.

Hegg, D. A., L. F. Radke, and P. V. Hobbs, Measurement of Aitken nuclei and cloud condensation nuclei in the marine atmosphere and their relation to the DMS-cloud-climate hypothesis, *J. Geophys. Res.*, 96, 8727-8733, 1991.

Hoppel, W. A., J. W. Fitzgerald, G. M. Frick, R. E. Larson, and E. J. Mack, *Atmospheric aerosol size distributions and optical properties in the marine boundary layer over the Atlantic Ocean*, NRL Rep. 9188, Natl. Res. Lab., Washington, D.C., 1989.

Hummelshoj, P., N. O. Jensen, and S. E. Larsen, Particle dry deposition to a sea surface, in *Precipitation Scavenging and Atmosphere Surface Exchange*, edited by S. E. Schwartz and W. G. N. Slinn, pp. 829-840, Hemisphere, Washington, D.C., 1992.

Jaecker-Voirol, A., and P. Mirabel, Heteromolecular nucleation in the sulfuric acid-water system, *Atmos. Environ.*, 23, 2053-2057, 1989.

Kreidenweis, S. M., and J.H. Seinfeld, Nucleation of sulfuric-acid water and methanesulfonic acid water solution particles, Implications for the atmospheric chemistry of organosulfur species, *Atmos. Environ.*, 22, 283-296, 1988.

Kreidenweis, S. M., F. Yin, S. C. Wang, D. Grosjean, R. C. Flagan, and J. H. Seinfeld, Aerosol formation during photooxidation of organosulfur species, *Atmos. Environ.*, 25A, 2491-2500, 1991.

Langner, J., H. Rodhe, P.J. Crutzen, and P. Zimmermann, Anthro-

pogenic influence on the distribution of trospheric sulphate aerosol, *Nature*, 359, 712-715, 1992.

Lawrence, M. G., An empirical analysis of the strength of the phytoplankton-dimethylsulfide-cloud-climate feedback cycle, *J. Geophys. Res.*, 98, 20663-20673, 1993.

Lin, X., and W. L. Chameides, CCN formation from DMS oxidation without SO_2 acting as an intermediate, *Geophys. Res. Lett.*, 20, 579-582, 1993.

Lin, X., W. L. Chameides, C. S. Kiang, A. W. Stelson, and H. J. Berresheim, A model study of the formation of cloud condensation nuclei in remote marine areas, *J. Geophys. Res.*, 97, 18161-18171, 1992.

Lin, X., W. L. Chameides, C. S. Kiang, A. W. Stelson, and H. J. Berresheim, Reply, *J. Geophys. Res.*, 98, 10815-10817, 1993a.

Lin, X., W. L. Chameides, C. S. Kiang, A. W. Stelson, and H. J. Berresheim, Reply, *J. Geophys. Res.*, 98, 20815-20816, 1993b.

Meszaros, E., On the possible role of the biosphere in the control of atmospheric clouds and precipitation, *Atmos. Environ.*, 22, 423-424, 1988.

Monahan, E. C., C. W. Fairall, K. L. Davidson, and P. Jones Boyle, Observed interrelations between 10m winds, ocean whitecaps and marine aerosols, *Quart. J. R. Met. Soc.*, 109, 379-392, 1983.

Pandis, S. N., L. M. Russell, and J. H. Seinfeld, The relationship between DMS flux and CCN concentration in remote marine regions, *J. Geophys. Res.*, 99, 16,945-16,958, 1994.

Pandis, S. N. and J. H. Seinfeld, Sensitivity analysis of a chemical mechanism for aqueous phase atmospheric chemistry, *J. Geophys. Res.*, 94, 1105-1126, 1989.

Pruppacher, H. R. and J. D. Klett, *Microphysics of Cloud and Precipitation*, D. Reidel, Norwell, MA, 1980.

Quinn, P. K., D. S. Covert, T. S. Bates, V. N. Kapustin, D. C. Ramsey-Bell, and L. M. McInnes, Dimethylsulfide cloud condensation nuclei system: Relevant size-resolved measurements of the chemical and physical properties of atmospheric aerosol particles, *J. Geophys. Res.*, 98, 10,411-10,428, 1993.

Radke, L. F., J. A. Coakley, Jr., and M. D. King, Direct and remote sensing observations of the effect of ships on clouds, *Science*, 246, 1146-1149, 1989.

Raes, F., A. Saltelli, and R. Van Dingenen, Modeling formation and growth of H_2SO_4-H2O aerosols: Uncertainty analysis and experimental evaluation, *J. Aerosol Sci.*, 23, 759-771, 1992a.

Raes, F. and R. Van Dingenen, Simulations of condensation and cloud condensation nuclei from biogenic SO_2 in the remote marine boundary layer, *J. Geophys. Res.*, 97, 12,901-12,912, 1992.

Raes, F., R. Van Dingenen, J. Wilson and A. Saltelli, Cloud condensation nuclei from dimethyl sulphide in the natural marine boundary layer:remote vs. in-situ production, in *Dimethylsulphide: Oceans, Atmosphere and Climate* (eds. G. Restelli and G. Angeletti), Kluwer Academic Publishers, Dordrecht, 311-330, 1992b.

Ray, J. D., C. C. Van Valin, M. Luria, and J. F. Boatman, Oxidants in the marine troposhere: H_2O_2 and O_3 over the western Atlantic Ocean, *Global Biochem. Cycles*, 4, 201-214, 1990.

Savoie, D. L., and J. M. Prospero, Comparison of oceanic and continental sources of non-sea-salt sulfate over the Pacific Ocean, *Nature*, 339, 685-687, 1989.

Scorer, R. S., Ship trails, *Atmos. Environ.*, 21, 1417-1425, 1987.

Seinfeld, J. H., *Atmospheric Chemistry and Physics of Air Pollution*, John Wiley, New York, 1986.

Shaw, G., Bio-controlled thermostasis involving the sulfur cycle, *Clim. Change*, 5, 297-303, 1983.

Slingo, A., Sensitivity of the earth's radiation budget to changes in low clouds, *Nature*, 343, 49-51, 1990.

Twomey, S., Pollution and planetary albedo, *Atmos. Environ.*, 8, 1251-1256, 1974.

Van Dingenen, R., and F. Raes, Determination of the condensation accommodation coefficient of sulfuric acid on water-sulfuric acid aerosol, *Aerosol Sci. Technol.*, 15, 93-106, 1991.

Warren, D. R. and J. H. Seinfeld, Simulation of aerosol size-distribution evolution in systems with simultaneous nucleation, condensation and coagulation, *Aerosol Sci. Technol.*, 4, 31-43, 1985.

Wigley, T. M. L. Possible climate change due to SO_2 derived cloud condensation nuclei, *Nature*, 339, 365-367, 1989.

Wyslouzil, B. E., J. H. Seinfeld, R. C. Flagan, and K. Okuyama, Binary nucleation in acid water systems, I, Methanesulfonic-acid water, *J. Chem. Phys.*, 94, 6827-6841, 1991a.

Wyslouzil, B. E., J. H. Seinfeld, R. C. Flagan, and K. Okuyama, Binary nucleation in acid water systems, II, Sulfuric acid-water and a comparison with methanesulfonic acid-water, *J. Chem. Phys.*, 94, 6842-6850, 1991b.

Chapter 3

Asymmetric Instrument Response Resulting from Mixing Effects in Accelerated DMA-CPC Measurements

Published in *Aerosol Science and Technology*, 1995 (23: 491-509).

Lynn M. Russell, Richard C. Flagan, and John H. Seinfeld

Department of Chemical Engineering, California Institute of Technology, Pasadena, CA

Knutson and Whitby (1975) and Hoppel (1978) introduced the design that is the basis for current mobility-based aerosol sizing. A major limitation in many of the applications of aerosol sizing by differential mobility measurement is the time required to determine a size distribution. In aircraft–based measurements, where sampling times limit the spatial resolution of measurements, or in observations of non–steady–state events such as nucleation of new particles in a polluted environment (Flagan et al., 1992), this limitation is crucial. Observing the dynamics of atmospheric aerosols where nucleation is occurring requires near real-time measurement of the particle size distribution under study.

Traditional mobility-based particle size distribution measurements employ stepping-mode operation of a differential mobility analyzer (DMA) in which the concentrations of particles transmitted through the DMA are measured at a sequence of discrete applied mobilities, as determined by steps in the applied electric field. Between measurements sufficient time is allowed to thoroughly purge the DMA column, the detector, and the transfer lines between the two components of the mobility analyzer system of particles from previous mobility steps. The size resolution of the mobility measurements is determined by the inherent DMA resolution and by the number of mobility intervals that are measured. Size resolution is enhanced at the expense of time resolution, however, since additional mobility intervals incur additional delays to purge the instrument. Although the total time required to acquire statistically significant counts on each channel may be quite short, several minutes are required to acquire a size distribution that spans the operating range of the DMA.

Wang and Flagan (1990) introduced a method for rapidly acquiring size distribution data over the entire mobility range of the DMA. They accelerated the measurements by classifying the aerosol in a time-varying electric field. Particles are continuously counted using a condensation nucleus counter (CNC) and stored in time bins in this scanning electrical mobility spectrometer (SEMS), thereby eliminating the delays between successive mobility measurements, while counting particles over the entire range of mobilities of the DMA. Another version of this measurement system is the Scanning Mobility Particle Sizer (SMPS) produced by TSI. The time that a particle is detected must be related to the corresponding particle mobility to determine the particle size distribution from scanning–mode mobility measurements. This relationship is complicated by the delay in the transmission of particles between the DMA outlet and the point at which particles are detected in the CNC.

In the original presentation of the SEMS, Wang and Flagan (1990) examined this relationship assuming that all particles experience the same delay between the time they leave the analyzer column and the time they are counted. When measurements are made during scans of both increasing and decreasing voltage, this delay time is apparent from a shift in the time after the scan starts at which the size distribution peaks. During the scan of increasing voltage, the peak is shifted toward lower mobilities (larger particle sizes), while the decreasing voltage scan produces a shift in the opposite direction. Wang and Flagan (1990) determined the time offset by time shifting the counts obtained during the two scans and matching the peaks in the increasing- and decreasing-ramp distribution measurements.

If the only shift in the measured distributions were that resulting from the aforementioned time delay, the scan speed in SEMS measurements would be limited only by the time required for particles to transit the analyzer column and the counting time required to acquire statistically significant particle counts. The latter limitation can be eliminated if insufficient counts have been obtained in a single scan since consecutive data measurements can be combined to obtain a true time–average size distribution measurement.

Figure 3.1 compares SMPS size distributions of the same mobility classified aerosol recorded at different scan rates during an instrument intercomparison (Flagan et al., 1995). Close examination of the distributions from the three up-scans shown in Figure 3.1 reveals an asymmetry, i.e., the distributions have tails at large mobility diameters (small electrical mobilities). This tail becomes more pronounced with increasing speed of voltage ramping in the DMA. At the same time, the peak height is reduced. The distribution determined with the slowest scan closely approximates that observed with stepping–mode DMA size distribution measurements, suggesting that the measurement is distorted at high scan rates (short scan times). This distortion results primarily from non–uniformities in the flow of aerosol from the outlet of the analyzer column to the point at which particles are detected in the CNC. Other factors may also contribute to such delays, e.g., differences in the rate of response of the high voltage power supply to increases or decreases in the specified voltage (although such effects are expected to be minor).

This paper examines the basis of the distortion of SEMS or SMPS measurements observed experimentally, by deriving a modified transfer func-

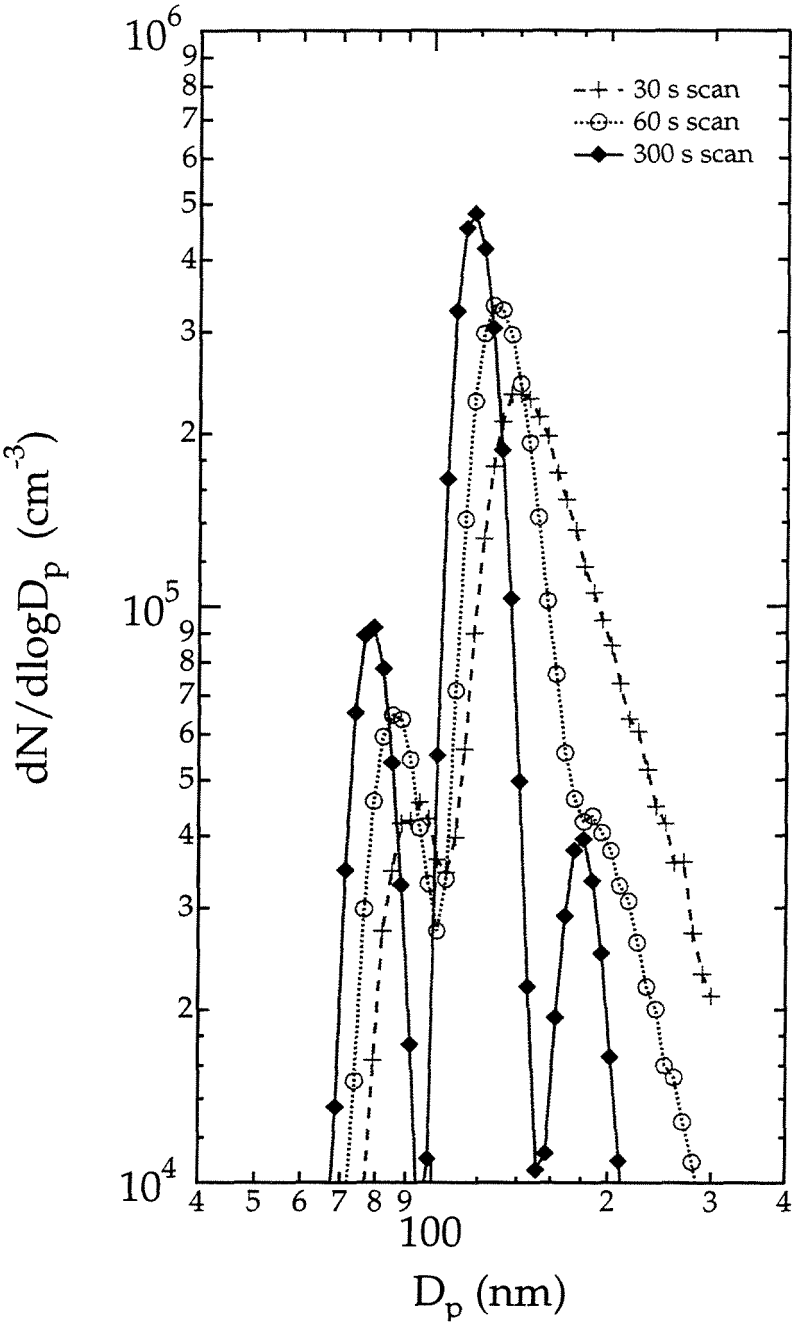

Figure 3.1: Experimental data from scanning measurements using commercial software (TSI SMPS) of a monodisperse aerosol with three different scanning speeds detected by a condensation particle counter with a 1 lpm flow rate (TSI Model 3010) (Flagan et al., 1995).

tion that accounts for the flow-induced smearing of the instrument response. Analogous effects will be seen as stepping-mode DMA measurements are accelerated, although the details of the solution will differ from those discussed here.

3.1 Kernel Function for Scanning Mobility Measurements

The response of the differential mobility analyzer operated at constant field strength has been investigated in several studies (Knutson and Whitby, 1975; Hoppel, 1978; Hagen and Alofs, 1983). The efficiency with which particles of mobility Z_p are transmitted through the DMA under a given applied field strength is known as the transfer function of the DMA and is denoted here as $\Omega(Z_p)$. Knutson and Whitby (1975) and Hoppel (1978) derived expressions for the transfer function and compared those predictions with experimental observations. Hagen and Alofs (1983) developed a method for linear inversion of mobility–based size distribution data that provides a framework for assessing the effects of multiple charging on conventional, stepping–mode operation of the differential mobility analyzer.

The signal for the i^{th} measurement channel (e.g., counts for CNC measurements or current for electrometer measurements) is

$$S_i = \int_0^\infty k_i(x) f(x) dx + \epsilon_i \quad i = 1, 2, \cdots, n \tag{3.1}$$

where $f(x)$ is the particle size distribution that is defined such that $f(x)dx$ is the number concentration of particles with diameters between x and $x + dx$, $k_i(x)$ is the so-called kernel function for channel i, n is the total number of measurement channels, and ϵ_i is the noise that is inherent in an experimental measurement. The estimation of the particle size distribution requires solution of the set of Fredholm integral equations for the n experimental measurements. Detailed knowledge of the kernel function is a prerequisite for this determination. The kernel function for DMA measurements of the particle size distribution can be expressed in terms of experimental parameters as

$$k_{i,j}(x) = Q_a \tau_c \sum_{\nu} s(x,\nu)\phi_\nu(x)\bar{\Omega}_{i,j}(\zeta(\nu,x)) \tag{3.2}$$

where $s(x,\nu)$ is the probability that the detector will count a particle of diameter x with ν charges (or alternatively, the analog detector response generated by such a particle), $\phi_\nu(x)$ is the fraction of particles of diameter x carrying an elementary charge of ν, Q_a is the volumetric flow rate of aerosol entering the DMA, and $\bar{\Omega}_{i,j}(\zeta(\nu,x))$ is the fraction of the particles of dimensionless mobility $\zeta(\nu,x)$ that will exit the analyzer during the counting interval of channel i of the j^{th} scan. The summation over all charge levels allows for a distribution of charges on the particles of size x and corresponding differences in the detector response. For the discussion that follows, the detector will be assumed to be a condensation nucleus counter, although the analysis can readily be generalized to other types of detectors.

For scanning–mode operation of the DMA, particles counted during a succession of intervals of duration τ_c are recorded in corresponding time-

bins. To determine the particle size distribution, it is necessary to relate the time in the scan at which a particle is detected to its mobility. Since each channel corresponds to a finite counting time during which the particle transmission through the DMA is continuously varying, the kernel function represents a time average of the instantaneous instrument response over the counting interval.

So far, we have assumed implicitly that only particles transmitted through the DMA during the present scan can contribute to the signal. Under extreme scan rates, or at the transition from one scan to another, the tails seen in Fig. 3.1 can extend from a previous scan into the present one, albeit with a continuously decreasing amplitude. The signal resulting from particles of size x may, thus, include contributions from previous scans. The kernel function for the j^{th} scan in a sequence of measurements must take these additional contributions into account. As will be shown in the next section, the SEMS transfer function describes the arrival of particles of a particular mobility emanating from the DMA during a particular scan at the detector for all later counting time intervals. The kernel function for scan j can be expressed as the sum of contributions from all previous scans in terms of the transfer function for each of those scans, i.e.,

$$k'_{i,j}(x) = Q_a \tau_c \sum_{\nu} s(x,\nu)\phi_\nu(x) \sum_{l=0}^{j} \bar{\Omega}_{i,j-l}(\zeta(x,\nu)) \tag{3.3}$$

The scan rate will generally be limited to minimize this smearing of the measurements, so only a few, if any, previous scans will contribute to the detected signal.

The transfer function for rapid DMA measurements depends upon the way the mobility range is scanned. For reasons that are discussed in Wang and Flagan (1990), the SEMS and SMPS employ an exponential voltage ramp, i.e.,

$$V(t) = V_o e^{\pm \frac{t}{\tau_r}} \tag{3.4}$$

where V_o is the voltage at the start of the scan, t is the time from the start of the scan, τ_r is the characteristic time for the voltage ramp, and the two signs given for the exponent represent the convention that we will use to describe the increasing and decreasing voltage scans, that is

$$V_o = \begin{cases} V_{min} & \text{for the top sign (increasing scan or "upscan," denoted SEMSu)} \\ V_{max} & \text{for the bottom sign (decreasing scans or "downscan," denoted SEMSd)} \end{cases}$$

Here we have defined

$$V_{max} = V_{min} e^{\pm \frac{n\tau_c}{\tau_r}} \tag{3.5}$$

where n is the number of channels in the scan. In the discussion that follows, we shall examine the transfer function for a particular scan, j, expressing the time as time after the start of the scan. Wang and Flagan (1990) modeled the particle trajectories in the DMA during scanning, leading to the results that the mobility of the particles that reach the outlet of the DMA at time t with greatest probability is

$$Z_p^*(t) = Z_o e^{\mp \frac{t}{\tau_r}} \tag{3.6}$$

where

$$Z_o \equiv \frac{(Q_c + Q_m)\ln\frac{b}{a}}{4\pi V_o L} \tag{3.7}$$

is the mobility at the beginning of the ramp, with L, b, and a being the length, outer radius, and inner radius of a cylindrical electrostatic classifier (Knutson and Whitby, 1975). In this work, we shall adopt the flow rate nomenclature of Knutson and Whitby (1975) as it predominates in practice, such that Q_c is the clean sheath flow entering the DMA, and Q_m is the main excess flow leaving the DMA. Particles with mobilities in an interval from $Z_p^*(t) - \Delta Z_p(t)$ to $Z_p^*(t) + \Delta Z_p(t)$ are transmitted through the DMA column at time t. The transfer function half-width is

$$\Delta Z_p(t) = \Delta_o e^{\mp\frac{t}{\tau_r}} \tag{3.8}$$

where

$$\Delta_o \equiv \frac{(Q_a + Q_s)\ln\frac{b}{a}}{4\pi V_o L} \tag{3.9}$$

is the transfer function half–width at the start of the scan if Q_s is the sample flow of size classified aerosol that exits the DMA.

The transfer function is expressed as a function of the dimensionless mobility,

$$\zeta \equiv \frac{Z_p}{\Delta_o} \tag{3.10}$$

For the ultimate data inversion, we will use the diameter as the variable of integration since it is the particle distribution with respect to size that we seek from mobility distribution measurements. Thus, the signal in the i^{th}

measurement channel is

$$\begin{aligned} S_{i,j} &= \int_o^\infty k'_{i,j}(x) f(x) dx \\ &= \int_o^\infty Q_a \tau_c \sum_{\nu=-\infty}^{\infty} s(x,\nu)\phi_\nu(x) \sum_{l=0}^{j} \bar{\Omega}_{i,j-l}(\zeta(\nu,x)) f(x) dx \end{aligned} \quad (3.11)$$

where

$$\zeta(\nu, x) = \frac{4\pi V_o}{(Q_s + Q_a)} \frac{L}{\ln \frac{b}{a}} \frac{\nu e C_c}{3\pi\mu x} \quad (3.12)$$

where C_c is the Cunningham correction factor, e is the magnitude of charge of an electron, and μ is the viscosity of the carrier gas. Once the system transfer function $\bar{\Omega}_i$ is known, the kernel function can be evaluated and scanning mobility data can be inverted. The response of the instrument can be described by a transfer function derived from consideration of the DMA response and the intervening plumbing system.

3.2 Instrument Response Characterization

The transfer function for the exponentially-ramped DMA, which we will denote $\Omega_j^e(\zeta, t)dt$, describes the probability that particles of mobility ζ will exit the DMA at time t to $t + dt$. Wang and Flagan (1990) further demonstrated that the probability that a particle of mobility Z_p will exit the DMA at time t has the same functional dependence on Z_p as does the transfer function for the DMA when operated at constant voltage. The resulting classifier transfer function for an exponentially ramped voltage scan may be written for the

interval $t = \{0, n\tau_c\}$ as

$$\Omega_j^e(\zeta,t) \equiv \begin{cases} 0 & t < \pm\tau_r \ln\frac{\zeta_o \mp 1}{\zeta} \quad (i) \\ \frac{\gamma+1}{2}\left(1 \mp \zeta_o \pm \zeta e^{\pm\frac{t}{\tau_r}}\right) & \pm\tau_r \ln\frac{\zeta_o \mp 1}{\zeta} \le t \le \pm\tau_r \ln\frac{\zeta_o \mp \beta}{\zeta} \quad (ii) \\ 1 & \pm\tau_r \ln\frac{\zeta_o \mp \beta}{\zeta} \le t \le \pm\tau_r \ln\frac{\zeta_o \pm \beta}{\zeta} \quad (iii) \\ \frac{\gamma+1}{2}\left(1 \pm \zeta_o \mp \zeta e^{\pm\frac{t}{\tau_r}}\right) & \pm\tau_r \ln\frac{\zeta_o \pm \beta}{\zeta} \le t \le \pm\tau_r \ln\frac{\zeta_o \pm 1}{\zeta} \quad (iv) \\ 0 & \pm\tau_r \ln\frac{\zeta_o \pm 1}{\zeta} < t \quad (v) \end{cases} \tag{3.13}$$

Outside this interval, that is for $t < 0$ and $t > n\tau_c$,

$$\Omega_j^e \equiv 0$$

The characteristic dimensionless mobility for the DMA is the ratio of the centroid mobility to the ideal transfer function half–width

$$\zeta_o \equiv \frac{Z_o}{\Delta_o} = \frac{Q_c + Q_m}{Q_s + Q_a} \tag{3.14}$$

We have defined

$$\gamma \equiv \frac{Q_s}{Q_a} \tag{3.15}$$

$$\delta \equiv \begin{cases} \frac{2}{\gamma+1} & \gamma > 1 \\ 1 & \gamma \le 1 \end{cases} \tag{3.16}$$

$$\beta \equiv \begin{cases} \frac{\gamma-1}{\gamma+1} & \gamma > 1 \\ 1 & \gamma \le 1 \end{cases} \tag{3.17}$$

The instrument response for scanning–mode (or rapid stepping) operation

is determined by the average probability that a particle of a given mobility will reach the detector during the counting time interval $\{t_i - \tau_c, t_i\}$. Since the probability that particles of a given mobility will be transmitted through the DMA changes continuously as particles are being counted, the quantity of interest is the time–averaged transfer function for the interval over the measurement interval, τ_c, of the i^{th} channel, $\bar{\Omega}_{i,j}(\zeta(\nu, x))$. Wang and Flagan (1990) implicitly applied a plug–flow model for the flow between the classifier and the detector in noting that particles detected at time t actually exited the DMA column at time $t - \tau_p$, but neglected the distortions to the instrument response that are wrought by more complex flows. Such a flow model requires a uniform flow profile throughout the tubing between the classifier and detector. The resulting time–averaged transfer function for the counting period for channel i can be expressed as

$$\bar{\Omega}_{i,j}^{WF}(\zeta) = \frac{1}{\tau_c} \int_{t_i - \tau_c}^{t_i} \Omega_j^e(\zeta, t - t_j - \tau_p) dt \tag{3.18}$$

in terms of the time-dependent transfer function, $\Omega_j^e(\zeta, t - t_j - \tau_p)$, defined above. To derive the time–averaged transfer function for instruments with more realistic and complex flows, we must first determine the instantaneous transfer function for the system that includes the scanning DMA and all of the flow passages between the DMA outlet and the point at which the particles are ultimately detected.

Flow non-idealities introduce a range of delays between discharge from the DMA and particle detection. We shall describe the influence of the flows between the DMA outlet and the point at which particles are ultimately

detected in terms of a residence time distribution (RTD) (Levenspiel, 1972). The transit time delays associated with the straight tubing lengths and the mixing effects associated with dead spaces, tubing bends, and velocity profiles within the straight tubes can be characterized in terms of this residence time distribution, $\mathbf{E}(t)$, that is defined such that the probability that a fluid element will be delayed by a time t to $t+dt$ is $\mathbf{E}(t)dt$. This function describes the age distribution of the fluid leaving a vessel in non-dimensional terms such that

$$\int_0^\infty \mathbf{E}(t)dt = 1 \tag{3.19}$$

When non–ideal flow effects are taken into account, particles emanating from the analyzer column at a range of previous times $\hat{t} \leq t$ can contribute to the signal. The instantaneous transfer function for the i^{th} counting interval resulting from particles transmitted through the DMA during the j^{th} scan which starts at $\hat{t} = t_j$ as measured at the detection point (rather than at the classifier outlet) is then given by integrating the product of the residence time distribution and the DMA transfer function as follows:

$$\tilde{\Omega}^e_{i,j}(\zeta) \equiv \int_{t_j}^{t_i} \Omega^e_j(\zeta, \hat{t} - t_j)\mathbf{E}(t - \hat{t})d\hat{t} \tag{3.20}$$

The time averaged system transfer function for the k^{th} scan then becomes

$$\bar{\Omega}^e_{i,j}(\zeta) = \frac{1}{\tau_c}\int_{t_i-\tau_c}^{t_i} \tilde{\Omega}^e_j(\zeta, t)dt \tag{3.21}$$

We can evaluate this integral in terms of a cumulative history function, which

we define to be

$$I_j^{cum}(\zeta, t) \equiv \int_{t_j}^{t} \tilde{\Omega}_j^e(\zeta, \hat{t}) d\hat{t} \tag{3.22}$$

where the integral begins at time t_j, the time at which the j^{th} scan begins, such that

$$\bar{\Omega}_{i,j}^e(\zeta) = \frac{1}{\tau_c} \int_{t_j}^{t_i} \tilde{\Omega}_j^e(\zeta, t - t_j) dt - \frac{1}{\tau_c} \int_{t_j}^{t_i - \tau_c} \tilde{\Omega}_j^e(\zeta, t - t_j) dt \tag{3.23}$$

$$= \frac{1}{\tau_c} \left[I_j^{cum}(\zeta, t_i) - I_j^{cum}(\zeta, t_i - \tau_c) \right] \tag{3.24}$$

3.2.1 History-Dependent Transfer Function

This formulation can be used to determine the scanning mode transfer function for arbitrary residence time distributions. Deviations of the residence time distribution from the ideal plug flow result from mixing effects in the detector as well as those in the plumbing between the detector and the DMA, although mixing within the detector frequently dominates. Figure 3.2 illustrates the transient particle counts measured in response to a step change in the aerosol concentration by Quant et al. (1992) for several commercial condensation particle counters (CPCs). The pronounced tail in the signals cannot be reproduced with the plug flow model. An alternative model of the inter-instrument flow would be the continuously stirred tank reactor (CSTR) flow model, in which incoming fluid is instantaneously and perfectly mixed with the fluid that is already present in the vessel. Consequently, disturbances in the incoming flow would be immediately reflected in the effluent from the vessel, but at a concentration diluted by the vessel's volume. Par-

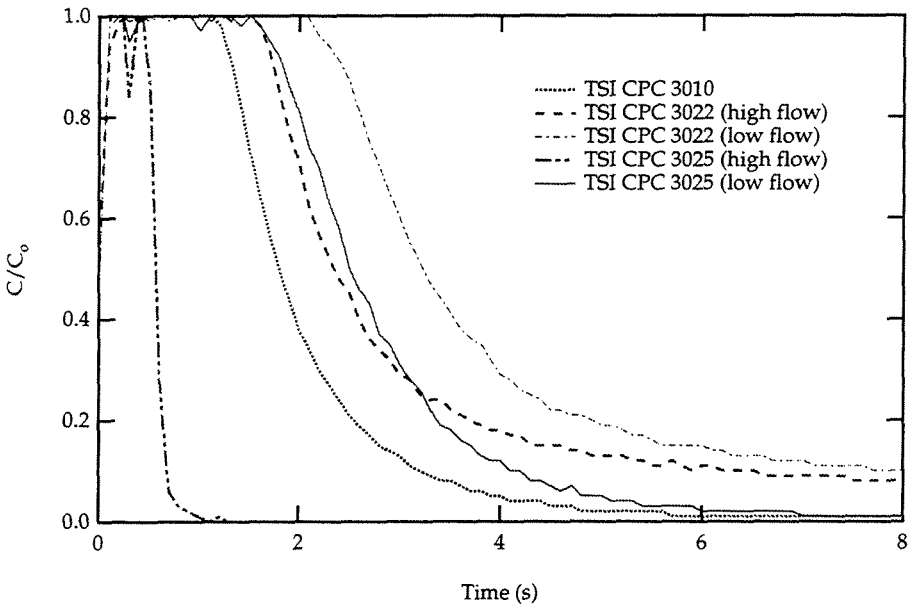

Figure 3.2: Response of commercial condensation particle counters (TSI Models 3010, 3022, and 3025) to a step change in concentration at the inlet at time $t = 0$ s. The data are taken from Quant et al. (1992).

ticles remaining in the vessel are gradually diluted with additional inflow, leading to a decaying response of the incoming fluid. The residence time distribution for this CSTR flow model is an exponential decay function (Levenspiel, 1972)

$$\mathbf{E}(t) = \frac{1}{\tau_s} e^{-\frac{t}{\tau_s}} \tag{3.25}$$

The residence time distribution functions of real flow systems can often be accurately represented by a combination of plug flow reactors (PFRs) and CSTRs in series.

We shall model the flow in the scanning mode DMA system as a single CSTR in series with a PFR. The resulting residence time distribution is given by

$$\mathbf{E}(t) = \begin{cases} 0 & t < \tau_p \\ \frac{1}{\tau_s} \exp\left(-\frac{t-\tau_p}{\tau_s}\right) & t \geq \tau_p \end{cases} \tag{3.26}$$

The instantaneous system transfer function $\tilde{\Omega}_j^e$ for the j^{th} scan becomes

$$\tilde{\Omega}_j^e(\zeta, t) = \int_{t_j}^{t} \Omega_j^e(\zeta, \hat{t} - t_j) \exp\left(-\frac{t - \hat{t} - \tau_p}{\tau_s}\right) \frac{d\hat{t}}{\tau_s} \tag{3.27}$$

Now, we employ the change of variables

$$\theta' \equiv \frac{t - t_j - \tau_p}{\tau_r} \tag{3.28}$$

and

$$\theta \equiv \frac{t}{\tau_r} \tag{3.29}$$

$$\theta_s \equiv \frac{\tau_s}{\tau_r} \tag{3.30}$$

$$\theta_j \equiv \frac{t_j}{\tau_r} \tag{3.31}$$

$$\theta_p \equiv \frac{\tau_p}{\tau_r} \tag{3.32}$$

such that

$$\tilde{\Omega}^e_j(\zeta,\theta') = \int_{\theta_j}^{\theta} \Omega^e_j(\zeta,\hat{\theta}-\theta_j) e^{\frac{\theta-\hat{\theta}-\theta_p}{\theta_s}} \frac{d\hat{\theta}}{\theta_s} \tag{3.33}$$

where $\hat{\theta}$ is the variable used for integration.

The system transfer function is derived by piecewise integration of Eqn. (3.33), (except for downscan with $\theta_s = 1$)

(i) $\theta' < \pm \ln \frac{\zeta_o \mp 1}{\zeta}$

$$\tilde{\Omega}^e_j(\zeta,\theta') = 0$$

(ii) $\pm \ln \frac{\zeta_o \mp 1}{\zeta} \leq \theta' \leq \pm \ln \frac{\zeta_o \mp \beta}{\zeta}$

$$\tilde{\Omega}^e_j(\zeta,\theta') = \frac{\gamma+1}{2} \left\{ \frac{\theta_s}{1\pm\theta_s} \frac{(\zeta_o \mp 1)^{\frac{\theta_s \pm 1}{\theta_s}}}{\zeta^{\pm\frac{1}{\theta_s}}} e^{-\frac{\theta'}{\theta_s}} \pm \frac{\zeta}{1\pm\theta_s} e^{\pm\theta'} + 1 \mp \zeta_o \right\}$$

(iii) $\pm \ln \frac{\zeta_o \mp \beta}{\zeta} < \theta' < \pm \ln \frac{\zeta_o \pm \beta}{\zeta}$

$$\tilde{\Omega}_j^e(\zeta, \theta') = \frac{\gamma+1}{2} \left\{ \frac{\theta_s}{1 \pm \theta_s} \left[\frac{(\zeta_o \mp 1)^{\frac{\theta_s \pm 1}{\theta_s}}}{\zeta^{\pm \frac{1}{\theta_s}}} - \frac{(\zeta_o \mp \beta)^{\frac{\theta_s \pm 1}{\theta_s}}}{\zeta^{\pm \frac{1}{\theta_s}}} \right] \right.$$

$$\left. + (1-\beta) \left(\frac{\zeta_o \mp \beta}{\zeta} \right)^{\pm \frac{1}{\theta_s}} \right\} e^{-\frac{\theta'}{\theta_s}}$$

$$+1 - \left(\frac{\zeta_o \mp \beta}{\zeta} \right)^{\pm \frac{1}{\theta_s}} e^{-\frac{\theta'}{\theta_s}}$$

(iv) $\pm \ln \frac{\zeta_o \pm \beta}{\zeta} \leq \theta' \leq \pm \ln \frac{\zeta_o \pm 1}{\zeta}$

$$\tilde{\Omega}_j^e(\zeta, \theta') = \frac{\gamma+1}{2} \left\{ \left[\frac{\theta_s}{1 \pm \theta_s} \left(\frac{(\zeta_o \mp 1)^{\frac{\theta_s \pm 1}{\theta_s}}}{\zeta^{\pm \frac{1}{\theta_s}}} - \frac{(\zeta_o \mp \beta)^{\frac{\theta_s \pm 1}{\theta_s}}}{\zeta^{\pm \frac{1}{\theta_s}}} \right.\right.\right.$$

$$\left.\left.\left. - \frac{(\zeta_o \pm \beta)^{\frac{\theta_s \pm 1}{\theta_s}}}{\zeta^{\pm \frac{1}{\theta_s}}} \right) + (1-\beta) \left[\left(\frac{\zeta_o \mp \beta}{\zeta} \right)^{\pm \frac{1}{\theta_s}} \right.\right.\right.$$

$$\left.\left.\left. - \left(\frac{\zeta_o \pm \beta}{\zeta} \right)^{\pm \frac{1}{\theta_s}} \right] \right] e^{-\frac{\theta'}{\theta_s}} + 1 \pm \zeta_o \mp \frac{\zeta}{1 \pm \theta_s} e^{\pm \theta'} \right\}$$

$$+ \left[\left(\frac{\zeta_o \pm \beta}{\zeta} \right)^{\pm \frac{1}{\theta_s}} - \left(\frac{\zeta_o \mp \beta}{\zeta} \right)^{\pm \frac{1}{\theta_s}} \right] e^{-\frac{\theta'}{\theta_s}}$$

(v) $\pm \ln \frac{\zeta \pm 1}{\zeta} < \theta'$

$$\begin{aligned}\tilde{\Omega}_j^e(\zeta,\theta') &= \left[\frac{\gamma+1}{2}\left\{\frac{\theta_s}{1\pm\theta_s}\left[\frac{(\zeta_o\mp 1)^{\frac{\theta_s\pm 1}{\theta_s}}}{\zeta^{\pm\frac{1}{\theta_s}}} - \frac{(\zeta_o\mp\beta)^{\frac{\theta_s\pm 1}{\theta_s}}}{\zeta^{\pm\frac{1}{\theta_s}}}\right.\right.\right. \\ &\quad \left. - \frac{(\zeta_o\pm\beta)^{\frac{\theta_s\pm 1}{\theta_s}}}{\zeta^{\pm\frac{1}{\theta_s}}} - \frac{(\zeta_o\pm 1)^{\frac{\theta_s\pm 1}{\theta_s}}}{\zeta^{\pm\frac{1}{\theta_s}}}\right] \\ &\quad + (1-\beta)\left[\left(\frac{\zeta_o\mp\beta}{\zeta}\right)^{\pm\frac{1}{\theta_s}} - \left(\frac{\zeta_o\pm\beta}{\zeta}\right)^{\pm\frac{1}{\theta_s}}\right]\Bigg\} \\ &\quad \left. + \left(\frac{\zeta_o\pm\beta}{\zeta}\right)^{\pm\frac{1}{\theta_s}} - \left(\frac{\zeta_o\mp\beta}{\zeta}\right)^{\pm\frac{1}{\theta_s}}\right] e^{-\frac{\theta'}{\theta_s}}\end{aligned} \tag{3.34}$$

For downscan with $\theta_s = 1$, the result is somewhat simpler:

(i) $\theta' < \ln \frac{\zeta}{\zeta_o+1}$

$$\tilde{\Omega}_j^e(\zeta,\theta') = 0$$

(ii) $\ln \frac{\zeta}{\zeta_o+1} \le \theta' \le \ln \frac{\zeta}{\zeta_o+\beta}$

$$\tilde{\Omega}_j^e(\zeta,\theta') = \frac{\gamma+1}{2}\left\{\zeta \ln \frac{\zeta}{\zeta_o+1} e^{-\theta'} + \zeta_o + 1 - \zeta(1+\theta)e^{-\theta'}\right\}$$

(iii) $\ln \frac{\zeta}{\zeta_o+\beta} < \theta' < \ln \frac{\zeta}{\zeta_o-\beta}$

$$\tilde{\Omega}_j^e(\zeta,\theta') = \tfrac{\gamma+1}{2}\left\{(1-\beta)\tfrac{\zeta}{\zeta_o+\beta} - \zeta \ln \tfrac{\zeta_o+1}{\zeta_o+\beta}\right\} e^{-\theta'} + 1 - \tfrac{\zeta}{\zeta_o+\beta} e^{-\theta'}$$

(iv) $\ln \frac{\zeta}{\zeta_o-\beta} \leq \theta' \leq \ln \frac{\zeta}{\zeta_o-1}$

$$\begin{aligned}\tilde{\Omega}_j^e(\zeta,\theta') &= \tfrac{\gamma+1}{2}\left\{(1-\beta)\left[\tfrac{\zeta}{\zeta_o+\beta} - \tfrac{\zeta}{\zeta_o-\beta}\right] e^{-\theta'}\right. \\ &\quad \left. + \zeta \ln\left(\tfrac{\zeta}{\zeta_o-\beta}\tfrac{\zeta_o+\beta}{\zeta_o+1}\right) e^{-\theta'} + 1 - \zeta_o + \zeta(1-\theta)e^{-\theta'}\right\} \\ &\quad + \left(\tfrac{\zeta}{\zeta_o-\beta} - \tfrac{\zeta}{\zeta_o+\beta}\right) e^{-\theta}\end{aligned}$$

(v) $\ln \frac{\zeta}{\zeta_o-1} < \theta'$

(3.35)

$$\begin{aligned}\tilde{\Omega}_j^e(\zeta,\theta') &= \left[\tfrac{\gamma+1}{2}\left\{(1-\beta)\left[\tfrac{\zeta}{\zeta_o+\beta} - \tfrac{\zeta}{\zeta_o-\beta}\right]\right.\right. \\ &\quad \left.\left. + \zeta \ln\left(\tfrac{\zeta_o-1}{\zeta_o-\beta}\tfrac{\zeta_o+\beta}{\zeta_o+1}\right)\right\} + \left(\tfrac{\zeta}{\zeta_o-\beta} - \tfrac{\zeta}{\zeta_o+\beta}\right)\right] e^{-\theta'}\end{aligned}$$

The system transfer function is illustrated in Fig. 3.3 for several values

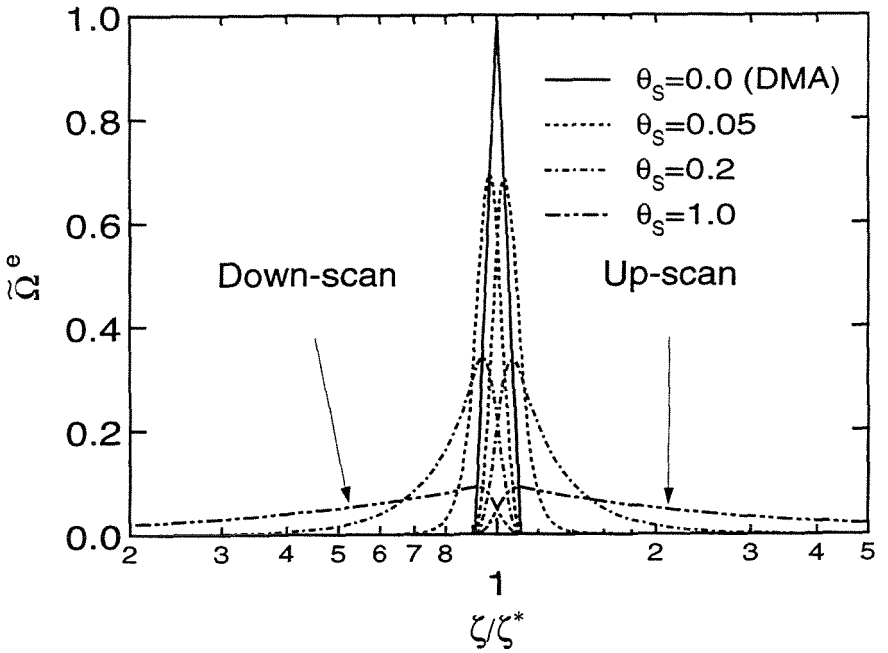

Figure 3.3: The system transfer function is illustrated for several values of θ_s for both SEMSu and SEMSd measurements with $\gamma = 1$, $\zeta_o = 10$.

of θ_s for both up- and down-scans for $\gamma = 1$, $\zeta_o = 10$. The DMA transfer function ($\theta_s = 0.0$) is the most sharply peaked transfer function. For larger θ_s, the distribution is shifted in the directions of the mobilities that are transmitted during the early part of the scan, i.e., the up-scan starts at high mobilities so the transfer function is shifted toward larger mobilities. The rise in the transfer function is nearly as sharp as that of the DMA, at least for θ_s less than about 0.1. The peak in the transfer function is shifted slightly and lies at the intersection of the shifted transfer function with the falling side of the DMA transfer function. The maximum value of the transfer function decreases rapidly with increasing θ_s, as is illustrated in Fig. 3.4.

The tail in the transfer function is far more pronounced than the peak shift, particularly for large θ_s. Figure 3.5 shows contours of the ratio of the values of ζ/ζ^* corresponding to various fractions of the peak value of Ω.

3.2.2 Measurement Channel Response

Inversion of scanning mobility data requires that the time–averaged transfer function be determined. As previously noted, this quantity can be evaluated as the cumulative transfer history integral for the total system response for a counting interval corresponding to channel i including "historical" effects from previous measurement channels to channel i, from the start of a scan to the current measurement time for the five regions of the discontinuous transfer function. The integral described in Eqn. (3.22), given the variable change introduced in Eqn. (3.28) – (3.32), such that

$$I_j^{cum}(\zeta, \theta') = \frac{1}{\tau_r} I_j^{cum}(\zeta, t) \tag{3.36}$$

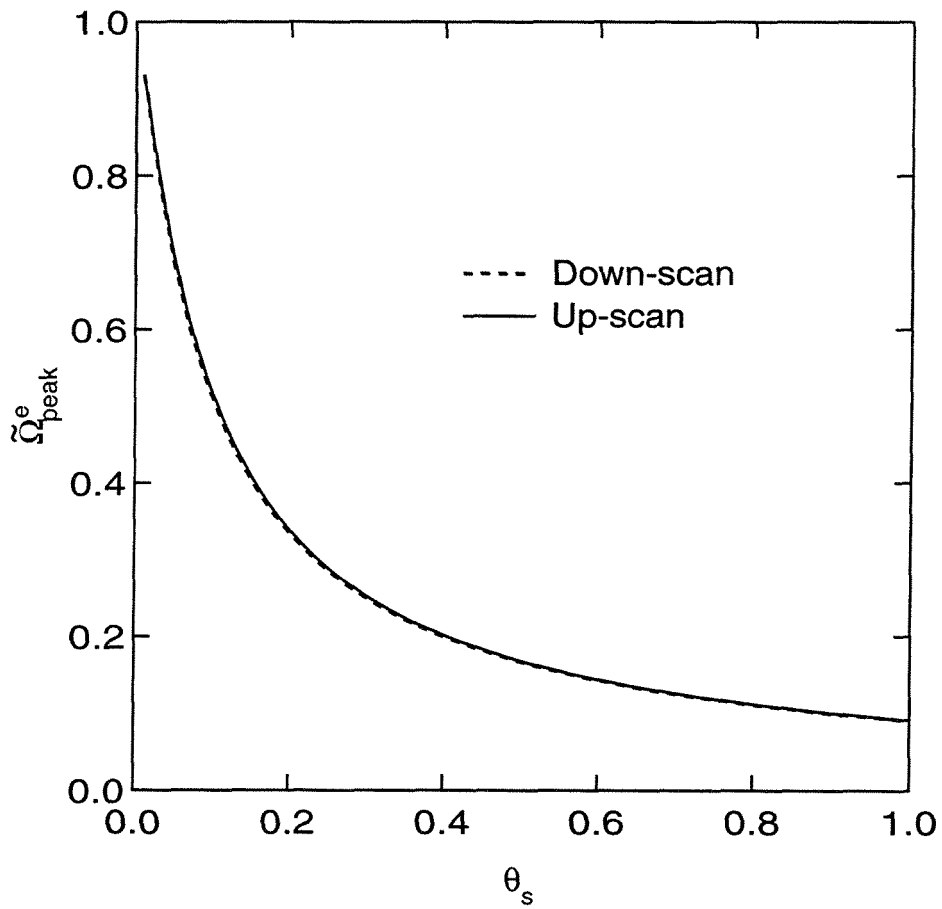

Figure 3.4: The maximum value of the transfer function, $\tilde{\Omega}^e_{peak}$, decreases rapidly with increasing θ_s.

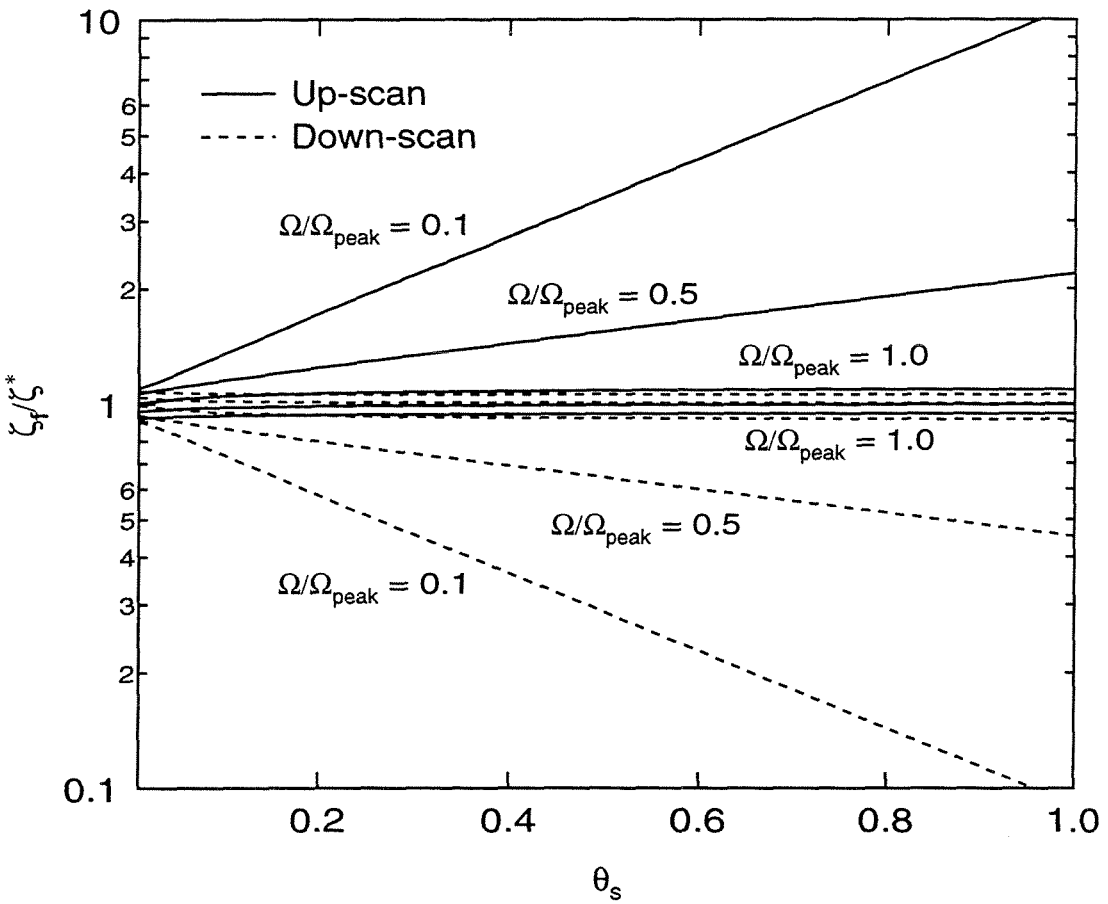

Figure 3.5: Constant-value contours of the ratio of the values of ζ/ζ^* corresponding to various fractions of the peak value of $\tilde{\Omega}^e_{peak}$.

gives the result:

$$(i) \quad \theta' + \frac{\tau_p}{\tau_r} < \pm \ln \frac{\zeta_o \mp 1}{\zeta}$$

$$I_j^{cum}(\zeta, \theta') = 0$$

$$(ii) \quad \pm \ln \frac{\zeta_o \mp 1}{\zeta} \leq \theta' \leq \pm \ln \frac{\zeta_o \mp \beta}{\zeta}$$

$$\begin{aligned} I_j^{cum}(\zeta, \theta') \; &= \frac{1 \pm \gamma}{2} \left\{ \frac{\zeta}{1 \pm \theta_s} e^{\theta'} - \frac{\zeta_o \mp 1}{1 \pm \theta_s} \right. \\ &\quad + \frac{\theta_s^2}{1 \pm \theta_s} (\zeta_o \mp 1) - \frac{\theta_s^2}{1 \pm \theta_s} \frac{(\zeta_o \mp 1)^{\frac{1 \pm \theta_s}{\pm \theta_s}}}{\zeta^{\pm \frac{1}{\theta_s}}} e^{-\frac{\theta'}{\theta_s}} \\ &\quad \left. \mp (\zeta_o \mp 1) \left(\theta' \mp \ln \frac{\zeta_o \mp 1}{\zeta} \right) \right\} \end{aligned}$$

$$(iii) \quad \pm \ln \frac{\zeta_o \mp \beta}{\zeta} < \theta' < \pm \ln \frac{\zeta_o \pm \beta}{\zeta}$$

$$I_j^{cum}(\zeta, \theta') = \frac{1 \pm \gamma}{2} \{ \pm \frac{1-\beta}{1 \pm \theta_s} \mp \frac{\theta_s^2}{1 \pm \theta_s}(1-\beta)$$

$$- \left(\frac{\theta_s^2}{1 \pm \theta_s} \left[\frac{(\zeta_o \mp 1)^{\frac{1 \pm \theta_s}{\pm \theta_s}}}{\zeta^{\pm \frac{1}{\theta_s}}} - \frac{(\zeta_o \mp \beta)^{\frac{1 \pm \theta_s}{\pm \theta_s}}}{\zeta^{\pm \frac{1}{\theta_s}}} \right] \right.$$

$$+ \theta_s(1 - \delta - \beta) \left(\frac{\zeta_o \mp \beta}{\zeta} \right)^{\pm \frac{1}{\theta_s}} \Bigg) e^{-\frac{\theta'}{\theta_s}}$$

$$+ \theta_s(1 - \delta - \beta) + (\zeta_o \mp 1) \ln \frac{\zeta_o \mp 1}{\zeta_o \mp \beta}$$

$$+ \delta \left(\theta' \mp \ln \frac{\zeta_o \mp \beta}{\zeta} \right) \}$$

$$(iv) \quad \pm \ln \frac{\zeta_o \pm \beta}{\zeta} \leq \theta' \leq \pm \ln \frac{\zeta_o \pm 1}{\zeta}$$

$$\begin{aligned} I_j^{cum}(\zeta, \theta') &= \frac{1+\gamma}{2} \left\{ \frac{\zeta_o \pm 1}{1 \pm \theta_s} - \frac{\theta_s^2}{1 \pm \theta_s}(\zeta_o \pm 1) \right. \\ &+ (\zeta_o \mp 1) \ln \frac{\zeta_o \mp 1}{\zeta_o \mp \beta} + \delta \ln \frac{\zeta_o + \beta}{\zeta_o - \beta} \\ &\pm (\zeta_o \pm 1) \left(\theta' \mp \ln \frac{\zeta_o \pm \beta}{\zeta} \right) - \frac{\zeta}{1 \pm \theta_s} e^{\theta'} \\ &- \left(\frac{\theta_s^2}{1 \pm \theta_s} \left[\frac{(\zeta_o \mp 1)^{\frac{1 \pm \theta_s}{\pm \theta_s}}}{\zeta^{\pm \frac{1}{\theta_s}}} - \frac{(\zeta_o - \beta)^{\frac{1 \pm \theta_s}{\pm \theta_s}}}{\zeta^{\pm \frac{1}{\theta_s}}} \right. \right. \\ &\left. - \frac{(\zeta_o + \beta)^{\frac{1 \pm \theta_s}{\pm \theta_s}}}{\zeta^{\pm \frac{1}{\theta_s}}} \right] + \theta_s (1 - \delta - \beta) \left[\left(\frac{\zeta_o \mp \beta}{\zeta} \right)^{\pm \frac{1}{\theta_s}} \right. \\ &\left. \left. - \left(\frac{\zeta_o \pm \beta}{\zeta} \right)^{\pm \frac{1}{\theta_s}} \right] \right) e^{-\frac{\theta'}{\theta_s}} \left. \right\} \end{aligned}$$

$$(v) \quad \pm \ln \frac{\zeta_o \pm 1}{\zeta} < \theta'$$

$$\begin{aligned} I_j^{cum}(\zeta, \theta') &= \frac{1+\gamma}{2} \Big\{ (\zeta_o - 1) \ln \frac{\zeta_o - 1}{\zeta_o - \beta} + \delta \ln \frac{\zeta_o + \beta}{\zeta_o - \beta} \\ &+ (\zeta_o + 1) \ln \frac{\zeta_o + 1}{\zeta_o + \beta} - \left(\frac{\theta_s^2}{1 \pm \theta_s} \left[\frac{(\zeta_o - 1)^{\frac{1 \pm \theta_s}{\pm \theta_s}}}{\zeta^{\pm \frac{1}{\theta_s}}} \right. \right. \\ &\left. - \frac{(\zeta_o - \beta)^{\frac{1 \pm \theta_s}{\pm \theta_s}}}{\zeta^{\pm \frac{1}{\theta_s}}} - \frac{(\zeta_o + \beta)^{\frac{1 \pm \theta_s}{\pm \theta_s}}}{\zeta^{\pm \frac{1}{\theta_s}}} + \frac{(\zeta_o + 1)^{\frac{1 \pm \theta_s}{\pm \theta_s}}}{\zeta^{\pm \frac{1}{\theta_s}}} \right] \\ &+ \theta_s (1 - \delta - \beta) \left[\left(\frac{\zeta_o \mp \beta}{\zeta} \right)^{\pm \frac{1}{\theta_s}} \right. \\ &\left. \left. - \left(\frac{\zeta_o \pm \beta}{\zeta} \right)^{\pm \frac{1}{\theta_s}} \right] \right) e^{-\frac{\theta'}{\theta_s}} \Big\} \end{aligned} \tag{3.37}$$

Again, for a downscan with $\theta_s = 1$, a separate derivation is required. Since, as we have seen from the presentation of $\tilde{\Omega}_j^e$, the resolution of the instrument is seriously degraded by the time θ_s approaches this value, the instrument will not generally be operated for θ_s even approaching this value, and it is not necessary to present that special case here.

3.3 Data Inversion

As scanning mobility particle size distribution measurements are accelerated, the size resolution deteriorates. This tradeoff may be formulated in terms of the information content of the measurement. Classical information theory then provides a framework for evaluating the competing requirements of size

precision and temporal constraints (Wolfenbarger and Seinfeld, 1990). In some applications, a gross characterization of the size distribution structure may be sufficient to characterize atmospheric aerosol evolution events. In others, details in the structure of relatively steady size distributions may reveal important aspects of the particle formation mechanisms.

Evaluating the amount of information required for a specific application requires knowledge of the instrument's kernel function. In the case of mobility–based particle size distribution measurements, the problem requires assessing how often a particle of a given mobility will be classified and detected. In effect, the kernel function is a description of the relationship between the size distribution measured and the signal reported by the instrument. In mathematical terms, a set of N experimental measurements S_i^M must be related to the particle size distribution $f(x)$ through N Fredholm integral equations

$$S_i^M = \int_I k_i(x) f(x) dx + \epsilon_i^t \tag{3.38}$$

where x is the diameter of aerosol particles, $k_i(x)$ is the instrument's kernel function or response for channel i, S_i^M is the measured signal for channel i, I is the interval outside of which $k_i(x)f(x) = 0$ always, and ϵ_i^t is the error that is inherent in any experimental measurement (Wolfenbarger and Seinfeld, 1991).

The Fredholm integral equation does not have a unique solution, but rather a set of allowed solutions that satisfy the equation. Numerous methods have been applied to the aerosol size distribution inversion problem (Twomey, 1975; Cooper and Spielman, 1976; Alofs and Balacumar, 1982; Hagen and

Alofs, 1983; Maher and Laird, 1985; Wolfenbarger and Seinfeld, 1990, 1991). Wolfenbarger and Seinfeld (1990; 1991) have reviewed these methods and proposed a method implementing constrained regularization and cross validation for finding the most realistic distribution given a set of measurements whose kernel function consists of overlapping channels. The software developed for implementing this inversion is called MICRON (Wolfenbarger and Seinfeld, 1990). This program uses the weighting information of the kernel function to select the most probable solution given specified constraints on the solution (namely non-zero smooth distributions) and is thus useful for comparing the predicted outcomes of different instrument configurations. In the discussion that follows, we employ MICRON for data inversion.

3.4 Simulations

As part of the kernel function, the non-ideal flow model introduced above can be used to predict the effects of changes in instrument configuration on the signals measured by the instrument. The dependence of the kernel function on the mixing time clearly illustrates the effects of changes in the inter-instrument plumbing. A comparison of increasing and decreasing scans illustrates the asymmetry expected to result when this effect is significant. And, finally, the ability to account for the width and overlapping of channels is illustrated in the inversion of a simulated bimodal distribution.

3.4.1 Distortion of Kernel Function with Mixing Time

The characteristic mixing time of a specified instrument configuration may be determined by evaluating the response of the instrument to a fixed input disturbance, such as a step change (Russell et al., 1995a,b). The contribution of τ_s to the distortion of the signal predicted from the measurement will also depend on τ_r, the characteristic time at which the voltage is increased (denoted SEMSu) or decreased (SEMSd). The ratio of these factors, or θ_s, illustrates this impact on the predicted kernel function for an instrument. Figure 3.6 shows an intermediate channel of the kernel function for a 30-channel SEMSu measurement (with $\tau_r = 5.0$ s, $\tau_c = 1.0$ s, $V_{min} = 15$ V, $Q_a = Q_s = 5$ cm^{3}s^{-1}, and $Q_c = Q_m = 50$ cm^{3}s^{-1}) with three different values of τ_s, and Figure 3.7 shows the corresponding channel for SEMSd measurements.

The trend illustrated by a comparison of these three kernel functions indicates that the larger the value of θ_s, the more "distorted" or wider the kernel function for a given channel becomes. The order of magnitude change in θ_s results in a factor of 5 decrease in the peak height and a more than doubling of the peak's width at its half height.

The combined effect of the kernel function illustrated here can be demonstrated by addressing the data inversion problem in reverse, namely by predicting the measurement expected (S_i) when $f(x)$ is known. A bimodal distribution with peaks of 50 cm^{-3} at 0.04 μm and 60 cm^{-3} at 0.15 μm, both with geometric standard deviations of 1.5, will serve as a test distribution for the following inversion. The measurements expected from a SEMSu

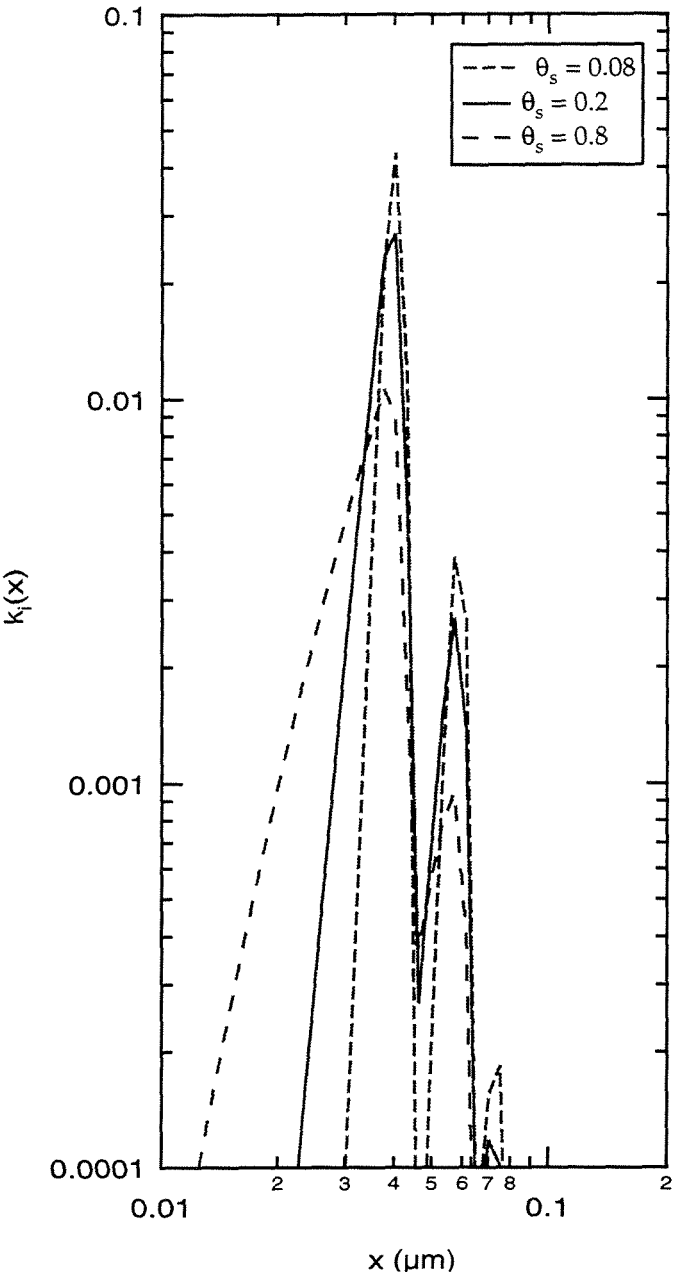

Figure 3.6: Kernel functions for channel 10 of a 30-channel SEMSu measurement (with $\tau_r = 5.0$ s, $\tau_c = 1.0$ s, $V_{min} = 15$ V, $Q_a = Q_s = 5$ cm^3, and $Q_c = Q_m = 50$ cm^{3}s^{-1}) with three different values of τ_s.

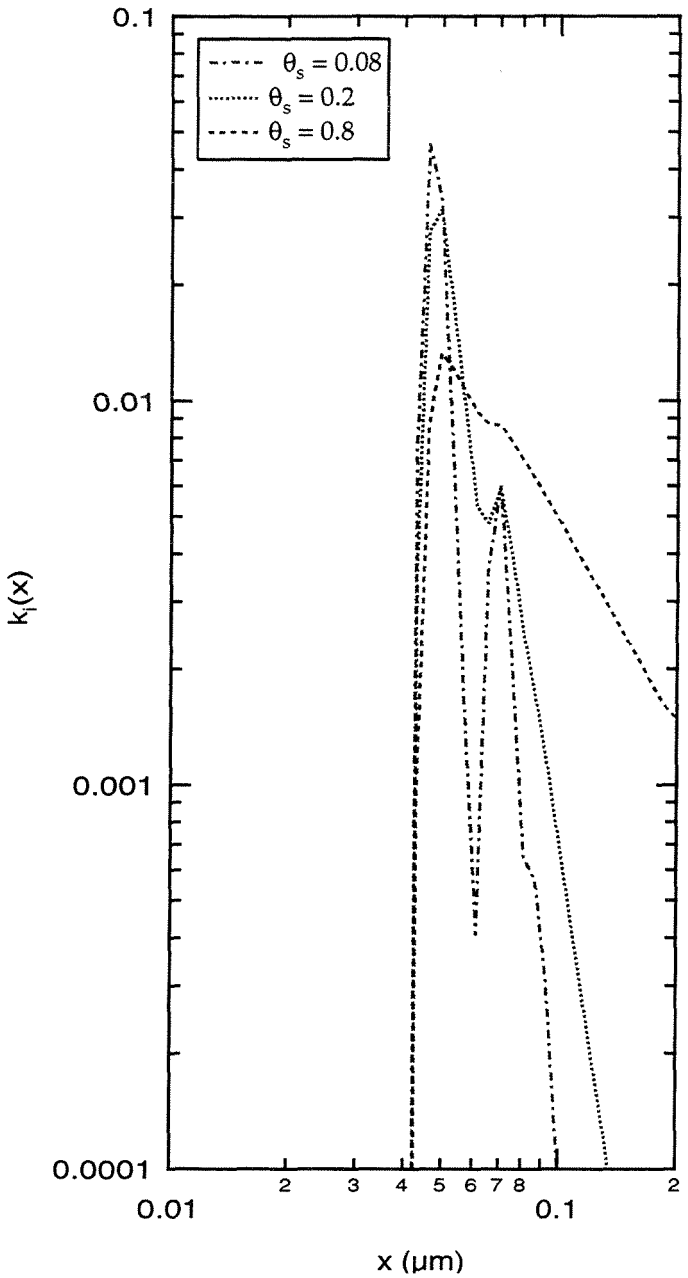

Figure 3.7: Kernel functions for channel 20 of a 30-channel SEMSd measurement (with $\tau_r = 5.0$ s, $\tau_c = 1.0$ s, $V_{min} = 15$ V, $Q_a = Q_s = 5$ cm^{3}s^{-1}, and $Q_c = Q_m = 50$ cm^{3}s^{-1}) with three different values of τ_s.

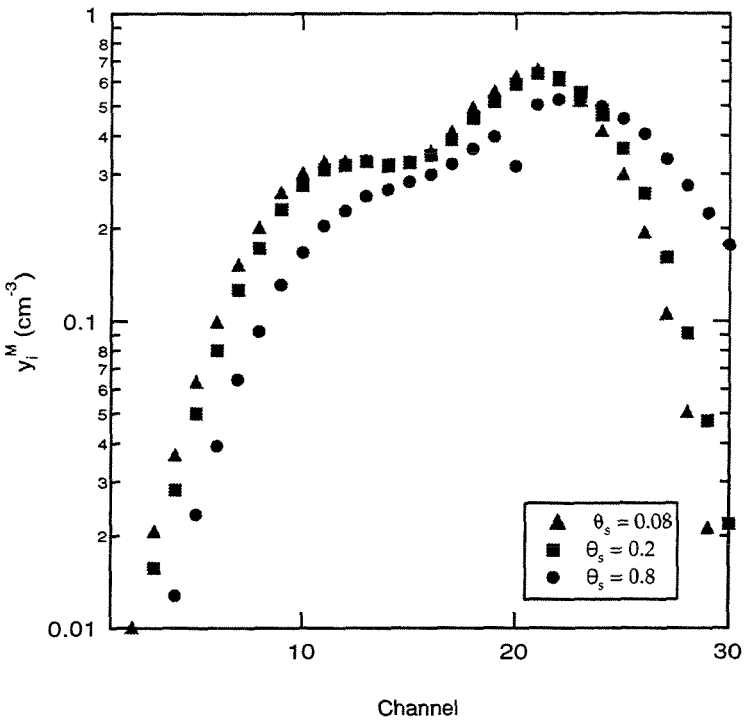

Figure 3.8: Raw measurements predicted for a bimodal distribution (with peaks of 50 cm^{-3} at 0.04 μm and 60 cm^{-3} at 0.15 μm, both with geometric standard deviations of 1.5) recorded with a 30-channel SEMSu instrument (with $\tau_r = 5.0$ s, $\tau_c = 1.0$ s, $V_{min} = 15$ V, $Q_a = Q_s = 5$ cm^{3}s^{-1}, and $Q_c = Q_m = 50$ cm^{3}s^{-1}) with three different values of τ_s.

instrument with $\tau_c = 1.0$ s and θ_s values of 0.08, 0.2, and 0.8, are illustrated in Figure 3.8, and those for a SEMSd measurement, in Figure 3.9. The apparent distortion in the measured distribution is evident in the "smearing" of the signals toward later channels (which correspond to larger particles). The resulting effect is that the uninverted data masks the separation between the two modes in the distribution. However, by applying the inversion described by the kernel derived here, we are able to retrieve the size distributions il-

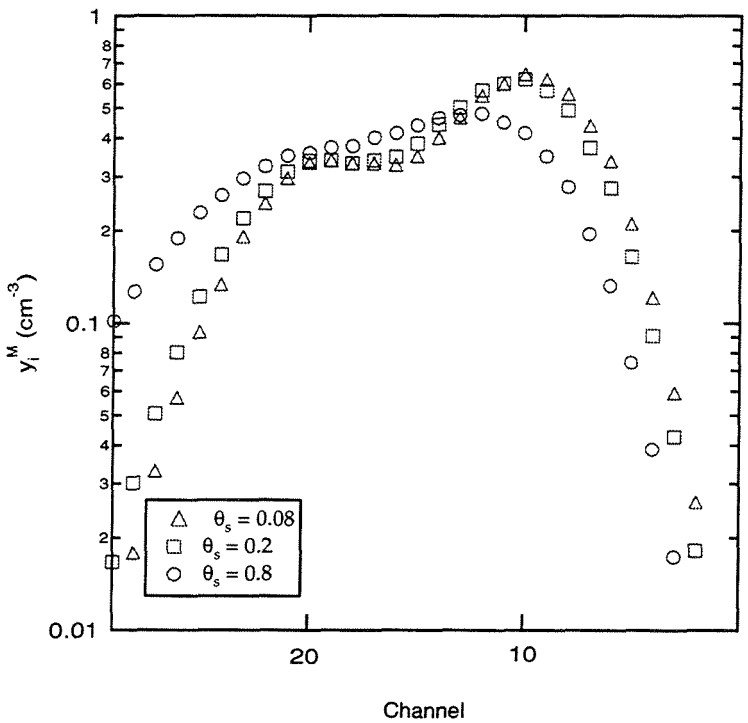

Figure 3.9: Raw measurements predicted for a bimodal distribution (with peaks of 50 cm^{-3} at 0.04 μm and 60 cm^{-3} at 0.15 μm, both with geometric standard deviations of 1.5) recorded with a 30-channel SEMSd instrument (with $\tau_r = 5.0$ s, $\tau_c = 1.0$ s, $V_{min} = 15$ V, $Q_a = Q_s = 5$ cm^{3}s^{-1}, and $Q_c = Q_m = 50$ cm^{3}s^{-1}) with three different values of τ_s.

lustrated in Figures 3.10 and 3.11, which are virtually colinear to the test distribution.

3.4.2 Predicted Asymmetry of Increasing and Decreasing Scans

A characteristic feature of the effects discussed here is that they are manifest in asymmetric distortions of the kernel function for analogous measurements, namely increasing and decreasing voltage scans of identical aerosol. Figure 3.12 shows channels 1, 10, 20, and 30 of the kernel functions for increasing and decreasing SEMS voltage scans for $\tau_r = 5.0$ s, $\tau_s = 1.0$ s, and $\tau_c = 1.0$ s. Comparison of the shape of the SEMSu and SEMSd kernels illustrates the inverse of the tailing effect observed experimentally in raw data. In the SEMSu kernel, particles from smaller sizes (which correspond to mobilities which would be classified at lower voltages) have been retained longer than τ_p and so contribute to channels measured later than predicted. The result is the tail toward smaller sizes observed in Figure 3.8. For SEMSd scans, the effect is reversed, resulting in larger particles (from higher-voltage channels) showing up in later (lower-voltage) channels.

3.5 Conclusions

These calculations illustrate the widening of the kernel function with increasing τ_s and decreasing τ_r. Consequently, the non-idealities in the instrument flow configuration represented by higher values of τ_s must be compensated

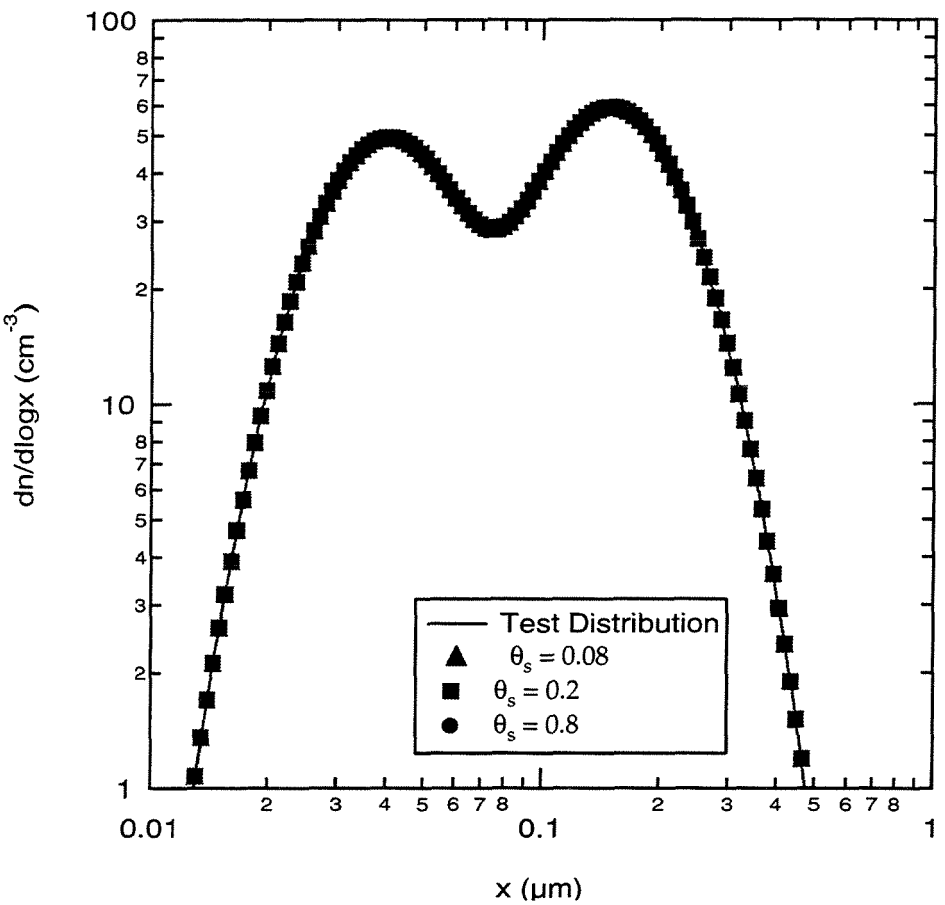

Figure 3.10: Size distribution retrieved from the SEMSu measurements shown in Figure 3.8, obtained using simultaneous multi-channel inversion with generalized cross validation. The initial test distribution used in the simulation is also illustrated.

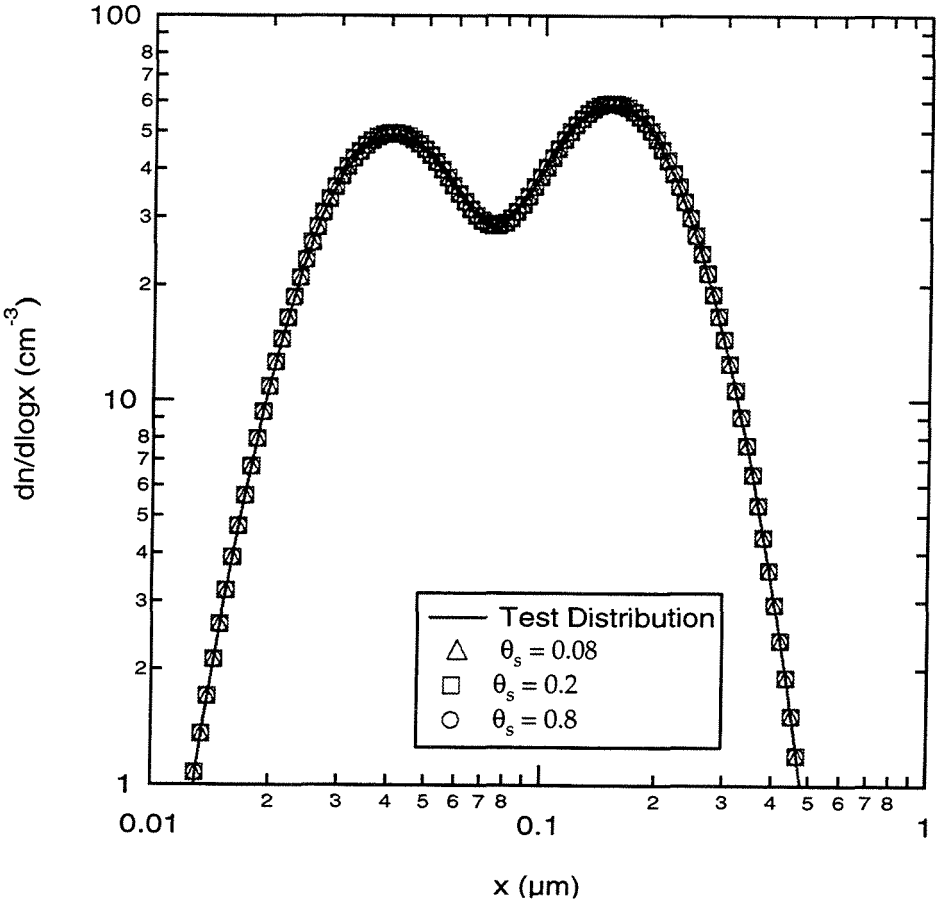

Figure 3.11: Size distribution retrieved from the SEMSd measurements shown in Figure 3.9, obtained using simultaneous multi-channel inversion with generalized cross validation. The initial test distribution used in the simulation is also illustrated.

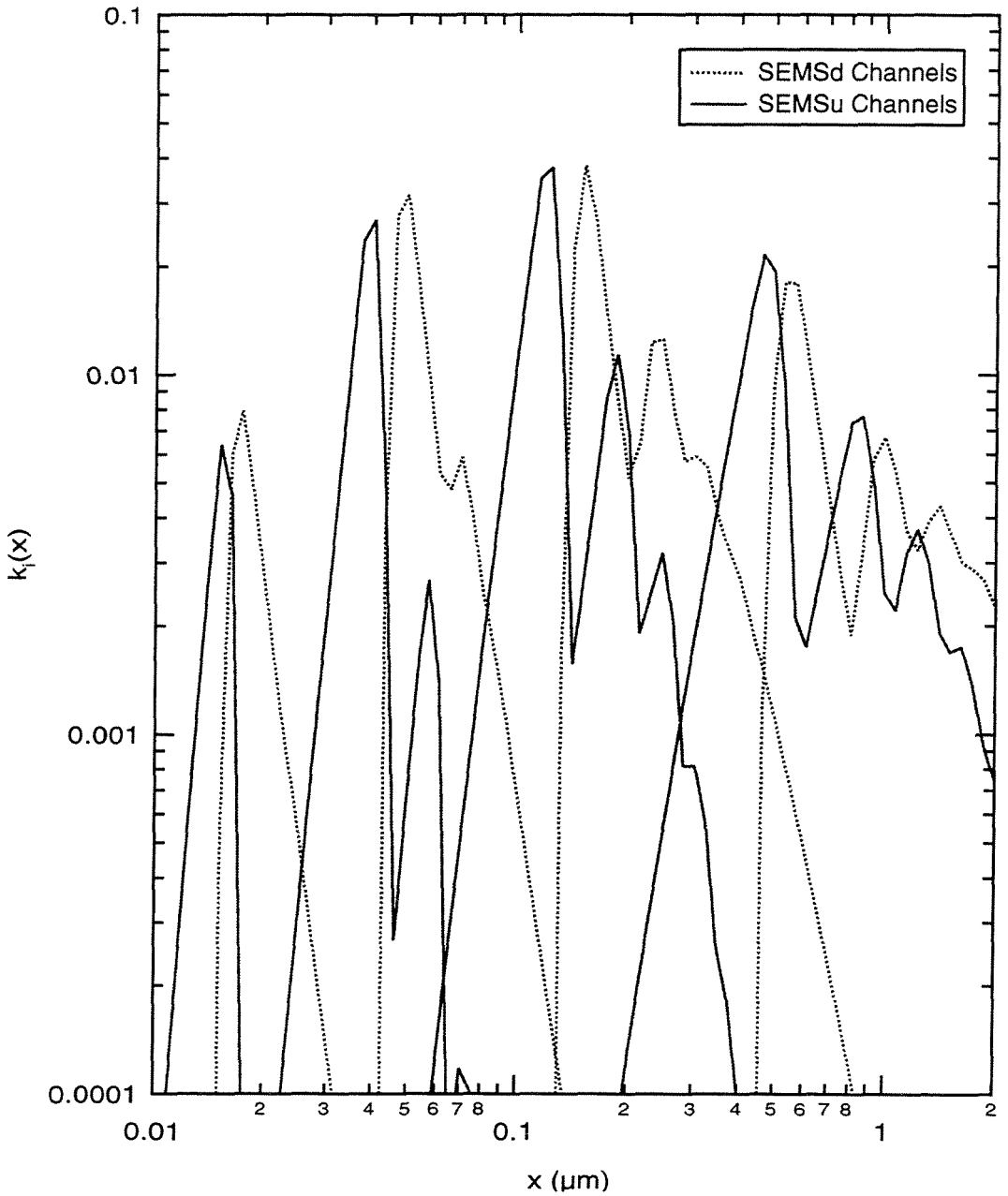

Figure 3.12: Four representative channels of the kernel functions for SEMSu and SEMSd voltage scans for $\tau_r = 5.0$ s, $\tau_s = 1.0$ s, and $\tau_c = 1.0$ s (with $V_{min} = 15$ V, $Q_a = Q_s = 5$ cm^{3}s^{-1}, and $Q_c = Q_m = 50$ cm^{3}s^{-1}).

for in longer measurement times (larger τ_r) in order to maintain commensurate precision in the measurements. Conversely, in order to optimize the time required for accelerated differential mobility measurements, the characteristic mixing time associated with the flow between classification and detection should be minimized. Configuring an instrument to meet this requirement entails shortening the overall "plumbing time" by either increasing flow rate or decreasing the plumbing volume and streamlining the flow path so that dead space may be eliminated. The asymmetry of increasing and decreasing scans serves as a diagnostic tool to assess the impact of flow non-idealities on measurement precision.

References

Alofs, D.J., and Balacumar, P. (1982) *J. Aerosol Sci.* 13: 512.

Cooper, D.W., and Spielman, L.A. (1976) *Atmos. Env.* 10: 723.

Flagan, R.C., Russell, L.M., Quant, F.R., Horton, K.D., Sem, G.J., and Havlicek, M.M. (1995) *Aer. Sci. Tech.* to be submitted.

Hagen, D.E., and Alofs, D.J. (1983) *Aer. Sci. Tech.* 2: 465.

Hoppel, W.A. (1978) *J. Aerosol Sci.* 9: 41.

Knutson, E.O., and Whitby, K.T. (1975) *J. Aerosol Sci.* 6: 453.

Levenspiel, O. (1972) *Chemical Reaction Engineering.*

Maher, E.F., and Laird, N.M. (1985) *J. Aerosl Sci.* 16: 557.

Quant, F.R., Caldow, R., Sem, F.J., and Addison, T.J. (1992) *J. Aerosol Sci.* 23: 405.

Russell, L.M., Huebert, B.J., Flagan, R.C., and Seinfeld, J.H. (1995a) *J. Geophys. Res.* in press.

Russell, L.M., Stolzenburg, M.R., Caldow, R., Zhang, S.H., Flagan, R.C., and Seinfeld, J.H. (1995b). *J. Atmos. Oceanic. Tech.* submitted.

Twomey, S. (1975) *J. Comp. Phys.* 18: 188.

Wang, S.C. and Flagan, R.C. (1990) *Aer. Sci. Tech.* 13: 230.

Wolfenbarger, J.K. and Seinfeld, J.H. (1990). *J. Aerosol Sci.* 21: 227.

Wolfenbarger, J.K. and Seinfeld, J.H. (1991). *SIAM J. Sci. Stat. Comput.* 12: 342.

Chapter 4

Characterization of Submicron Aerosol Size Distributions from Time-Resolved Measurements in ASTEX/MAGE

In press in the *Journal of Geophysical Research.*

Lynn M. Russell[1], Barry J. Huebert[2], Richard C. Flagan[1], and John H. Seinfeld[1]

[1]Department of Chemical Engineering, California Institute of Technology, Pasadena, CA

[2]Department of Oceanography, University of Hawaii, Honolulu, HI

Fundamental questions about the relative importance of processes governing formation and evolution of marine aerosols continue to challenge the frontiers of both current measurement and modeling efforts. From what marine source are new particles in the atmosphere generated? What are the mechanisms by which, in the absence of continental influence, such particles grow to sizes sufficient to activate to cloud droplets? Which mechanisms govern the formation and persistence of the characteristic features of the marine aerosol size distributions? How do continental influences impact both the structure of the size distribution and the relative number of cloud condensation nuclei (CCN) that are formed? Once formed, what removal processes determine the lifetime of CCN in the boundary layer? How closely are the CCN concentrations in the boundary layer related to the droplet concentrations of the clouds produced when this aerosol is activated?

Aerosol particles are the cynosure of these questions concerning the processes that govern the chemistry of the marine boundary layer. Models of marine aerosol processes have provided several alternate frameworks for addressing the questions posed above. Recently, Russell et al. [1994] have compared discrepancies among the diverse approaches taken to modeling the growth of marine aerosol to CCN and have shown that one crux of the disagreement is the uncertainty associated with two semiempirical parameters used to predict the relative rates of nucleation and condensation of sulfuric acid in the atmosphere.

To determine the relative importance of the mechanisms governing marine aerosol dynamics, the predictions made by these models can be evaluated with observations over the ocean. One means of achieving this evaluation is to

perform simultaneous observations of aerosol evolution and gas-phase chemistry in an individual air mass. As part of the Atlantic Stratocumulus Transition Experiment and Marine Aerosol and Gas Exchange (ASTEX/MAGE), the scientists aboard the R/V *Oceanus* endeavored to characterize the aerosol in air masses over the remote Atlantic. Located predominantly northeast of the Azores during June of 1992, the R/V *Oceanus* served as a platform for continuous sampling of gas- and aerosol-phase species and as the platform from which tetroons used to tag air masses for the Lagrangian experiments described by Huebert et al. (1995) were launched. During this cruise, ambient aerosol was sampled continuously while steaming into the wind to avoid contamination from the ship. The data presented here demonstrate the use of accelerated aerosol size distribution measurements to characterize the degree of temporal variability in the aerosol size distribution, to identify the regions of transition in the air masses encountered, and to elucidate the distinct mechanisms governing the life cycles of marine- and continentally-derived aerosols.

Fitzgerald [1991] has reviewed many of the previous measurements of marine aerosol size distributions [e.g., Hoppel et al., 1989; Gras and Ayers, 1983; Meszaros and Vissy, 1974; and Haaf and Jaenicke, 1980], and concluded that a common feature of these data is a bimodal structure in the submicron range. Hoppel and Frick [1990] have reported extensive measurements of marine aerosol size distributions (over the range of 0.016 μm to 1.4 μm diameter) that have provided a view of successive stages in aerosol evolution. Brand et al. [1991] report data for a size spectrum ranging from 0.01 μm to 25 μm diameter. According to the measurements summarized by Fitzgerald [1991],

the first mode in the submicron bimodal distribution typical of marine air is characterized by a peak between 0.04- and 0.06-μm diameter. The second, or accumulation mode, includes a peak between 0.18- and 0.30-μm diameter. Over the Atlantic Ocean, reported values of aerosol total number concentrations range from 6000 cm^{-3} near the east coast of the United States to a minimum concentration of 100 cm^{-3} in the remote Atlantic in air that had been over the ocean for more than ten days. This range of concentration is indicative of the range of aerosol that may be encountered during sampling over the ocean, distinguished not only by total concentration, but also by relative distribution with size. Aerosol with a recent continental influence, for example, is characterized not only by higher number concentrations (i.e., greater than 400 cm^{-3}), but often by only a single mode in the submicron size range. Examples of different types of marine aerosol distributions over the Atlantic Ocean were reported by Hoppel et al. [1990]. All of the reported distributions included a peak at about 0.1- μm diameter, while one at smaller sizes, typically 0.02- to 0.04-μm diameter, was missing in several air masses that were known to have advected from a continent less than 3 days previously. Hoppel et al. [1990] observed abrupt increases in the total aerosol number concentration in air masses that had been advected off the Iberian peninsula, including substantial numbers of particles too small to be detected with the differential mobility analyzer (DMA) systems being used (that is, particles smaller than about 0.02-μm diameter) that were, however, detectable with a condensation nucleus counter (CNC).

Observations of variations in aerosol size distributions have been used to interpret the mechanisms controlling marine aerosol dynamics. Hoppel

and Frick [1988] reported observations of new particle formation in remote tropical regions far from the influence of any land masses. Hoppel and Frick [1990] estimated that the aerosol particles measured were being formed at a rate of about 50 cm^{-3} d^{-1} and grew to about 0.08-μm diameter in four days to become cloud condensation nuclei (CCN). Hoppel et al. [1990] concluded that the distributions they observed would require production rates ranging from 10 to 100 cm^{-3} d^{-1}. Calculations by Russell et al. [1994] indicate that, given the current uncertainty on estimates of nucleation rates, a DMS flux exceeding 2.5 μmol m^{-2} d^{-1} would be sufficient to sustain the rates of aerosol production necessary to produce quasi-steady-state aerosol concentrations of 100 to 200 cm^{-3}. Our focus in ASTEX/MAGE was on taking near real-time measurements of complete submicron aerosol size distributions. The fast aerosol measurements that we report here illustrate the resolution possible with DMA measurements and the degree of temporal variability of submicron aerosol number concentration and size distributions in this particular field campaign.

4.1 Characterizing Atmospheric Aerosols in Situ

In 1974, Knutson and Whitby introduced a method for classifying submicron particles by electrical mobility with a precision based on single particle counts that had been heretofore not possible with existing impaction and diffusion battery instruments. The advent of this DMA for measuring aerosol

size distributions extended the range of particles that may be counted to below 0.01-μm diameter [Knutson and Whitby, 1975; Hoppel, 1978; Ten Brink et al., 1983; Winklmayr et al., 1992]. However, for in situ measurements the time required to scan a DMA over the entire size distribution has traditionally limited the temporal, spatial, and size resolution with which observations may be made. Most methods for measuring submicron aerosol size distributions involve successively measuring the concentrations of different size-classified aerosols [Hoppel, 1978; Knutson and Whitby, 1975]. Because of this approach, the frequency with which measurements may be made is limited by the response time of the detector (typically a CNC) and the flow profile from the point at which the aerosols are classified (typically an electrostatic classifier). In addition, the low aerosol concentrations that are typical of marine atmospheres may require measurements to be averaged over several seconds for each size bin in order to improve the counting statistics by increasing the signal-to-noise ratio. Consequently, existing ambient marine aerosol measurements represent samples collected over a period of 10 min or more [Hoppel et al., 1990; Quinn et al., 1993]. Improving this speed using conventional measurement methods requires that the size resolution with which the distribution is characterized be sacrificed. The scanning electrical mobility spectrometer (SEMS) algorithm [Wang and Flagan, 1990; Flagan et al., 1991] for scanning a DMA continuously over the size range of interest eliminates the delay associated with the flow time between classification and detection, although corrections to number distributions are required to account for mixing effects during fluid flow between the DMA and CNC [Russell et al., 1995]. In order to accommodate the low counting statistics in the ma-

rine atmosphere, the flow ratios through the classifier can be adjusted, thus increasing the width of each channel for which concentration measurements are made. Furthermore, since the SEMS capability increases the number of individual size measurements that can be made in a given period of time by over an order of magnitude, the loss of resolution of each channel is compensated by the additional number of channels available, whose increased overlap improves the instrument resolution. The result is the ability to collect a complete aerosol size distribution in less than 2 min.

4.2 Accelerated Aerosol Mobility Measurements

The aerosol size measurement instrumentation package employed consisted of an electrostatic classifier (TSI model 3071) in series with a CNC (TSI model 3020), as illustrated in Figure 4.1. This package was mounted on the bow of the R/V *Oceanus*, so that sampling line losses would be minimized. A reflective, weather-resistant case was designed to shelter the instruments from sea spray and to minimize fluctuations in the operating conditions to which the instruments were exposed. Aerosol was sampled through 6.3 m of 2.5-cm-diameter reinforced Tygon line feeding into this case from a dual port mounted on a tower canted over the bow. Tygon tubing was used for its flexibility and its high reported penetration efficiency for submicron aerosol sampling [Liu et al., 1985]. Spurious generation of particles in the sampling train was not observed during daily checks for zero concentrations during

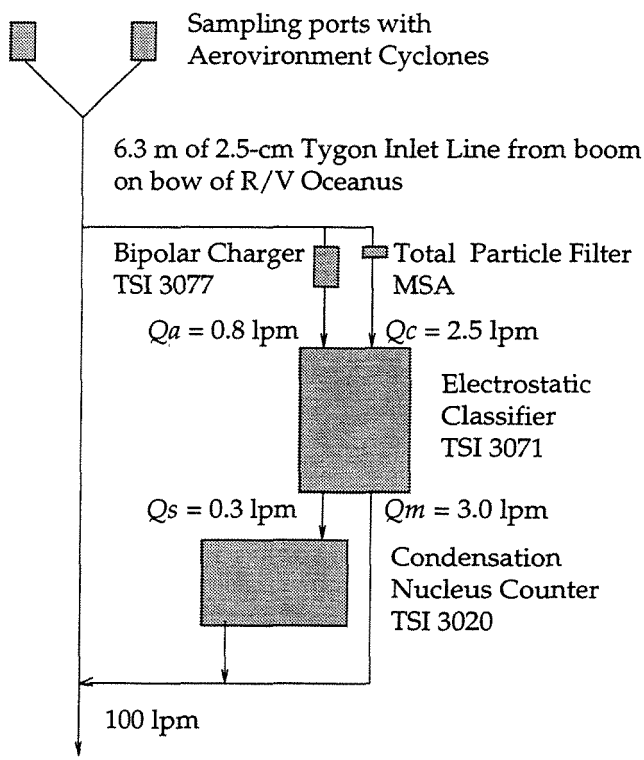

Figure 4.1: Schematic diagram of the SEMS-DMA instrumentation package mounted on the bow of the R/V *Oceanus* (lpm, liters per minute).

the cruise. The dual port sampled air through two identical cyclones that remove the supermicron aerosol fraction (Aerovironment, 2 μm cutsize at 50 L min^{-1}). The sample was pulled continuously through the sample line at a flow rate of 100 L min^{-1} using a carbon-vane pump (Gast model 823), from which 3.3 L min^{-1} was pulled through the DMA. This high flow rate minimized the residence time and reduced expected particle losses to the tubing walls during transit to the DMA. Based on correlations for turbulent mass transfer in a tube [Fuchs, 1964], we estimate these losses to be less than 23% for particles of 0.04-μm diameter and less than 8% for particles of 0.6-μm diameter.

The clean sheath flow (Q_c) to the DMA was composed of 2.5 L min^{-1} of ambient air passed through a total filter. The aerosol flow (Q_a) was composed of 0.8 L min^{-1} of ambient air fed through a Kr 85 bipolar charger (TSI model 3077) into the polydisperse aerosol flow port. The main excess flow (Qm) was set to 3.0 L min^{-1} and the sample flow (Q_s) to 0.3 L min^{-1}. These flows were adjusted using needle valves on three of the four flows and calibrated periodically with a bubble flow meter. The voltage applied across the electrostatic classifier ranged from 40 V to 4000 V using an exponential ramp generated from digital signals sent by the SEMS software [Wang and Flagan, 1990] through a 16-bit analog to digital (A/D) converter (Data Translation model 2823). During both increasing and decreasing voltage ramps, data were recorded in 1-s intervals, for a total of 74 size bins per 90-s ramp. Sixteen size bins have been eliminated from the start of both the increasing ramp (henceforth denoted SEMSu) and the decreasing ramp (SEMSd) measurements as a result of a delay in data recording, so that the SEMSu

and SEMSd measurements correspond to slightly offset size ranges. This difference between the two measurements is reflected in the kernel functions that describe the number and size of particles that are represented by the counts detected in each instrument channel. The sample flow (Q_s) was drawn through the CNC, where for concentrations less than 1000 cm^{-3}, particles were detected optically in a single counting mode. The pulses corresponding to individual counts were summed on a counting board and recorded with the SEMS software. Flow through the CNC was held constant at 0.3 L min^{-1} by an internal pump and metering system. The SEMS software recorded size distributions at 90-s intervals separated by delays of 10 s, during which data were written to disk.

The flow characteristics of the SEMS-DMA system were characterized after the experiment by calibration with monodisperse aerosol sources covering the size range measured, from 0.04-μm to 0.6-μm diameter. The effect of flow nonidealities was included by modeling the residence time distribution of the interinstrument flow [Russell et al., 1995]. For the instrument configuration employed for these measurements, the fluid transport time between the electrostatic classification of particles and their detection in the CNC was determined to be 13.3 s, with a characteristic mixing time of 4.7 s. This residence time distribution model was incorporated into the kernel function for the DMA. Figure 4.2 shows the kernel function for representative channels of both the SEMSu and SEMSd measurements. This modified kernel function was then used in the multichannel inversion routine, MICRON [Wolfenbarger and Seinfeld, 1990], in order to recover size distributions from the raw data. A trolley system was also mounted on the boom over the bow and included

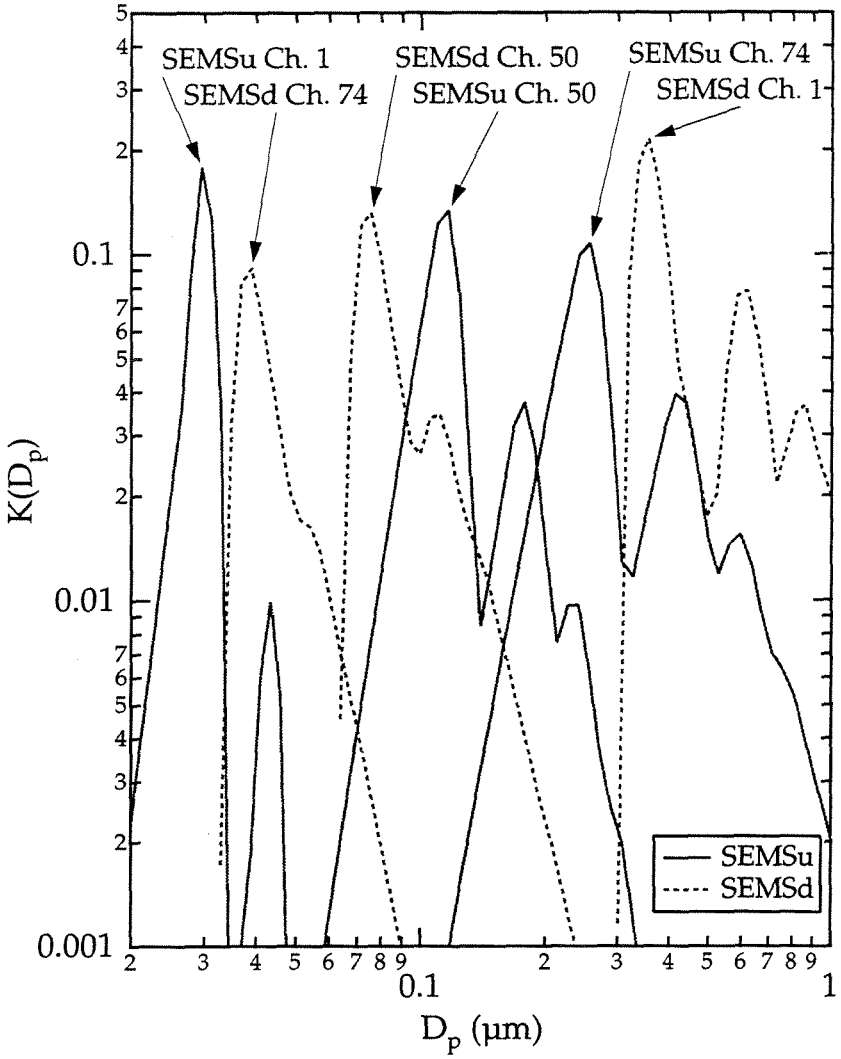

Figure 4.2: Kernel functions illustrating the signal expected for 3 of the 74 channels employed for both the SEMSu (solid line) and the SEMSd (dotted line) measurements. The first and last channels illustrate the differing ranges of the SEMSu and SEMSd measurements, which have resulted from offsets in the times for which data were recorded for increasing and decreasing voltage ramps.

a CNC (TSI model 3760) that was used to measure the total aerosol concentration continuously. The CNC was mounted with its inlet facing forward on the bow, in front of a micro-orifice uniform deposit impactor (MOUDI) also on board. The maximum and average concentrations were measured for 10-min intervals by pulling 1.5 L min^{-1} (regulated by an internal critical orifice) of aerosol through a short piece of 0.6 cm tygon tubing.

4.3 Time-Resolved Aerosol Measurements in ASTEX/MAGE

At Julian date (JDT) 160.0 (June 8, 1992), the R/V *Oceanus* travelled on a northwesterly course from 40°13.83'N and 22°10.32'W, reaching 41°08.71'N and 23°13.68'W at JDT 162.0. The prevailing winds were north to northwesterly at 3 to 5 m s^{-1}, and the region was primarily covered by patchy stratocumulus clouds [Bluth and Albrecht, 1993]. Isentropic back-trajectories from the experiment operations area suggest that the air mass sampled during this time had been over the northern Atlantic for several days [Bluth and Albrecht, 1993], as was confirmed by a 1000 mbar back-trajectory calculated from the position of the R/V *Oceanus* at JDT 160.5 (C. Bretherton, private communication, 1994). This trajectory is illustrated in Figure 4.3.

Figure 4.4 summarizes the results of aerosol measurements from these two days along with the wind speed and direction. A comparison of integrated total number concentration from SEMS measurements with continuous condensation nuclei (CN) counts reveals considerable scatter on the short

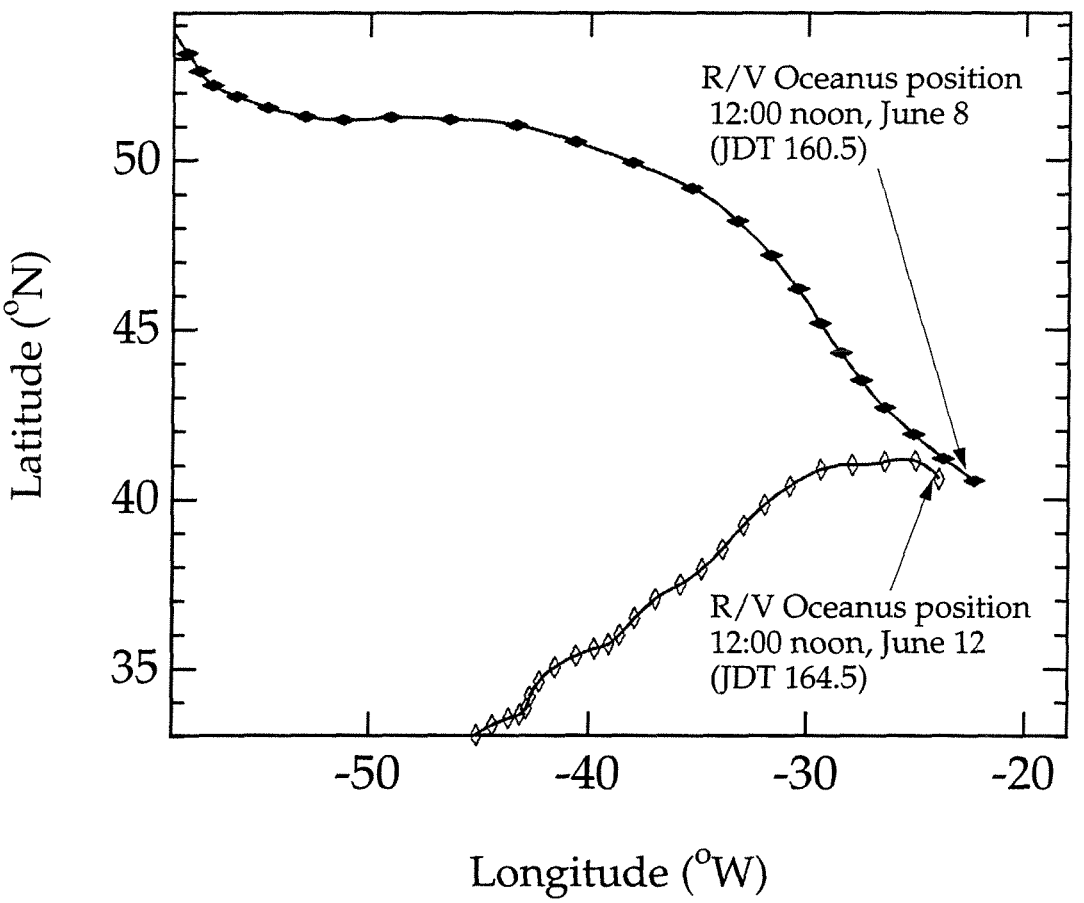

Figure 4.3: Back-trajectories for the position of the R/V *Oceanus* at JDT 160.5 and 164.5. These 1000-mbar trajectories were calculated by C. Bretherton (private communication, 1994).

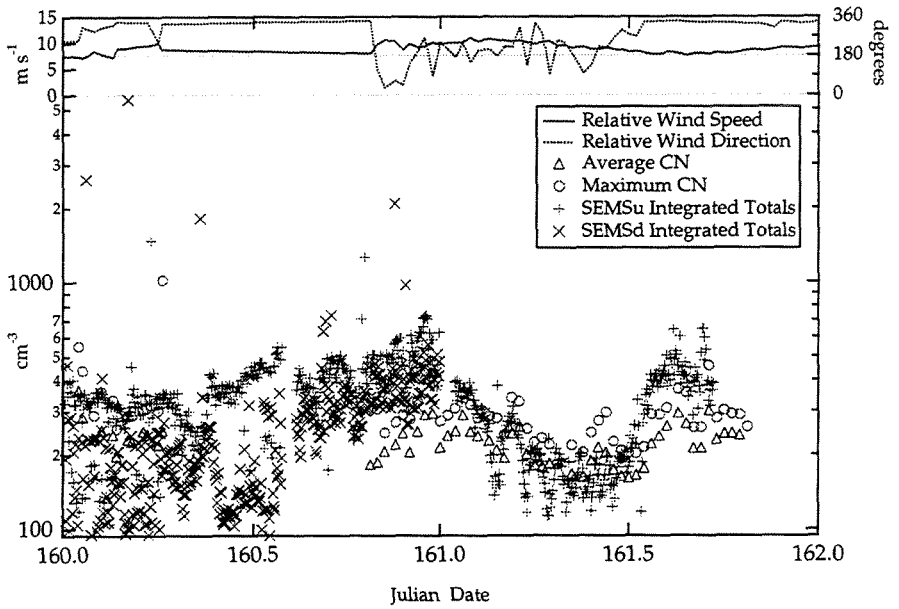

Figure 4.4: Summary of total particle concentrations from average (triangles) and maximum (circles) continuous CN, SEMSu (pluses) and SEMSd (crosses) for JDT 160 and 161 (June 8 and 9). The relative wind speed and direction are also plotted for the same time period. No SEMSd data are plotted for JDT 161 due to instrument problems on that day.

timescales sampled with the SEMS compared with the 10-min averages from the continuous CN record. The figure includes totals from both SEMSu and SEMSd measurements for JDT 160, but because of electrostatic arcing in the classifier on JDT 161, only the SEMSu distributions were reliable for that day.

During a period of simultaneous operation on JDT 161, from JDT 161.1 to 161.5, the continuous CN measurements averaged 180 cm^{-3} and the SEMSu measurements averaged 190 cm^{-3}. The integrated SEMSu totals reflect concentrations ranging between 100 and 2000 cm^{-3}. The greater range of concentrations recorded by the SEMS measurements results in the higher average values of the SEMSu concentrations compared with the continuous CN count measurements. These concentrations also decreased during the morning of JDT 161 to reach a minimum at JDT 161.5. These data suggest good agreement in the trends of the two measurements. However, the SEMS measurements are frequently higher than the continuous CN record, which results in part from uncertainty in the corrections made for particle charging at small sizes. Quantifying this systematic bias is the focus of continuing studies of the dependence of bipolar charging efficiencies on such variable environmental factors as relative humidity.

On JDT 161, a comparison of the SEMS and CNC measurements indicates significant discrepancies. During this time, the wind was shifting frequently and the bow was often downwind of the ship's stacks. Since the CNC was positioned on the tower lower than the SEMS inlet, and its sample inlet was protected from contamination from the ship by its position behind the trolley instrument package, the differing concentrations during 180°

relative winds are likely the result of contamination of both measurements, to differing degrees, from ship-generated aerosol. The performance of the clean-room type CNC used here may be degraded by scavenging action of the porous saturator under high humidity conditions, potentially resulting in underprediction of small particles by that instrument.

CN concentrations of 100 to 200 cm^{-3} at sea level are considered representative of clean marine air [Fitzgerald, 1991]. These relatively low aerosol concentrations are consistent with a mechanism in which accumulation mode particles have been scavenged by precipitation so that a large fraction of the particles remaining are less than 0.1 μm in diameter. Figure 4.5 illustrates eight of the size distributions measured on June 8 (JDT 160), between 2032 and 2048 (UT) in the evening. These distributions reflect the low number concentrations and bimodal structure characteristic of marine aerosol. The peak of the accumulation mode between 0.2-and 0.3-μm diameter is consistent with observations in the literature, as is the fine particle peak at 0.03-to 0.04-μm diameter. The smaller peaks present in the structure are a consequence of the fine size resolution (over 70 channels) used to make these measurements and persist throughout the smoothing algorithms applied as part of data inversion. Although this result suggests that these smaller peaks cannot be explained by instrument noise, they could be the product of fluctuations in the air mass sampled. The good agreement of the overlap range of consecutive SEMSu and SEMSd measurements, as well as the similarities of the entire 15 min of distributions, indicate a time period in which a consistent air mass was sampled continuously. SEMSu aerosol distributions from June 9 (JDT 161) illustrated in Figure 4.6 reflect a similar bimodal structure

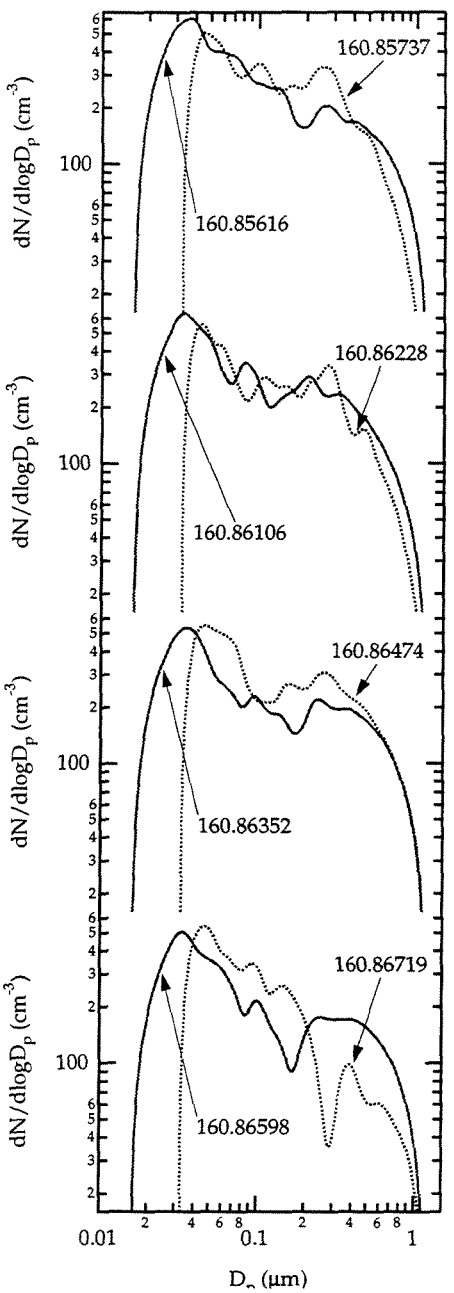

Figure 4.5: Aerosol size distributions measured with SEMSu (solid line) and SEMSd (dotted line) instruments from 2032 to 2048 on June 8. Note that the measurement range for the SEMSu and SEMSd measurements are not the same, as illustrated in Figure 4.2.

but with slightly lower concentrations overall compared with distributions measured the previous day (shown in Figure 4.5). The accumulation mode peak, in addition to having fewer particles in total, has a smaller fraction of the submicron particles and has shifted to a slightly smaller size range, falling closer to 0.2 μm at its peak.

On JDT 163.5 (June 11) the R/V *Oceanus* had left Santa Maria and was steaming on a northeasterly course toward the designated point 40°00'N, 24°00'W. From there she travelled north to 41°00'N, 24°00'W, arriving on station at JDT 164.6 to begin the first Lagrangian. Winds from the west-northwest at 3 to 5 m s^{-1} prevailed and the region's shallow boundary layer was topped with drizzling stratocumulus clouds [Bluth and Albrecht, 1993]. Isentropic back trajectories from the operations area indicate that the air mass sampled probably came from west of the Azorean Islands [Bluth and Albrecht, 1993], but the ongoing subsidence from the free troposphere may have contributed to transporting continental air to the region (C. Bretherton, private communication, 1994). The 1000-mbar back-trajectory for this case is illustrated in Figure 4.3.

With the exception of measurements contaminated by the ship's stack gases, both the SEMS integrated total concentrations and the continuous CN counts show general agreement during this time period, as can be seen from Figure 4.7. The continuous CN measurements from JDT 164 indicated an average of 340 cm^{-3}, while the SEMS totals produced average values of 440 cm^{-3} (SEMSu) and 390 cm^{-3} (SEMSd). From 0322 to 0336 on June 11 (JDT 164.14079 to 164.15053) the submicron size distribution consisted of a single mode with a peak falling between 0.2- and 0.4-μm diameter,

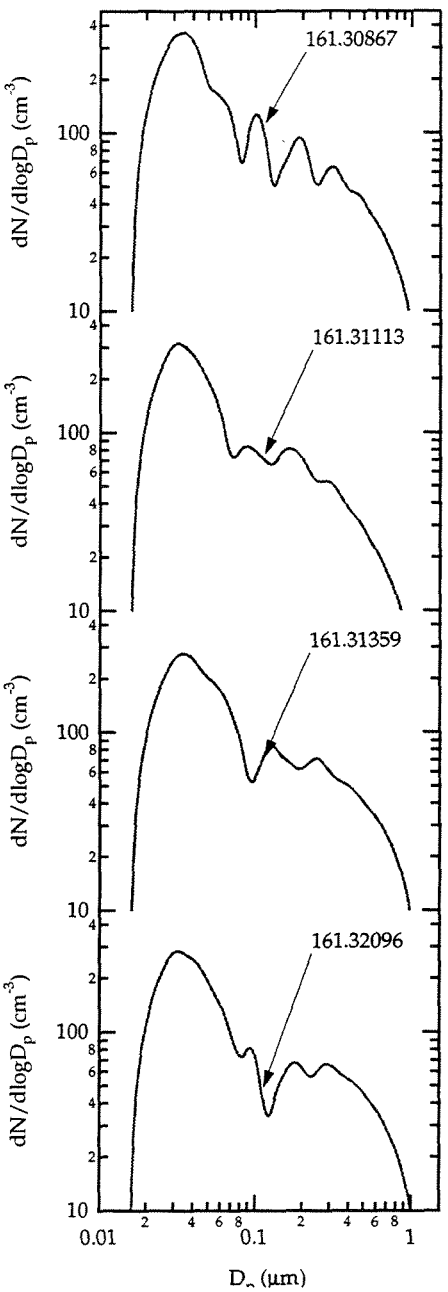

Figure 4.6: Aerosol size distributions measured with SEMSu from 0724 to 0742 on June 9.

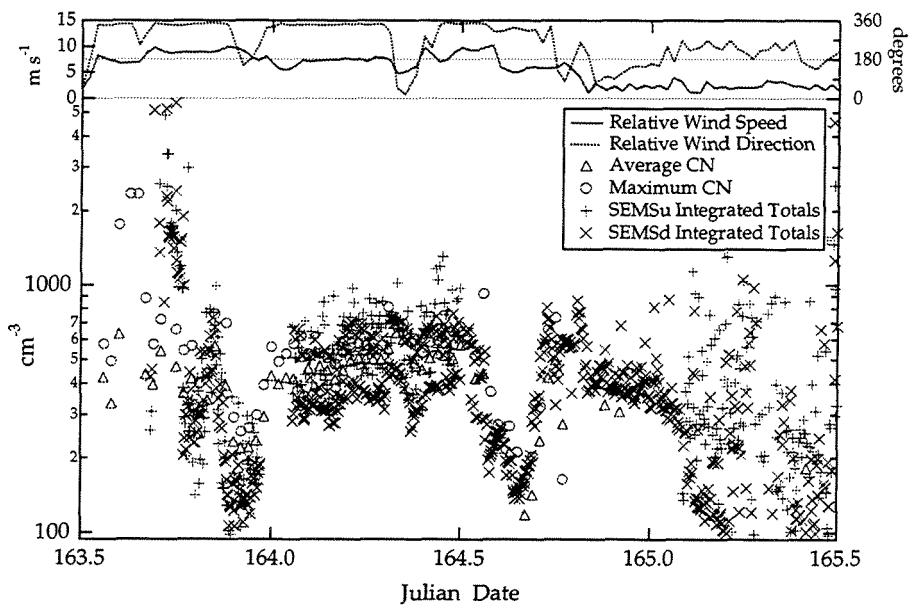

Figure 4.7: Summary of total particle concentrations from average (triangles) and maximum (circles) continuous CN, SEMSu (pluses) and SEMSd (crosses) from JDT 163.5 to 165.5 (June 11 to 13). The relative wind speed and direction are also plotted for the same time period.

as can be seen from the eight distributions in Figure 4.8. A log mean fit of the distribution indicates a peak for the aerosol measured at 164.14690 (0332 on June 11) at 0.261-μm diameter with a geometric standard deviation of 1.29; at the following SEMSd measurement the peak was at 0.311 μm with a standard deviation of 1.26. The steepness of the distribution may be exaggerated in these distributions as the concentrations at sizes smaller than this mode were below the detection limit of the SEMS-DMA system, thus making a smooth solution to the inversion problem unlikely. Both the elevated concentrations and the monomodal size distributions are consistent with an anthropogenically influenced aerosol which has aged over the ocean allowing the fine particles time to coagulate or to be scavenged during cycling through the stratus layer. For the time period considered in Figure 4.8, the concentration of particles below 0.1 μm diameter was below the detection limit of the system. The persistence of this feature seems indicative of high concentrations of accumulation-mode particles.

An additional feature of these distributions is the presence of a minor mode, particularly in the distributions from 164.14566 and 164.15053. The appearance of a second peak near 0.5-μm diameter at 164.15053 might be indicative of the beginning of growth of the population of aerosol that acts as CCN during cloud processing, and is preceded by a minor mode in measurements at 164.14446, 164.14566, 164.14690, and 164.14810. Since the particles that activate to droplets in cloud may accumulate more mass by scavenging while in cloud, their size after evaporation will have increased relative to the interstitial particles that were not activated, causing the appearance of a distinct particle mode.

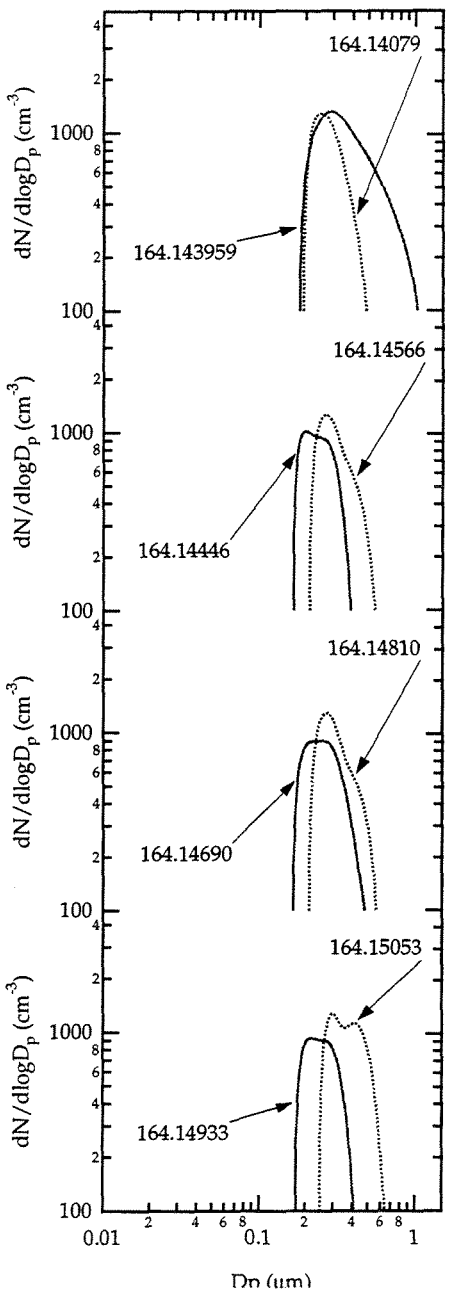

Figure 4.8: Aerosol size distributions measured with SEMSu (solid line) and SEMSd (dotted line) instruments from 0322 to 0336 on June 12. Note that the measurement range for the SEMSu and SEMSd measurements are not the same, as illustrated in Figure 4.2.

During the period from 1843 to 2330 on June 10, the aerosol concentration fluctuated from below 400 cm^{-3} to above 1000 cm^{-3} and then decreased to below 200 cm^{-3} as illustrated in Figure 4.9. Representative distributions from this time period illustrate that the initial monomodal distribution sampled at 163.80295 (1916) first increased to higher concentrations, peaking near 163.84. After that point, the aerosol measured was a lower concentration aerosol, where this transition is exemplified in the distribution shown from 163.85137 (2026). The subsequent distributions from 163.88570 (2115) and 163.96160 (2304) illustrate the less concentrated, but still monomodal, aerosol characteristic of the air sampled for the remainder of June 10.

The results indicate general agreement between the SEMS size distributions and the continuous CN measurements. The higher concentrations of the integrated SEMS totals compared with the continuous CN measurements are partially an artifact of low charging probabilities for fine particles which can overpredict the fraction of particles smaller than 0.05 μm. In addition, the trapezoidal approximation used in integrating the inverted data tends to include contributions weighted to the small-size end of the measured range. The role of this contribution would be consistent with the fact that the overprediction is greatest when a large fraction of particles are in the small size ranges. The effects of varying operating conditions on the counting efficiency of the CNC is also most pronounced below 0.05 μm, and increases the uncertainty in the kernel function in this range.

The SEMS-DMA system provides an effective way to measure submicron aerosol size distributions with high temporal, spatial, and size resolution. The additional weighting of the inlet aerosol flow rate, relative to sheath air, pro-

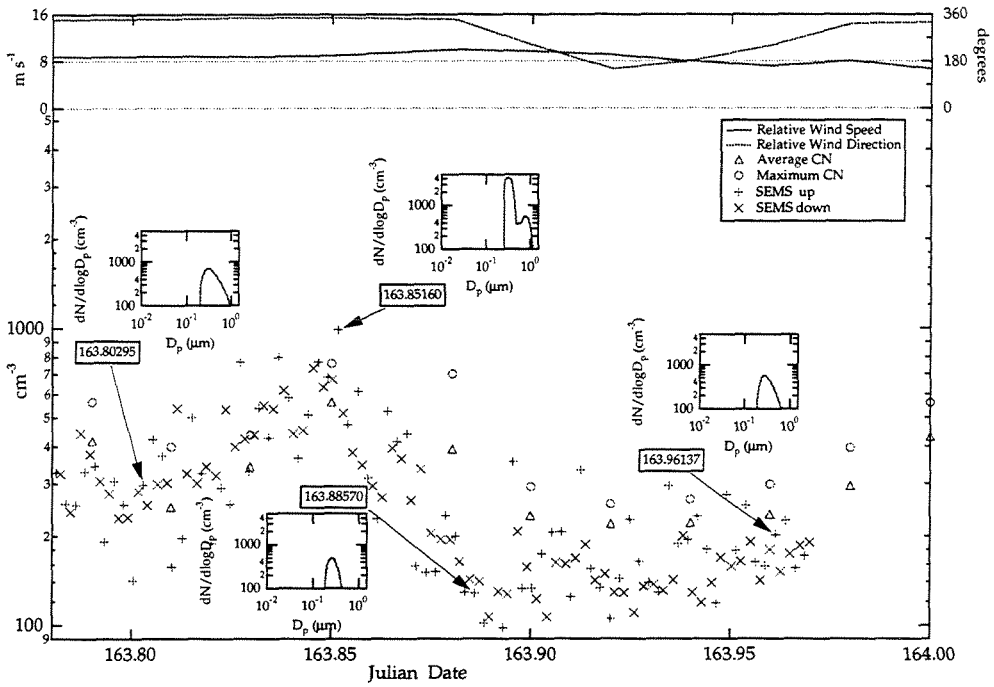

Figure 4.9: Summary of total particle concentrations from average (triangles) and maximum (circles) continuous CN, SEMSu (pluses) and SEMSd (crosses) from JDT 163.78 to 164.00 (June 12). The relative wind speed and direction are also plotted for the same time period. The SEMSu aerosol distributions measured during this time period are shown in the graph insets for the times 1916 (163.80295), 2026 (163.85137), 2115 (163.88570), and 2304 (163.96160).

vides higher counting statistics, although the resulting size channels are wider than would be expected from operating with the traditional balanced inlet and outlet flows in 10:1 ratios. The finite width of each measurement channel is accounted for in the simultaneous multichannel inversion performed using the modified MICRON software, so that the additional information provided by the increased number of channels that are recorded with SEMS may be used to constrain the solution to the data inversion problem.

4.4 Implications for Aerosol Processing Over the Ocean

Measurements discussed above illustrate characteristic differences in marine aerosol. One air mass was consistent with aged continental aerosol, whereas another contained fewer total particles and more fine particles, characteristics of background marine aerosol. The measurements illustrate observations of two very distinct air masses, each of which exhibited spatial or temporal variability evident in successive measurements. In the first case considered here for JDT 160 and 161, a reasonable interpretation is that the aerosol had been depleted by precipitation during its several days over the ocean as evidenced by back-trajectories from Bluth and Albrecht [1993], leaving an air mass containing clean background aerosol. This aerosol was also found to be comparable to the marine boundary layer aerosol distributions reported by Fitzgerald [1991] and Quinn et al. [1993], as is illustrated by the similarities in the distributions presented in Figure 4.10. In the cases examined for JDT

163 to 165, the polluted aerosol consisted of a single mode. This aerosol would be consistent with an aged continental air mass.

The contrasts in the structure of the aerosol distributions suggest differing roles for cloud processing in the marine- and anthropogenically-influenced aerosols. In the case of marine background air, cycling through nonprecipitating clouds has been suggested to produce a minimum between 0.1- and 0.2-μm diameter in the characteristic bimodal structure of aerosol distributions, as in those distributions shown in Figure 4.5 and 4.6, corresponding to the probable cutoff for particles that are capable of acting as CCN [Hoppel et al., 1990]. Hence the particles above this cutoff may accumulate mass by additional mechanisms during cloud processing, from coalescence of fine particles and condensation of sulfates. However, intermittent precipitation can periodically deplete the particle concentration, thus diminishing the amount of particulate surface area on which gas-phase species may condense. Since this process reduces one of the primary competing sinks for gas-phase condensible material, it increases the fraction of condensible material available to form new particles and grow new CCN [Pandis et al., 1994; Russell et al., 1994]. Hence, for low particle concentrations such as in distributions in Figure 4.6, where the concentrations under 200 cm^{-3} include primarily small particles resulting in a low particulate surface area, the growth by condensation would be much less than that expected for the high particle concentrations illustrated in Figure 4.8 (over 500 cm^{-3}) and their higher particulate surface areas.

In the case of the monomodal distributions characteristic of air with more recent continental influence, the concentrations of accumulation-mode aerosol

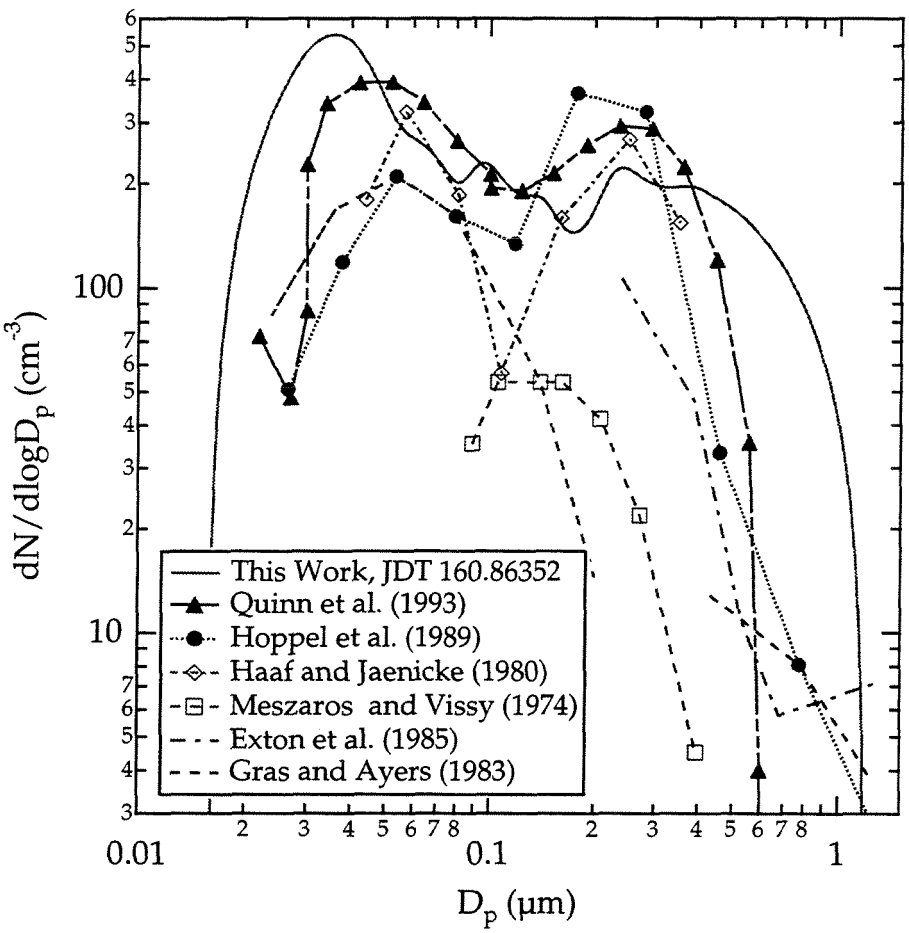

Figure 4.10: The data are taken from Fitzgerald [1991] (including Hoppel et al. [1989], Exton et al. [1985], Meszaros and Vissy [1974], Haaf and Jaenicke [1980], and Gras and Ayers [1983]) and Quinn et al. [1993].

are high, thus effectively inhibiting the formation of new particles to replace those scavenged during cloud processing [Russell et al., 1994; Pandis et al., 1994]. An interesting point is that despite observations of drizzle in the general study area, there was no corresponding depletion of submicron aerosol particles, as would be expected from precipitation scavenging. However, there is support for the effects of processing by nonprecipitating clouds in the appearance of a minor peak growing faster than the dominant single mode, as such differential rates of growth would be consistent with a selective mechanism that impacts only a subset of the aerosol population, namely those particles that act as CCN.

References

Bluth, R.T., and B.A. Albrecht, *Atlantic Stratocumulus Transition Experiment and Marine Aerosol and Gas Exchange June 1992 Experiment Summary*, United States Office of Naval Research, University Park, PA, 1993.

Brand, P., J. Gebhart, M. Below, B. Georgi, and J. Heyder, Characterization of environmental aerosols on Heligoland Island, *Atmos. Environ.*, 25A, 581-585, 1991.

Exton, H.J., J. Latham, P.M. Park, S.J. Perry, M.H. Smith, and R.R. Allan, The production and dispersal of marine aerosol, *Quat. J. Royal Met. Soc.*, 111, 817-837, 1985.

Fitzgerald, J.W, Marine aerosols: A review, *Atmos. Environ.*, 25A, 533-545, 1991.

Flagan, R.C., S.C. Wang, F. Yin, J.H. Seinfeld, G. Reischl, W. Winklmayr, and R. Karch, Electrical mobility measurements of fine-particle formation during chamber studies of atmospheric photochemical reactions, *Environ. Sci. Technol.*, 25, 883-890, 1991.

Fuchs, N.A., *The Mechanics of Aerosols*, Pergamon Press, New York, NY, 1964.

Gras, J.L., and G.P. Ayers, Marine aerosol at southern mid-latitudes, *J. Geophys. Res.*, 88, 661-666, 1983.

Haaf, W., and R. Jaenicke, Results of improved size distribution measurements in the Aitken range of atmospheric aerosols, *J. Aerosol Sci.*, 11, 321-330, 1980.

Hoppel, W.A., Determination of the aerosol size distribution from the mobility distribution of the charged fraction of aerosols, *J. Aerosol Sci.*, 9, 41-54, 1978.

Hoppel, W.A., and G.M. Frick, Evidences of particle formation by homogeneous nucleation over the oceans, in *Atmospheric Nucleation*, Lecture Notes in Phys. Ser., edited by P.E. Wagner and G. Vali, pp. 241-244, Springer-Verlag, New York, 1988.

Hoppel, W.A., J.W. Fitzgerald, G.M. Frick, R.E. Larson, and E.J. Mack, *Atmospheric aerosol size distributions and properties found in the marine boundary layer over the Atlantic Ocean*, NRL Report 9188, 1989.

Hoppel, W.A., and G.M. Frick, Submicron aerosol size distributions measured over the tropical and south Pacific, *Atmos. Environ.*, 24A, 645-659, 1990.

Hoppel, W.A., J.W. Fitzgerald, G.M. Frick, R.E. Larson, and E.J. Mack, Aerosol size distributions and optical properties found in the marine boundary layer over the Atlantic Ocean, *J. Geophys. Res.*, 95, 3659-3686, 1990.

Huebert, B.J., A. Pszenny, and B. Blomquist, The Atlantic Stratocu-

mulus Transition Experiment/Marine Aerosol and Gas Exchange (ASTEX/MAGE) experiment, *J. Geophys. Res.*, this issue.

Knutson, E.O., and K.T. Whitby, Aerosol classification by electric mobility: Apparatus, theory, and applications, *J. Aerosol Sci.*, 6, 443-461, 1975.

Liu, B.Y.H., D.Y.H. Pui, K.L. Rubow, and W.W. Szymanski, Electrostatic effects in aerosol sampling and filtration, *Ann. Occup. Hyg.*, 29, 251-269, 1985.

Meszaros, A., and K. Vissy, Concentration, size distribution and chemical nature of atmospheric aerosol particles in remote ocean areas, *J. Aerosol Sci.*, 5, 101-109, 1974.

Pandis, S.N., L.M. Russell, and J.H. Seinfeld, The relationship between DMS flux and CCN concentration in remote marine regions, *J. Geophys. Res.*, 99, 16,945- 16,957, 1994.

Quinn, P.K., D.S. Covert, T.S. Bates, V.N. Kapustin, D.C. Ramsey-Bell, and L.M. McInnes, Dimethylsulfide cloud condensation nuclei climate system: Relevant size-resolved measurements of the chemical and physical properties of atmospheric aerosol particles, *J. Geophys. Res.*, 98, 10411- 10427, 1993.

Russell, L.M., R.C. Flagan, and J.H. Seinfeld, Asymmetric instrument response resulting from mixing effects in accelerated DMA-CPC measurements, *Aerosol Sci. Technol.*, in press, 1995.

Russell, L.M., S.N. Pandis, and J.H. Seinfeld, Aerosol production and growth in the marine boundary layer, *J. Geophys. Res.*, 99, 20989-21003, 1994.

Ten Brink, H.M., A. Plomp, H. Spoelstra, and J.F. Vandevate, A high-resolution electrical mobility aerosol spectrometer (MAS), *J. Aerosol Sci.*, 14, 589-597, 1983.

Wang, S.C., and R.C. Flagan, Scanning electrical mobility spectrometer, *Aerosol Sci. Technol.*, 13, 230-240, 1990.

Winklmayr, W., G.P. Reischl, and A.O. Lindner, A new electromobility spectrometer for the measurement of aerosol size distributions in the size range from 1 to 1000 nm, *J. Aerosol Sci.*, 22, 289-296, 1992.

Wolfenbarger, J.K., and J.H. Seinfeld, Inversion of aerosol size distribution data, *J. Aerosol Sci.*, 21, 227-247, 1990.

Chapter 5

Radially-Classified Aerosol Detector for Aircraft-Based Submicron Aerosol Measurements

Submitted to the *Journal of Atmospheric and Oceanic Technology.*

Lynn M. Russell[1], Mark R. Stolzenburg[2], Shou-Hua Zhang[1], Robert Caldow[3], Richard C. Flagan[1] and John H. Seinfeld[1]

[1]Department of Chemical Engineering, California Institute of Technology, Pasadena, CA

[2]Aerosol Dynamics, Inc., Berkeley, CA

[3]TSI, Inc., St. Paul, MN

A primary need in atmospheric research instrumentation is the capability to perform high-resolution, in-situ aerosol measurements from aircraft and ships to probe the spatial and temporal variability of the tropospheric aerosol (Daum and Springston, 1993). A striking example of the effect of spatial variability of aerosol characteristics on cloud properties is provided by so-called "ship tracks," first observed from satellites (Conover, 1966), and later from aircraft measurements (Radke et al., 1989; King et al., 1993). Ship tracks provide a dramatic example of the interaction between aerosol features and resulting cloud characteristics; measuring this microphysical evolution by means of in-situ measurements was an important goal of the Monterey Area Ship Track (MAST) Experiment. These spatially well-defined perturbations of the aerosol concentration and composition and of cloud properties provide an opportunity to study the broader question of the impact of anthropogenic emissions on cloud properties.

Theoretical studies have predicted that both marine and anthropogenically-influenced tropospheric aerosols should vary diurnally as a result of photochemical reactions resulting in secondary new particle formation and aerosol growth (Russell et al., 1994). Such work suggests that the aerosol size distribution will evolve during the day through a series of characteristic size distributions indicative of periods of nucleation and condensation. Providing in-situ evidence for such direct dependence of aerosol properties on other atmospheric variables suggests studies of marine boundary layer and free tropospheric aerosol with aircraft instrumented to measure size distributions quickly and automatically.

In order to characterize small-scale or ephemeral features in the atmo-

spheric aerosol, airborne measurements of submicron aerosol size distributions at a frequency capable of resolving the differences, for example, between the cloud line features and surrounding clouds are required. Commercially-available submicron aerosol classification and counter designs are not suited for this application because of the long sampling times required to characterize two or more decades of the submicron size distribution. We describe here the design and implementation of a new system for aircraft-based sampling of tropospheric aerosol.

5.1 Aircraft-based Aerosol Measurements

Aircraft-based aerosol measurements with optical particle counters aboard aircraft have provided valuable insight into the variation of aerosol with altitude, and the character of aerosol in and above cloud (Clarke, 1991; Hegg, 1993; Radke et al., 1989; King et al., 1993). Radke et al. (1989) described a system for obtaining size distribution information with an optical particle counter (OPC) for particles greater than 0.1 μm diameter. Clarke et al. (1991) introduced the Thermo-Optical Aerosol Detector (TOAD) to characterize both the dry aerosol distribution and its volatility. Hegg et al. (1993) and Clarke (1993) have extended the effective size range of aerosol measurement using mobility-classification to below 20 nm diameter.

Several constraints are inherent to aircraft-based submicron aerosol measurement, including limitations on size, weight, and power as well as the

necessity for making fast measurements while adjusting rapidly for changing pressure, temperature, and humidity conditions. Previous investigations measuring submicron aerosol from aircraft are listed in Tab. 5.1. The need for rapid measurements derives from the aircraft's speed relative to the spatial scale of changes in aerosol properties. The spatial resolution possible with an airborne instrument is determined both by the speed of the instrument and the speed of the aircraft. Conventional differential mobility analyzer analysis requires a sampling period of about 10 min. If continuous sampling methods were employed, the resulting size distribution would represent, for example, at a speed of 100 m s^{-1}, a composite distribution of sized aerosol concentrations for a 60-km flight leg. Since air mass characteristics can change drastically over 60 km, several groups have employed a grab sampling approach in which air is drawn into a holding chamber and stored while a single measurement is processed (Radke et al., 1989; Hegg et al., 1993; Clarke, 1993). Radke et al. (1989) employed a 90 l steel cylindrical chamber with a floating piston filled by ram pressure to store the aerosol for size classification, and were thus able to store a sample collected in ca. 5 s. Hegg et al. (1993) also employed a large (2.5 m^3) polyethylene bag for analysis over a ten minute period of size classification.

The approach of grab sampling has successfully provided in-flight snapshots of aerosol in air masses, which have been coupled with continuous condensation nuclei (CN) measurements to determine the aerosol's spatial

Table 5.1: Comparison of ranges, sampling times, and control methods of aircraft instrumentation for measuring size-classified submicron aerosol particles. The characteristics contained in the table are based on published descriptions from Brock et al. (1989), Hudson and Clarke (1992), Hegg et al. (1993), Frick and Hoppel (1993), and the present work.

Reference	Platform	Diameter Range	Instrument	Sampling Time
Brock et al. (1989)	UW C131a	0.010 to 1.0 μm	Electrostatic Aerosol Analyzer (TSI)	not specified
			Diffusion Battery (TSI)	
Hegg et al. (1993)	UW C131a	0.020 to 0.6 μm	Differential Mobility Analyzer (TSI)	4 min
Frick and Hoppel (1993)	NRL Airship	0.010 to 1.2 μm	Differential Mobility Analyzer (NRL)	10 min
Hudson and Clarke (1992)	NCAR Electra	0.020 to 0.6 μm	Differential Mobility Analyzer (TSI)	not specified
This work	UW C131a	0.005 to 0.2 μm	Differential Mobility Analyzer (CIT)	45 s

variability. Measurement speed still limits both the frequency with which complete distributions can be acquired and the instrument's lower detection limit. Diffusional deposition of aerosol particles on the walls of a sampling vessel can reduce the number concentrations dramatically for long counting times (Fuchs, 1964; Crump and Seinfeld, 1981). Consequently, the chamber's volume must be chosen such that particle losses during sampling and analysis are minimized. Particle losses in a chamber are also exacerbated by electrostatic enhancement of charged particles on the chamber walls (McMurry and Rader, 1985). Hegg et al. (1993) measured ultrafine particles during a 10-min. sample measurement protocol by employing a 2.5-m^3 chamber.

The speed with which aerosol size distributions may be characterized is limited by the time required to obtain significant particle counts for each size channel, which, for a given ambient concentration, is a function of the counting statistics and efficiency of the detector and the flow profile in the measurement system (Wang and Flagan, 1990; Russell et al., 1995). In single-particle counting operation, the counting statistics of condensation particle counters (CPCs) are governed by the number of particles that can be counted in a specified time interval. For a stream of air containing N_i particles (cm^{-3}) with flow rate Q_s at the detector and detection efficiency $s(D_p, \nu)$ for particles of diameter D_p and charge ν, the signal for channel i measured (S_i) is proportional to the product, $N_i Q_s s(D_p, \nu)$.

Of commercially available counters, the TSI 3025 has the highest detec-

tion efficiency for ultrafine (less than 10-nm diameter) particles (Stolzenburg and McMurry, 1989; Quant et al., 1992). However, in order to obtain uniform saturation the sample flow is surrounded by a sheath flow that dilutes the flow to the counter of 0.3 L min^{-1} by a factor of 10, so that Q_s is 0.03 L min^{-1}. Other counters, in particular TSI models 3010 and 3022, have detector flow rates of 1 L min^{-1}, but have 50% detection efficiency cutoffs of 10 nm and 8 nm, respectively, such that size distributions may not be extended to the ultrafine range (Quant et al., 1992).

Airborne measurements of particle size distributions by differential mobility analysis are further complicated by pressure variations that accompany altitude changes. Mobility classification requires precise control of several coupled flow rates. Continuous measurements require immediate and accurate adjustment of those flows in response to changes caused by pressure variations.

5.2 Instrument Design

A radially-classified aerosol detector (RCAD) has been developed for unattended, high-resolution airborne measurement of particle size distributions of atmospheric aerosols. The principal components of the system are an alternating grab-bag sampler, an aerosol charger-neutralizer, a radial differential mobility analyzer (RDMA), and an ultrafine condensation particle counter (CPC). The integrated size measurement system is shown schematically in

Table 5.2: Dimensions of six differential mobility analyzer (DMA) designs.

Geometry	Group	Reference	Diameter Range[a]	Dimensions[b] (H x D)
Cylindrical - "long"	TSI, Inc.	Knutson and Whitby (1975)	0.020 to 1.000 μm	44 cm x 3.9 cm
	NRL	Hoppel (1978)	0.010 to 1.2 μm	86 cm x 10 cm
	Hauke	Winklmayr et al. (1991)	0.010 to 1.000 μm	60 cm x 6.6 cm
Cylindrical - "short"	TSI, Inc.	Adachi et al. (1990)		10 cm x 3.9 cm
	Hauke	Winklmayr et al. (1991)	0.001[c] to 0.150 μm	11 cm x 6.6 cm
Radial	ISPN	Fissan et al. (1994)	0.007 to 1.000 μm	0.4 cm x 13 cm
	CIT	Zhang et al. (1995)	0.003[d] to 0.500 μm	1.0 cm x 10 cm

[a]Unless otherwise noted, the lower bound is the 50% cutoff in transmission efficiency.
[b]Dimensions given are outer dimensions of flow volume. In each case the height (H) and diameter (D) are given.
[c]Transmission efficiencies were not measured. Lower bound is range specified in paper.
[d]Transmission efficiency measured at this diameter is 92%. No data is available for smaller sizes.

Fig. 5.1. Through a series of valves, the bag sampler captures a fixed volume of air from which the aerosol is drawn into the classifier and detector. After filling a bag, flow is extracted at approximately 6 L min^{-1} through the radioactive charger in which the aerosol attains a steady-state bipolar charge distribution.

The RDMA effectively eliminates most of the signal degradation associated with diffusion broadening in conventional electrostatic classifiers (Zhang et al., 1995). The RDMA has an aerosol inlet with minimal particle losses and a residence time one-fifth that of the most common commercial cylindrical DMA (TSI, St. Paul, Minnesota, model 3071) leading to reduced diffusion losses and broadening for small particles. In addition, as shown in Table 5.2, the RDMA is more compact and lighter weight than its cylindrical counterparts, thus facilitating its use aboard aircraft. We have further enhanced this

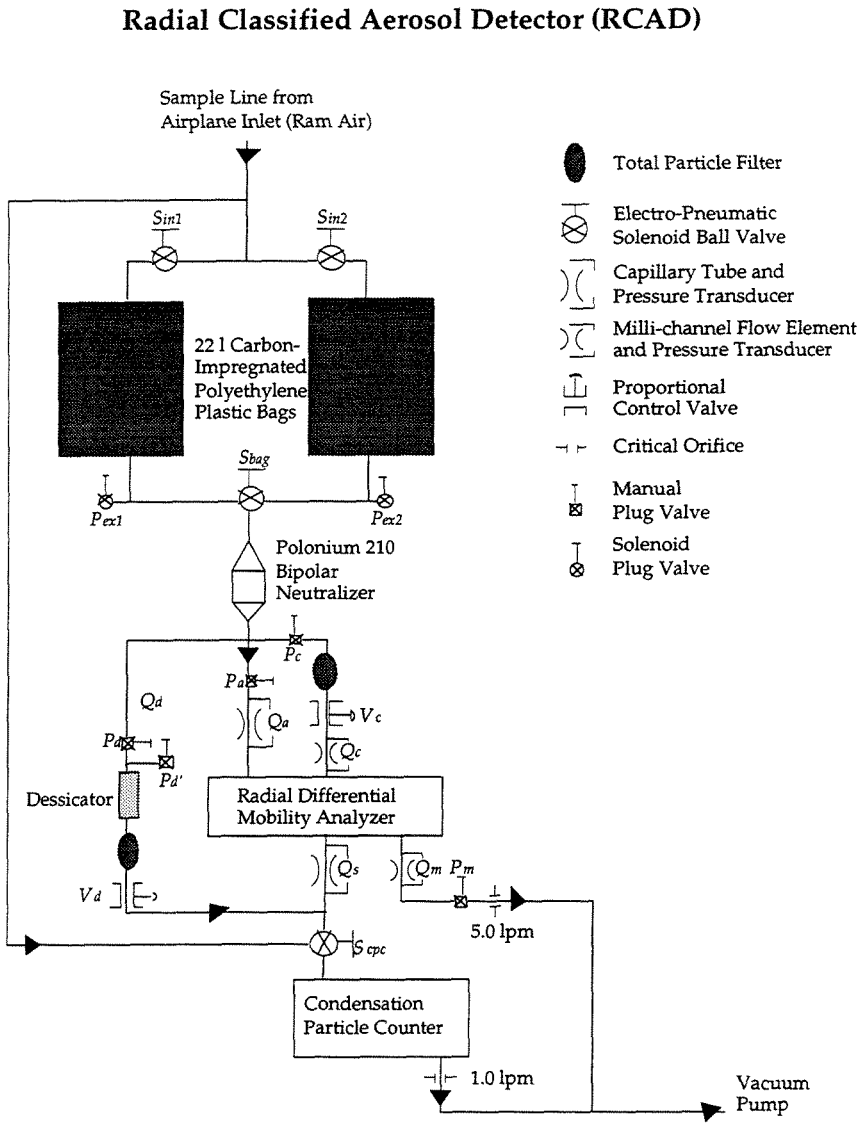

Figure 5.1: Components and configuration of the Radial Classified Aerosol Detector (RCAD).

instrument by extending the range of sizes that can be measured by employing an analog voltage ramp circuit to control the high voltage applied across the classifier, thereby providing accurate voltage control over four decades.

The ultrafine CPC combines the condensation efficiency of ultrafine particles in the Stolzenburg and McMurry (1989) design with the higher flow rates of conventional clean-room type CPCs. As a result, counting rates are sufficiently large to provide adequate signal-to-noise ratios even at low number concentrations. Counting efficiency for ultrafine particles was improved by increasing the difference in temperatures in the saturator and the condenser. The resulting instrument shows both high efficiency in detecting ultrafine particles and good counting statistics at low concentrations.

5.2.1 Alternating Double-Bag Sampler

The grab-bag sampling system operates with two identical sampling bags in parallel, such that one bag may be flushed then filled while the other bag is used for measuring the collected aerosol. The photograph in Fig. 5.2 shows the dimensions of the apparatus. The valves regulating the direction of aerosol flow employ ball valves operated by an electropneumatic solenoid system (Whitey). The bags are constructed from custom-cut carbon-impregnated polyethylene mounted between two steel-shim-covered Plexiglas disks. The air enters the aircraft through 1.9-cm (i.d.) tubing (carbon-impregnated polyethylene), shown in Fig. 5.1.

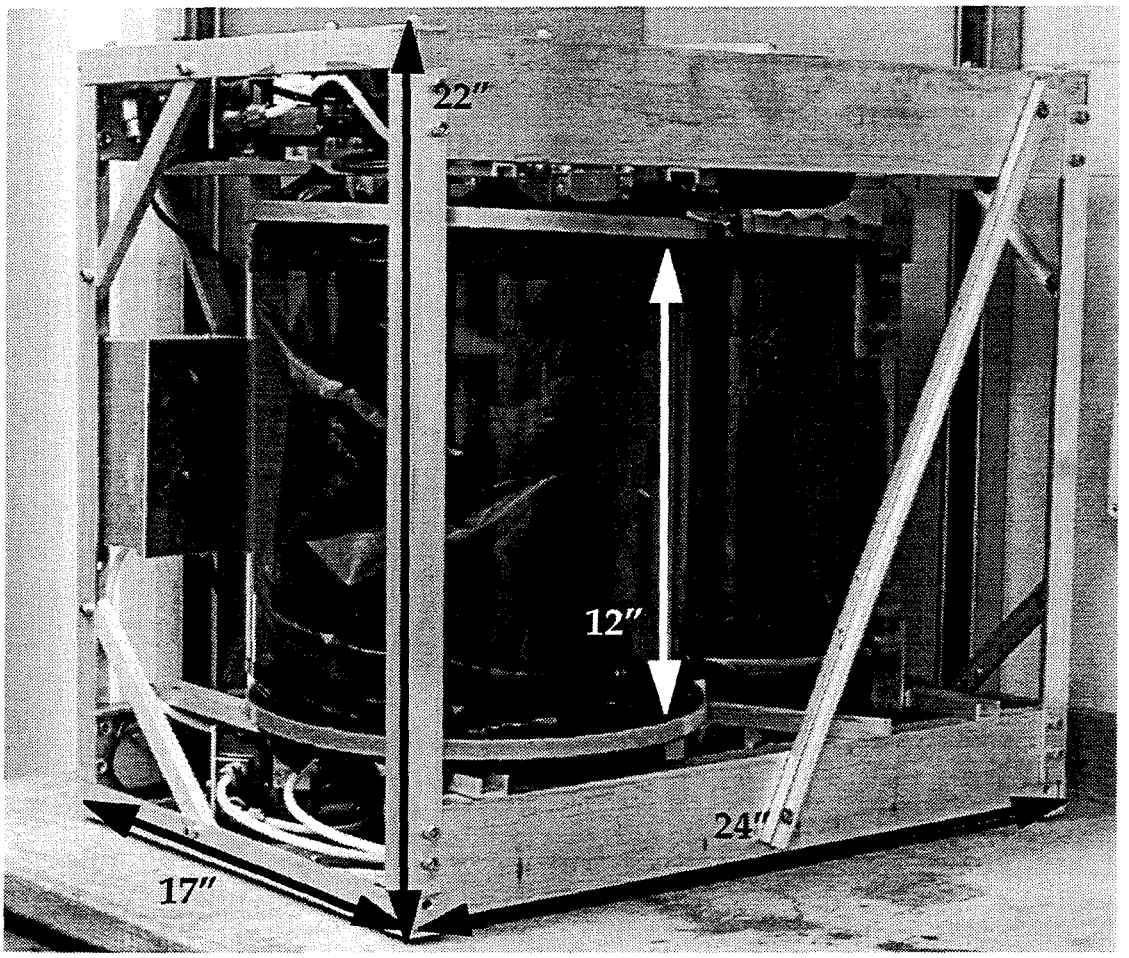

Figure 5.2: Grab sampling apparatus. The aluminum frame is designed to mount in a standard 19" rack. The apparatus weighs 35 kg.

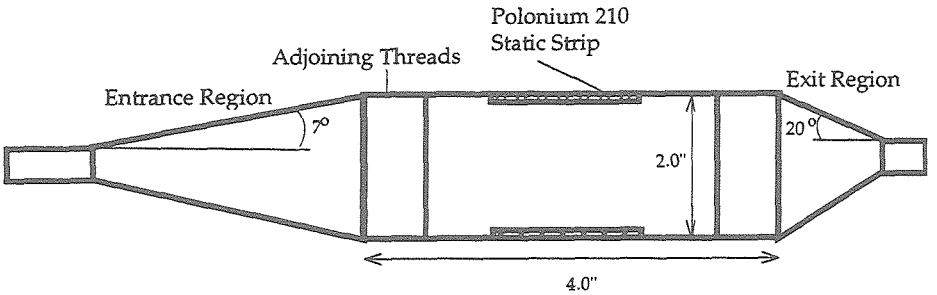

Figure 5.3: Design of the housing for a bipolar charger that supports four Polonium 210 static strips, modified from earlier work at Aerosol Dynamics, Inc.

5.2.2 Neutralizer

A bipolar neutralizer containing four Polonium 210 static strips (Static Master, model 2U500) was employed to charge the aerosol sample. The charger casing was designed to maximize uniform exposure to the Polonium alpha emissions while minimizing dead time and mixing and is illustrated in Fig. 5.3. The 7° angle at the neutralizer entrance prevents recirculation of streamlines. The neutralizer was designed to attain an equilibrium charge distribution for residence times corresponding to flow rates of up to 15 L min^{-1}, but has been operated at 6 L min^{-1}. The charge distribution resulting by diffusion charging of particles by collision with ions produced by alpha particles is described by Wiedensohler (1988) in Fig. 5.4. The charging probability has been checked experimentally (D. Covert, private communication) and was found to be within the experimental uncertainty of the theoretically

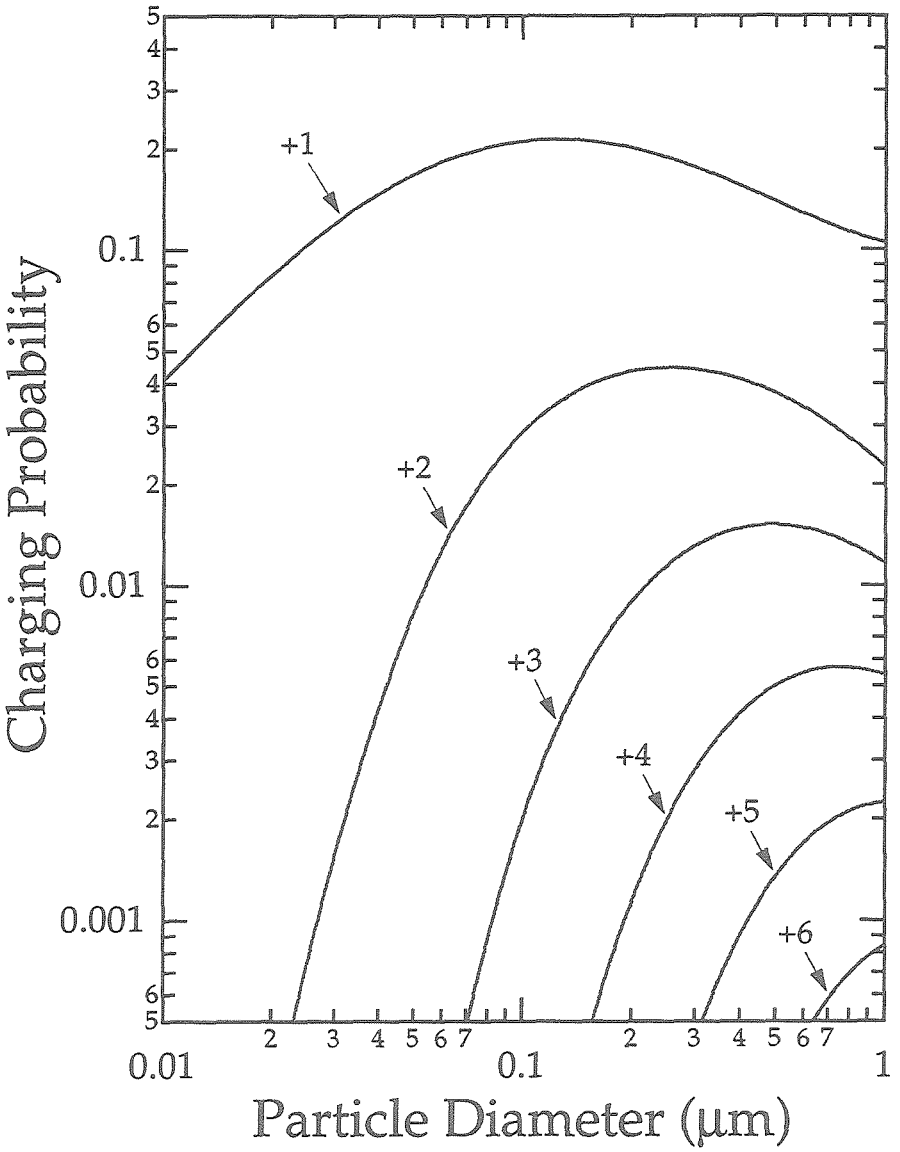

Figure 5.4: Particle charging efficiency in the bipolar neutralizer, based on calculations described in Fuchs (1963) and Wiedensohler (1988).

expected value for distributing an equilibrium charge on a charged aerosol.

5.2.3 Flow Control

The flow passing through the neutralizer is divided into three streams as illustrated in Fig. 5.1: the aerosol and clean sheath flows for the RDMA (Q_a and Q_c, respectively) and the dilution flow to the CPC (Q_d). The electric field controlled by the voltage difference between the two parallel disks in the RDMA selects particles of a narrow range of mobilities into the sample flow (Q_s) exiting the RDMA while the main excess flow (Q_m) removes the remainder of the flow. The sample flow is mixed with the dilution flow, which has been filtered and dried. The three-way valve (S_{cpc}) at the CPC inlet allows direct sampling of the inlet stream by bypassing the bag sampler and RDMA. The CPC flow is set by a 1 L min^{-1} critical orifice. The excess RDMA flow (Q_m) exits the main outlet of the RDMA to a 5 L min^{-1} critical orifice. At the Q_m stream exiting the RDMA, probes are installed to monitor temperature, and relative humidity (Vaisala, Woeburn, Massachusetts), and pressure is measured with an absolute pressure transducer (Validyne, Northridge, California). The flows controlled by the two critical orifices are pulled by a vacuum pump connected downstream.

Four flow rates are monitored in the system by measuring the pressure drop with electronic differential pressure transducers (Validyne) across laminar flow elements in the lines. In the sheath flow lines (Q_c and Q_m) of 5

L min^{-1}, the pressure drops consist of "milli-channel flow elements," consisting of more than a hundred millimeter-width parallel channels formed by corrugated stainless steel shim stock with pressure taps just upstream and downstream of the restriction. In the aerosol flow lines (Q_a and Q_s) of 0.5 L min^{-1}, each restriction consists of a capillary tube with one pressure tap far enough downstream from the entrance to be beyond the hydrodynamic development region of the flow and a second pressure tap just before the capillary exit. The relationship of pressure drop to flow through the restrictions is linear for the flow ranges for both elements. The transducer output signals are proportional to the pressure drops. Five plug valves (P_c, P_m, P_a, P_d, $P_{d'}$) in the system along with the valve S_{cpc} allow isolation of the aerosol and sheath flows so that the flow transducers can be calibrated in place with a flowmeter standard installed upstream of the charger.

Five flows – Q_a, Q_c, Q_s, Q_m, and Q_d – are fixed by three steady state relationships and two controlled ratios in the RCAD system. Two of the relationships are set by critical orifices:

$$Q_m = 5.0 \text{ Lmin}^{-1} \tag{5.1}$$

$$Q_s + Q_d = 1.0 \text{ Lmin}^{-1} \tag{5.2}$$

and the steady-state mass balance for the four RDMA flows provides an

additional condition:

$$Q_a + Q_c = Q_s + Q_m \tag{5.3}$$

Continuous monitoring of the four flows allows the flow control system to respond to variations in the sampling pressure. Deviations from the setpoint in the four RDMA flows are used to control two independent controllers: one maintains a constant RDMA inlet flow ratio and the other a constant RDMA outlet flow ratio:

$$\frac{Q_a}{Q_c} = 0.1 \tag{5.4}$$

$$\frac{Q_s}{Q_m} = 0.1 \tag{5.5}$$

Because of the linear relationships between flow and pressure drop across the restrictions, this algorithm results in a constant flow ratio within a few tenths of one percent over the limited range of operation.

5.2.4 Radial DMA

Zhang et al. (1995) have characterized the losses in the RDMA, and their data have been interpolated to estimate the losses at the flow rates used here. The radial DMA operates in a manner similar to a conventional cylindrical DMA (Knutson and Whitby, 1975; Hoppel, 1978), but is designed to reduce residence times and diffusion losses so that it can effectively measure ultrafine particles as small as 3 nm. The RDMA used in the system described here has inner dimensions identical to those described by Zhang et al. (1995), with a

disk separation, h, of 1.00 cm, an entrance radius, r_2, of 5.09 cm and an exit radius, r_1, of 0.25 cm, but has been modified to minimize its weight by thinning the outer dimensions and using Delrin© in place of steel for structural support. The resulting classifier weighs 4 kg, is 5 cm thick and 20 cm in diameter. It is fastened to vertical struts and rests on a notched and rubber-lined aluminum support. The absolute pressure is monitored in the RDMA with a transducer (Validyne) mounted at the excess flow exit (Q_m), and relative humidity and temperature are measured with probes downstream.

5.2.5 Voltage Ramp

Rapid mobility measurements are made by classifying particles in an electric field that varies exponentially with time (Wang and Flagan, 1990). In both the original implementations of this method and its recent commercial version (TSI Scanning Mobility Particle Sizer), the high voltage was controlled using a high-resolution (16 bit) digital-to-analog converter. Although this approach produces a smooth exponential ramp at high voltages, the discrete voltage steps become appreciable at low voltages, introducing uncertainty at the fine particle end of the size spectrum.

In the RCAD, a smooth exponential ramp is provided over the entire voltage range using an analog exponential ramp circuit (ERC) that consists of an integrator and an inverter/follower. This circuit, illustrated in Fig. 5.5, provides a 0 to 5 volt analog signal that drives the high voltage module (Bertan,

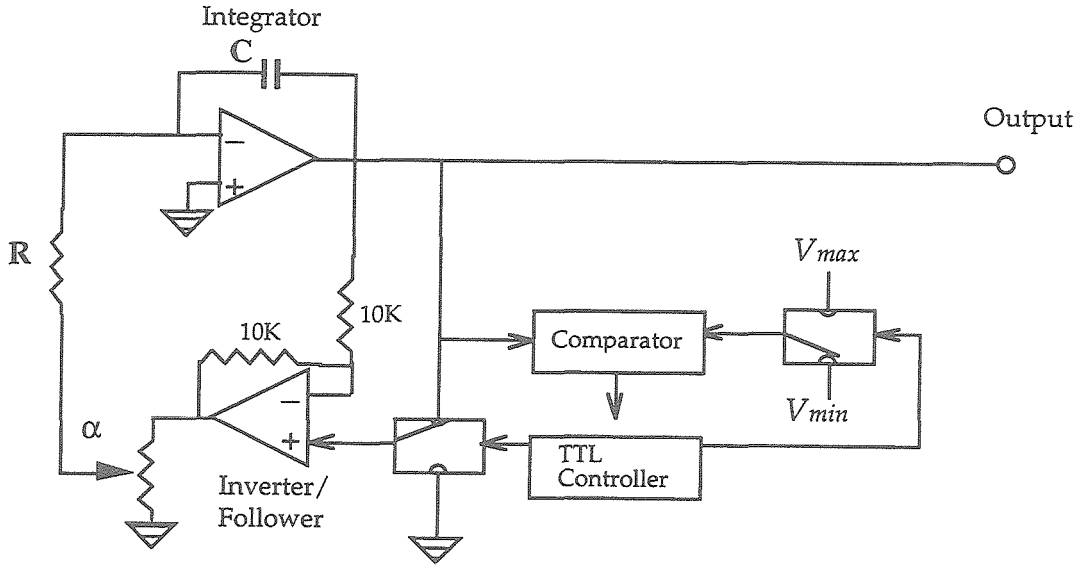

Figure 5.5: Exponential Ramp Circuit (ERC).

model 602C-100N:CS2562) to provide voltage output of 3 to 10000 volts. For an increasing voltage ramp, the second operational amplifier functions as an inverter, while it serves as a follower to provide a decreasing voltage ramp. The characteristic time for the voltage ramp τ_r, defined by the relation

$$V = V_o \exp\left[\pm\frac{t}{\tau_r}\right] \tag{5.6}$$

where

$$V_o = \begin{cases} V_{min} & \text{for increasing scan or "upscan," denoted SEMSu} \\ V_{max} & \text{for decreasing scans or "downscan," denoted SEMSd,} \end{cases}$$

is determined in the ERC circuit by

$$\tau_r \equiv \frac{RC}{\alpha} \tag{5.7}$$

where α is the potentiometer ratio in the circuit and provides coarse adjustment of τ_r. The capacitance C is fixed. τ_r is varied by changing R, with fine adjustment being provided with a 10-turn potentiometer. The ERC ramp is initiated by a TTL (Transistor Transistor Logic) low pulse. When the ramping voltage reaches V_{min} or V_{max}, the comparator sends a signal to the TTL circuit, thus changing the analog switch to convert the operational amplifier from an inverter to a follower.

5.2.6 Turbo CPC

Condensation particle counters operate on the principle of growing aerosol particles from the fine or ultrafine size range to sizes that are large enough to be optically detected. The sample is first saturated with condensible vapor at an elevated temperature (T_s) in the saturator; the vapor is then condensed onto the particles by cooling the sample stream to T_c in the condenser. The supersaturation in the condenser, and hence the probability that particles of a given size will grow by condensation, is controlled primarily by the difference in the temperatures T_s and T_c, as described by the following relation based

on the Clausius-Clapeyron equation for liquid-gas equilibrium:

$$S \equiv \frac{P_c}{P_{\text{sat}}(T_c)} = \frac{P_{\text{sat}}(T_s)}{P_{\text{sat}}(T_c)} = \exp\left[\frac{\Delta H_v}{R}\left(\frac{1}{T_c} - \frac{1}{T_s}\right)\right] \tag{5.8}$$

where ΔH_v is the vapor's latent heat of vaporization.

Scanning mobility measurements limit the time available for counting particles in any channel. Acquiring a statistically significant number of counts within the available counting time (1 s) requires that particles be counted from a large sample flow rate. The TSI model 3010 Condensation Particle Counter provides an adequate flow rate (1 L min^{-1}), but its 50% detection cutoff is 12 nm in its standard configuration (Quant et al., 1992). In order to extend its detection limit to smaller sizes, a modified instrument was constructed that increased the temperature difference ΔT =T_s-T_c from the nominal value of 17°C. Laboratory results had previously shown that this cutoff could be decreased to 8 nm by increasing ΔT to 25°C. By augmenting the heating capabilities in the saturator with a heating mat and the cooling in the condenser with an additional thermo-electric device (TED) placed adjacent to the original TED, the counting efficiency can be further enhanced. These modifications were implemented in a custom-built 3010 CPC (TSI) that has been dubbed the "Turbo 3010." In the original 3010 CPC, only the temperature difference, ΔT, is controlled. Specifying only ΔT can lead to drift in T_s and T_c as the operating conditions (e.g., cabin temperature) shift. Since the supersaturation in the condenser is sensitive to the absolute

temperature, this drift can alter the expected counting efficiency of the instrument. The EPROM (Erasable Programmable Read-Only Memory) chip in the CPC was modified to allow T_s and T_c to be specified and controlled independently to 38°C and 2°C respectively, eliminating the sensitivity of the instrument performance to the ambient (cabin) temperature. The counting efficiency was measured by comparison of calibration aerosols of salt and agglomerated silver with an electrometer standard for particles as small as 4.5 nm.

5.2.7 RCAD Software

Software to drive each of these components synchronously and to record data from them was written using a C-compatible development program (National Instruments, LabWindows CVI) on a notebook-style computer (IBM, Thinkpad 750). The user interface allows the user to initiate different modes of operation (automatic or manual trigger) and switch sampling ports (bag sampling or DMA-bypass), while monitoring the flow rates, temperature, pressure, humidity, valve states, and CPC performance. Digital and analog data acquisition are accomplished with a PCMCIA card with 16 single-ended analog channels and 16 digital input/output channels (National Instruments, DAQCard 700). The software coordinates the filling and sampling from the double-bag sampler so that a sample is drawn immediately after a bag is filled. The voltage ramp in the RDMA is started after a 5-s delay to allow

new sample to reach the DMA and the flow controls to reestablish constant flow ratios after the perturbation of the valve switch. Particle counts detected by the CPC during 1-s intervals are transmitted serially from the CPC to the computer using the hardware-coded EPROM downloading commands in the CPC. A real-time display shows the raw counts recorded against the current RDMA voltage, so that the raw data illustrate general distribution characteristics on a time-shifted axis.

5.3 Characterization of Instrument Components

The performance of each of the instrument components described above has been characterized. Losses in aerosol transport lines have been estimated theoretically. The RDMA and CPC have been calibrated to determine the particle transmission efficiency and instrument response functions. This section summarizes these instrument characterization studies.

5.3.1 Particle Losses in Tubing and Sampling Chamber

An essential part of an aerosol sampling system is the design of the plumbing so as to minimize particle losses in the sampling train. These losses may be estimated with careful calculations. Particle losses may also occur in the RDMA. Particle losses expected in the tubing preceding the detector can be

estimated from the expected diffusion of particles in known flow conditions.

The flow rate in the 1.9-cm tubing preceding the sampling chamber is driven by ram pressure, which for a typical aircraft speed of 100 m s^{-1}, is estimated to be 470 L min^{-1}. This flow has a Reynolds number of 38000 for air of density 1.2 kg m^{-3} and viscosity 2.0 kg m^{-3} s^{-1}. If we define ϕ to be the number concentration of particles remaining at the end of tubing of length L and diameter d for an entrance number concentration of ϕ_o particles and flow rate Q, then for turbulent flow conditions, the particle losses may be determined from

$$\frac{\phi}{\phi_o} = \exp\left[-\frac{\pi d L k}{Q}\right] \tag{5.9}$$

where the mass transfer coefficient, k, is given by (Friedlander, 1977):

$$\frac{kd}{D} = 0.079 Re f^{\frac{1}{2}} Sc^{\frac{1}{4}} \tag{5.10}$$

where Re is the Reynolds number, Sc the Schmidt number, f the friction factor for the flow conditions, and D is the diffusivity of the particles.

The air sample is held in the chamber for less than 1 min. Figure 5.6 illustrates the bounds on the particle losses in the chamber calculated based on the eddy diffusivity for the range of flow rates at which air is withdrawn from the sampler. The turbulent kinetic energy introduced in the sampling chamber by the fill rate of the inlet of ca. 500 L min^{-1} decays rapidly, such that the eddy diffusivity for the sample holding period can be estimated

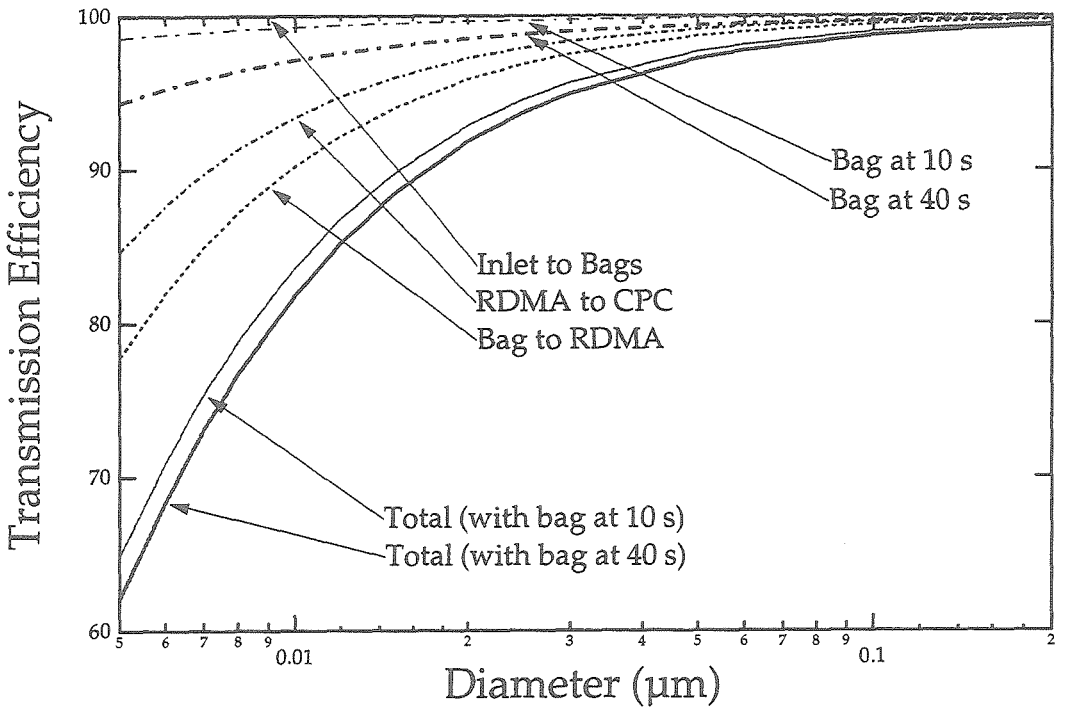

Figure 5.6: Particle transmission efficiency through the inlet tubing, the bag sampler, the connections from the bag sampler to the RDMA, and from the RDMA to the CPC. The transmission efficiency for each section is described as the concentration of particles persisting, ϕ, divided by the inlet concentration of particles, ϕ_o. The broken lines illustrate contributions from each of the segments described as well as for the losses in the bag for holding times of 10 s (thin alternating dashes) and 40 s (thick alternating dashes). The solid lines show the total losses expected for all of the instrument regions, for bag holding times of both 10 s (thin broken line) and 40 s (thick broken line).

from eddies generated by the withdrawal of air from the chamber using the expression proposed by Okuyama et al. (1977):

$$k_e = 0.00918 Q^{\frac{3}{2}}. \tag{5.11}$$

The losses can then be calculated from the particle deposition coefficient, β, where

$$\beta = \frac{v}{H} + \frac{SD}{\Upsilon\sigma} \tag{5.12}$$

for particles of settling velocity v and a vessel of height H, surface area S, volume Υ and a diffusion boundary layer σ, which may be calculated from k_e (Corner and Pendlebury, 1951; Crump and Seinfeld, 1981).

$$\frac{\phi}{\phi_o} = \exp\left[-\beta t\right] \tag{5.13}$$

The bag volume shrinks continuously during sampling, beginning at a volume of 22 l, and ending at a volume of 16 l; the calculation is done by integrating over the sampling period.

The air withdrawn out of the chamber flows at 6 L min^{-1}, and is then split so that 0.5 L min^{-1} of sample air transits the DMA, before it is diluted to 1 L min^{-1} and enters the detector. An upper bound on the straight tube losses for these regimes of laminar flow may be estimated from the expression

provided by Gormley and Kennedy (1949) for laminar flow:

$$\frac{\phi}{\phi_o} = 1 - 2.56\eta^{2/3} + 1.2\eta + 0.177\eta^{4/3} \quad \eta \leq 0.01 \tag{5.14}$$

where

$$\eta = \frac{\pi D L}{Q}. \tag{5.15}$$

Figure 5.6 illustrates the combined magnitude of each of these particle losses. These losses occur sequentially and are proportional to the particle number concentration, so that the overall losses are the product of each of these contributions, and are also illustrated in Fig. 5.6. Since particle diffusion losses are dependent on Brownian diffusivity, ultrafine particles will be most affected; 35% of 5 nm particles are estimated to be lost by diffusion in the tubing and bag sampler (for a 10 s holding time) as illustrated in Fig. 5.6, whereas <1% of 200 nm particles are lost.

5.3.2 Classifier Resolution

Resolution of the particle classification possible with the RDMA is presented in Zhang et al. (1995). Expected diffusion losses for ultrafine particles are significantly lower than for conventional cylindrical DMAs (Knutson and Whitby, 1975; Hoppel, 1978; Winklmayr et al., 1991). For the flow rates used here the diffusion loss data from Zhang et al. (1995) may be interpolated to provide the estimate of expected diffusion losses of particles in

the RDMA at the flow rates used for this configuration. The transfer function for the RDMA has the same functional form as that for the cylindrical DMA, although the geometric factors differ for the two instruments. The selection of particle size is controlled by the voltage applied to the RDMA, which is controlled by the ERC. The operation of the ERC is compared to the exponential rate predicted theoretically from Eqn. 5.6 in Fig. 5.7.

5.3.3 Particle Counting Efficiency

The counting efficiency of the modified particle counter was determined by comparing the modified counter's performance to a known electrometer standard (TSI, model 3068). The apparatus for this calibration study is illustrated in Fig. 5.8. A vaporization/condensation source generated aerosol at a flow of 2 L min^{-1} (Scheibel and Porstendörfer, 1983) that was classified to a known particle size in a mobility classifier (TSI, model 3071) and then diluted to 22 L min^{-1} with particle-free air. The resulting flow was divided equally in a low-angle flow splitter (TSI, model 2009) between the electrometer (calibrated at 11 L min^{-1}) and the modified CPC (pulling 1 L min^{-1} with 10 L min^{-1} bypass flow). The tubing leading to both instruments was identical up to the instrument entrances, using flexible conductive tubing to connect the flow splitter to the inlets. Hence, the number of particles counted in both cases could be compared in order to calculate the counting efficiencies. The results of these experiments are illustrated in Fig. 5.9 for

FIG. 7

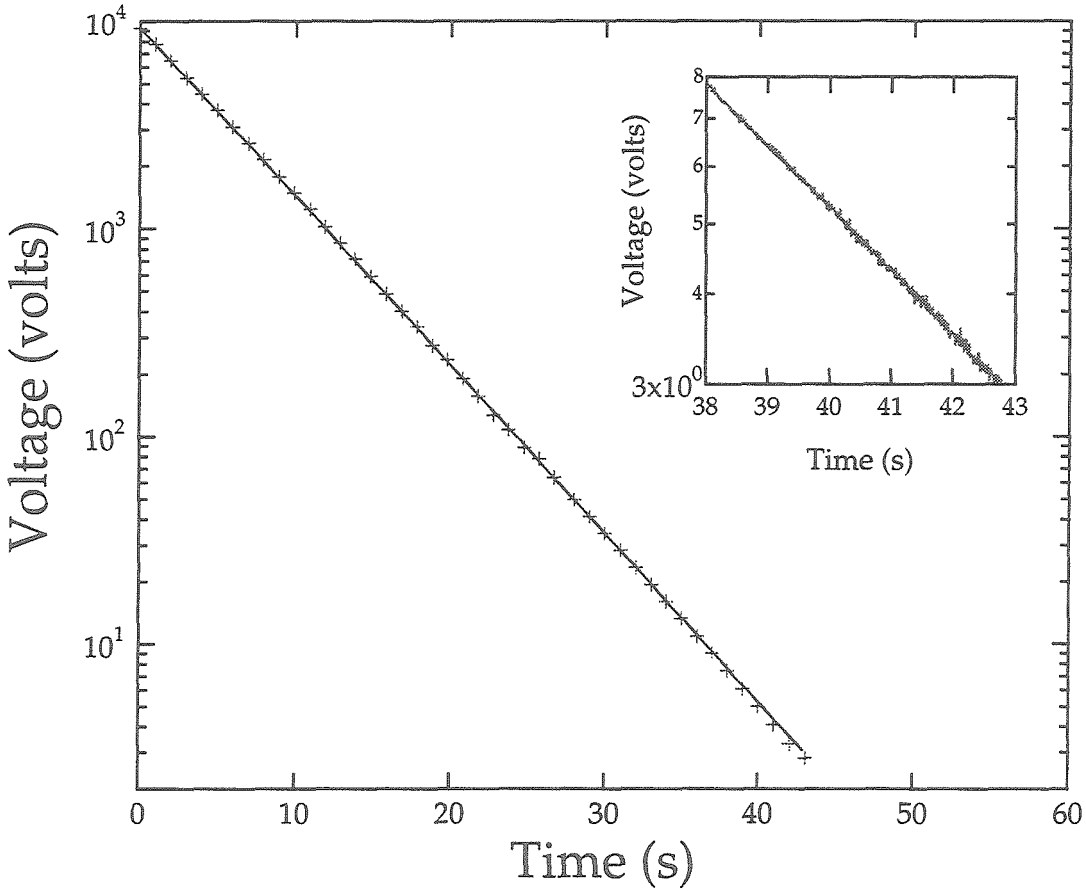

Figure 5.7: Performance of the exponential ramp circuit is illustrated by a plot of increasing and decreasing voltage with time. Data points illustrate voltages (on a logarithmic scale) measured at 1 s intervals, and the solid lines show the exponential ideal function of the form indicated by Eqn. 5.6, with $\tau_r = 5.35$ s, $V_{min} = 3$ volts and $V_{max} = 9490$ volts. The inset illustrates high resolution data (100 Hz) for the lowest voltages on an expanded log scale.

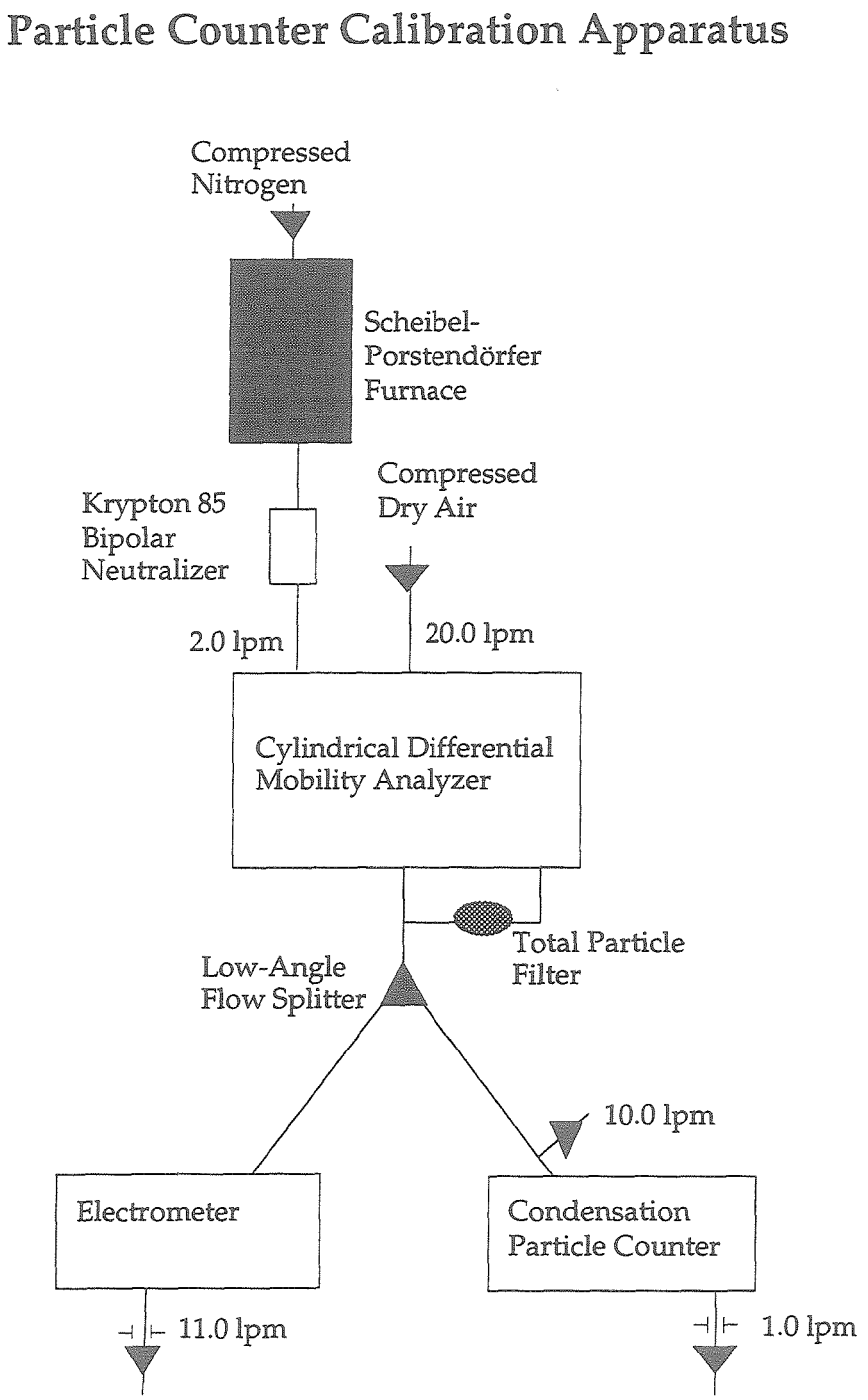

Figure 5.8: Apparatus for calibration of modified condensation particle counter.

two types of source aerosol, silver (Ag) and salt (NaCl).

A potential limitation in improving counting efficiency by increasing ΔT is the possible artifact of homogeneous nucleation in the CPC leading to spurious counts in the measurements. The conditions most susceptible to allowing homogeneous nucleation are high supersaturation of condensible vapor and low preexisting aerosol surface area (Seinfeld, 1986). For ΔT up to 36°C, no particles were detected for a particle-free air stream, demonstrating that for the operating temperatures of $T_s = 38$°C and $T_c = 2$°C spurious counts should not be detected.

5.3.4 Kernel Function for RCAD Operation

The measurement capabilities of the instrument are described by the probability that a particle of a given size will be detected, and this relationship is known as the instrument's kernel function. The kernel function for the RCAD is defined by the following relationship for the counts recorded in the i^{th} measurement channel

$$S_i = \int_0^\infty k_i(D_p) f(D_p) dD_p + \epsilon_i \quad i = 1, 2, \cdots, n \tag{5.16}$$

where $f(D_p)$ is the particle size distribution that is defined such that $f(D_p)dD_p$ is the number concentration of particles with diameters between D_p and $D_p + dD_p$, $k_i(D_p)$ is the so-called kernel function for channel i, n is the total number of measurement channels, and ϵ_i is the noise that is inherent

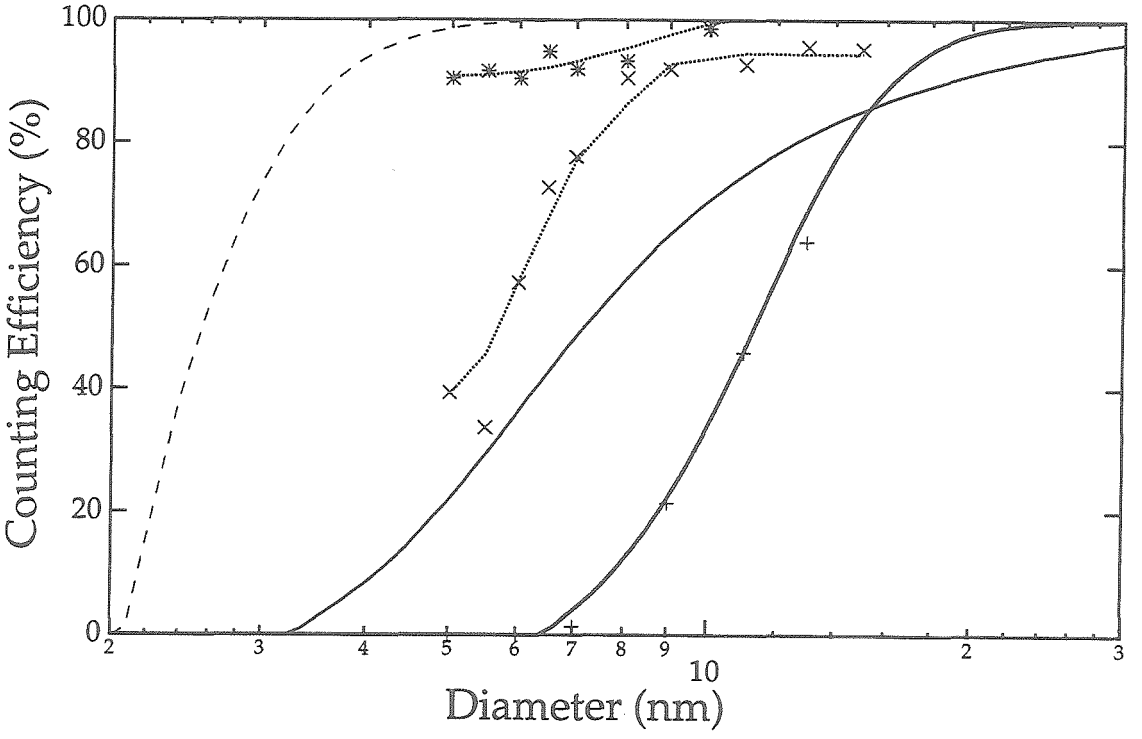

Figure 5.9: Particle counting efficiency for the modified CPC, compared with several commercially available models. The data were taken with the apparatus illustrated in Fig. 5.8, where salt (NaCl) was used to generate aerosol for the $\Delta T = 25°C$ data, indicated by crosses (X), and silver (Ag) for the $\Delta T = 17°C$ and $\Delta T = 36°C$ data, indicated by pluses (+) and asterisks (*), respectively. The thick solid, thin solid and broken lines indicate the calibration curve of a standard TSI 3010 CPC, 3022 CPC and 3025 CPC, respectively (Quant et al., 1992).

in any experimental measurement (Russell et al., 1995). Detailed knowledge of the kernel function is a prerequisite for determination of the particle size distribution from the recorded signals. Russell et al. (1995) define the kernel function for DMA measurements of the particle size distribution in terms of experimental parameters as

$$k_i(D_p) = Q_a \sum_{\nu} s(D_p, \nu)\phi_\nu(D_p)\bar{\Omega}_i(\zeta(\nu, D_p)) \tag{5.17}$$

where $s(D_p, \nu)$ is the probability that the detector will count a particle of diameter D_p with ν charges, $\phi_\nu(D_p)$ is the fraction of particles of diameter D_p carrying an elementary charge of ν, Q_a is the volumetric flow rate of aerosol entering the DMA, and $\bar{\Omega}_i(\zeta(\nu, D_p))$ is the fraction of the particles of dimensionless mobility $\zeta(\nu, D_p)$ that will exit the analyzer during the counting interval of channel i. Note that the measurement procedure used here used sufficiently long delays between scans that carryover effects from previous scans can be neglected, hence we have omitted references to the scan number in the subscripts of the kernel (k) and transfer (Ω) functions. For the RDMA,

$$\zeta(\nu, D_p) = \frac{2\pi V_o}{(Q_s + Q_a)} \frac{r_2^2 - r_1^2}{h} \frac{\nu e C_c}{3\pi\mu D_p} \tag{5.18}$$

where C_c is the Cunningham correction factor, e is the charge of an electron, and μ is the viscosity of the carrier gas (Zhang et al., 1995). For exponential voltage scanning operation, $\bar{\Omega}_i(\zeta(\nu, D_p))$ is replaced by $\bar{\Omega}_i^e(\zeta(\nu, D_p))$, which

can be shown to be dependent on the flow characteristics of the instrument configuration (Russell et al., 1995). The characteristic mixing time for the instrument (τ_s) and the corresponding plumbing time (τ_p) have been evaluated for the RCAD's intra-instrument plumbing. The response of the CPC to a step change in concentration at the classifier was measured by recording particle counts as a function of time as the voltage at the classifier is switched from 500 to 0 volts, with the resulting concentrations plotted in Fig. 5.10. The best fit to the resulting residence time distribution was obtained for $\tau_p = 8.0$ s and $\tau_s = 1.1$ s, corresponding to the modeled flow pattern illustrated in Fig. 5.10 by the solid line.

A significant advance in the speed of operation of the differential mobility analyzer can be achieved when the voltage is scanned continuously rather than stepped in increments (Wang and Flagan, 1990). The operation of a DMA in scanning-mode operation at a given measurement speed differs from stepping mode operation in that the characteristic mixing time of the DMA-CPC configuration limits the speed with which the voltage can be scanned (Russell et al., 1995). This limitation of the scanning speed is, in fact, independent of the geometry of the DMA (i.e., radial vs. cylindrical), as it results entirely from the residence time of particles from the exit of the DMA to the point of detection in the CPC (which are determined by the plumbing configuration and the CPC geometry). The dependence of scan accuracy on the flow configuration between the instruments has been investigated experimen-

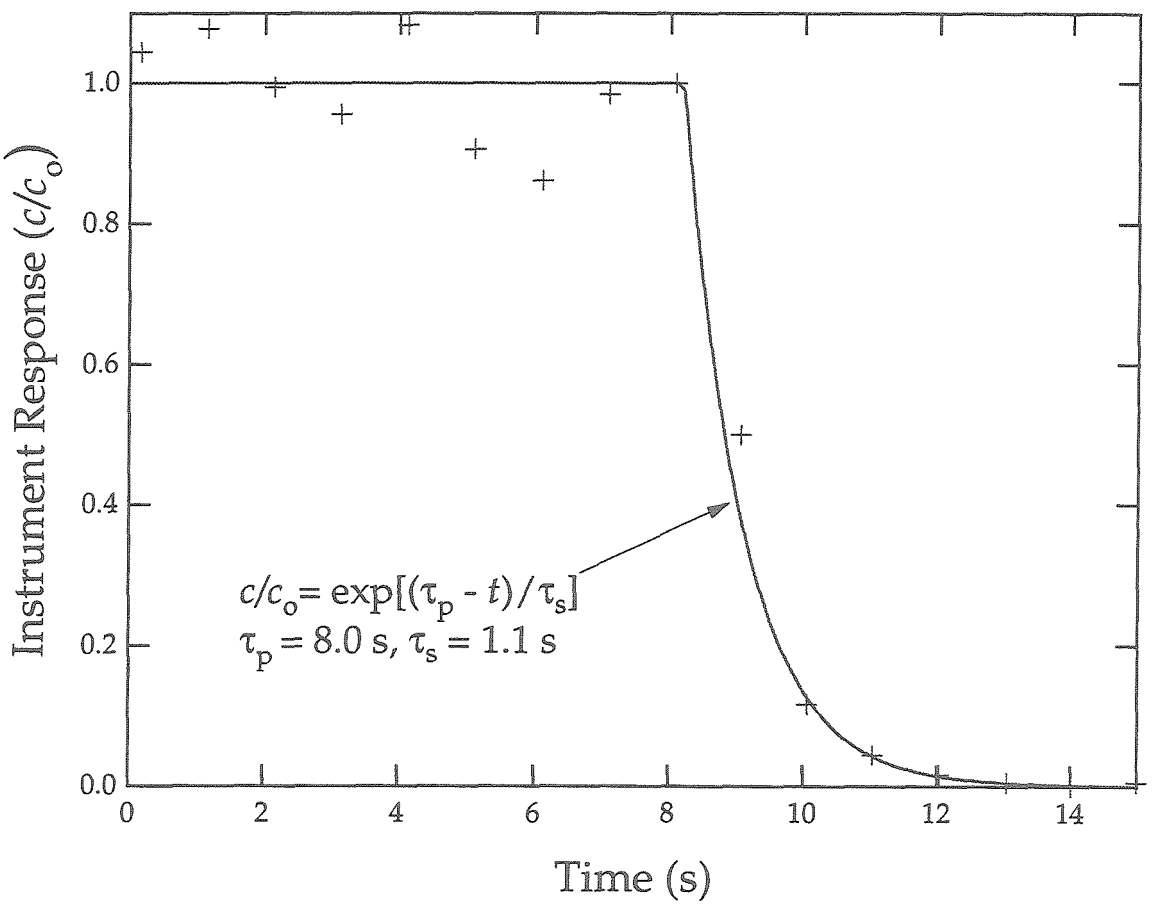

Figure 5.10: Response of the RCAD to a step change in concentration at the classifier. The line illustrates the flow model used to represent the residence time distribution.

tally by Flagan et al. (1993), showing that fast measurement speeds result in the asymmetric response described by Russell et al. (1995).

This flow pattern is then used to calculate the kernel function for each instrument channel, as illustrated by the representative channels shown in Fig. 5.11. Estimation of the particle size distribution requires solution of the set of Fredholm integral equations (Eqn. 5.16) for the n experimental measurements. For this purpose, the MICRON algorithm is employed to retrieve size distributions from each set of scanned measurements (Wolfenbarger and Seinfeld, 1990).

5.4 In-flight Performance

The RCAD instrument package described above has been mounted aboard the University of Washington C131a research aircraft. A series of flights based out of Monterey, California, during June, 1994, provided an opportunity to demonstrate the performance of the instrument in measurement of aerosol size distributions in the marine boundary layer. For this purpose, the measurement conditions in the instrument were carefully monitored. Results are presented here for in-flight variations in temperature, relative humidity, pressure and flow. Temperature and pressures monitored in the airstream are used to correct the kernel function in order to interpret the data signals, since particle mobility is a function of both air pressure and temperature.

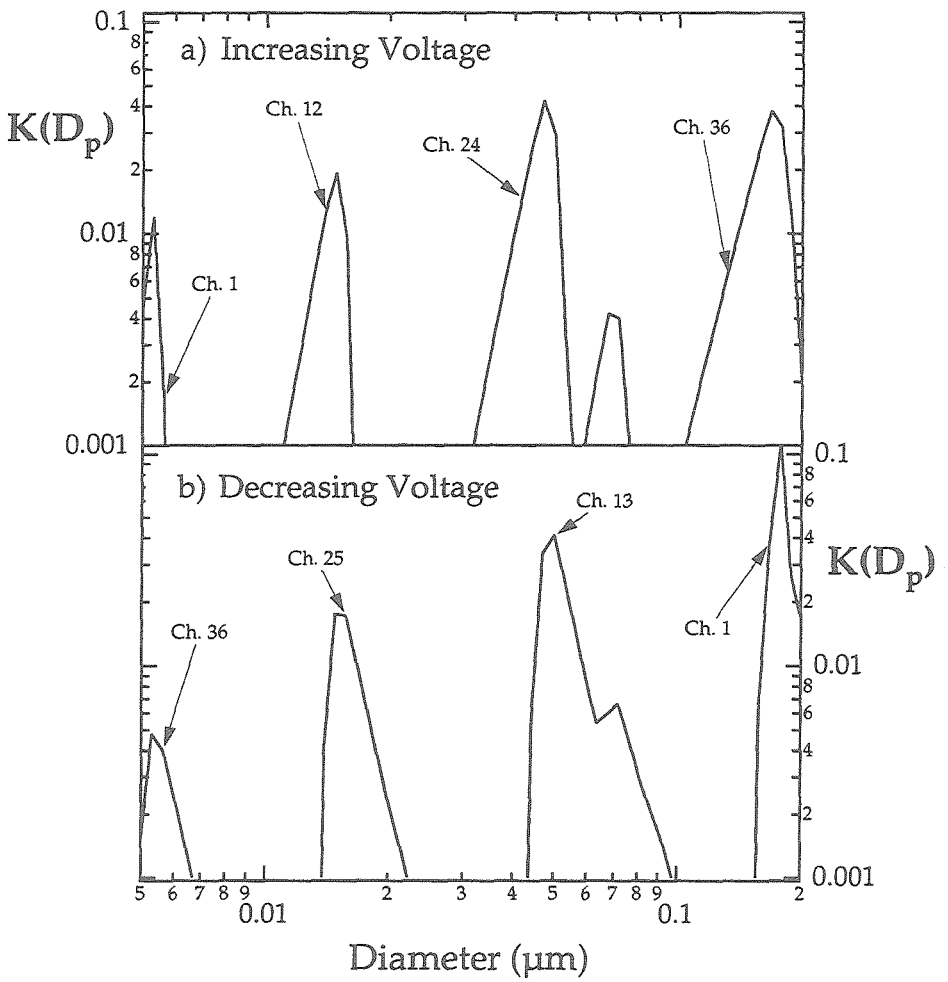

Figure 5.11: Kernel function of (a) an increasing-voltage scan of the RCAD system and (b) a decreasing-voltage scan of the RCAD system. Channels 1, 12, 24, and 36 are illustrated for an increasing voltage scan, and the corresponding channels (channels 1,13, 25, and 36) are illustrated for a decreasing voltage scan.

5.4.1 Temperature and Humidity

The air sample entering the instrument is heated from the ambient temperature by deceleration of the air on entering the aircraft. The resulting temperature is plotted in Fig. 5.12. The instrument and cabin temperature measurements have electrically-generated noise in the signals resulting in $\pm 3^{o}$C. In Fig. 5.12, these fluctuations have been removed by evaluating the mean values for each 45 s measurement period. The temperature of the air at the point of measurement in the classifier tracks the cabin temperature closely, since heating of the instrument package can result in additional warming of the sampled air.

During the course of the flight, increase in the aircraft cabin temperature can preclude the CPC condenser from maintaining the temperature setpoint of 2^{o}C. The resulting drift in the temperatures of the saturator and the condenser will alter the counting efficiency for ultrafine particles. By monitoring the temperatures of the saturator and condenser as illustrated in Fig. 5.12, we can correct for diminished CPC performance for each size distribution.

Heating of the sampled air dries the airstream, so that the humidity at which particles are measured is between 20% and 40% throughout the flight. The resulting particle sizes measured are dry nuclei diameters.

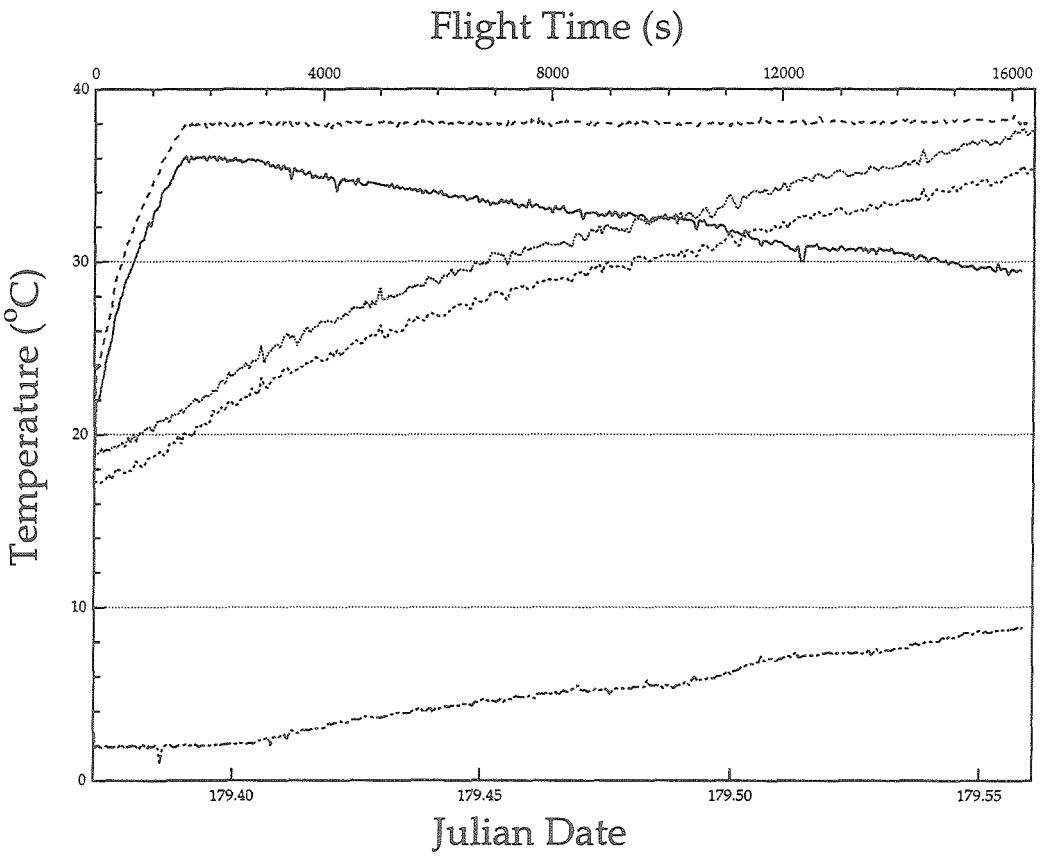

Figure 5.12: Illustration of temperature variation in flight. The temperature in the CPC condenser (T_c, indicated by the alternating dashed line) and saturator (T_s, indicated by the long-dashed line) varies with changes in cabin temperature (shown as a dotted line) and instrument temperature (short-dashed line) during a flight on the University of Washington C131a aircraft on June 28, 1994. The temperature difference, $\Delta T = T_s - T_c$, is also illustrated by the solid line.

5.4.2 Pressure and Flow Rates

Air is drawn into the instrument from the bag sampler, which is in equilibrium with the aircraft's unpressurized cabin. Consequently, the pressure in the instrument varies with altitude. The feedback algorithm used in controlling the flow rates in the instrument provides constant volumetric flow rates in the instrument, so that the shape of the transfer function, and hence the size resolution of the measurement, is maintained. The effectiveness of the control algorithm is illustrated by Fig. 5.13 in which the flow rates are illustrated for a single flight, during both ascents and descents through the boundary layer. The high frequency fluctuations of ± 6 torr in pressure result in part from electrically generated noise in the signal.

When the absolute pressure within the system changes due to ascent or descent of the aircraft, flow imbalances develop within the system. In particular, conservation of mass dictates a net inflow to or outflow from the RDMA in order to effect a change in the pressure of the finite volume of air contained therein. During such changes the controllers still maintain constant inlet and outlet flow ratios, thereby maintaining the shape of the RDMA transfer function under these transient conditions.

In Fig. 5.13, the switch between the dual sampling bags is marked by a spike in the flow rates of ± 0.5 L min^{-1} in Q_c and ± 0.3 L min^{-1} in Q_a. Switching between bags results in an interruption of the flow to the instrument, which must be compensated by the flow control. These perturbations

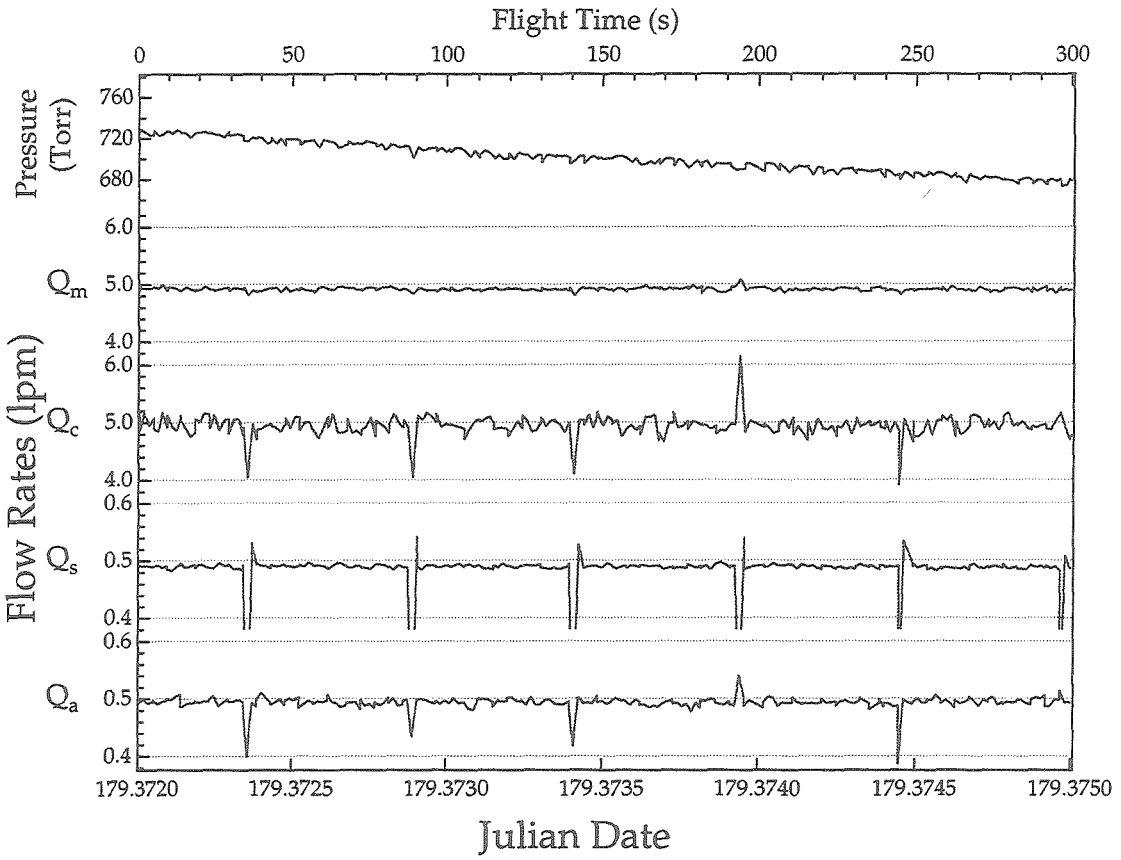

Figure 5.13: Performance of the flow control system in flight on June 28, 1994, during an ascent through the boundary layer that resulted in a pressure drop of 50 torr in 300 s.

are almost instantaneous, corresponding to the valve actuation time of $\ll 1$ s. From the 1-Hz frequency data illustrated in Fig. 5.13, the recovery time of the flow rates is estimated to be < 1 s, so that the flow has stabilized before data is recorded for the measurement. Electrical noise in the flow metering results in ca. $\pm 1\%$ of the reported flow rates.

Changes in pressure corresponding to altitude changes of the aircraft occur at gradual rates corresponding to the climb or descent rate of the aircraft. For the time period illustrated in Fig. 5.13, the pressure drops 50 torr during 300 s. Adjusting the flow rate to the resulting gradual change in absolute pressure in the instrument requires fine adjustment of the flows. As shown in Fig. 5.13, the volumetric flow rates are maintained to their designed flow settings during sampling intervals, within the precision of the flow measurement for the time period illustrated.

References

Adachi, M., K. Okuyama., Y. Kousaka, S.W. Moon, and J.H. Seinfeld, 1990: Facilitated aerosol sizing using the differential mobility analyzer. *Aer. Sci. Tech.*, 12: 225-239.

Brock, C.A., L.F. Radke, J.H. Lyons, and P.V. Hobbs, 1989: Arctic hazes in summer over Greenland and the North American Arctic I: Incidence and Origins. *J. Atmos. Chem.*, 9:129-148.

Clarke, A.D., 1991: A thermo-optic technique for in-situ analysis of size-resolved aerosol physicochemistry. *Atmos. Env.*, 25A: 635-644.

Clarke, A.D., 1992: Atmospheric nuclei in the remote free-troposhere. *J. Atmos. Chem.*, 14:479-488.

Clarke, A.D., 1993: Airborne measurements of aerosol properties in clean and polluted air masses during ASTEX. *EOS Proceedings of the 1993 AGU Spring Meeting*, April 20.

Conover, J.H., 1966: Anomalous cloud lines. *J. Atmos. Sci.*, 23: 778-785.

Corner, J., and E.D. Pendlebury, 1951: *Proc. Phys. Soc.*, B64: 645.

Crump, J.G., and J.H. Seinfeld, 1981: Turbulent deposition and gravitational sedimentation of an aerosol in a vessel of arbitrary shape. *J.*

Aerosol Sci. 12: 405-415.

Crump, J.G., R.C. Flagan, and J.H. Seinfeld, 1983: Particle wall loss rates in vessels. *Aer. Sci. Tech*, 2:303.

Daum, P.H., and S.R. Springston, 1993: Tropospheric sampling with aircraft. *Measurement Challenges in Atmospheric Chemistry*, 101-132.

Ferek, R.J., D.A. Hegg, J.A. Herring, and P.V. Hobbs, 1991: An improved filter pack technique for airborne measurement of low concentrations of SO2. *J. Geophys. Res.* 96: 22373-22378.

Fissan, H., P. Büscher, S. Neumann, F. Stratmann, Da-Ren Chen, and David Y.H. Pui, 1994: *Fourth Intl. Aer. Res. Conf.*, 462.

Flagan, R.C., F.R. Quant, K.D. Horton, L.M. Russell, G.J. Sem, and M.M. Havlicek, 1993: Twelfth Amer. Assoc. Aer. Research Conf., 292.

Frick, G.M., and W.A. Hoppel, 1993: Airship measurements of aerosol size distributions, cloud droplet spectra, and trace gas concentrations in the marine boundary layer. *Bull. Am. Met. Soc.*, 74: 2195-2202.

Friedlander, S.K., 1977: *Smoke, Dust and Haze*, John Wiley and Sons, 317.

Fuchs, N.A., 1963: On the stationary charge distribution of aerosol particles in a bipolar ionic atmosphere. *Geofis. Pura. Appl.*, 56: 185-193.

Fuchs, N.A., 1964: *The Mechanics of Aerosols,* Pergamon Press, 408.

Gormley, P., and M. Kennedy, 1949: Diffusion from a stream flowing through a cylindrical tube. *Proc. Roy. Irish Acad.*, 52A: 163.

Hagen, D.E., and D.J. Alofs, 1983: Linear inversion method to obtain aerosol size distributions from measurements with a differential mobility analyzer. *Aer. Sci. Tech.*, 2: 465-475.

Hegg, D.A., R.J. Ferek, and P.V. Hobbs, 1993: Aerosol size distributions in the cloudy atmospheric boundary layer of the North Atlantic Ocean. *J. Geophys. Res.* 98: 8841-8846.

Hoppel, W.A., 1978: Determination of the aerosol size distribution from the mobility distribution of the charged fraction of aerosols. *J. Aerosol Sci.*, 9: 41-54.

Hoppel, W.A., J.W. Fitzgerald, G.M. Frick, and R.E. Larson, 1990: Aerosol size distributions and optical properties found in the marine boundary layer over the Atlantic Ocean. *J. Geophys. Res.*, 95: 3559-3886.

Hudson, J.G., and A.D. Clarke, 1992: Aerosol and cloud condensation nuclei measurements in the Kuwait plume. *J. Geophys. Res.*, 97: 14533-14536.

King, M.D., L.F. Radke, and P.V. Hobbs, 1993: Optical properties of marine stratocumulus clouds modified by ships. *J. Geophys. Res.*, 98: 2729-2739.

Knutson, E.O., and K.T. Whitby, 1975: Aerosol classification by electrical mobility. *J. Aerosol Sci.*, 6: 453.

McMurry, P.H., and D.J. Rader, 1985: Aerosol wall losses in electrically-charged chambers. *Aer. Sci. Tech.*, 4: 249-268.

Okuyama, K., Y. Kousaka, Y. Kida, and T. Yoshida, 1977: *J. Chem. Eng. Jpn.*, 10: 142.

Porter, J.N., A.D. Clarke, G. Ferry, and R.F. Pueschel, 1992: Aircraft studies of size-dependent aerosol sampling through inlets. *J. Geophys. Res.*, 97: 3815-3824.

Quant, F.R., R. Caldow, G.J. Sem, and T.J. Addison, 1992: *J. Aerosol Sci.*, 23: 405.

Radke, L.F., C.A. Brock, J.H. Lyons, P.V. Hobbs, and R.C. Schnell, 1989: *Atmos. Envir.*, 23: 2417.

Radke, L.F., J.A. Coakley, and M.D. King, 1989: Direct and remote sensing observations of the effects of ships on clouds. *Science*, 246: 1146-1149.

Russell, L.M., R.C. Flagan, and J.H. Seinfeld, 1995: Asymmetric instrument response due to mixing effects in DMA-CPC measurements. *Aer. Sci. Tech.*, in press.

Russell, L.M., S.N. Pandis, and J.H. Seinfeld, 1994: Aerosol production and growth in the marine boundary layer. *J. Geophys. Res.*, 99: 20989-21003.

Scheibel, H.G., and J. Porstendörfer, 1983: Generation of monodisperse Ag-aerosol and NaCl-aerosol with particle diameters between 2-nm and 300-nm. *J. Aerosol Sci.*, 14: 113.

Seinfeld, J.H., 1986: *Atmospheric Chemistry and Physics of Air Pollution*, John Wiley and Sons, 738.

Stolzenburg, M.R., and P.H. McMurry, An ultrafine aerosol condensation nucleus counter. *Aer. Sci. Tech.*, 14: 48-65.

Wang, S.C., and R.C. Flagan, 1990: Scanning electrical mobility spectrometer. *Aer. Sci. Tech.*, 13: 230-240.

Wiedensohler, A., 1988: An approximation of the bipolar charge-distribution for particles in the sub-micron size range. *J. Aerosol Sci.*,

19: 387.

Winklmayr, W., G.P. Reischl, A.O. Lindner, and A. Berner, 1991: A new electromobility spectrometer for the measurement of aerosol size distributions in the size range from 1 to 1000 nm. *J. Aerosol Sci.*, 22: 289-296.

Wolfenbarger, J.K., and J.H. Seinfeld, 1990: Inversion of aerosol size distribution data. *J. Aerosol Sci.*, 21: 227-247.

Zhang, S.H., Y. Okutsu, L.M. Russell, R.C. Flagan, and J.H. Seinfeld, 1995: Radial differential mobility analyzer. *Aer. Sci. Tech.*, in press.

Chapter 6

Submicron Aerosol Size Distribution Measurements in Ship Tracks During the MAST Experiment

The appearance and persistence of anomalous lines in cloud structures visible in satellite imagery, commonly attributed as ship tracks, provide an opportunity to study cloud processing through a surrogate, thereby enhancing both our picture of marine boundary layer chemistry and of the nature of its interaction with anthropogenic aerosols. However, in order to take advantage of this atmospheric-scale experiment, techniques with resolution higher and faster than commercial designs are required.

As part of the MAST Experiment, we have designed instrumentation for fast characterization of fine particle size distributions, implementing both a radially-designed aerosol classifier (Zhang et al., 1995) and a high-flow, high-effiency condensation nuclei counter (Russell et al., 1995). This instrumentation, coupled with feedback control of flows for airborne adjustments, has provided detailed physical descriptions of the precursors of cloud condensation nuclei both in and near ship tracks. The Radially Classified Aerosol Detector (RCAD) measures the concentration of mobility-classified aerosol in the range 5 nm to 200 nm (Russell et al., 1995). Each distribution is characterized by 36 channels of data, and requires one minute for analysis. The resulting measurements aboard the C131a provide unprecedented spatial resolution of submicron aerosol size distributions aloft. With this capability, we have characterized the submicron features of ship tracks and have determined that most of the particles (in some cases 95% of the number concentration) are submicron in size.

The RCAD provides fast-response (< 1 min) size distributions that are ideal for airborne measurements. An example of this capability is provided by size distributions of the background aerosol present in the marine boundary layer that were obtained during the Monterey Area Ship Track (MAST) experiment. During this experiment, the C131 of the University of Washington flew over the Pacific Ocean west of Monterey, California. During that program, both continentally-influenced aerosol and typical background marine conditions were sampled, and measurements were made at several altitudes within the boundary layer, in the cloud layer, and in the free troposphere.

Supporting data describing the meteorological conditions and other microphysical data from the MAST Experiment are described in a series of works (Durkee et al., 1996; Ferek et al., 1996; Johnson et al., 1996; Noone et al., 1996a,b). Supporting information about the MAST operations and about the ships sampled during the experiment are described by Gasparovic (1995).

The measurements collected as part of this experiment were designed to provide evidence for assessing the following three of the working hypotheses about ship track formation processes (Gasparovic, 1995):

> Submicron aerosol particles from the ship stack are responsible for cloud droplet and radiative features of ship tracks (Hypothesis 1.1a).
>
> Submicron aerosol particles from the water wake are responsible for cloud droplet and radiative features of ship tracks (Hypothesis 1.1b).

Gas-to-particle conversion provides a source of cloud condensation nuclei (CCN) for cloud modification downtrack (Hypothesis 1.3).

Significant evidence supports Hypothesis 1.1a and contradicts Hypothesis 1.1b, as discussed by Johnson et al. (1996). Resolving Hypothesis 1.3 requires modeling the competing aerosol evolution processes and will be addressed in future work.

Here the submicron aerosol size distributions obtained with the RCAD instrument are summarized for five flights during the MAST Experiment. The data are presented in surface contour plots to illustrate changes in the air mass characteristics that exceed the variability between successive measurements. Case studies incorporating these data with simultaneous measurements of other microphysical, chemical and meteorological parameters appear elsewhere (Johnson et al., 1996; Noone et al., 1996a,b; Ferek et al., 1996; Garrett et al., 1996).

6.1 June 11 (JDT 162)

As noted in the flight summaries of the C131 in Gasparovic (1995), the ambient background and cloud during this flight reflected high condensation nuclei and cloud droplet concentrations. Figures 6.1-6.4 illustrate the aerosol size distributions measured on June 11, 1994. The aerosol signature of the track is similar to the background air in number concentration as well as

mean diameter of the major modes. In cloud, there is a peak at 0.15 μm dry diameter and no detectable particles below 0.05 μm. However, in track there is a significant (ca. 20%) increase in number concentration at or below 0.1 μm dry diameter, resulting in a shift in the accumulation mode to a smaller diameter. This shift can be seen by comparing the in-track interstitial aerosol distributions at JDT 162.567 in Fig. 6.3 to the background distributions at JDT 162.483 and 162.487 in Fig. 6.1. In addition, there are particles detected below 0.02 μm for the "younger" tracks (less than 2 h since emission).

Variability in the interstitial aerosol in the ambient cloud is also illustrated in the plot by the fluctuations of the contour boundaries in regions of uniform concentrations. The track interstitial aerosol are similar in structure to the ambient cloud (out of track), but includes additional aerosol, particularly near the "Hoppel minimum" at 0.1 μm diameter (Hoppel et al., 1990). For instance, from JDT 162.570 to 162.590 in Fig. 6.3, the boundary of the mode at 80 nm for 500 cm^{-3} grows wider indicating that the concentration increases and the mode broadens.

Comparing distributions at different ages in the track reveals that the mean accumulation mode diameter shifts to smaller sizes as the track ages. This effect would be consistent with a larger fraction of the submicron particles being activated as more particles are depleted downtrack. This effect is illustrated by comparing a 5.5-hr track at JDT 162.567 in Fig. 6.3 to a 6.4-hr track at JDT162.571, where the larger mode has gone from 70 nm to

50 nm mean diameter. This depletion of the nuclei from the ship emissions provides evidence for the hypothesis that it is the reservoir of particles provided from the plume which are responsible for the persistence of the track (Hypothesis 1.1a). In addition, the fine particles (< 1 μm diameter) initially present in the plume and in some of the track are below detection at 6.4 hr after emission as illustrated by the distribution from a track intersection at JDT 162.571 in Fig. 6.3, as would be consistent with coalescence of particles by repeated cloud processing. The consequence is that there are indications that the cutoff diameter for activation to cloud droplets is decreasing as the track gets older, corresponding to increasing supersaturations downtrack.

6.2 June 27 (JDT 178)

The stratus cloud on this flight was characterized by high levels of background particles as indicated by the condensation nuclei and cloud droplet number measurements reported by the UW research group in Gasparovic (1995). Figures 6.9-6.12 illustrate the aerosol size distributions measured on June 27, 1994. The background aerosol is characterized by two modes, one at 0.05 μm (dry diameter) and a smaller mode at 0.01 μm, with concentrations of 400 to 500 cm^{-3} as illustrated at JDT 178.561 in Fig. 6.7 below cloud and at JDT 178.547 in Fig. 6.6 in cloud. The variability in the background is illustrated in the changes in the size distributions in cloud during JDT 178.535 through 178.545 in Fig. 6.6 and below cloud during JDT 178.570

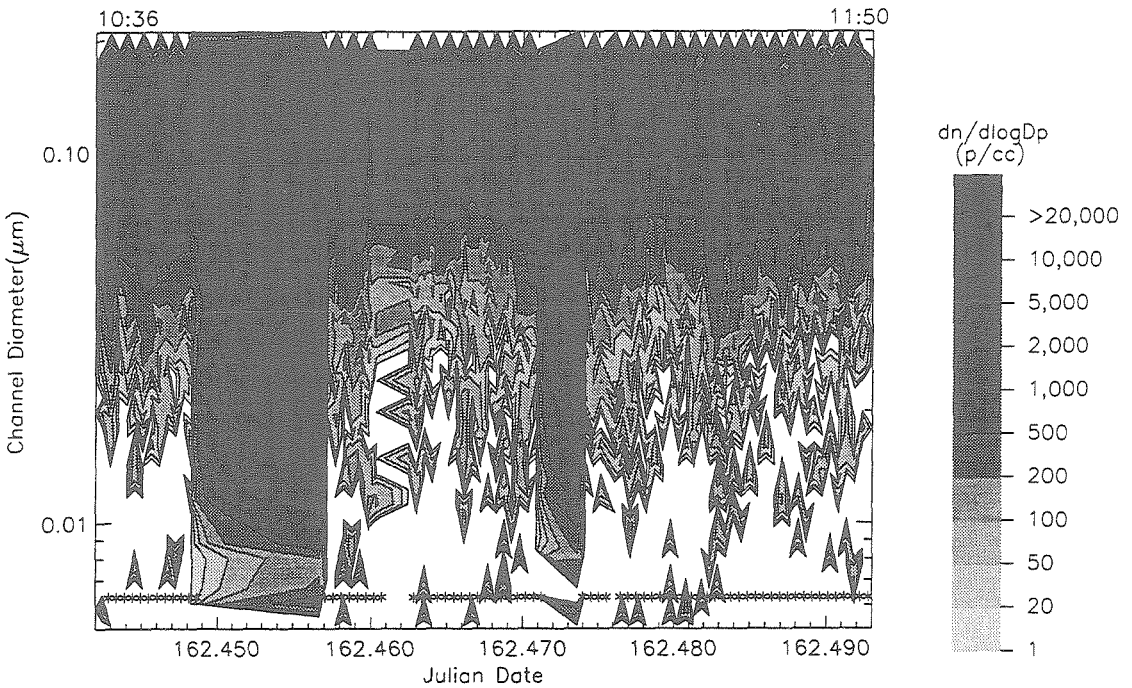

Figure 6.1: RCAD Aerosol Size Distributions, June 11, 1994: Flight 1641.1. Data are corrected to ambient concentrations by assuming single-charging in a matrix-type inversion, in which non-ideal flow effects during scan have been included. Stars indicate times at which individual measurements were made.

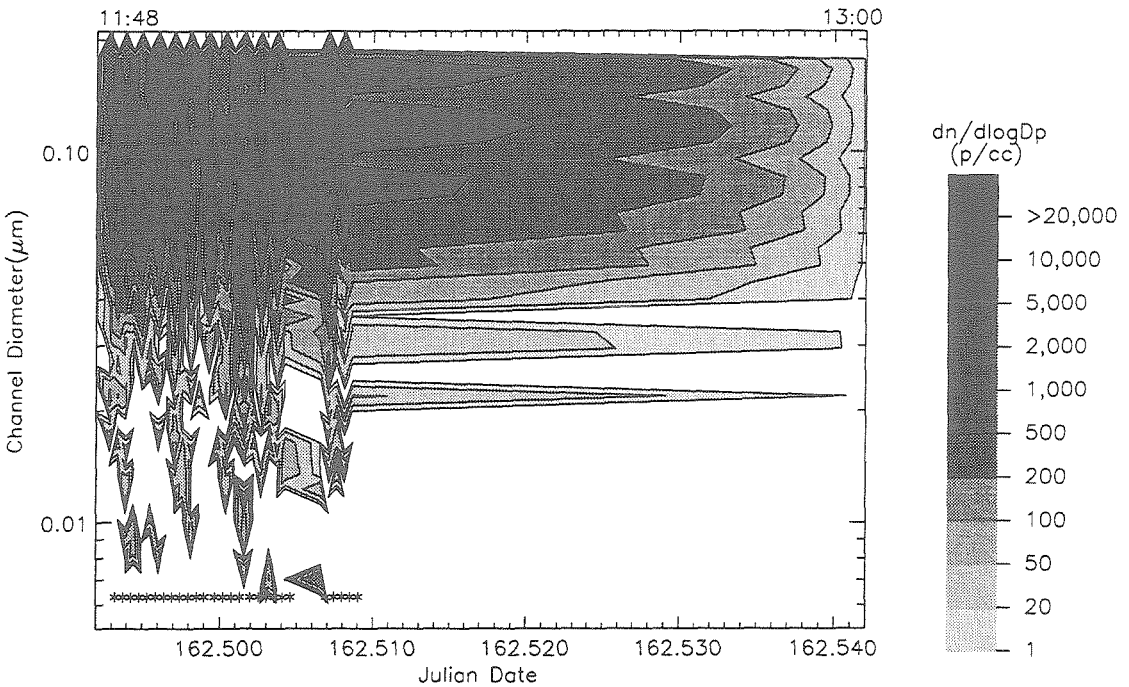

Figure 6.2: RCAD Aerosol Size Distributions, June 11, 1994: Flight 1641.2. Data are corrected to ambient concentrations by assuming single-charging in a matrix-type inversion, in which non-ideal flow effects during scan have been included. Stars indicate times at which individual measurements were made.

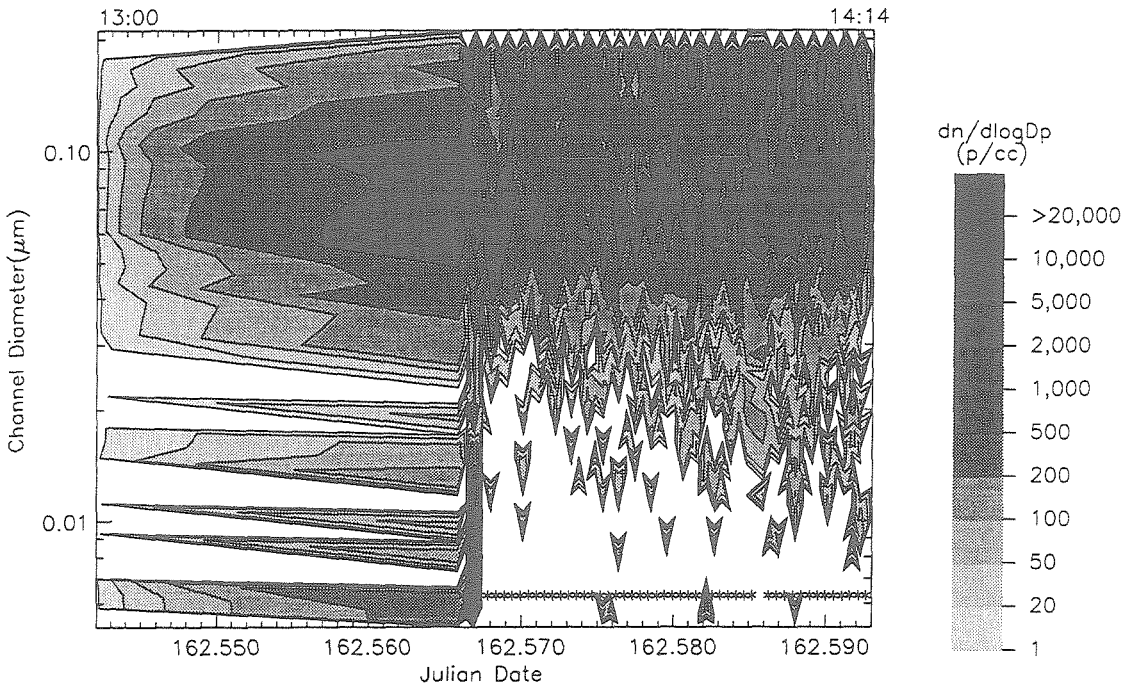

Figure 6.3: RCAD Aerosol Size Distributions, June 11, 1994: Flight 1641.3. Data are corrected to ambient concentrations by assuming single-charging in a matrix-type inversion, in which non-ideal flow effects during scan have been included. Stars indicate times at which individual measurements were made.

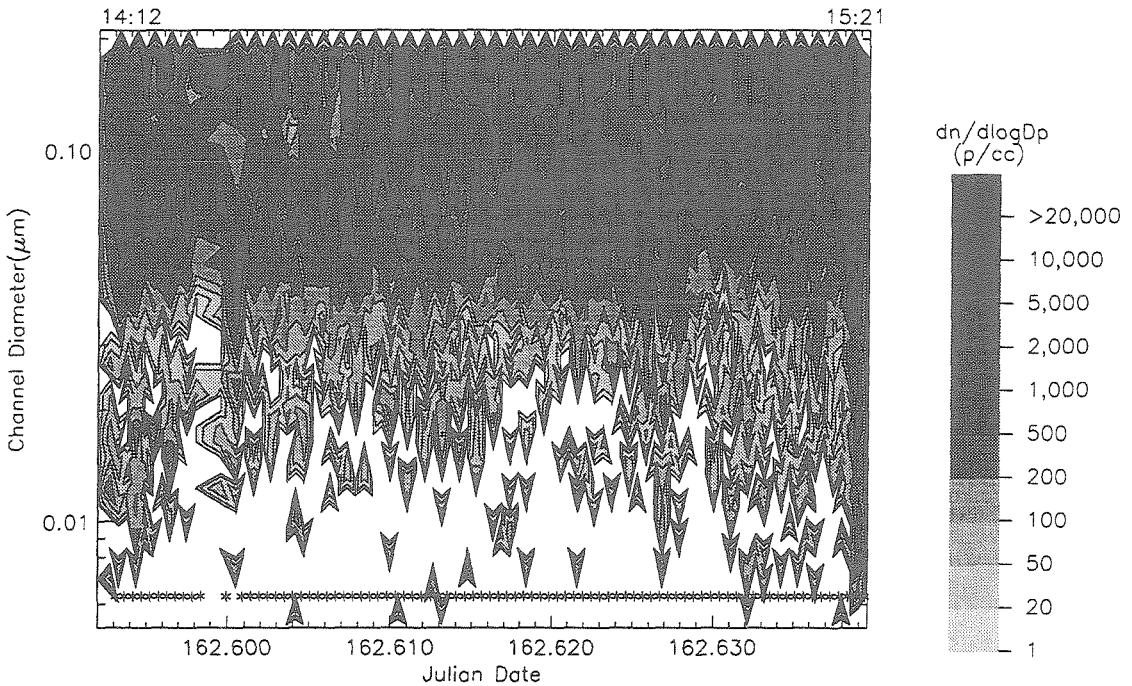

Figure 6.4: RCAD Aerosol Size Distributions, June 11, 1994: Flight 1641.4. Data are corrected to ambient concentrations by assuming single-charging in a matrix-type inversion, in which non-ideal flow effects during scan have been included. Stars indicate times at which individual measurements were made.

through 178.585 in Fig. 6.7.

The plumes of ships sampled are characterized by additional fine particles in the below cloud aerosol. The plume of the *Tai He* included a peak at 0.08 μm at JDT 178.563 in Fig. 6.7, while the *Mount Vernon*'s particle emissions were smaller with a peak mode at 0.04 μm at JDT 178.624 in Fig. 6.8. This distinction in the plumes is consistent with the combustion characteristics of the two ships (i.e., diesel vs. steam turbine). It also provides evidence for the role of particles in ship track formation, since the satellite signature of the *Mount Vernon* was not detected (Hypothesis 1.1a).

In cloud, the track of the *Tai He* was characterized by increased interstitial aerosol and a minor mode at 0.015 μm (dry diameter) at JDT 178.545 and 178.548 in Fig. 6.6. In the "track" behind the *Mount Vernon*'s plume, there were also elevated concentrations of fine particles but no discernible change in the cloud microphysics as shown from JDT 178.634 through 178.638 in Fig. 6.8.

6.3 June 28 (JDT 179)

Figures 6.9-6.12 illustrate the aerosol size distributions measured on June 28, 1994. The stratus cloud coverage on this day included clouds with high background aerosol concentrations. However, rather than a single-mode continental aerosol, the in-track interstitial aerosol were characterized by three modes, each of low concentration at JDT 179.480 and 179.482 in Fig. 6.11.

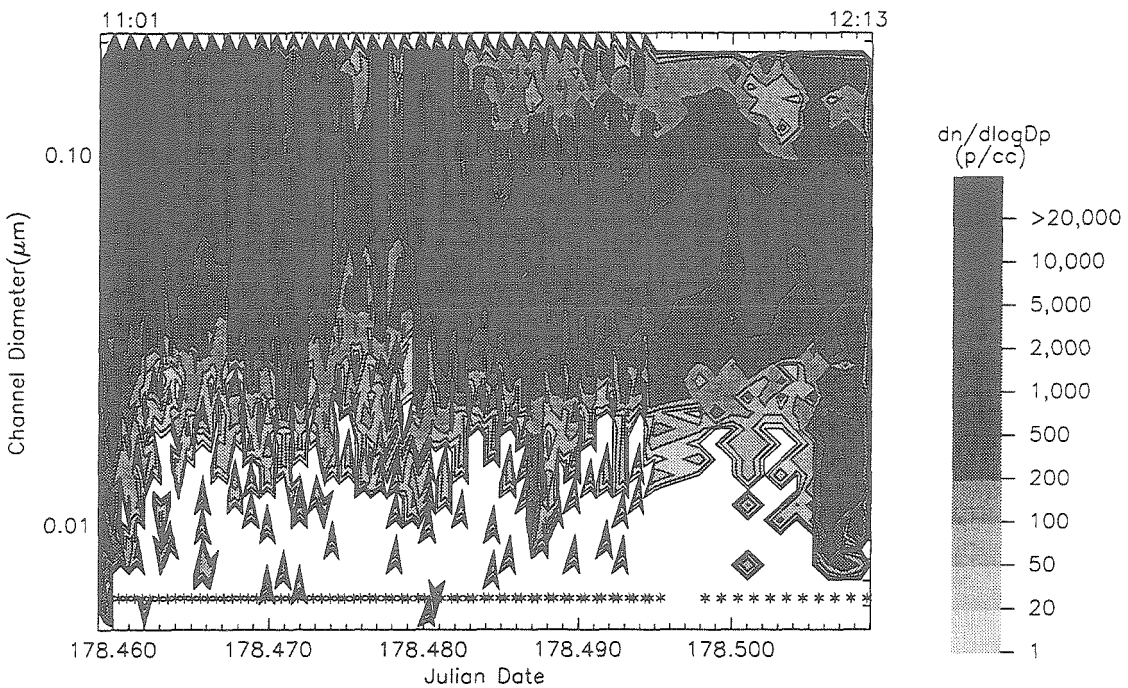

Figure 6.5: RCAD Aerosol Size Distributions, June 27, 1994: Flight 1646.1. Data are corrected to ambient concentrations by assuming single-charging in a matrix-type inversion, in which non-ideal flow effects during scan have been included. Stars indicate times at which individual measurements were made.

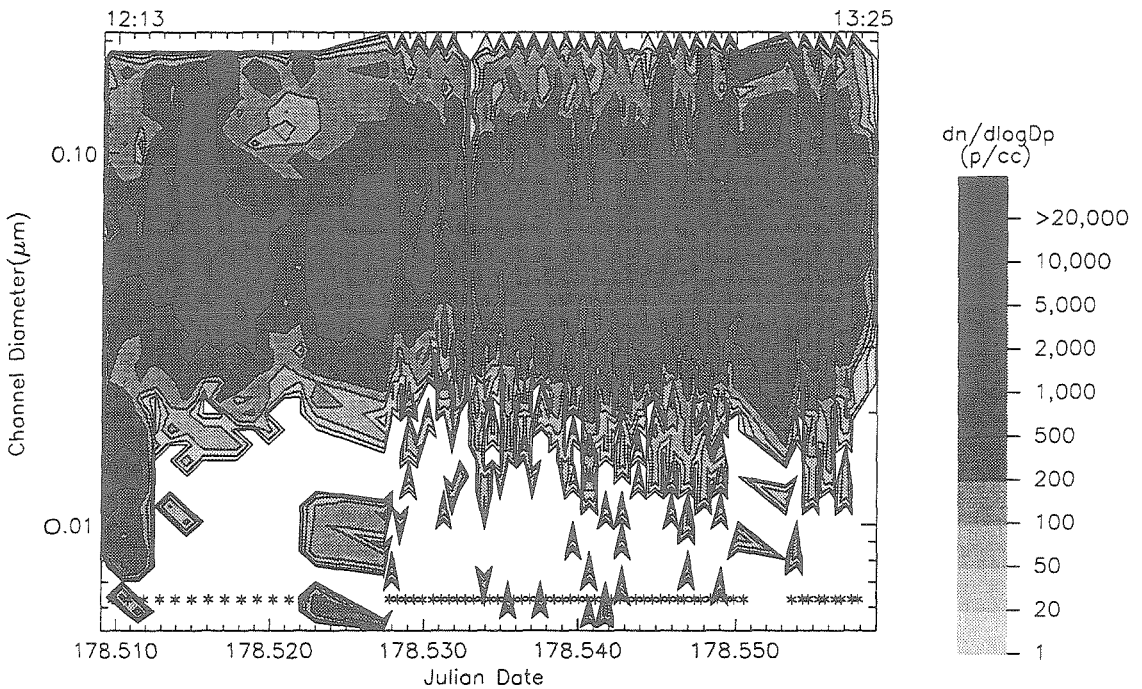

Figure 6.6: RCAD Aerosol Size Distributions, June 27, 1994: Flight 1646.2. Data are corrected to ambient concentrations by assuming single-charging in a matrix-type inversion, in which non-ideal flow effects during scan have been included. Stars indicate times at which individual measurements were made.

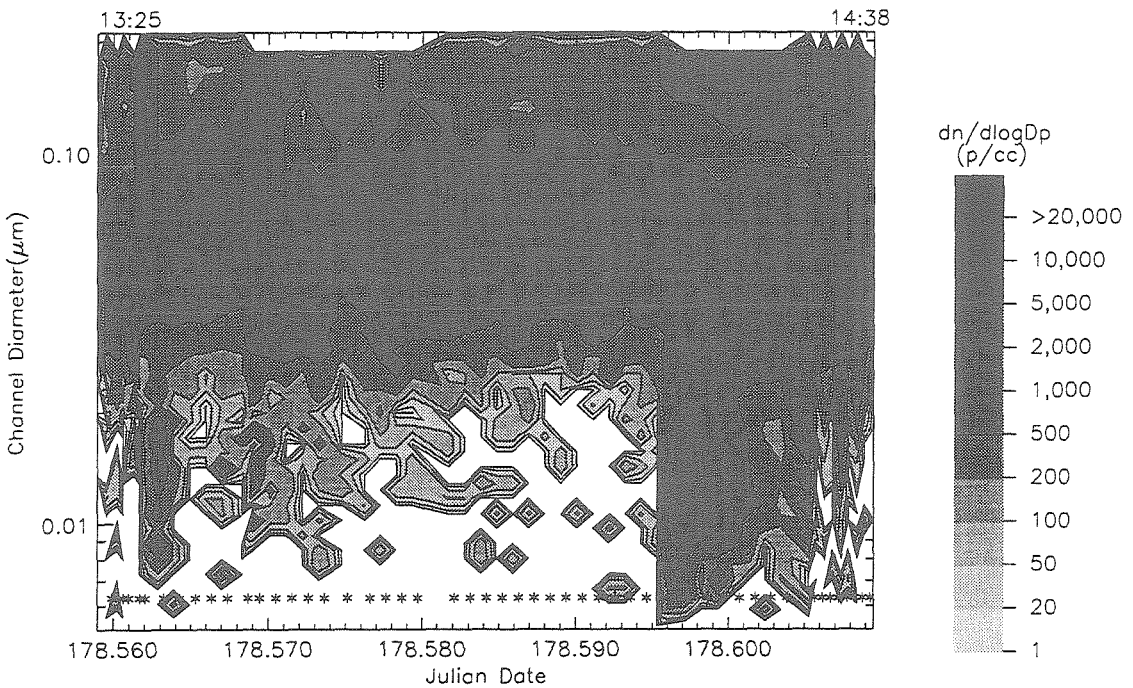

Figure 6.7: RCAD Aerosol Size Distributions, June 27, 1994: Flight 1646.3. Data are corrected to ambient concentrations by assuming single-charging in a matrix-type inversion, in which non-ideal flow effects during scan have been included. Stars indicate times at which individual measurements were made.

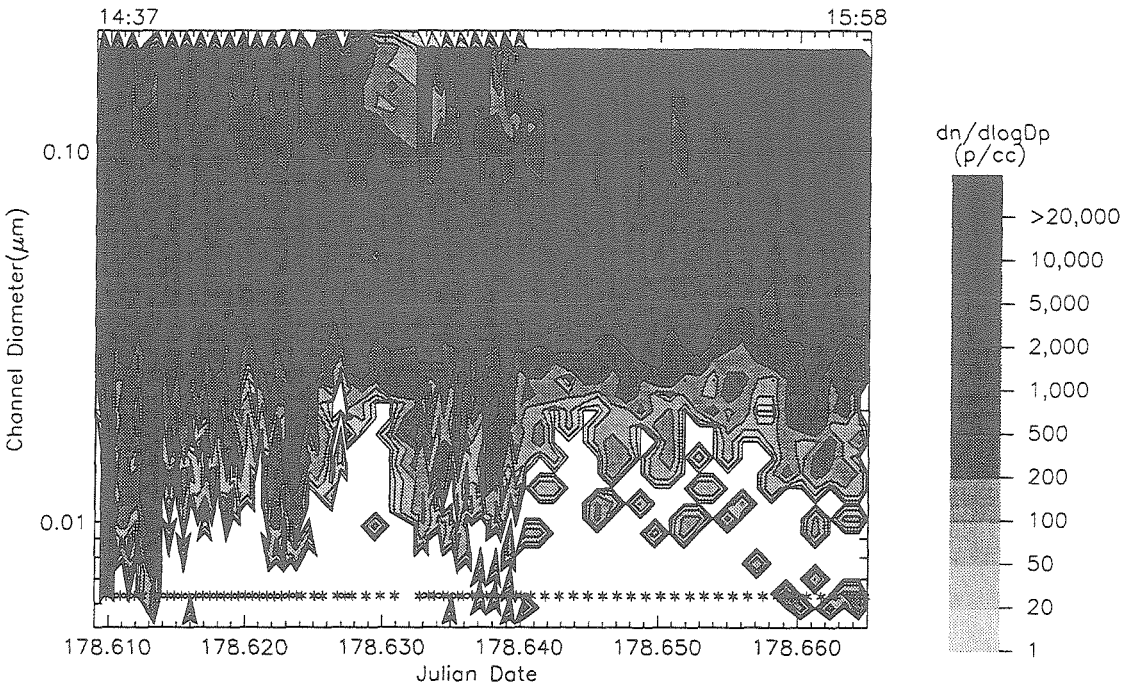

Figure 6.8: RCAD Aerosol Size Distributions, June 27, 1994: Flight 1646.4. Data are corrected to ambient concentrations by assuming single-charging in a matrix-type inversion, in which non-ideal flow effects during scan have been included. Stars indicate times at which individual measurements were made.

The total condensation nuclei concentration was approximately 300 cm^{-3}. The background in cloud size distribution was typically bimodal, with peaks at 0.05 and above 0.15 μm (dry diameter) at JDT 179.500 in Fig. 6.11.

The plumes sampled (from the *Mount Vernon*) included additional fine particles at 0.01 μm at JDT 179.494 in Fig. 6.11. In the "track" behind the *Mount Vernon*, there were elevated concentrations of particles at 0.05 μm (dry diameter) at JDT 179.480 in Fig. 6.11. However, there was no consistently discernible microphysical change in the cloud droplet number distribution (Gasparovic, 1995).

6.4 June 29 (JDT 180)

Figures 6.13-6.17 illustrate the aerosol size distributions measured on June 29, 1994. The particle number concentrations measured were very low, indicative of clean marine air (Hoppel, 1989). For these concentrations, the signal-to-noise ratio for individual (45-s duration) measurements are very low. Higher certainty measurements can be obtained by averaging a number of successive scans from within a homogeneous air mass.

The plume of the *Star Livorno* was characterized by a peak at 0.05 μm (dry) diameter as measured directly after emission from the stack below cloud at JDT 180.584 in Fig. 6.16. The associated track measured in cloud was characterized by a corresponding peak of interstitial particles at 0.05 μm (dry) diameter at JDT 180.555 in Fig. 6.15. For the length of track

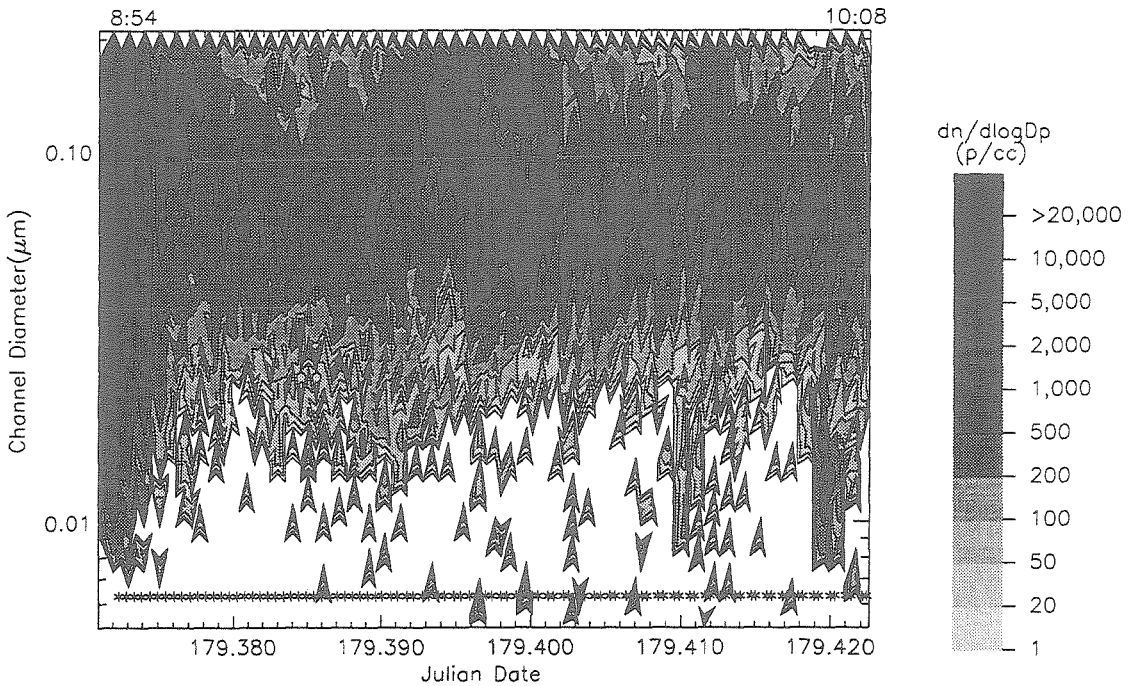

Figure 6.9: RCAD Aerosol Size Distributions, June 28, 1994: Flight 1647.1. Data are corrected to ambient concentrations by assuming single-charging in a matrix-type inversion, in which non-ideal flow effects during scan have been included. Stars indicate times at which individual measurements were made.

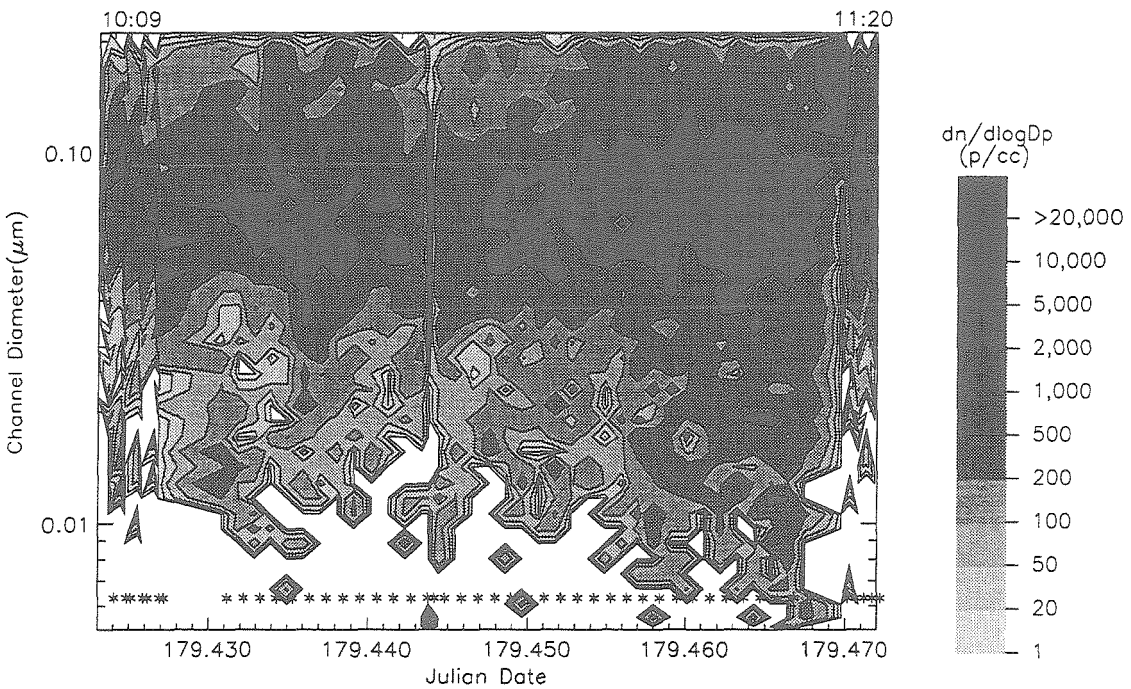

Figure 6.10: RCAD Aerosol Size Distributions, June 28, 1994: Flight 1647.2. Data are corrected to ambient concentrations by assuming single-charging in a matrix-type inversion, in which non-ideal flow effects during scan have been included. Stars indicate times at which individual measurements were made.

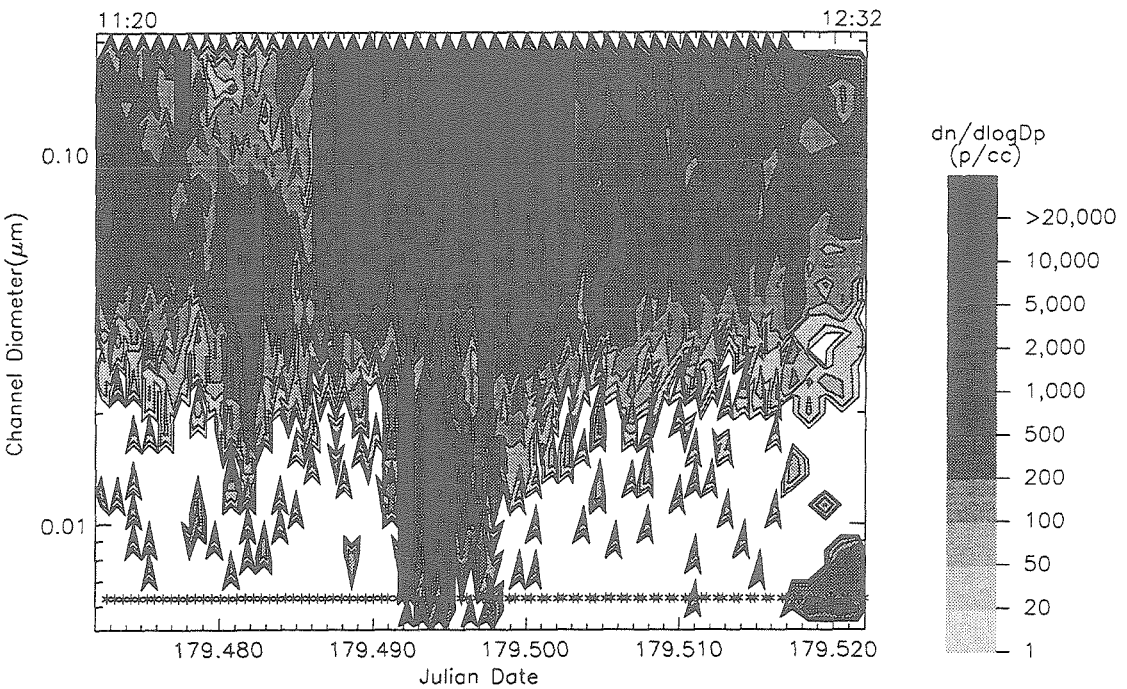

Figure 6.11: RCAD Aerosol Size Distributions, June 28, 1994: Flight 1647.3. Data are corrected to ambient concentrations by assuming single-charging in a matrix-type inversion, in which non-ideal flow effects during scan have been included. Stars indicate times at which individual measurements were made.

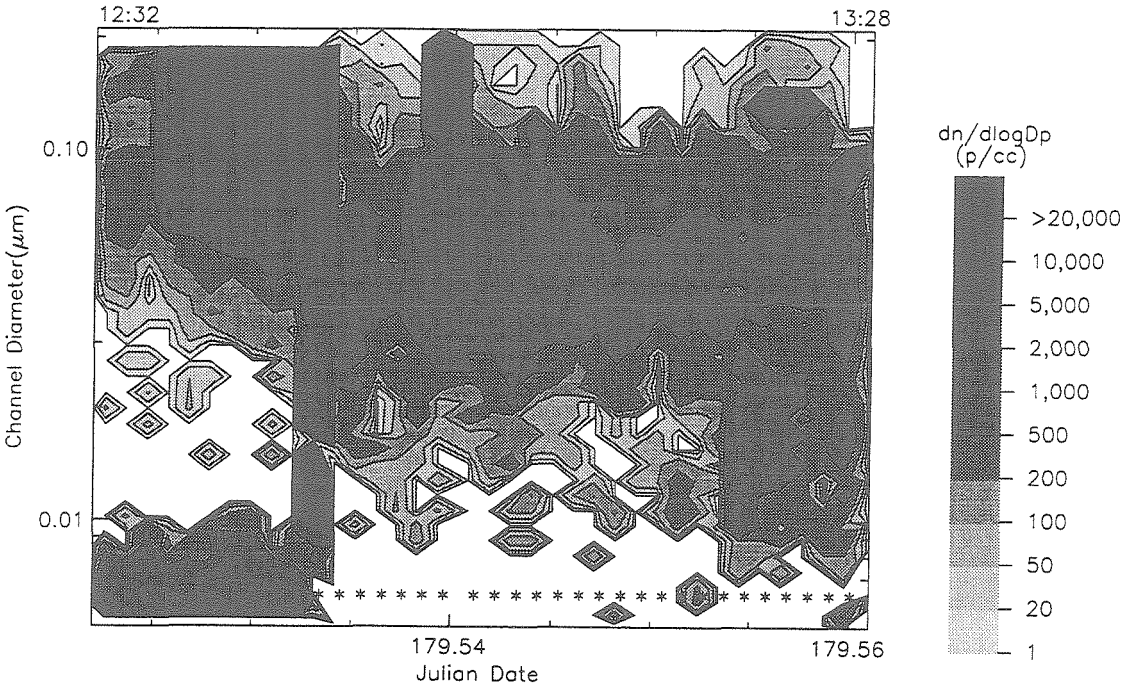

Figure 6.12: RCAD Aerosol Size Distributions, June 28, 1994: Flight 1647.4. Data are corrected to ambient concentrations by assuming single-charging in a matrix-type inversion, in which non-ideal flow effects during scan have been included. Stars indicate times at which individual measurements were made.

sampled (from 0.8 hr after emission from the ship, measured at JDT 180.564 in Fig. 6.15, to 1.5 hr after emission from the ship, measured at JDT 180.538 in Fig. 6.14), particles from that mode were depleted, the larger particles being preferentially lost from the upper side of the mode. The result is that the log-mean diameter of the mode decreases downtrack as can be seen by comparing size distributions at JDT 180.538, 180.564, and 180.555 in Fig. 6.14 and 6.15. This evidence is consistent with particles from the stack plume acting as CCN to result in higher droplet concentrations in track.

Submicron aerosol size distributions illustrate the evolution of particles as the track increases in age. In particular, there is a depletion of particles at 0.1 μm (dry) diameter and simultaneous appearance of particles at larger sizes 0.2-0.3 μm (dry) diameter as the track ages.

6.5 June 30 (JDT 181)

Figures 6.18-6.23 illustrate the aerosol size distributions obtained on June 30, 1994. Stratus clouds with high droplet concentrations at the start of this flight dissipated near the middle of the flight. The background levels of condensation nuclei were between 100 and 200 cm^{-3}.

Below-cloud background particle distributions were characterized by modes at 0.04 μm and 0.01 μm and a minimum at 0.1 μm as exemplified by the distribution at JDT 181.679 in Fig. 6.23. In addition, there are a large number of particles indicated above 0.1 μm in the distributions col-

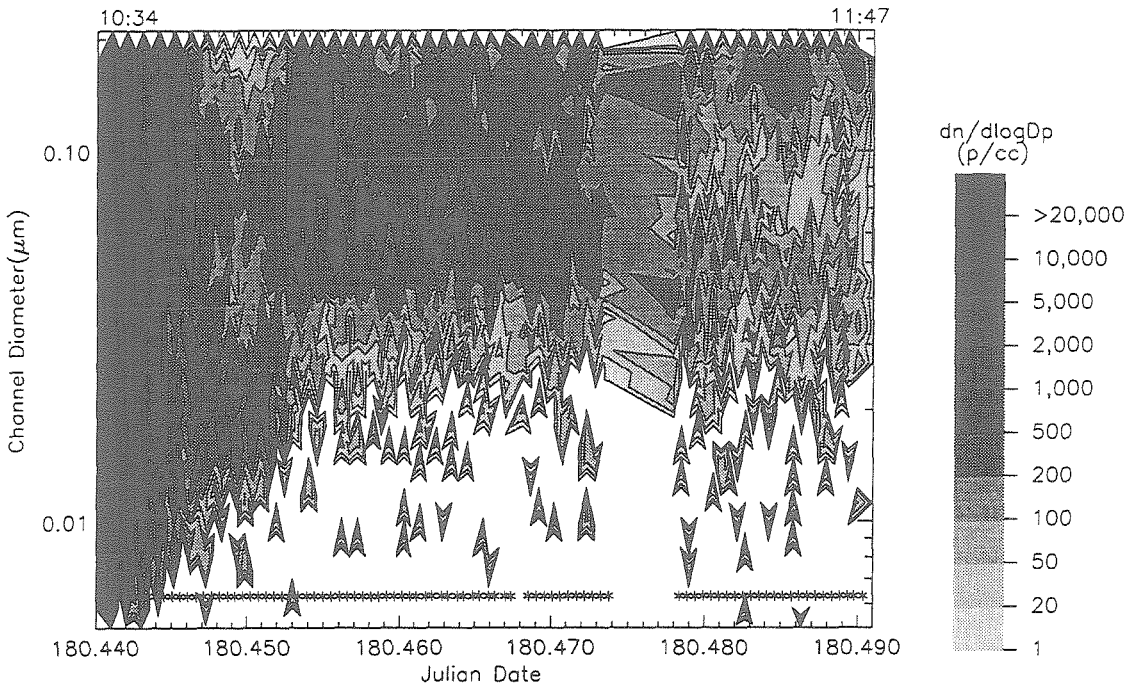

Figure 6.13: RCAD Aerosol Size Distributions, June 29, 1994: Flight 1648.1. Data are corrected to ambient concentrations by assuming single-charging in a matrix-type inversion, in which non-ideal flow effects during scan have been included. Stars indicate times at which individual measurements were made.

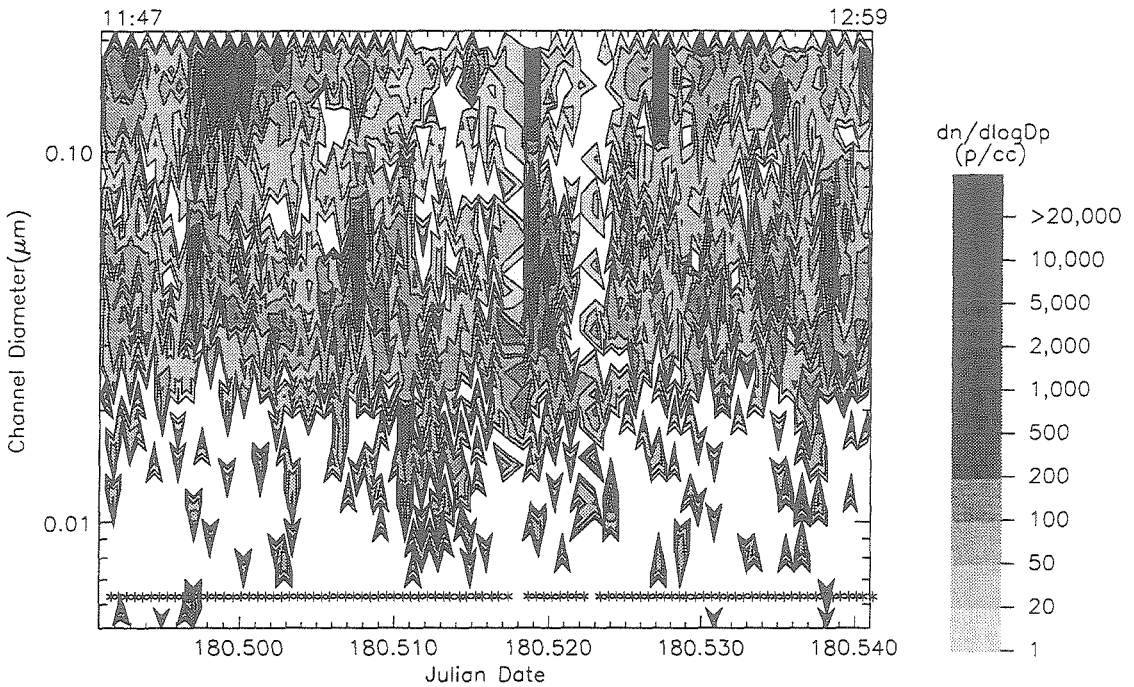

Figure 6.14: RCAD Aerosol Size Distributions, June 29, 1994: Flight 1648.2. Data are corrected to ambient concentrations by assuming single-charging in a matrix-type inversion, in which non-ideal flow effects during scan have been included. Stars indicate times at which individual measurements were made.

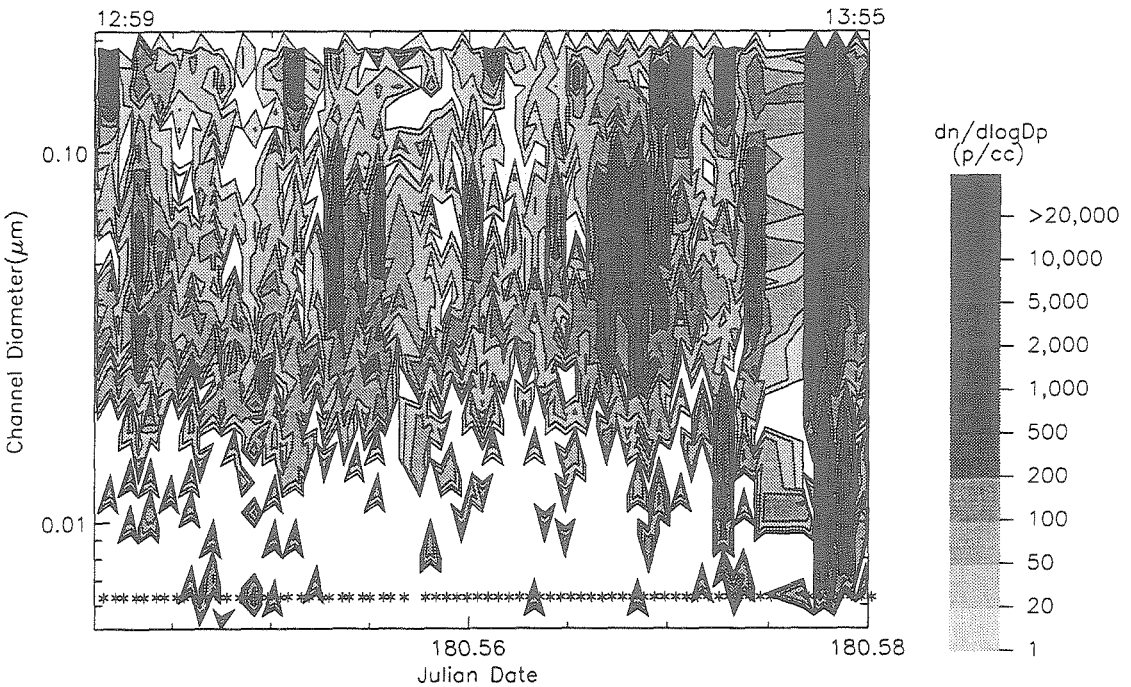

Figure 6.15: RCAD Aerosol Size Distributions, June 29, 1994: Flight 1648.3. Data are corrected to ambient concentrations by assuming single-charging in a matrix-type inversion, in which non-ideal flow effects during scan have been included. Stars indicate times at which individual measurements were made.

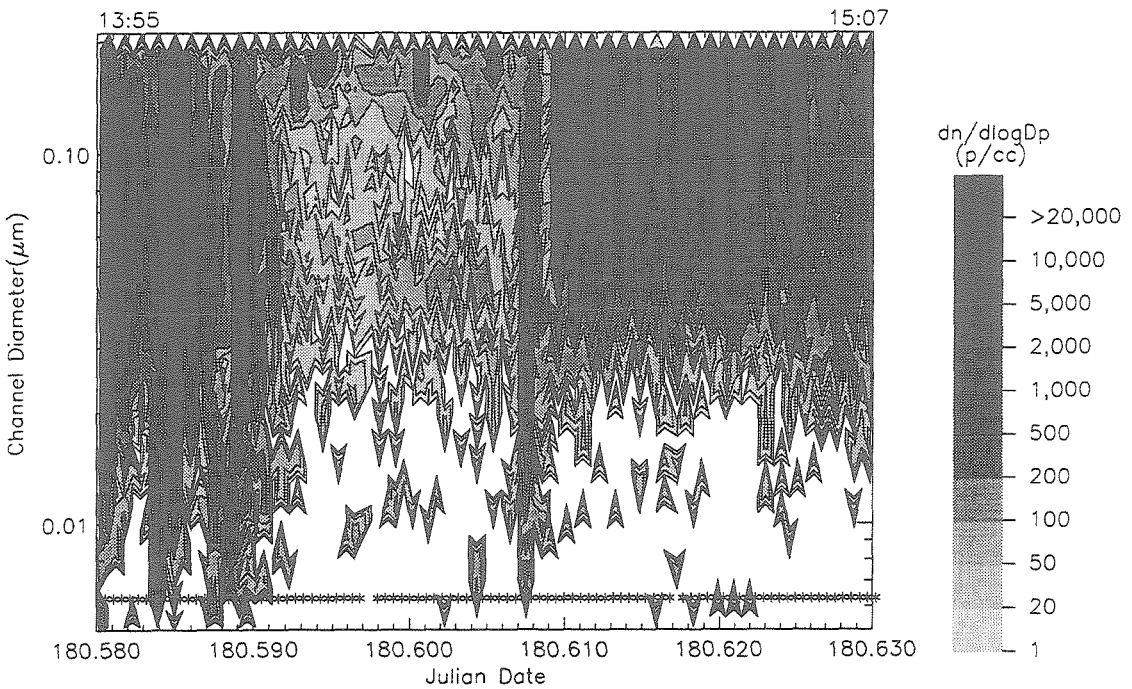

Figure 6.16: RCAD Aerosol Size Distributions, June 29, 1994: Flight 1648.4. Data are corrected to ambient concentrations by assuming single-charging in a matrix-type inversion, in which non-ideal flow effects during scan have been included. Stars indicate times at which individual measurements were made.

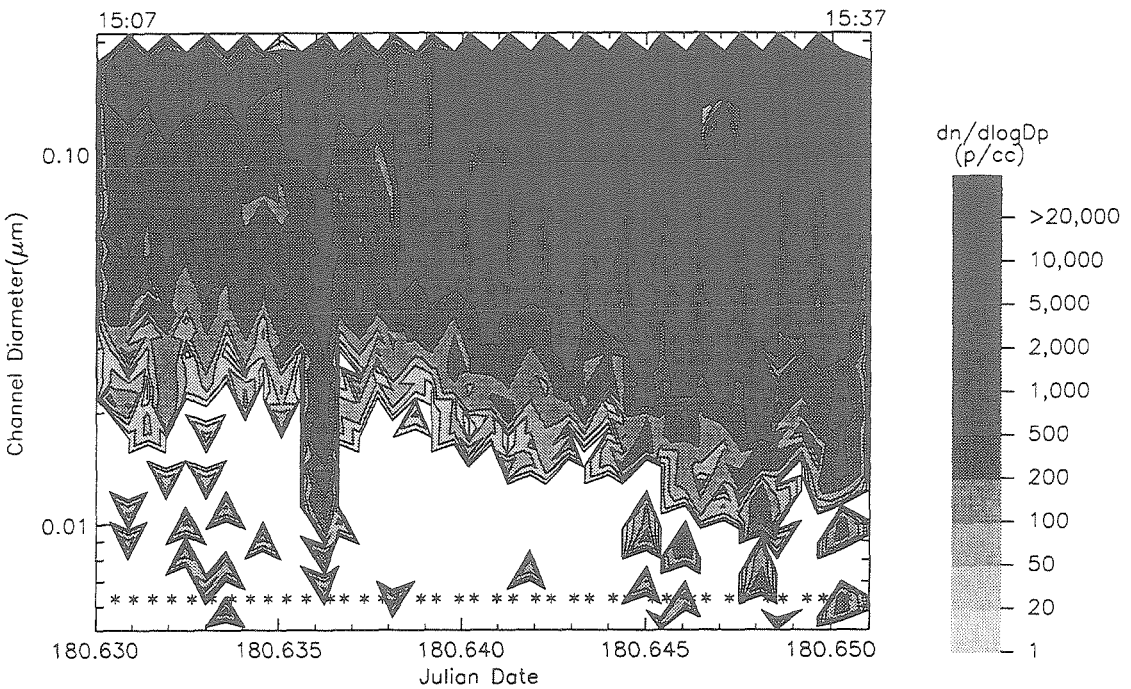

Figure 6.17: RCAD Aerosol Size Distributions, June 29, 1994: Flight 1648.5. Data are corrected to ambient concentrations by assuming single-charging in a matrix-type inversion, in which non-ideal flow effects during scan have been included. Stars indicate times at which individual measurements were made.

lected between JDT 181.605 through 181.615 in Fig. 6.21, up to the detection limit of the instrument (0.2 μm). The plumes are characterized by additional fine particles in a mode at 0.08 μm as shown at JDT 181.636 and 181.655 in Fig. 6.22.

The interstitial aerosol concentrations in cloud are characterzied by similar features during JDT 181.539 through 181.543 in Fig. 6.19. In the track, the distributions are distinguished by increased fine particle concentrations, at 0.06 μm and above 0.1 μm. This increase is evident at JDT 181.537 in Fig. 6.19 and at JDT 181.502 in Fig. 6.18.

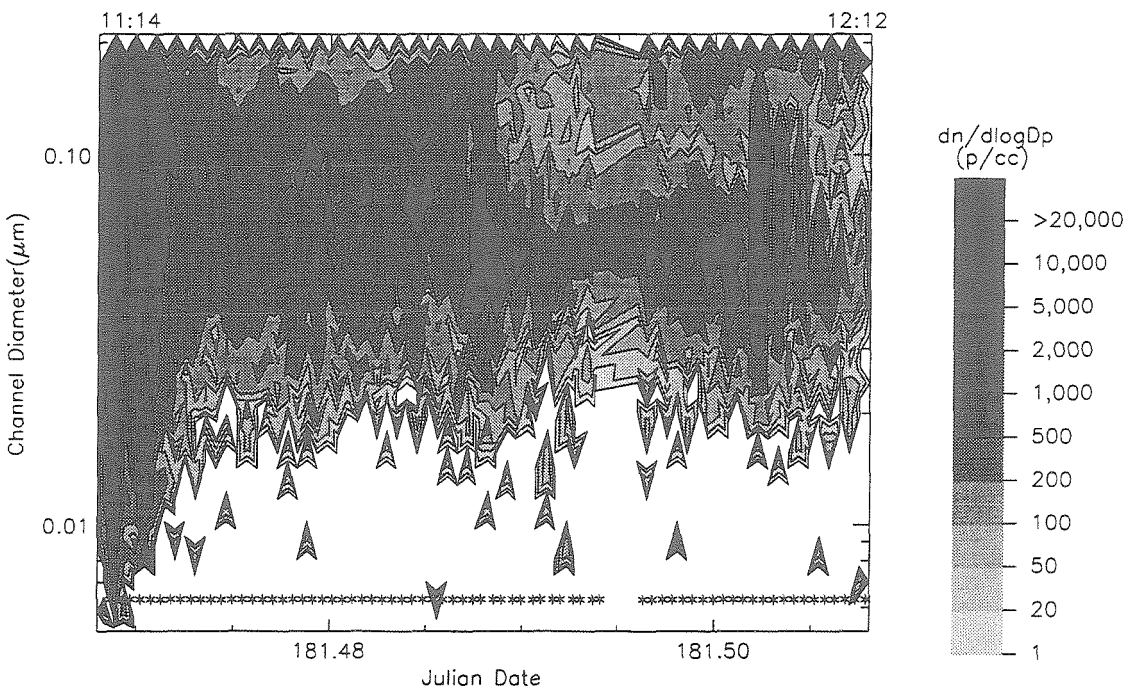

Figure 6.18: RCAD Aerosol Size Distributions, June 30, 1994: Flight 1649.1. Data are corrected to ambient concentrations by assuming single-charging in a matrix-type inversion, in which non-ideal flow effects during scan have been included. Stars indicate times at which individual measurements were made.

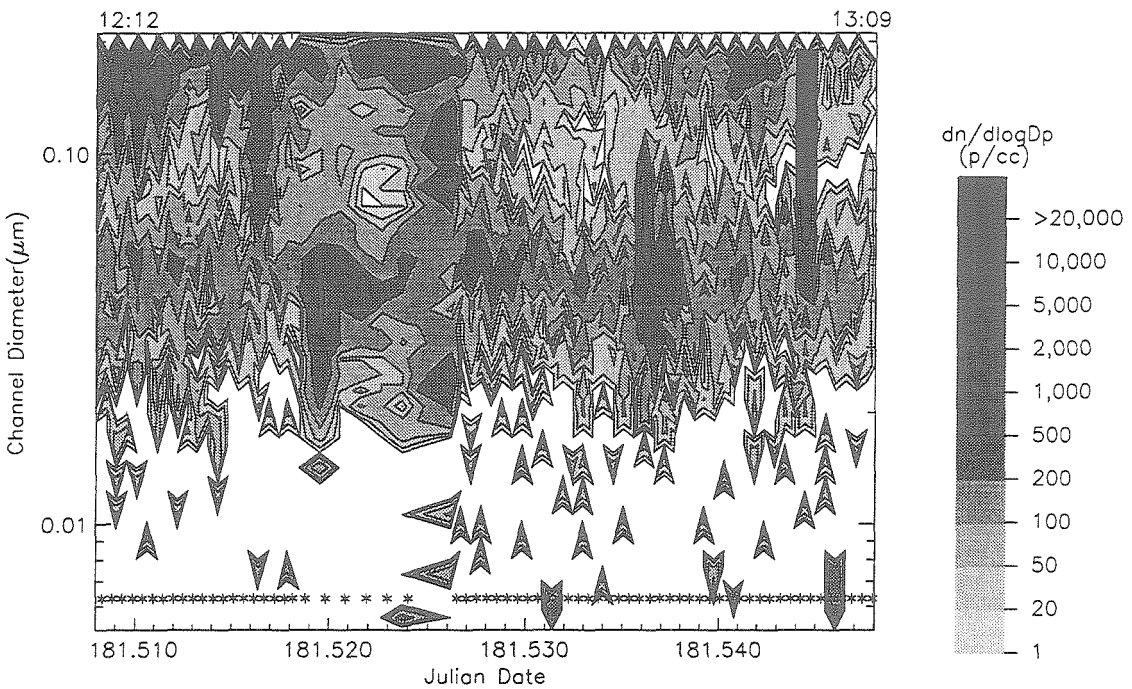

Figure 6.19: RCAD Aerosol Size Distributions, June 30, 1994: Flight 1649.2. Data are corrected to ambient concentrations by assuming single-charging in a matrix-type inversion, in which non-ideal flow effects during scan have been included. Stars indicate times at which individual measurements were made.

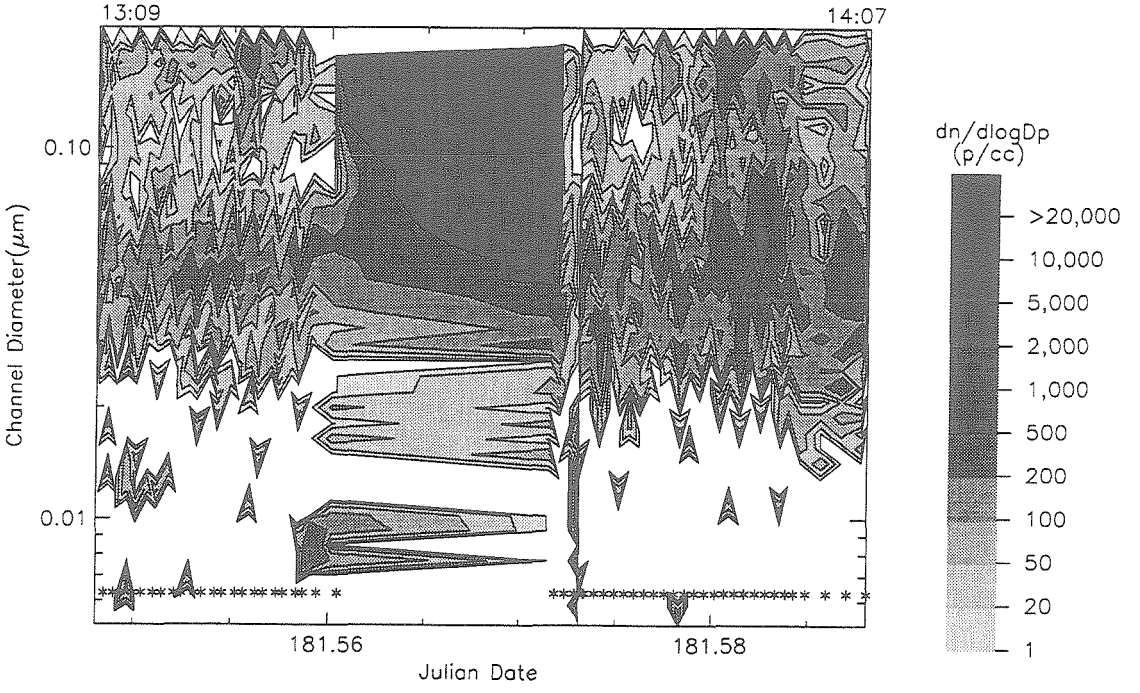

Figure 6.20: RCAD Aerosol Size Distributions, June 30, 1994: Flight 1649.3. Data are corrected to ambient concentrations by assuming single-charging in a matrix-type inversion, in which non-ideal flow effects during scan have been included. Stars indicate times at which individual measurements were made.

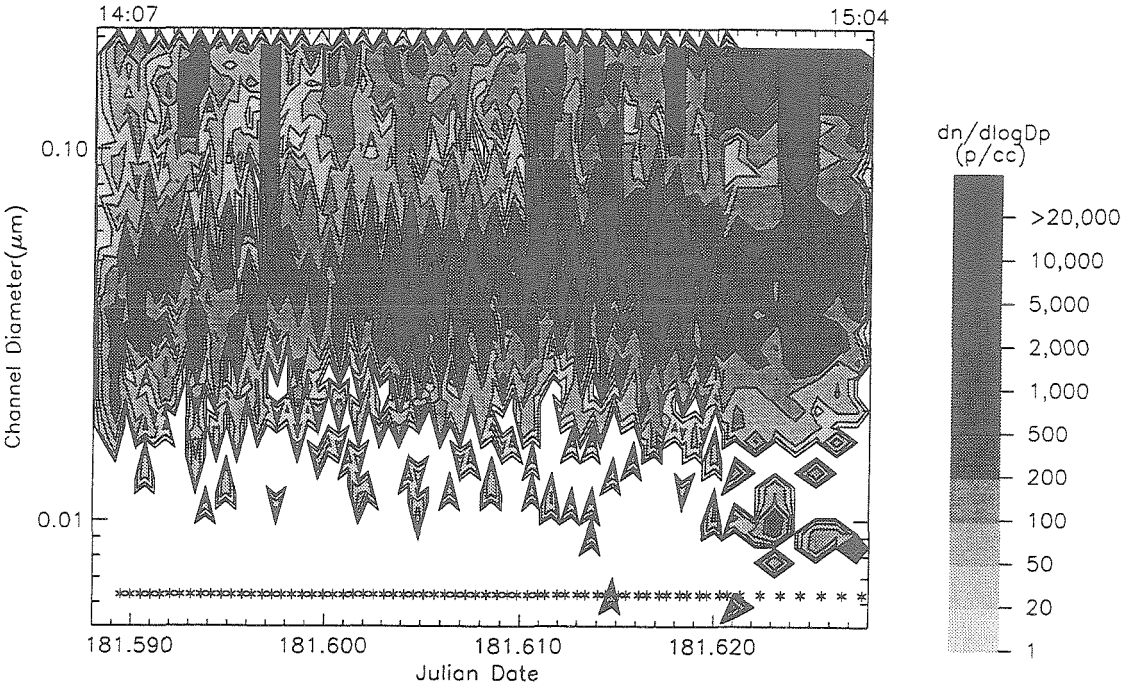

Figure 6.21: RCAD Aerosol Size Distributions, June 30, 1994: Flight 1649.4. Data are corrected to ambient concentrations by assuming single-charging in a matrix-type inversion, in which non-ideal flow effects during scan have been included. Stars indicate times at which individual measurements were made.

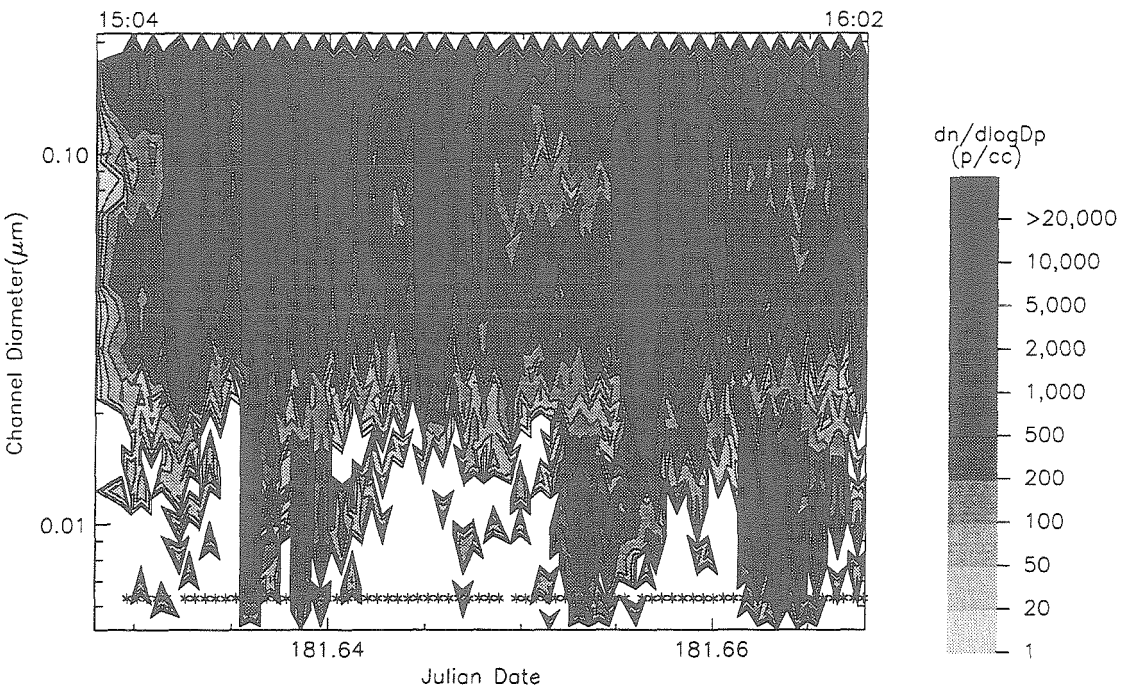

Figure 6.22: RCAD Aerosol Size Distributions, June 30, 1994: Flight 1649.5. Data are corrected to ambient concentrations by assuming single-charging in a matrix-type inversion, in which non-ideal flow effects during scan have been included. Stars indicate times at which individual measurements were made.

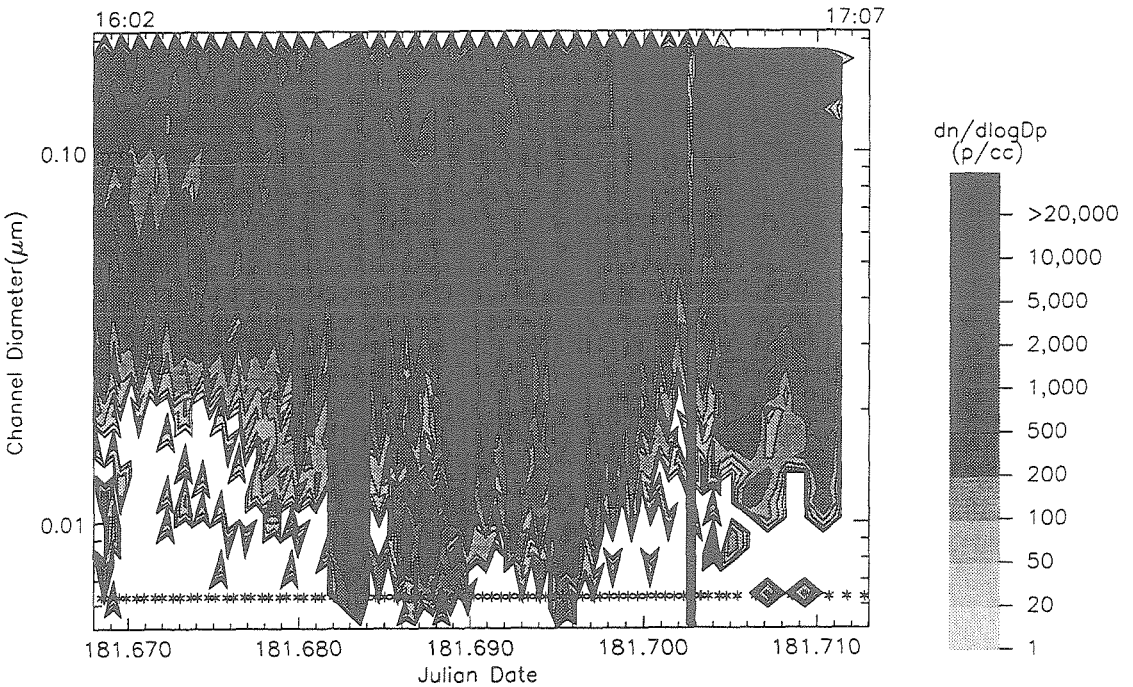

Figure 6.23: RCAD Aerosol Size Distributions, June 30, 1994: Flight 1649.6. Data are corrected to ambient concentrations by assuming single-charging in a matrix-type inversion, in which non-ideal flow effects during scan have been included. Stars indicate times at which individual measurements were made.

References

Durkee, P.A., R.J. Ferek, D.W. Johnson, J. Coakley, S. Platnick, D. Babb, G. Innis, A. Ackerman, J.G. Hudson, L.M. Russell, and W. Hoppel, 1996: Tests of the role of ambient cloud properties in ship track formation. *J. Atmos. Sci.* In preparation.

Ferek, R.J., P. Hobbs, T. Garrett, K.J. Noone, J.G. Hudson, L.M. Russell, J.H. Seinfeld, R.C. Flagan, P.A. Durkee, K. Nielsen, D.W. Johnson, J.P. Taylor, C. O'Dowd, I. Brooks, D. Rogers, S. Osborne, and S. Platnick, 1996: Star Livorno/Hanjin Barcelona case study. *J. Atmos. Sci.* In preparation.

Garrett, T., P. Hobbs, Ferek, R.J., J.G. Hudson, L.M. Russell, J.H. Seinfeld, R.C. Flagan, P.A. Durkee, K. Nielsen, D.W. Johnson, C. O'Dowd, W. Hoppel, J. Frick, K.J. Noone, and S. Platnick, 1996: Airborne Sampling of the emissions from ships with references to their effects on clouds. *J. Atmos. Sci.* In preparation.

Gasparovic, R.F., 1995: *MAST Experiment Operations Summary.* Johns Hopkins University, Maryland.

Hoppel, W.A., J.W. Fitzgerald, G.M. Frick, and R.E. Larson, 1990: Aerosol size distributions and optical properties found in the marine boundary layer over the Atlantic Ocean. *J. Geophys. Res.*, 95, 3559-

3886.

Johnson, D.W., R.J. Ferek, T. Garrett, P. Hobbs, J.G. Hudson, K.J. Noone, L.M. Russell, S. Platnick, J.P. Taylor, C. O'Dowd, W. Hooper, P.A. Durkee, K. Nielson, W. Hindmann, A. Ackerman, C. Bretherton, G. Innis, Y. Kogan, R.C. Flagan, J.H. Seinfield, M. Smith, and W. Hoppel, 1996: The impact of ship produced aerosols on the microphysical characteristics of warm stratocumulus clouds: A test of Hypotheses 1.1a and 1.1b. *J. Atmos. Sci.* In preparation.

King, M.D., L.F. Radke, and P.V. Hobbs, 1993: Optical properties of marine stratocumulus clouds modified by ships. *J. Geophys. Res.*, 98: 2729-2739.

Noone, K.J., C. Ostrom, R.J. Ferek, P. Hobbs, T. Garrett, D.W. Johnson, J.P. Taylor, I. Brooks, L.M. Russell, R.C. Flagan, J.H. Seinfeld, J.G. Hudson, S. Platnick, C. O'Dowd, M. Smith, J. Frick, W.B. Hoppel, W. Hooper, P.A. Durkee, K. Nielson, and D. Babb, 1996a: A case study of ship track formation in a polluted boundary layer *J. Atmos. Sci.* In preparation.

Noone, K.J., C. Ostrom, R.J. Ferek, P. Hobbs, T. Garrett, D.W. Johnson, J.P. Taylor, L.M. Russell, R.C. Flagan, J.H. Seinfeld, J.G. Hudson, C. O'Dowd, M. Smith, J. Frick, W.B. Hoppel, W. Hooper P.A. Durkee, K. Nielson, and D. Babb, 1996b: A case study of ships forming and

not forming tracks in a moderately polluted boundary layer. *J. Atmos. Sci.* In preparation.

Russell, L.M., R.C. Flagan, and J.H. Seinfeld, 1995: Asymmetric instrument response due to mixing effects in DMA-CPC measurements. *Aer. Sci. Tech.*, in press.

Russell, L.M., M.R. Stolzenburg, S.H. Zhang, R. Caldow, R.C. Flagan, and J.H. Seinfeld, 1995: Radially-classified aerosol detector for aircraft-based submicron aerosol measurements. *J. Atmos. Oceanic Tech.*, in review.

Zhang, S.H., Y. Okutsu, L.M. Russell, R.C. Flagan, and J.H. Seinfeld, 1995: Radial differential mobility analyzer. *Aer. Sci. Tech.*, in press.

Chapter 7

Combustion Organic Aerosol as Cloud Condensation Nuclei in Ship Tracks

To be submitted to the *Journal of Atmospheric Sciences.*

Lynn M. Russell[1], Kevin J. Noone[2], Ronald J. Ferek[3], Robert Pockalny[4], Richard C. Flagan[1] and John H. Seinfeld[1]

[1]Department of Chemical Engineering, California Institute of Technology, Pasadena, CA

[2]Meteorological Institute, Stockholm University, Stockholm, Sweden

[3]Department of Atmospheric Sciences, University of Washington, Seattle, WA

[4]Graduate School of Oceanography, University of Rhode Island, Narragansett, RI

The so-called indirect effect of aerosols on climate is based on the influence of anthropogenic aerosol emissions (or formation of aerosol by gas-to-particle conversion of anthropogenic emissions) on the number concentration of cloud condensation nuclei (CCN), with a resulting impact on the cloud droplet number concentration (CDNC) and sizes (Charlson et al., 1992; Penner et al., 1994). To assess the importance of the indirect climatic effect of aerosols, it is necessary to relate mass emissions of aerosols and their precursors (such as SO_2) to aerosol number concentrations, to CCN concentrations (not all particles act as CCN), to CDNCs, and finally to cloud optical properties. An important link in this chain is the CCN properties of anthropogenic aerosols. Whereas the CCN properties of inorganic sulfate aerosols are reasonably well characterized, those of organic particles emitted from combustion processes are far less well understood. There exist neither adequate laboratory studies nor field measurements of the CCN properties of combustion-derived carbonaceous aerosols to allow one to predict the effect of such aerosols on cloud droplet activation.

Ship tracks provide an ideal environment for studying the effects of anthropogenic emissions on marine stratocumulus. The present work provides an initial investigation of the fate of organic aerosols emitted from ship exhaust in the marine stratocumulus layer. A major question is – to what extent can the well-known features of ship tracks be attributed to organic aerosols emitted in the combustion exhaust of ships?

Table 7.1: Previous measurements of polycyclic aromatic hydrocarbons, quinones, and ketones in ship and engine emissions, urban areas, and marine aerosol.

	Reported Concentrations (1)		Engine Emissions		
	Urban (Pasadena)	Marine (San Nicolas)	Fuel Oil Container Ship (3)	Gas Oil Barge (3)	Diesel Emissions (2)
	µg m-3	µg m-3	µg m-3	µg m-3	µg km-1
Polycyclic Aromatic Hydrocarbons					
anthracene	NR	<0.01	0.197	0.7	1.60
phenanthrene	NR	<0.01	8.77	20	12.20
flouranthene	0.13	<0.01	3.89	5.2	13.00
pyrene	0.17	<0.01	4.67	5.4	22.60
benzo[a]flourene	NR	<0.01	NR	NR	1.90
benzo[b]flourene	NR	<0.01	1.64	8.5	NR
benz[a]anthracene	0.25	<0.01	0.249	<0.009	3.60
chrysene	0.43	<0.01	2.572	1.6	9.90
triphenylene	0.43	<0.01	5.856	6	NR
benzo[a]pyrene	0.44	<0.01	0.058	0.03	1.30
benzo[k]fluoranthene	0.93	<0.01	<0.026	2.8	2.60
benzo[e]pyrene	1.20	<0.01	0.057	0.03	2.70
perylene	NR	<0.01	0.896	0.1	1.00
indeno[1,2,3-cd]pyrene	0.42	<0.01	0.183	<0.01	ND
benzo[ghi]perylene	4.43	<0.01	0.678	<0.01	1.60
dibenz[a,h]anthracene	NR	<0.01	1.569	<0.03	ND
Polycyclic Aromatic Ketones and Quinones					
9H-flouren-9-one (flourenone)	NR	<0.01	NR	NR	65.00
9,10-anthracenedione (anthraquinone)	NR	<0.01	NR	NR	23.50
9H-xanthen-9-one (xanthone)	NR	<0.01	NR	NR	2.70
7H-benz[de]anthracen-7-one	0.84	<0.01	NR	NR	5.60

NR - compound not resolved NQ - compound not quantified

(1) Diesel emission concentrations are reported from Rogge et al., 1993a.

(2) Pasadena ambient and San Nicolas Island ambient concen trations are reported from Rogge et al., 1993c.

(3) Marine vessel emissions are reported from Banisoleiman et al., 1994. Values reflect maximum measured during emission trials.

There is adequate evidence for the presence of an organic signature of combustion products in the aerosol phase of combustion emissions (Hildemann et al., 1989, 1991; Rogge et al., 1993a; Henderson et al., 1984; Banisoleiman et al., 1993; J. Tilman, private communication). Banisoleiman et al. (1994) report high concentrations of polycyclic aromatic hydrocarbons (PAHs) in the emissions of two fuel-oil powered ships (a ferry and a container ship) and of a gas-oil powered barge as illustrated in Table 7.1. Phenanthrene, fluoranthene, pyrene, triphenylene, chrysene, and benzo[b]fluorene appeared

in all samples in concentrations exceeding 1 μg m^{-3} (Banisoleiman et al., 1994). Trace amounts of benzo[g,h,i]perylene, dibenzo[a,h]anthracene, and indeno[1,2,3-c,d]pyrene were also reported. These authors estimate that the total worldwide emissions of aerosol-phase PAHs from marine vessels are between 66 and 466 metric tons (Banisoleiman et al., 1993). PAH signatures have been found in ambient urban and anthropogenically-influenced samples (Rogge et al., 1993c). As noted, the key question for climatic effects is to what extent the anthropogenic aerosol mass creates additional CCN so as to alter cloud reflective properties from those in the absence of such aerosols. Frisbie and Hudson (1993) and Hudson (1991) have, in one study, shown that anthropogenic aerosol increased the concentrations of efficient CCN.

Early efforts to speciate the organic fraction of urban aerosol were undertaken by Cronn et al. (1977), who developed a method for using high resolution mass spectrometry to identify individual organic compounds in the atmospheric aerosol. Duce et al. (1983) collected field samples of marine organic aerosol providing evidence that background oceanic sources contribute straight chain alkanes of 9 to 20 carbons, as well as organic acids. Few other species were found at levels exceeding 1 ng m^{-3} in the marine air samples (Duce and Gagosian, 1982; Duce et al., 1983; Schneider et al., 1983; Kawamura and Gagosian, 1987; Peltzer and Gagosian, 1987). Sicre et al. (1990) have used long-chain unsaturated ketones in aerosol particles as tracers for long range transport.

The data of Rogge et al. (1993c) provide an indication of the contrast in organic aerosols between background marine sources at San Nicholas Island 100 miles west of Los Angeles and urban sources at seven inland sites. The off-coast site showed straight chain alkanes in concentrations of up to 300 ng m^{-3}, consistent with earlier work (Duce et al., 1983), but most other species were below the detection limit for their method (Rogge et al., 1993c). The high PAH concentration and the large quantities of branched alkanes resulting in unresolved spectral peaks at Rubidoux, CA, and Pasadena, CA, contrast markedly with the low background concentration at the upwind island site, suggesting a characteristic signature for marine sources of low concentrations and straight-chain alkanes, compared to the urban PAH and branched alkane species. Examples of such anthropogenic PAH tracers are fluoranthene, pyrene, benz[a]anthracene, and benzo[e]pyrene, which were found to vary in concentration between 100 and 4000 ng m^{-3} at Downtown Los Angeles, but were below the PAH detection limit of 30 ng m^{-3} for the San Nicolas Island measurement (Rogge et al., 1993c). Grosjean's (1993) measurements of PAHs are consistent with these concentrations.

Recent studies of the total organic content of aerosol allow one to assess the lifetime of organic aerosols in the atmosphere, and consequently the range over which such compounds may be transported (Novakov and Penner, 1993). The observations of Novakov and Penner (1993) suggest that in regions downwind of major continental sources, organics can be a significant

fraction of the marine aerosol that serves as CCN. Chemical analysis of size-segregated particles showed that particles larger than 0.05 μm diameter are likely to be predominantly composed of sulfate and organics. Calculations of Novakov and Penner (1993) suggest that, on average, particles larger than 0.05 μm contain organic mass, and that at 0.5% supersaturation, those particles are active as CCN. Although their data set is limited and does not relate directly to marine stratus clouds (where supersaturations typically do not exceed 0.1%), their data indicate that, if the size of particles activated at 0.5% supersaturation is assumed to be 0.05 μm, then the mass of organics present at and above this size is required to account for the number of CCN measured. Simultaneous quantification of organic and sulfate mass on shorter time scales as well as more detailed size and time-resolved data would, however, be needed to identify whether the organics are present in an internal or an external aerosol mixture. In addition, to establish the role of organics in marine CCN, one needs the CCN activation spectrum for the organic aerosol, or to analyze the composition of cloud droplet residuals (the particles remaining after cloud drops have been evaporated).

Analysis of continental fog droplet residual composition was undertaken in the Po Valley study by employing a counterflow virtual impactor (CVI) (Ogren et al., 1985; Noone et al., 1988; Noone et al., 1992). Data suggested a chemical difference in the residual composition of droplets, which would be consistent with an external mixture of hydrophobic and hygroscopic particle

populations. However, their data are not conclusive about the degree to which these two chemical characteristics are the result of an internal versus an external mixture. Moreover, the composition of the droplet residuals was consistent with the hygroscopic, or soluble, population. In addition to the highly polluted anthropogenic nature of the Po Valley aerosol, the authors note that the thermodynamic conditions of the continental fogs they studied may not be representative of the conditions found in convective clouds and may lead to activation of far fewer particles (i.e., as few as 50% at ca. 0.5 μm diameter) than has been found in convective clouds.

In experiments at Kleiner Feldberg (Germany), Hallberg et al. (1992) obtained results similar to those at Po Valley with chemical analysis of impactor samples by demonstrating that the insoluble fraction (elemental carbon) will preferentially remain in the interstitial aerosol rather than activating to cloud droplets.

Gillani et al. (1995) have provided evidence that the role of anthropogenic aerosol in continental stratiform clouds was primarily determined by the number concentration of accumulation-mode particles, rather than by the mass fraction of soluble material in those particles. These authors concluded that the particles they sampled contained sufficient water-soluble mass to make other factors (particle size and thermodynamic conditions) dominant in the activation process. Their findings are consistent with those of Martin et al. (1994) in predicting that the cloud droplet number concen-

trations are largely determined by the boundary layer aerosol concentration and are independent of the chemical composition of the aerosol. Hudson et al. (1991) and Hallett et al. (1989) have demonstrated with laboratory and field measurements that a larger fraction of smoke aerosol particles can serve as CCN than of jet-fuel produced aerosols.

The role of chemical composition in determining the hygroscopic properties of an aerosol has been well characterized for soluble inorganic species (Pruppacher and Klett, 1978; Tang and Munkelwitz, 1994). However, for many organic species little is known about their impact on nuclei activation to droplets in actual supersaturated environments. Hansson et al. (1990) have investigated the effect of hydrophobic organic coatings on particles consisting of aqueous salt solutions on the growth of particles. They measured these effects for tetracosane, octadecane, and dioctyl phthalate by measuring the change in the particle's growth by water uptake for a specified change in relative humidity as a function of the thickness of the coating applied to the particles. For all of the hydrocarbons studied, they found a decrease of 0.2% in this hygroscopic growth per nm of hydrophobic coating applied to NaCl(aq) particles and 0.6% for $(NH_4)_2SO_{4(aq)}$ particles. Conversely, Andrews and Larson (1993) have shown that an organic coating of a water-soluble surfactant can increase the relative mass uptake of water at 90% relative humidity by 20% over that of uncoated black carbon particles. Wyslouzil et al. (1994) have demonstrated that a sulfate layer effectively increases

the hygroscopic properties of hydrophobic black carbon particles (which do not take up water at 80% relative humidity), allowing a mass increase of 30% of the particle mass at 80% relative humidity.

Saxena and Hildemann (1996) have estimated the solubilities of a number of organic aerosol species. Shulman et al. (1995) have suggested that particles containing partially soluble compounds such as carboxylic acids mixed with soluble components such as ammonium sulfate can serve as CCN, although the diameter at which the particle activates is predicted to be higher than that of pure ammonium sulfate. Their work suggests a need for further characterization of the solubilities of organics in other classes.

7.1 Airborne Sampling of Interstitial and Cloud Droplet Residual Aerosol

The Monterey Area Ship Tracks (MAST) Experiment, conducted in June 1994, provided an opportunity to characterize and compare organic aerosol species, both in interstitial aerosol and droplet residual particles, present in ambient air masses as well as in ship track cloud lines. Samples of interstitial aerosol and cloud droplet residual particles were collected aboard the University of Washington C131A aircraft. The 12 flights yielded 35 interstitial and below cloud aerosol samples, 17 cloud droplet residual samples, and 24 blanks. Samples were subsequently analyzed to identify the organic species

present. The collection and analysis method was designed to allow the identification of the maximum number of organic species from the limited particle samples possible from aircraft sampling of track features.

7.1.1 Sample Collection Protocol

Samples were collected on quartz fiber filters (Tissuquartz 2500-QAOT, Pallflex Corp., Putnam, CT) on two types of filter holders. Submicron aerosol filter holders employing quartz substrates of 135 mm diameter were constructed of anodized aluminum. The filter holders are sealed by an O-ring compressed by tightening a screw opposing a hinged support. The filter substrate rests on a support consisting of stainless steel wire mesh overlaying perforated aluminum supports. A Teflon ring is used to hold the quartz-filter substrate in place. The flow rate of air over these filters is 100 L min^{-1}.

A counterflow virtual impactor (CVI) was used to sample cloud droplets while the aircraft was in cloud during the experiment (Ogren et al., 1985; Noone et al., 1988). This device uses a second opposing air stream to separate cloud droplets from the interstitial aerosol. The cloud droplets were then evaporated and sized in an optical particle counter (OPC). The cloud droplet residual samples from the CVI inlet were collected in stainless steel filter holders supporting 25-mm diameter quartz substrates (Gelman Sciences) (Ogren et al., 1985; Noone et al., 1988).

Prior to sampling, all quartz filters were baked overnight above 550°C

(Rogge et al., 1993) to remove background blank contamination. The filters were wrapped in foil and placed in petri dishes for baking. After cooling, the petri dishes were sealed with Teflon tape until use (up to 60 days).

Substrates for both submicron aerosol and droplet residuals were installed in and removed from the filter holders in a glove box at the field site in a container van serving as a laboratory. The glove box was lined with Teflon and supplied with a continuous stream of air stripped of water and organic vapor-phase constituents. Aerosol was removed from the clean air stream by a total particle filter. Sample holders were cleaned between consecutive samples with methanol and allowed to dry in the glove box. Exposed samples were stored in cleaned glass vials (Protocol B for VOC Sampling, U.S. Environmental Protection Agency) with Teflon lids (sealed externally with Teflon tape) that were then frozen for storage (at or below 0°C). Samples were transported from the field site (Monterey, CA) to the analysis center (Bank of America Environmental Analysis Center, California Institute of Technology, Pasadena, CA) in insulated containers packed with dry ice. Samples were then stored frozen (below 0°C) for up to 6 months before analysis.

Each sample was collected with an in-field blank sample so that field and storage contamination could be quantified. For each flight, one of the six parallel filter holders was reserved as a blank. Samples stored in the glove box were also taken daily to check the cleanliness of the glove box. Blanks and samples were analyzed by the identical procedure, and the masses of

the compounds present in the blank were subtracted from the masses in the samples, and the resulting mass was divided by the volume of air filtered to give the ambient concentration for all values reported here.

7.1.2 Extraction and Identification Procedure

Particulate matter was extracted from the filters using supercritical fluid extraction (SFE). The extraction uses high-purity CO_2 (SFC/SFE-grade CO_2 with 2000 psi Helium, Air Products, Allentown, PA) compressed in an extraction module equipped with a pump for adding solvent modifiers (model Prepmaster and MPA1, Suprex Corp., Pittsburgh, PA). The 135-mm filters were folded and rolled into a 10-ml cylindrical extraction vessel, 10 cm long and 1 cm diameter. The 25-mm filters were extracted using a 0.5-ml extraction chamber.

The SFE was connected to the gas chromatograph (GC) via a heated transfer line (model 050-020, Suprex Corp.). At the GC inlet a cryotrap (Hewlett-Packard) was installed to concentrate the sample transferred from the SFE. The heated transfer line consists of 1/16" flexible stainless steel tubing in a heating jacket regulated by a proportional temperature controller set to 290°C. Separation of chemical species was performed in a gas chromatograph (GC, model 5890, Hewlett-Packard, Wilmington, DE) using one of two columns. The first, designated HP5MS (model HP-5MS, Hewlett-Packard), optimizes resolution with low carrier gas bleed at temperatures up to 320°C.

Its packing of 5% Phenyl Methyl Siloxane is efficient for separating nonpolar and some polar compounds. The second DB1701 (model DB-1701, J and W Scientific, Folsom, CA) column has a wider bore that is packed with 14% Cyanopropylphenyl Methylpolysiloxane. The HP5MS column was conditioned for 12 hours at 325°C before use, and the DB1701 at 280°C. Both columns were characterized for the following procedures with a suite of over 50 standards, as summarized in Table 7.2.

The extraction procedure begins with raising the sample pressure to 300 atm and the temperature to 150°C. After a 50-min equilibration time, the pressure is ramped to 450 atm over 10 min while maintaining constant temperature. A valve is then opened for 10 min to allow the carrier CO_2 and the volatilized aerosol species to flow through the heated transfer line into the GC inlet, where species solidifying at -40°C are held as the CO_2 carrier gas continues through to the GC vent. The SFE vessel is then equilibrated for an additional 10 min before another transfer step of 20 min. During the transfer phases a modifier solution of 10% acetic acid in methanol is added to the CO_2 carrier gas at a fixed volumetric rate of 5%.

At the end of the extraction, the HP5MS GC column is then heated in four stages: (1) from -45°C to 35°C at 20°C min^{-1}, (2) remaining at 35°C for an additional 5 min, (3) from 35°C to 320°C at a uniform heating rate of 2°C min^{-1}, and (4) constant at 320°C for 5 min. The procedure followed for the DB1701 column is similar: (1) from -45°C to 35°C at 20°C min^{-1},

Table 7.2: Characterization of detection limits by SFE/GC-MS for polycyclic aromatic hydrocarbon, quinone, and ketone standards used.

	Carbon Index	Major Mass Spectral Peaks M/Z	Retention Time DB-1701 min	Retention Time HP-5MS min	Detection Limit DB-1701 µg	Detection Limit HP-5MS µg
Polycyclic Aromatic Hydrocarbons						
anthracene	C-14	178, 89, 76	39.53	69.74	0.173	0.023
phenanthrene	C-14	178, 89, 76	39.53	69.30	NQ	0.028
flouranthene	C-16	202, 101, 87	53.00	82.42	0.031	0.023
pyrene	C-16	202, 101, 88	54.97	84.54	0.033	0.028
benzo[a]flourene	C-17	216, 108, 187	59.24	88.99	0.068	0.152
benzo[b]flourene	C-17	216, 108,189	60.01	89.73	0.078	0.180
benz[a]anthracene	C-18	228, 114, 164	69.39	98.33	0.036	0.039
chrysene (1)	C-18	228, 114, 202	69.69	98.75	0.029	0.073
triphenylene (1)	C-18	228, 114, 202	69.69	98.75	NQ	NQ
benzo[a]pyrene (2)	C-20	252, 126, 113	81.38	109.61	0.058	0.063
benzo[k]fluoranthene (2)	C-20	252, 126, 112	81.05	109.61	NQ	NQ
benzo[e]pyrene	C-20	252, 126, 113	84.79	NR	0.070	0.363
perylene	C-20	252, 126, 113	83.42	111.99	0.029	0.328
indeno[1,2,3-cd]pyrene	C-22	276, 138, 125	94.21	122.32	0.034	0.368
benzo[ghi]perylene	C-22	276, 138, 125	95.93	124.14	0.032	0.305
dibenz[a,h]anthracene	C-22	278, 139, 125	95.03	122.98	0.034	1.124
Polycyclic Aromatic Ketones and Quinones						
9H-flouren-9-one (flourenone)	C-13	180, 152, 126	39.06	67.23	0.124	0.046
9,10-anthracenedione (anthraquinone)	C-14	180, 208, 152	50.34	78.26	0.031	0.103
9H-xanthen-9-one (xanthone)	C-13	196, 168, 139	44.84	73.37	0.072	0.145
7H-benz[de]anthracen-7-one	C-17	230, 202, 101	72.89	99.94	0.063	0.412

NR - compound not resolved NQ - compound not quantified

(1) Since the chromatographic elution peaks of chrysene and triphenylene were not resolved, their concentrations are reported together.

(2) Since the chromatographic elution peaks of benz[a]pyrene and benzo[k]fluoranthene were not resolved, their concentrations are reported together.

(3) Diesel emission concentrations are reported from Rogge et al., 1993a.

(2) remaining at 105°C for an additional 5 min, (3) from 35°C to 280°C at a uniform heating rate of 2°C min^{-1}, and (4) constant at 280°C for 5 min.

Compounds separated in the GC are detected in a quadropole mass spectrometer (MS) using electron impact ionization (model 5989A, Hewlett-Packard). Concentrations are calculated both as a fraction relative to the total ions detected in each sample and by reference to external standards for the compounds noted in Table 7.1. The external standards were purchased from Accustandard (New Haven, CT). The detection limit for the standards studied varied from 10 ng to 1μg. Hence, the effective detection limit varies in terms of atmospheric concentration. The blanks collected have been taken into account by subtracting the concentration of the corresponding blank for each sample.

7.2 Organic Species in Marine Stratus

Chemical analysis of species from aircraft sampling of ship tracks is constrained by the limited flow volumes, the short sampling times, and the low flow rates available in flight. Identifying localized spatial characteristics associated with ship tracks requires a protocol optimized for obtaining the best chemical identification possible with as little as 1 m^3 air. As a result of the constraints associated with the samples collected during MAST, the primary focus in the chemical analysis is the relative differences between the compositions of interstitial and residual aerosol. This information pro-

vides a characteristic signature for the air masses and track features sampled. Compiling the results of the MAST samples, the organic species illustrate the variability in the background air masses sampled during the experiment. The eight ships sampled serve to characterize organic aerosol species from typical emissions of ships with diesel, gas and steam turbine engines.

The MAST Experiment involved the University of Washington C131, the United Kingdom Meteorological Research Flight C130, the Research Vessel *Glorita*, the Naval Research Laboratory research airship, several naval and commercial vessels, and intensive satellite observations, measuring cloud and boundary layer charateristics in the stratus off the coast of Monterey, CA, in June 1994 (Durkee et al., 1996). Aerosol physics and chemistry measurements aboard the C131 are reported elsewhere (Ferek et al., 1996; Noone et al., 1996a,b; Johnson et al., 1996). The methodology used for interstitial aerosol samples for organic speciation required collecting three bag samples of air for each composite measurement of the aerosol in and below cloud. A continuous total condensation nuclei counter (CNC) measurement was used to trigger manually bag collection in flight. Below-cloud measurements include background (bkgd) samples (with CN concentrations near the average observed in the air mass) and plume samples (in sight of the ship's stack with CN concentrations roughly 100 times higher than the ambient). In-cloud measurements included interstitial aerosol in track (high droplet and CN) and ambient (background levels of droplets and CN), as well as cloud

droplet residuals in track and ambient. The CVI samples were collected continuously during all track intersections and during ambient cloud transits, also using CN concentrations to distinguish track effluents.

To identify anthropogenic effects, we use PAHs as tracers for combustion emissions. The presence of PAHs as well as polycyclic aromatic ketones and quinones (PAKs and PAQs, respectively) in the particulate phase of emissions of combustion of petroleum products has been well-documented (Rogge et al., 1993a; Banisoleiman et al., 1994). There is evidence that the concentrations of these compounds in the background marine atmosphere are significantly lower than those expected in regions impacted by anthropogenic emissions (Hildemann et al., 1991; Rogge et al., 1993c).

Ship emissions result in increased concentrations of particulate PAHs and PAKs in the marine aerosol. For the samples collected, as summarized in Table 7.3, more PAHs, PAKs and PAQs were identified in plume and track samples than in any of the background below or in-cloud samples. These results are summarized by the frequency distribution of the number of samples in which each of the compounds were detected in Fig. 7.1. This figure illustrates the number of samples in which each compound noted was detected. Parts a and b show the cloud droplet residuals samples in and out of track, c and d, the interstitial samples, and parts e and f, the out of cloud aerosol samples. The out-of-cloud samples (parts e and f) illustrate clearly the difference between plume and background aerosol, with higher

Table 7.3: Summary of samples analyzed presented as a matrix of sample type vs. case day (total numbers of samples in and below cloud, and in and out of tracks and plumes).

Sample Date	JDT	Droplet Residuals		In-Cloud Interstitial		Boundary Layer Aerosol	
		a) In track	b) Ambient	c) In track	d) Ambient	e) In plume	f) Background
6/1/94	152	1	1	0	0	1	1
6/8/94	159	1	1	0	0	1	2
6/9/94	160	0	0	0	0	1	0
6/11/94	162	0	0	1	1	0	0
6/12/94	163	1	1	1	0	1	1
6/15/94	166	0	0	0	0	1	1
6/17/94	168	0	1	0	0	0	0
6/21/94	172	1	1	1	1	1	1
6/27/94	178	1	1	1	1	2	1
6/28/94	179	1	1	0	1	1	1
6/29/94	180	1	1	1	2	1	1
6/30/94	181	1	1	1	1	2	1
Totals		8	9	6	7	12	10

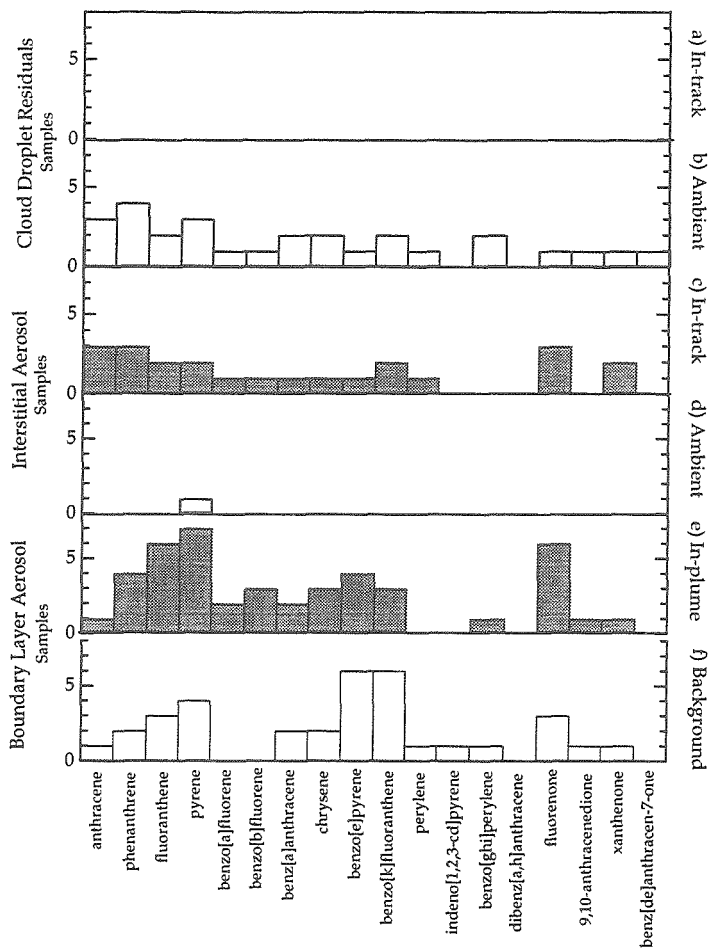

Figure 7.1: Distribution of compounds detected for all samples (PAHs, PAQs, and PAKs) by class: (a) track residual droplets (in cloud), (b) ambient residual droplets (in cloud, out of track), (c) track interstitial (in cloud), (d) ambient interstitial (in cloud, not in track), (e) plume aerosol (below cloud), and (f) background boundary layer aerosol (below cloud, not in exhaust plume). All aerosol samples were collected with a 2 μm effective upper cutoff using a 10 m^3 bag sampler. All droplet samples were collected from a CVI inlet.

frequencies of detection of fluorenone, pyrene, fluoranthene, phenanthrene, benzo[a]fluorene, and benzo[b]fluorene in plume exhaust samples than in the background samples. The results illustrated in part a are inconclusive since all of the in-track cloud droplet residual samples were below detection. However, the background aerosol also shows clear indications of anthropogenic influence from combustion emissions in the background boundary layer sampled air as well, particularly in the concentrations of benzo[e]pyrene and benzo[k]fluoranthene (or benzo[a]pyrene). This influence may be a result of continental sources advected over the ocean, or of exhaust from ships previously encountered by the air mass. Both of these explanations are consistent with supporting physical measurements (satellite retrievals, aerosol size distributions, droplet concentrations) during the MAST Experiment (Durkee et al., 1996; Johnson et al., 1996; Ferek et al., 1996; Noone et al., 1996).

The interstitial aerosol (parts c and d of Fig. 7.1) also shows elevated levels of PAHs and PAKs in track areas as compared to the ambient (out of track) interstitial aerosols. In fact, in the ambient background cloud, only one PAH was detected in one sample (pyrene). In track, the interstitial aerosol showed detectable amounts of most PAHs. As noted, the cloud droplet residual in-track samples (part a of Fig. 7.1) were inconclusive for determining the concentrations of PAHs in the in-cloud droplets. Since the CVI samples were collected at a constant flow rate (instead of the bag sampling method used for the interstitial aerosols), the sample volumes collected were, in general,

too small to yield detectable levels of compounds. In addition, the decrease in mean droplet size in several of the tracks sampled may have sufficiently degraded the collection efficiency of the CVI inlet to also limit collection of droplets (Radke et al., 1989; Johnson et al., 1996). However, the presence of PAHs in the ambient cloud droplets is consistent with the role of PAHs contributing to particles that act as CCN at the supersaturations of convective marine clouds.

7.2.1 Variability of Background Conditions

To assess the influence of ship emissions, it is helpful to first understand the variability in the background boundary layer particulate composition and the cloud droplet and aerosol compositions. Figure 7.2 describes the ambient conditions encountered during the MAST experiment for which samples were collected. The ambient values of anthracene, benzo[e]pyerene, and benzo[k]fluoranthene over 10 ng m^{-3} suggest that at least some of the ambient samples included anthropogenic aerosol sources, since the data of Rogge et al. (1993b) suggest that "clean" marine air as measured at San Nicholas Island are under this level, whereas urban areas are likely to have much higher concentrations (typically between 100 and 1000 ng m^{-3}). The average suggests background levels that are consistent with anthropogenically influenced air masses, as suggested by the values reported in Table 7.1. However, the variability in samples, illustrated by the large standard deviations for in-

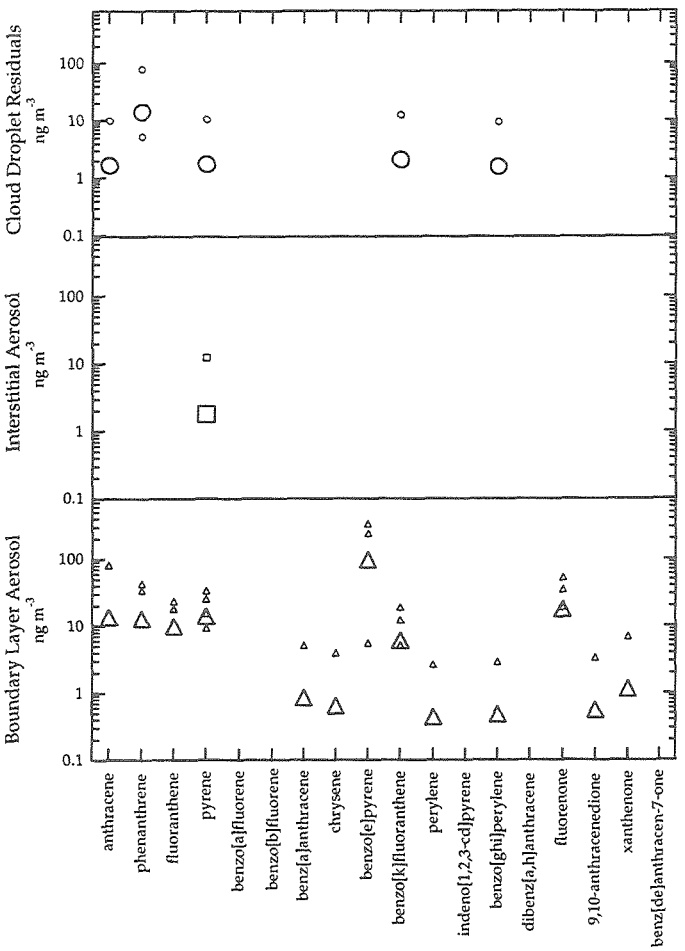

Figure 7.2: Variability in and average concentrations of PAHs, PAQs, and PAKs in the background and ambient conditions during MAST for JDT 163, 168, 172, 178, 179, 180, and 181. Samples collected in cloud include droplet residuals and interstitial aerosol and were collected in regions without tracks. Below cloud aerosol also is representative of background boundary layer aerosol. Large symbols represent average concentrations, small symbols represent individual measurement from different sampling days. Measurements below detection capabilities are not shown on the graph and are averaged as 0 μg m^{-3}.

dividual compound in Fig. 7.2, accounts for the fact that several samples included concentrations below the detection limit.

Although the variability from day to day during the experiment complicates the interpretation of these average concentrations, accounting for the variability is important to illustrate the trends consistent throughout the data set. With the exception of one sample showing a very low concentration of pyrene (2 ng m^{-3}) on JDT 180, all of the interstitial aerosol concentrations were below detection for PAHs, PAKs and PAQs. By contrast, both the out-of-cloud aerosol and the in-cloud droplet residuals showed PAHs and PAKs. This observation is consistent with the majority of the PAHs and PAKs in the submicron aerosol being present in the fraction of aerosol that activated in the clouds observed here, and hence served as CCN.

All PAHs and PAKs detected in the boundary layer aerosol were also detected in the cloud droplet residuals at equal, or greater concentrations, both calculated on a basis of a cubic meter of air. The greater-than-ambient concentrations in the cloud droplet residuals may result, in part, from contamination of these out-of-track samples with in-track air during the sampling process since the CVI samples were manually switched based on the total aerosol concentration.

7.2.2 Ship Track and Plume Characteristics

Concentrations of PAHs and PAKs in ship emissions vary with the type of ship, and are thought to be influenced by the engine size, condition, and speed, ship tonnage, and fuel type and composition (Banisoleiman et al., 1994). Consequently, the emissions sampled during the MAST Experiment are expected to include a variety of source compositions resulting in different PAH/PAK signatures. In addition, since bag samples of submicron aerosol were taken at different distances from the ship and in boundary layers of varying heights, the concentrations in the samples will have been influenced by different amounts of dilution. Figure 7.3 illustrates the variation found in the aerosol compositions in plumes and tracks sampled during MAST. For almost all PAHs, the range encompasses a span from over 100 ng m^{-3} to below the detection limit.

In the out-of-cloud aerosol samples, four compounds are sufficiently concentrated in the plumes to exceed the ambient variability among all of the samples to result in measurable differences in Fig. 7.3. Those four PAH/PAK tracers are pyrene, benzo[a]fluorene, benzo[b]fluorene and 9,10-anthracenedione.

In the cloud interstitial aerosol, there is a much clearer distinction than in the out-of-cloud aerosol between the in-track particles, and the out-of-track particles, where there were no significant concentrations of PAHs, PAKs, or PAQs detected. The strongest signals in the in-track interstitial aerosol

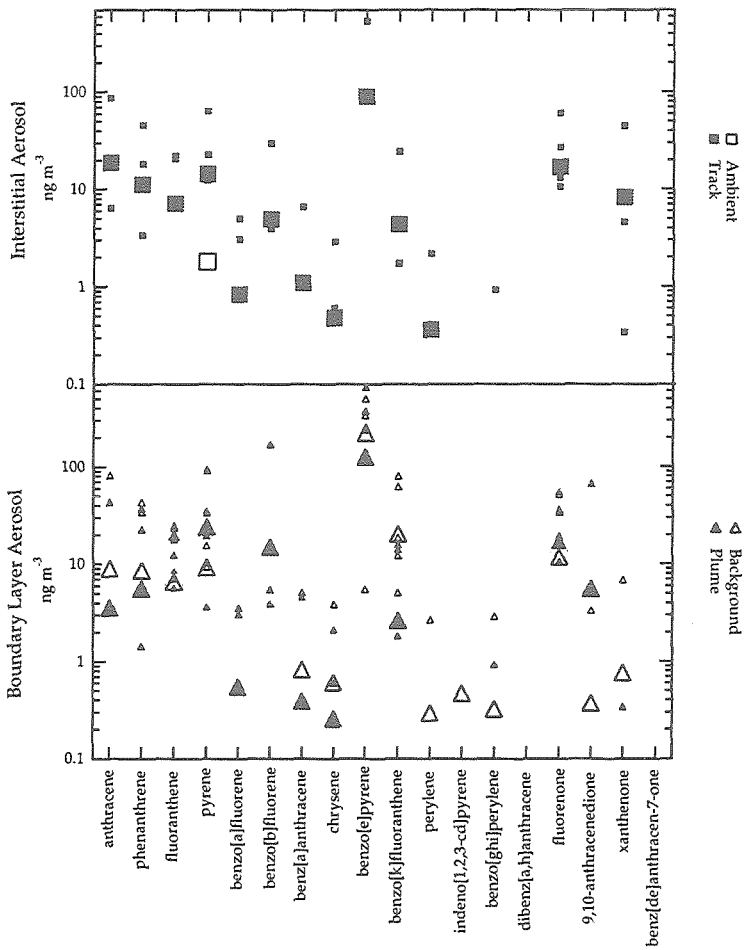

Figure 7.3: Variability in and average concentrations of PAHs, PAQs and PAKs detected in aerosol samples collected for JDT 159, 160, 162, 163, 168, 172, 178, 179, 180, and 181. The graph illustrates data collected in and out of track of both interstitial aerosol and boundary layer aerosol. Large symbols represent average concentrations, and small symbols represent individual measurement from different sampling days. Measurements below detection capabilities are not shown on the graph and are averaged as 0 μg m^{-3}.

shown in Fig. 7.3 include five compounds (anthracene, phenanthrene, pyrene, benzo[e]pyrene, and fluorenone) with concentrations over 10 ng m^{-3}. In general, one would expect the concentrations of plume compounds to exceed those observed in the in-track interstitial aerosol, since the plume is closer to the ship and hence would be more concentrated. However, since the spatial extent of the plumes, sampled at a distance of 100-300 m behind the ship, was smaller and less predictable in-flight, the in-plume bag samples were more likely to consist of several seconds (out of the 10 s required to fill the bag) of air from the edges of the plume, where the emissions were dilute. By contrast, the high in-track concentrations (at 1 to 3 h after emission) result from the uniform and predictable boundaries of well-mixed high aerosol number concentrations, which characterize the length of ship tracks (Johnson et al., 1996).

A notable feature of Fig. 7.3 is the absence of PAHs in the in-cloud interstitial out-of-track aerosol, despite their presence in the below cloud aerosol. There are, however, numerous PAHs in the in-cloud, out-of-track droplet residuals. As discussed above, the absence of PAHs in the ambient interstitial aerosol indicates that organics exist in aerosol below cloud that serve as CCN and hence partition to the droplet phase, rather than the interstitial aerosol. This is supported by the presence of PAHs in the ambient droplet residual samples collected by the CVI (Fig. 7.2).

In track, as shown in Fig. 7.3, there remain significant PAHs in the inter-

stitial aerosol (and the residual samples are inconclusive due to small sample volumes), suggesting two possibilities. The first would be to conclude that in ship tracks the particles containing PAHs do not serve as CCN, at least during the initial phases of track formation (all samples considered here are for tracks younger than 3 h from stack emission). However, this explanation is inconsistent with the cloud droplet residual information showing the presence of PAHs in Fig. 7.2. Hence, the alternative interpretation of these data is more probable, namely that some of the PAH-laden particles have activated in cloud to form droplets, but that CCN are sufficiently abundant that many such particles remain unactivated in the interstitial aerosol. This phenomenon has been observed in anthropogenically-influenced air by Gillani et al. (1995), who note that at sufficiently high accumulation mode particle concentrations, the activation process becomes water-limited and decreases the effective supersaturation in cloud. This latter interpretation is also supported by submicron size distribution measurements taken aboard the C131 that show high concentrations of particles larger than 0.1 μm, over 500 cm^{-3} in many cases, many of which remain in the interstitial phase in cloud (Noone et al., 1996b; Johnson et al., 1996).

7.2.3 Case Studies from MAST

Because of the complications introduced by the day-to-day variability in both the background and the ship sources in interpreting the distribution of PAHs

in the boundary layer, we limit our discussion here to samples collected on two specific days during the MAST Experiment. During both of these days (June 12 and 27, 1994), the C131 sampled in cloud-topped boundary layers where an unbroken cloud layer persisted throughout the flight.

June 12 (JDT 163)

During this flight, two diesel-powered vessels – a pusher tug (*Moku Pahu*) and a naval salvage ship (*Safeguard*) – were sampled (Gasparovic, 1995). The clouds were about 300 m thick with the base at 200 m above sea level and contained droplet concentrations of about 40 cm^{-3}. Two distinct tracks were observed.

Figure 7.4 shows the PAHs, PAKs and PAQs detected in the five samples collected on this flight: track and ambient cloud droplet residuals, track interstitial aerosol, below-cloud plume and background aerosol. The background below-cloud concentrations show that many PAHs and PAKs were present in the boundary layer aerosol in the air mass surrounding the ship. For all of the compounds for which there were detectable amounts of PAH in the background aerosol, those concentrations were greater than or equal to those in the plume. However, the differences in these concentrations were not large enough to exceed both the detection uncertainty and the possibility for contamination of background samples by plume. The background concentrations of anthracene, phenanthrene, and pyrene were between 10 and 100 ng m^{-3}

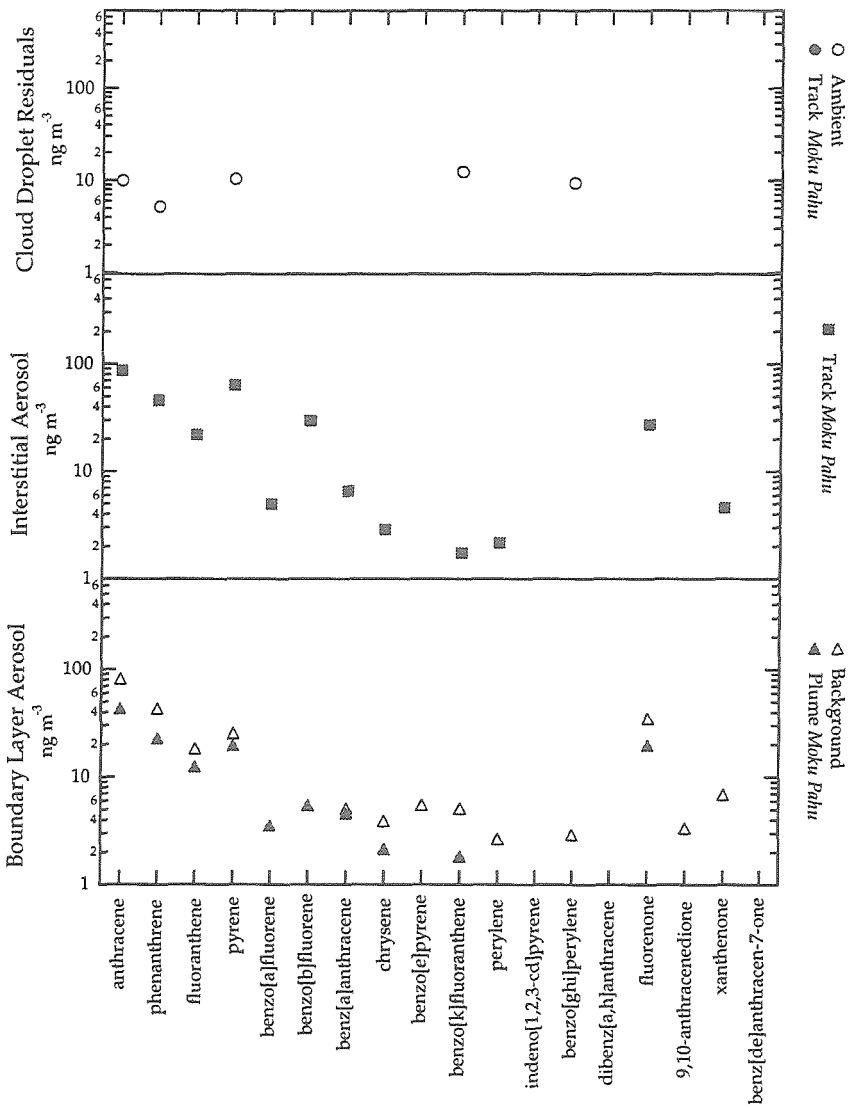

Figure 7.4: Case study for MAST study day 163 (June 12, 1994), illustrating the concentrations of PAHs, PAQs, and PAKs detected in and out of track and plumes, in and below cloud. Samples collected in cloud include droplet residuals and interstitial aerosol and were collected in regions without tracks.

in both the background and the plume sample. In this case the difference between the background and plume concentrations showed few qualitative differences. The track interstitial aerosol showed similar concentrations. The residual track measurement yielded no compounds above the detection limit because of the small sample volume (0.12 m^3), but the ambient sample indicated the presence of anthracene, phenanthrene, benzo[k]fluoranthene (or benzo[a]pyrene), and benzo[ghi]perylene. The concentrations of these compounds in the droplet residuals were, however, between 6 and 20 ng m^{-3}, significantly less than in the boundary layer aerosol. This result suggests that some of the background PAHs were in particles that did activate to form droplets in the clouds sampled.

June 27 (JDT 178)

On this day, the track and plume of the container ship *Tai He* were sampled, as well as the plume of the naval landing ship *USS Mount Vernon.* The *Tai He* was powered by a 6-cylinder diesel engine and the *Mount Vernon* by a steam turbine (Gasparovic, 1995). Cloud base in the sampled region was at 250 m, cloud tops at over 400 m, with unbroken stratus for most of the sampling period. Droplet concentrations were above 150 cm^{-3}. The high background particle and droplet concentrations showed anthropogenic influence.

Although the background air on Flight 1646 also indicated the presence

of some combustion aerosols, the in-track and plume concentrations were significantly higher than those in the surrounding air. Figure 7.5 shows the data from the six samples collected on this day. The ambient interstitial concentrations, most of the ambient droplet residual concentrations and the track residual concentrations were below the detection limits. Fluoranthene is present in detectable amounts in both plume samples. In addition, the differences in the two plume samples suggest the emissions of this steam turbine engine differed significantly from that of the diesel *Tai He*. Specifically, the *Tai He* showed much higher levels of phenanthrene, benzo[b]fluorene, and 9,10-anthracenedione.

7.3 Partitioning of PAHs Between Cloud Droplets and Interstitial Aerosol

The activation of aerosol particles to cloud droplets is determined both by the thermodynamic conditions of the forming cloud (supersaturation and updraft velocity) and the size and composition of the aerosol particles (Pruppacher and Klett, 1978). Identifying which particles will activate to droplets at prescribed supersaturation conditions is important to assess the radiative impact of different aerosol sources. The solubilities of the components present in the aerosol are important in determining a particle's ability to serve as a CCN: the higher the concentration of soluble components, the lower the

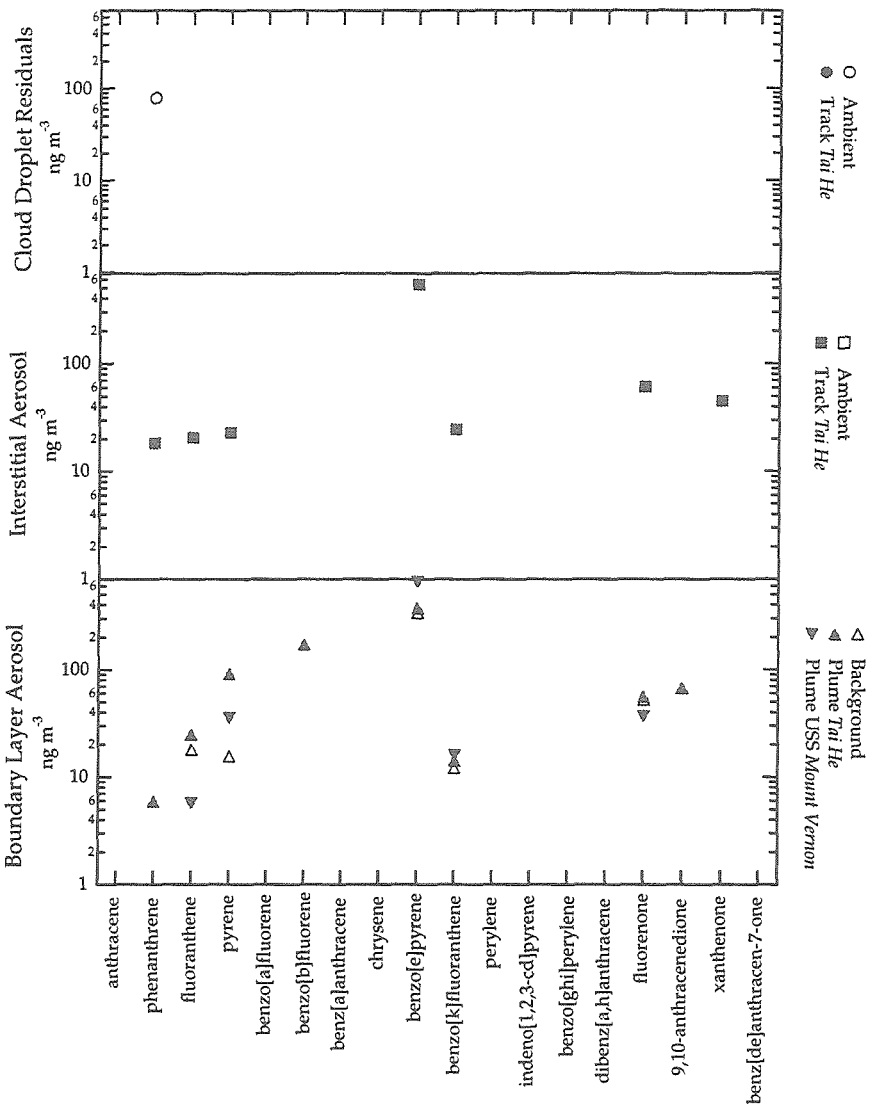

Figure 7.5: Case study for MAST study day 178 (June 27, 1994), illustrating the concentrations of PAHs, PAQs, and PAKs detected in and out of track and plumes, in and below cloud. Two plume samples were collected on this day, one from the *USS Mount Vernon* and the other from the *Tai He*.

supersaturation at which a particle of a given size will activate (Pruppacher and Klett, 1978). Investigations of the uptake of water on insoluble black carbon has shown that such insoluble particles do not serve as CCN (Hudson, 1993). If the insoluble particles were coated with a soluble layer, however, the uptake of water can increase (Andrews and Larson, 1991; Wyslouzil et al., 1994).

The water solubilities of several of the PAHs, PAKs and PAQs studied here are listed in Table 7.4. Values for all solubilities are less than 0.0001 M at both 293 K and 300 K. The solubilities of these compounds in salt solutions is uncharacterized, but is also likely to be low.

Phenanthrene has the highest solubility of the compounds reported in Table 7.4. Figure 7.1 illustrates that it was detected in 5 out of 9 of the ambient cloud droplet residual samples, even though only 2 of the 10 background out-of-cloud aerosol samples showed detectable concentrations. This trend suggests that phenanthrene has a higher probability of being in particles that served as CCN than the other components studied. The frequency that a compound (i) will activate to a cloud droplet can be estimated by comparing the frequency a compound is detected in cloud P^i_{cloud} to the frequency a compound was detected in the out-of-cloud aerosol P^i_{aerosol}, where in both cases the frequency from Fig. 7.1 has been normalized by the total number of samples in Table 7.3 to give the two detection probabilities. The

Table 7.4: Water solubilities reported for polycyclic aromatic hydrocarbons (Seidell and Linke, 1952).

	Molecular Weight	Solubility (1,2) at 300K	at 293K
	amu	M	M
Polycyclic Aromatic Hydrocarbons			
anthracene	178.1	4.21E-07	5.00E-07
phenanthrene	178.1	8.98E-06	1.50E-05
flouranthene	202.1	NV	NV
pyrene	202.1	8.16E-07	1.00E-06
benzo[a]flourene	216.1	NV	NV
benzo[b]flourene	216.1	NV	NV
benz[a]anthracene	228.1	4.82E-08	NV
chrysene	228.1	6.58E-09	3.40E-06
triphenylene	228.1	1.67E-07	NV
benzo[a]pyrene	252.1	NV	NV
benzo[k]fluoranthene	252.1	NV	NV
benzo[e]pyrene	252.1	1.59E-08	2.40E-08
perylene	252.1	1.98E-09	NV

NV - no values reported for this compound

(1) Solubilities are reported from Seidell and Linke, 1952. Results at 300 K were determined by nephelometric method.

(2) Solubilities are reported from Seidell and Linke, 1952. Results at 293 K were determined by fluorimetrically.

resulting ratio,

$$k^i_{\text{act}} = \frac{P^i_{\text{cloud}}}{P^i_{\text{aerosol}}}, \tag{7.1}$$

then serves as an activation index for each compound. The activation index for phenanthrene is 2.8.

The lowest solubility reported is for benzo[e]pyrene of 2.40 x 10^{-8} M. Benzo[e]pyrene was detected in 6 of the 10 background out-of-cloud aerosol samples, but only 3 of the 9 ambient droplet residual samples contained detectable amounts. The activation index in this case would be only 0.4.

Figure 7.6 compares the activation frequencies calculated from the MAST ambient data set with the reported water solubilities. The activation frequencies are generally higher for the higher water solubilities, and lower for the lower solubilities. This correspondence suggests that water solubility, and associated properties such as solubility in salt solutions, is related to the ability of particles to serve as CCN. However, it also provides a clear indication that insoluble compounds may be components in CCN.

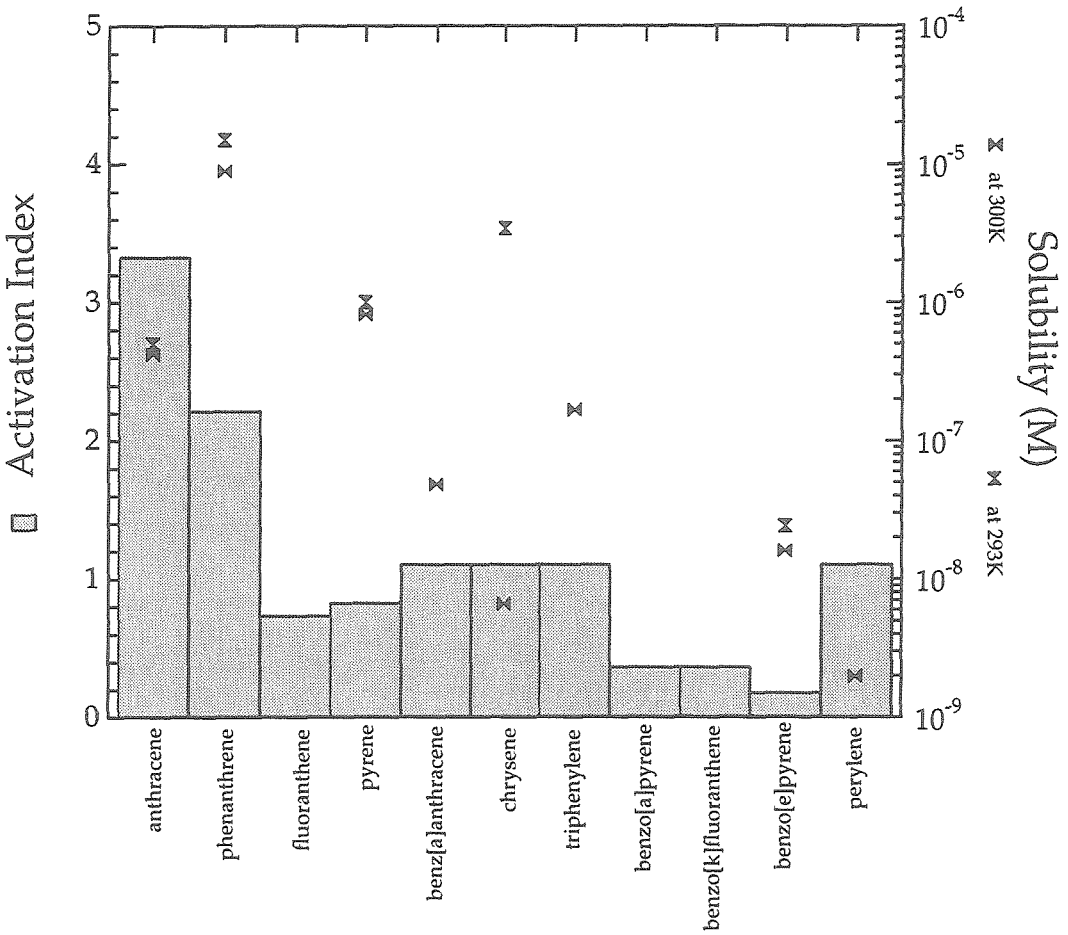

Figure 7.6: Comparison of calculated activation indices and water solubilities. The activation index is the ratio of the normalized frequency of detection in cloud over the normalized frequency of detection in the boundary layer aerosol (Eqn. 7.1). The water solubilities are reported by Seidell and Linke (1952) at temperatures of 293 K and 300 K.

References

Andrews, E., and S.M. Larson, 1993: Effect of surfactant layers on the size changes of aerosol particles as a function of relative humidity. *Env. Sci. Tech.*, 27: 857-865.

Banisoleiman, K., Z. Bazari, J.S. Carlton, R.J. Coker, S.D. Danton, R.W. Gawen, J.S. Hobday, K.A. Lavender, N.M. Mathieson, A.G. Newell, G.L. Reynolds, L.A. Smith, P.A. Stanney, A.D. Webster, C.M.R. Wills, A.A. Wright, and J.A. Zinn, 1993. *Marine exhaust emissions research programme: Phase II summary report.* Lloyd's Register of Shipping, Croydon, UK.

Banisoleiman, K., Z. Bazari, J.S. Carlton, R.J. Coker, S.D. Danton, R.W. Gawen, J.S. Hobday, K.A. Lavender, N.M. Mathieson, A.G. Newell, G.L. Reynolds, L.A. Smith, P.A. Stanney, A.D. Webster, C.M.R. Wills, A.A. Wright, and J.A. Zinn, 1994. *Marine exhaust emissions research programme: Phase II transient emission trials.* Lloyd's Register of Shipping, Croydon, UK.

Bretherton, C., C. Skupkiewicz, T. Garrett, D.W. Johnson, I. Brooks, and G. Innis, 1996: Ship Track Dispersion. *J. Atmos. Sci.* In preparation.

Choudhury, D.R., 1982: Characterization of polycyclic ketones and

quinones in diesel emission particulates by gas chromatography/mass spectrometry. *Env. Sci. Tech.*, 16: 102-106.

Coakley, J.A. et al., 1987: Effects of ship effluents on cloud reflectivity. *Science*, 237: 1020-1022.

Conover, J.H., 1966: Anomalous cloud lines. *J. Atmos. Sci.*, 23: 778-785.

Cronn, D.R., R.J. Charlson, R.L. Knights, A.L. Crittenden, and B.R. Appel, 1977: A survey of the molecular nature of primary and secondary components of particles in urban air by high resolution mass spectrometry. *Atmos. Env.*, 11: 929-937.

Duce, R.A., and R.B. Gagosian, 1982: The input of atmospheric n-C10 to n-C30 alkanes to the ocean. *J. Geophys. Res.*, 87: 7192-7200.

Duce, R.A., V.A. Mohnen, P.R. Zimmerman, D. Grosjean, W. Cautreels, R. Chatfield, R. Jaenicke, J.A. Ogren, E.D. Pellizzari, and G.T. Wallace, 1983: Organic material in the troposphere. *J. Geophys. Res.*, 21: 921-952.

Durkee, P.A., R.J. Ferek, D.W. Johnson, J. Coakley, S. Platnick, D. Babb, G. Innis, A. Ackerman, J.G. Hudson, L.M. Russell, and W. Hoppel, 1996: Tests of the role of ambient cloud properties in ship track formation. *J. Atmos. Sci.* In preparation.

Ferek, R.J., P. Hobbs, T. Garrett, K.J. Noone, J.G. Hudson, L.M. Russell, J.H. Seinfeld, R.C. Flagan, P.A. Durkee, K. Nielsen, D.W. Johnson, J.P. Taylor, C. O'Dowd, I. Brooks, D. Rogers, S. Osborne, and S. Platnick, 1996: Star Livorno/Hanjin Barcelona Case Study. *J. Atmos. Sci.* In preparation.

Frisbie, P.R., and J.G. Hudson, 1993: Urban cloud condensation nuclei spectral flux. *J. Appl. Met.*, 32: 666.

Gasparovic, R.F., 1995: *MAST Experiment Operations Summary.* Johns Hopkins University, Maryland.

Gillani, N.V., S.E. Schwartz, W.R. Leaitch, J.W. Strapp, and G.A. Isaac, 1995: Field observations in continental stratiform clouds: Partitioning of cloud particles between droplets and unactivated interstitial aerosols. *J. Geophys. Res.*, 100: 18687-18706.

Grosjean, D., 1983: Polycyclic aromatic hydrocarbons in Los Angeles air from samples collected on Teflon, glass and quartz filters. *Atmos. Env.*, 12:2265-2573.

Hallberg, A., J.A. Ogren, K.J. Noone, J. Heintzenberg, A. Berner, I. Solly, C. Kruisz, G. Reischl, S. Fuzzi, M.C. Facchini, H.C. Hansson, A. Wiedensohler, and I.B. Svenningsson, 1992: Phase partitioning for different aerosol species in fog. *Tellus*, 44B: 545-555.

Hallett, J., J.G. Hudson, and C.F. Rogers, 1989: Characterization of combustion aerosols for haze and cloud formation. *Aerosol Sci. Tech.*, 10: 70-83.

Hansson, H.C., A. Wiedensohler, M.J. Rood, and D.S. Covert, 1990: Experimental determination of the hygroscopic properties of organically coated aerosol particles. *J. Aerosol Sci.*, 21: S241-S244.

Henderson, T.R., J.D. Sun, A.P. Li, R.L. Hanson, W.E. Bechtold, T.M. Harvey, J. Shabanowitz, and D.F. Hunt, 1984: GC/MS and MS/MS studies of diesel exhaust mutagenicity and emissions from chemically defined fuels. *Env. Sci. Tech.*, 18: 428-434.

Hildemann, L.M., G.R. Cass, and G.R. Markowski, 1989: A dilution stack sampler for collection of organic aerosol emissions: Design, characterization and field tests. *Aerosol Sci. Tech.*, 10: 193-204.

Hildemann, L.M., G.R. Cass, M.A. Mazurek, and B.T. Simoneit, 1993: Mathematical modeling of urban organic aerosol: Properties measured by high-resolution gas chromatography. *Env. Sci. Tech.*, 27: 2045-2055.

Hildemann, L.M., G.R. Markowski, M.C. Jones, and G.R. Cass, 1991: Submicrometer aerosol mass distributions of emissions from boilers, fireplaces, automobiles, diesel trucks, and meat-cooking operations. *Aerosol Sci. Tech.*, 14: 138-152.

Hildemann, L.M., M.A. Mazurek, G.R. Cass, and B.T. Simoneit, 1994: Seasonal trends in Los Angeles ambient organic aerosol observed by high-resolution gas chromatography. *Aerosol Sci. Tech.*, 20: 303-317.

Hudson, J.G., 1991: Observations of anthropogenic cloud condensation nuclei. *Atmos. Environment*, 25A: 2449.

Hudson, J.G., and A.D. Clarke, 1992: Aerosol and cloud condensation nuclei measurements in the Kuwait plume. *J. Geophys. Res.*, 97: 14533-14536.

Hudson, J.G., and P.R. Frisbie, 1991: Cloud condensation nuclei near marine stratus. *J. Geophys. Res.*, 96: 20795-20808.

Hudson, J.G., J. Hallett, and C.F. Rogers, 1991: Field and laboratory measurements of cloud-forming properties of combustion aerosols. *J. Geophys. Res.*, 96: 10847-10859.

Johnson, D.W., R.J. Ferek, T. Garrett, P. Hobbs, J.G. Hudson, K.J. Noone, L.M. Russell, S. Platnick, J.P. Taylor, C. O'Dowd, W. Hooper, P.A. Durkee, K. Nielson, W. Hindmann, A. Ackerman, C. Bretherton, G. Innis, Y. Kogan, R.C. Flagan, J.H. Seinfield, M. Smith, and W. Hoppel, 1996: The impact of ship produced aerosols on the microphysical characteristics of warm stratocumulus clouds: A test of Hypotheses 1.1a and 1.1b. *J. Atmos. Sci.* In preparation.

Kawamura, K., and R.B. Gagosian, 1987: Implications of ω-oxocarboxylic acids in the remote marine atmosphere for photo-oxidation of unsaturated fatty acids. *Nature*, 325: 330-332.

King, M.D., L.F. Radke, and P.V. Hobbs, 1993: Optical properties of marine stratocumulus clouds modified by ships. *J. Geophys. Res.*, 98: 2729-2739.

Kittelson, D.B., K.C. Moon, and D.Y.H. Pui, 1982: *Filter media for sampling diesel particles: Final report.* Particle Technology Laboratories, Minneapolis, MN: Particle Technology Publication Number 435, 43 pp.

Martin, G.M., D.W. Johnson, and A. Spice, 1994: The measurement and parameterization of effective radius of droplets in warm stratocumulus clouds. *J. Atmos. Sci.*, 51: 1823-1842.

Noone, K.J., J.A. Ogren, A. Hallberg, J. Heintzenberg, J. Strom, H.-C. Hansson, B. Svenningson, A. Wiedensohler, S. Fuzzi, M. C. Facchini, B.G. Arends, and A. Berner, 1992: Changes in aerosol size- and phase distributions due to physical and chemical processes in fog. *Tellus*, 44B: 489.

Noone, K.J., J.A. Ogren, J. Heintzenberg, R.J. Charlson, and D.S. Covert, 1988: Design and calibration of a counterflow virtual impactor

for sampling of atmospheric fog and cloud droplets. *Aerosol Sci. Tech.*, 8: 235-244.

Noone, K.J., C. Ostrom, R.J. Ferek, P. Hobbs, T. Garrett, D.W. Johnson, J.P. Taylor, I. Brooks, L.M. Russell, R.C. Flagan, J.H. Seinfeld, J.G. Hudson, S. Platnick, C. O'Dowd, M. Smith, J. Frick, W.B. Hoppel, W. Hooper P.A. Durkee, K. Nielson, and D. Babb, 1996a: A case study of ship track formation in a polluted boundary layer *J. Atmos. Sci.* In preparation.

Noone, K.J., C. Ostrom, R.J. Ferek, P. Hobbs, T. Garrett, D.W. Johnson, J.P. Taylor, L.M. Russell, R.C. Flagan, J.H. Seinfeld, J.G. Hudson, C. O'Dowd, M. Smith, J. Frick, W.B. Hoppel, W. Hooper P.A. Durkee, K. Nielson, and D. Babb, 1996b: A case study of ships forming and not forming tracks in a moderately polluted boundary layer. *J. Atmos. Sci.* In preparation.

Novakov, T., and J.E. Penner, 1993: Large contribution of organic aerosols to cloud-condensation-nuclei concentrations. *Nature*, 365: 823-826.

Ogren, J.A., J. Heintzenberg, and R.J. Charlson, 1985: In-situ sampling of clouds with a droplet to aerosol converter. *Geophys. Res. Lett.*, 12: 121-124.

Peltzer, E.T., and R.B. Gagosian, 1987: Sampling and quantitation of lipids in aerosols from the remote marine atmosphere. *Anal. Chim. Acta*, 198: 125-144.

Pruppacher, H.R., and J.D. Klett, 1978: *Microphysics of clouds and precipitation*, D. Reidel, Dordrecht, Holland.

Quant, F.R., R. Caldow, G.J. Sem, and T.J. Addison, 1992: *J. Aerosol Sci.*, 23: 405.

Radke, L.F., C.A. Brock, J.H. Lyons, P.V. Hobbs, and R.C. Schnell, 1989: *Atmos. Envir.*, 23: 2417.

Radke, L.F., J.A. Coakley, and M.D. King, 1989: Direct and remote sensing observations of the effects of ships on clouds. *Science*, 246: 1146-1149.

Rogge, W.F., L.M. Hildemann, M.A. Mazurek, G.R. Cass and B.R.T. Simoneit, 1993a. Sources of fine organic aerosol. 2. Noncatalyst and catalyst-equipped automobiles and heavy-duty diesel trucks. *Env. Sci. Tech.*, 27: 636-651.

Rogge, W.F., L.M. Hildemann, M.A. Mazurek, G.R. Cass and B.R.T. Simoneit, 1993b. Sources of fine organic aerosol. 3. Road dust, tire debris, and organometallic brake lining dust: Roads as sources and sinks. *Env. Sci. Tech.*, 27: 1892-1904.

Rogge, W.F., M.A. Mazurek, L.M. Hildemann, G.R. Cass and B.R.T. Simoneit, 1993c. Quantification of urban organic aerosols at a molecular level: Identification, abundance and seasonal variation. *Atmos. Env.*, 27A: 1309-1330.

Saxena, P.R., and L.M. Hildemann, 1996: Water-soluble organic compounds in atmospheric particles: A thermodynamic approach to characterizing the molecular composition. *J. Atmos. Chem.*, in review.

Schneider, J.K., R.B. Gagosian, J.K. Cochran, and T.W. Trull, 1983: Particle size distributions of n-alkanes and 210Pb in aerosols off the coast of Peru. *Nature*, 304: 429-432.

Seidell, A., and W.F. Linke, 1952: *Solubilities of inorganic and organic compounds: Supplement to the third edition.* D. Van Nostrand Co., New York.

Shulman, M.L., M.C. Jacobson, and R.J. Charlson, 1995: Alteration of cloud droplet growth by organic compounds. *Nature*, in review.

Sicre, M.-A., R.B. Gagosian, and E.T. Peltzer, 1990: Evaluation of the atmospheric transport of marine-derived particles using long-chain unsaturated ketones. *J. Geophys. Res.*, 95: 1789-1795.

Svenningsson, I.B., H.-C. Hansson, A. Wiedensohler, J.A. Ogren, K.J. Noone, and A. Hallberg, 1992: Hygroscopic growth of aerosol particles

in the Po Valley. *Tellus*, 44B: 556.

Tang, I.N., and H.R. Munkelwitz, 1994: Aerosol phase transformation and growth in the atmosphere. *J. Appl. Met.*, 33: 791-796.

Wyslouzil, B.E., K.L. Carleton, D.M. Sonnenfroh, W.T. Rawlins, and S. Arnold, 1994: Observation of hydration of single, modified carbon aerosols. *Geophys. Res. Lett.*, 21: 2107-2110.

Chapter 8

Conclusions

Interpreting the chemical and physical evolution of aerosol particles in the marine environment requires both theoretical and experimental investigations. In this work, both approaches have been undertaken to provide a balanced perspective on the current state of understanding of some of the key processes for the evolution of the marine aerosol, such as nucleation of new particles from gas-phase components, growth of particles by vapor condensation, accelerated condensational growth during activation to droplets in cloud, and addition of new particles from marine and anthropogenic sources.

I have proposed looking at the aerosol evolution in the marine atmosphere through a simple model. Through this model I have identified the roles of key atmospheric processes, including cloud processing and sea salt generation. In assessing the performance of the model, I have evaluated the uncertainties which remain, both in these processes and in the fundamental dynamic processes of nucleation of new particles and condensational growth of preexisting particles.

By collecting observations of aerosol in the marine environement, I have provided a part of the data set required to evaluate the predictions of such a model. My observations over the Atlantic Ocean of surface-level aerosol size distributions are consistent with the structures reported in previous work, but have provided additional detail. However, further interpretation of aerosol processing from these data requires the ability to identify the history of the air mass as well as meteorological structure through the boundary layer to

cloud level.

Collecting observations of the vertical distribution of aerosol by aircraft-based measurements required novel approaches to existing measurement techniques. The design modifications I have implemented have been successfully demonstrated in flight and have provided essential information for case studies of aerosol in stratus cloud. Challenges to the capabilities of our instrumentation still remain: in order to make aerosol classification practical for aircraft observations on scales comparable to microscale meteorological fluctuations, compact devices with increased size ranges and speed are required. The measurements described here of aerosol size distributions in stratus clouds and ship tracks provide a set of observations sufficiently detailed to allow evaluation of more advanced models of aerosol evolution. The unique feature of this data set is that the coordination with satellite observations of ship tracks will be able to provide a pseudo-Lagrangian tracer by which processing in the aerosol may be linked to a time history.

Observations of organic concentrations in both aerosol and cloud droplets provide a first step toward better defining the chemical composition and processes contributing to marine aerosol, particularly under the impact of anthropogenically-influenced air masses. Ship tracks provide an ideal surrogate for such a study, since they provide a well-defined perturbation to the background in a meteorologically homogeneous boundary layer. In determining the partitioning of organics between the unactivated interstitial aerosol

and the activated cloud droplet phases, I have presented a framework for addressing the role of organics in terms of the behavior of aerosols: what role does the composition of particles play in determining the properties of clouds?

Clearly, further study is required to answer this question. Models of cloud formation and other atmospheric processes need to incorporate more chemical species and to provide accurate accounting of particles. Aerosol instrumentation requires an order of magnitude improvement in time resolution for it to be comparable to simultaneous meteorological parameters and a further reduction in size and complexity to be practical for aircraft-based observations. And, continued measurements need to be collected over sufficient time spans for a unique air mass to allow diurnal variations to be evaluated on a Lagrangian basis.

Appendix A

The Relationship Between DMS Flux and CCN Concentrations in Remote Marine Regions

JOURNAL OF GEOPHYSICAL RESEARCH, VOL. 99, NO. D8, PAGES 16,945–16,957, AUGUST 20, 1994

The relationship between DMS flux and CCN concentration in remote marine regions

Spyros N. Pandis

Department of Chemical Engineering and Engineering and Public Policy, Carnegie Mellon University, Pittsburgh, Pennsylvania

Lynn M. Russell and John H. Seinfeld

Department of Chemical Engineering, California Institute of Technology, Pasadena

Abstract. The relationship between the steady state cloud condensation nuclei (CCN) concentration and the dimethylsulfide (DMS) emission flux in remote marine regions is investigated by modeling the principal gas-, aerosol-, and aqueous-phase processes in the marine boundary layer (MBL). Results are in reasonable quantitative agreement with the available measurements of DMS, SO_2, H_2SO_4, CCN, and condensation nuclei (CN) concentrations in remote marine regions of the globe and suggest that indeed DMS plays a major role in the particle dynamics of the MBL. For sufficiently low DMS fluxes practically all the SO_2 produced by DMS photooxidation is predicted to be heterogeneously converted to sulfate in sea-salt aerosol particles. For DMS fluxes higher than approximately 2.5 μmole m^{-2} d^{-1} a linear relationship is found to exist between the CCN number concentration and the DMS flux.

1. Introduction

To establish a causal relationship between anthropogenic emissions and global climate effects we must understand the biogeochemical processes that govern the background troposphere. Two-thirds of the earth is covered by oceans, and this relatively dark water surface could absorb over 90% of the incident solar radiation. The presence of clouds over these oceans decreases the amount of energy reaching the sea-surface. These marine clouds can influence, through their albedo, the earth's climate.

Charlson et al. [1987] have postulated the existence of a feedback relationship by which perturbations caused by anthropogenic influences may be either dampened or accelerated by interaction with dimethyl sulfide (DMS), a metabolic by-product of marine phytoplankton. According to this hypothesis, DMS is oxidized in the atmosphere and the products of these reactions contribute to cloud condensation nuclei (CCN) formation, resulting in regulation of the earth's albedo. This change in the earth's albedo alters the radiative flux to the surface which in turn may alter the production of DMS. For a given cloud liquid water content the cloud albedo is determined largely by the number of particles that can nucleate to form droplets, namely the CCN.

An essential step in demonstrating this feedback mechanism is understanding the relationship between the source strength (flux) of DMS and the number concentration of CCN in the marine boundary layer [*Fitzgerald*, 1991]. If there is such a link, there should exist a direct correlation between DMS flux and CCN levels, at least under conditions not influenced by anthropogenic emissions. Field studies have provided some preliminary evidence of a positive correlation between DMS and CCN. *Bates et al.* [1987] demonstrated a strong correlation between DMS and condensation nuclei (CN) levels, providing indirect evidence of this link as CCN are a subset of CN. Satellite observations have provided more direct links between DMS flux and the earth's albedo, as reported by *Durkee et al.* [1991]. *Quinn et al.'s* [1993] data from the Pacific Ocean provides direct in situ evidence of a link between DMS and CCN, as they found a weak but positive correlation between particulate non-sea salt sulfate and CCN concentrations. The large number of the DMS-CCN system variables, their spatial and temporal variability, and the highly variable time constants involved, have made it difficult to quantify through field campaigns the relationship between DMS and cloud albedo.

The next step then is to probe the theoretical basis for the link between DMS emissions and CCN concentrations by constructing a model incorporating all of the appropriate chemical and physical mechanisms. As a first approximation, this gas-to-particle link can be investigated using a time-dependent nucleation and condensation model. *Kreidenweis and Seinfeld* [1988] proposed a framework for such a model using the three-variable aerosol parameterization developed by *Warren and Seinfeld* [1986], focusing on the kinetics of the H_2SO_4/MSA split, and demonstrated the primary role of H_2SO_4 as the nucleating agent under typical ambient conditions. *Hegg et al.* [1990, 1991, 1992] have adapted this model to make predictions of behavior under specific observed conditions leading to predictions of what regions of the troposphere and what ambient conditions might

Paper number 94JD01119.
0148-0227/94/94JD-01119$05.00

foster nucleation. However, as *Raes et al.* [1992a] demonstrated, the outcome of such a prediction may be heavily dependent on the parameters chosen in the model, as the present range of uncertainty in, for example, the condensation and nucleation rates spans several orders of magnitude. The model of *Raes and Van Dingenen* [1992] is based on a computationally-rigorous multi-sectional aerosol representation and has also been used to simulate the effect of boundary layer/free troposphere interaction on CCN levels [*Raes et al.*, 1992b]. *Lin et al.* [1992, 1993] have evaluated the competing mechanisms involved in the process of CCN formation by comparing their characteristic times and have estimated that heterogeneous SO_2 conversion is not important for the growth of submicron sulfate particles. However, *Chameides and Stelson* [1992] have shown with an aqueous chemistry model that heterogeneous conversion is a significant sink for sulfur when larger, less acidic sea-salt particles are present.

Each of the above studies has focused on some aspects of the DMS/CCN system, neglecting the rest. The present study combines for the first time a description of the full system, adopting the perspective of a steady-state model to probe the underlying behavior of the DMS/CCN link. A similar approach has been followed by *Baker and Charlson* [1990], who studied the steady-state behavior of the CCN concentration together with MBL energy and total water balances. While *Baker and Charlson* [1990] lumped all the processes resulting in CCN production into a generic CCN source term, they demonstrated that a steady-state approach can provide valuable insights into this problem. Our goal here is to integrate the present understanding concerning the individual gas-, aerosol- and aqueous-phase processes to determine the relationship between the DMS flux and the CCN number concentration. The model sensitivity to values of various parameters and to the parametrizations used in the model itself will be probed.

2. The DMS-CCN System

We focus on processes occurring in the MBL, which we assume to be well-mixed vertically. The processes considered are gas-phase chemistry, heterogeneous removal of SO_2 in sea-salt particles, heterogeneous oxidation of SO_2 in both the sea-salt aerosol particles and cloud droplets, coagulation between the interstitial aerosol and the cloud droplets, and wet and dry deposition of the gas and aerosol species to the ocean surface. The pathways for interaction among these processes are illustrated in Figure 1. The air parcel in the MBL is assumed to go through cloud condensation-evaporation cycles and also to pass through raining cloud systems.

The aerosol size distribution in the marine boundary layer is generally observed to be bimodal with a so-called nucleation mode containing particles of diameter smaller than roughly 0.12 μm and a so-called accumulation mode containing particles of diameter from approximately 0.12 to 0.6 μm [*Quinn* et *al.*, 1993]. The source of the aerosol in the nucleation mode is assumed to be H_2SO_4 nucleation, and the particles are assumed to consist of a

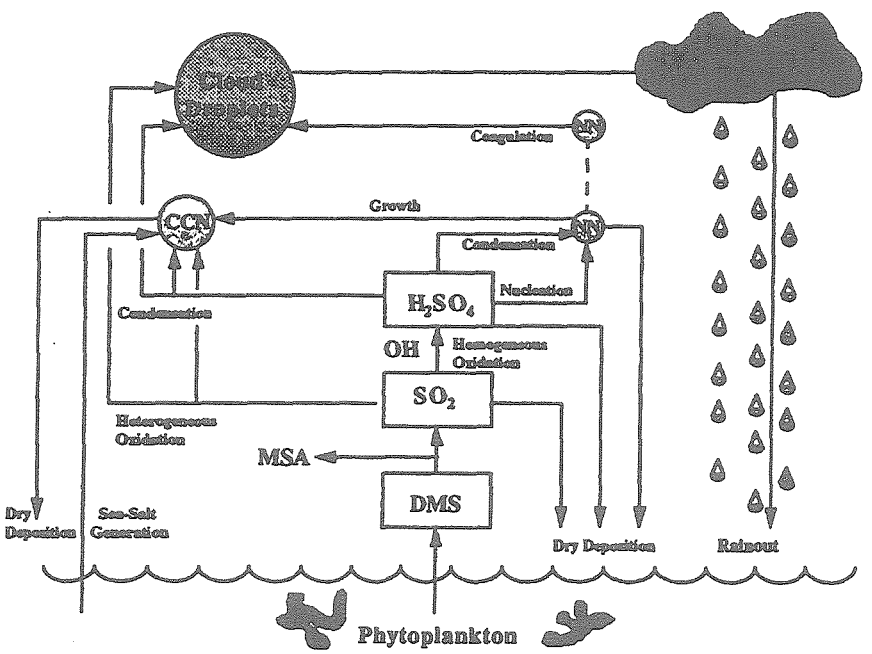

Figure 1. The DMS-CCN cycle in the remote marine boundary layer (MBL). The aerosol distribution is simulated by using two monodisperse groups of particles corresponding to the nucleation mode (NN) and to the accumulation mode (CCN). The accumulation mode particles can grow to cloud droplets, while the nuclei mode remain in the clouds as interstitial aerosol.

solution of ammonium sulfate and sulfuric acid. The particles in the accumulation mode include both the sea salt particles emitted by the ocean and the ammonium sulfate particles that have grown from the smaller mode by condensation of sulfuric acid and water. Approaches of varying complexity have been used in the past for the description of this MBL aerosol distribution. *Baker and Charlson* [1990] assumed a monodisperse CCN mode. A single mode aerosol model was also employed by *Kreidenweis and Seinfeld* [1988]. *Hegg* [1990] used a bimodal aerosol model with a monodisperse nuclei mode. *Lin et al.* [1992] grouped all particles generated during a half hour interval together and used up to 144 distinct sizes of particles. *Raes and Van Dingenen* [1992] represented the aerosol with 70 size sections. In an effort to describe the aerosol size distribution in the MBL with a modest number of parameters we will use the sectional approximation [*Warren and Seinfeld*, 1985], in which the continuous aerosol size distribution is approximated by a series of step functions. Two size sections have been used for the present work with the first corresponding to the nucleation and the second to the accumulation mode. The logarithm of the particle diameter has been selected as the independent variable for the aerosol number distribution, $n(\log_{10}D_p) = n(x)$. Five parameters are therefore required for the complete distribution description, the three sectional boundaries (D_1, D_a, and D_2) and the two distribution values n_1 and n_2. The definition of the size distribution function is therefore:

$$n(x) = 0,\ x < \log_{10}(D_1)$$
$$n(x) = n_1,\ \log_{10}(D_1) < x < \log_{10}(D_a)$$
$$n(x) = n_2,\ \log_{10}(D_a) < x < \log_{10}(D_2)$$
$$n(x) = 0,\ \log_{10}(D_2) < x.$$

From available measurements of aerosol size distributions in the MBL [*Quinn et al.*, 1993; *Hoppel*, 1988; *Hoppel and Frick*, 1990], we have selected D_1 = 0.023 μm, D_a = 0.1 μm and D_2 = 0.6 μm. A comparison of the sectional distribution with some of the measured distributions of *Quinn et al.* (1993) is depicted in Figure 2. Accumulation mode particles with diameters larger than 0.1 μm can grow to cloud droplets for supersaturations larger than S_c=0.1%, typical of marine stratiform clouds [*Baker and Charlson*, 1990]. On the contrary, the nucleation mode particles are too small to be activated and to become cloud droplets under typical stratus supersaturations. Particles in the accumulation section are therefore defined here as CCN [*Hegg and Hobbs*, 1992].

The selection of the diameter D_a that divides the two aerosol modes is reasonable but by no means unique. Supersaturations in stratiform clouds can approach 0.5% (corresponding to an activation diameter of around 0.07 μm) and in cumuliform clouds up to 2% (activation diameter around 0.04 μm) [*Raes and Van Dingenen*, 1992]. The sensitivity of the model to this choice of the sectional boundary will be explored subsequently. The variables simulated by the model described below are the DMS, SO_2, and H_2SO_4 gas-phase concentrations and the number concentrations of the two aerosol sections N_1 and N_2. Note that

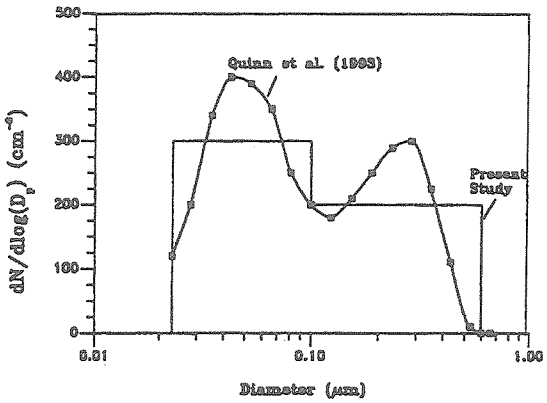

Figure 2. Modeling the remote marine aerosol size distribution with two sections. Modeled distribution vs typical measured distribution by Quinn et al. [1993].The values n_1 and n_2 of the distribution have been chosen for this example, so that total number is conserved.

$$N_1 = n_1\left(\log_{10}(D_a) - \log_{10}(D_1)\right)$$
$$N_2 = n_2\left(\log_{10}(D_2) - \log_{10}(D_a)\right).$$

2.1. Dimethylsulfide (DMS)

DMS enters the boundary layer at the air-ocean interface (flux F_{DMS}) and its major sink is assumed to be its reaction with the hydroxyl (OH) radical resulting in the production of both SO_2 and methane sulfonic acid (MSA). The DMS-OH reaction rate constant, k_{DMS}, is 8×10^{-12} cm^3 $molec^{-1}$ s^{-1} at 298 K [*Atkinson et al.*, 1984]. The SO_2 and MSA yields from this reaction are not firmly established and appear to depend both on temperature and NO_x availability. Field measurements have shown that MSA yields range from 6% in tropical areas [*Saltzman et al.*, 1983] to about 20% in mid latitudes [*Berresheim et al.*, 1990] to around 30% near the polar regions [*Berresheim*, 1987]. An SO_2 yield, y_{SO_2}, of 0.9 has been selected for the base case of the present calculations. Considerable uncertainty still surrounds the DMS oxidation and *Berresheim et al.* [1993] recently suggested that the dominant oxidation product of DMS may be dimethylsulfone ($DMSO_2$). Moreover *Bandy et al.* [1992] proposed that the major pathway for oxidation of DMS to H_2SO_4 was via SO_3 and not SO_2, and *Lin and Chameides* [1993] showed that such a mechanism is compatible with the MSA/non-sea-salt sulfate ratios measured in remote marine air. The implications of these alternative reaction pathways will be discussed in the sensitivity analysis section. A hydroxyl radical concentration, $(OH)_g$ of 2×10^6 molec cm^{-3} is assumed, typical of summer conditions [*Crutzen and Zimmermann*, 1991]. Nighttime nitrate radical (NO_3) concentrations are low in the remote marine atmosphere so that its reaction with DMS can be neglected in the present calculations [*Langner and Rodhe*, 1991]. Recent measurements by *Daykin and Wine* [1990] indicate that the DMS reaction with iodine oxide (IO) is very slow and can also be neglected. The ocean surface is

supersaturated with DMS and thus oceanic deposition of DMS is zero. The temporal variation of the DMS gas-phase concentration, $(DMS)_g$, is thus described by

$$\frac{d(DMS)_g}{dt} = F_{DMS} - k_{DMS}(OH)_g(DMS)_g \quad (1)$$

MSA has been measured in marine aerosol but in concentrations not exceeding 20% of the measured non-sea-salt sulfate [*Quinn et al.*, 1993; *Fitzgerald*, 1991]. MSA is incorporated in the particles by condensation and not nucleation [*Kreidenweis and Seinfeld*, 1988; *Wyslouzil et al.*, 1991a, b] and therefore neglecting MSA does not influence the aerosol number concentration predicted by the model. For the purpose of the present calculations, the influence of MSA condensation in the DMS-CCN system has been neglected, resulting in an error in predicted particle diameter less than 6%.

2.2. Sulfur Dioxide (SO_2)

Sulfur dioxide is produced during the DMS oxidation with a yield of y_{SO_2} and is lost by reacting in the gas-phase with OH, by heterogeneous oxidation in the aerosol phase and in the cloud droplets, and finally by depositing on the ocean surface. The rate of change of its concentration, $(SO_2)_g$, is

$$\frac{d(SO_2)_g}{dt} = y_{SO_2}k_{DMS}(OH)_g(DMS)_g - K_{dep}^{SO_2}(SO_2)_g - k_{SO_2}(OH)_g(SO_2)_g - R_{aeros} - R_{cloud}^{SO_2} \quad (2)$$

The deposition rate constant, K_{dep} of a species is defined as the ratio of its deposition velocity to the mixing height (H_{mix}) of the marine boundary layer. A deposition velocity of 0.5 cm s^{-1} is used for SO_2 in the base case corresponding to a deposition rate constant of 0.43 d^{-1} for a mixing height of 1000 m. A reaction constant k_{SO_2} of 10^{-12} cm^3 $molec^{-1}$ s^{-1} is used for the SO_2 gas-phase oxidation by the OH radical [*Atkinson and Lloyd*, 1984].

There is considerable evidence that SO_2 can be removed from the marine boundary layer by heterogeneous reaction with O_3 in the water associated with sea-salt aerosol particles [*Sievering et al.*, 1992]. *Chameides and Stelson* [1992] have shown that the amount of SO_2 removed from the atmosphere by this mechanism should be roughly equal to the flux of alkalinity that cycles through the atmosphere in sea-salt aerosols. The time scale for this removal of SO_2 is estimated by *Chameides and Stelson* [1992] to be less than an hour and to be essentially limited only by the rates of mass transfer of the reactants to the aerosol. The loss rate (in equivalents) of SO_2 by heterogeneous reactions in the aerosol phase, R_{aeros}, is therefore set equal to the alkalinity flux, or equivalently to the product of the sea salt mass flux [*Fitzgerald*, 1991; *Monahan et al.*, 1983] and the sea water alkalinity concentration [*Riley and Chester*, 1971]. For a wind speed of 8 m s^{-1} this loss rate is calculated to be 18 ppt SO_2 d^{-1}. When the DMS emission rate is sufficiently small so that the gas-phase production rate of SO_2 is less than its heterogeneous loss rate, then the loss rate is set equal to the production rate and the steady-state SO_2 concentration is negligibly small. In this case, at steady state, all the SO_2 produced is rapidly oxidized in the sea-salt aerosol particles.

Sulfur dioxide is also depleted by oxidation in cloud droplets by dissolved H_2O_2, O_3, O_2 (catalyzed by Fe^{3+} and Mn^{2+}) [*Pandis and Seinfeld*, 1989]. Concentrations of $H_2O_2(g)$ in the marine atmosphere have been found to be 0.5-1.5 ppb [*Ray et al.*, 1990], substantially exceeding the measured $SO_2(g)$ concentrations of 0.06-0.1 ppb [*Luria et al.*, 1990]. Under these conditions all the SO_2 will be oxidized in the aqueous phase to sulfate in much less than the 2 h average residence time of the air parcel in the cloud. Therefore the average loss rate of SO_2 can be approximated by

$$R_{cloud}^{SO_2} = f_{cloud}(SO_2)_g$$

where f_{cloud} is the average frequency of cloud occurrence in the MBL assumed to be 1 d^{-1} [*Hamrud and Rodhe*, 1986; *Raes et al.*, 1992b]. The model sensitivity to this assumed cloud frequency will be examined subsequently.

2.3. Sulfuric Acid Vapor (H_2SO_4)

The homogeneous oxidation of SO_2 is the principal gas-phase source of sulfuric acid in the marine boundary layer. The sulfuric acid vapor formed by this reaction can nucleate with water molecules and form sulfuric acid droplets, condense on the existing aerosol particles, condense on cloud droplets, and deposit to the ocean surface. The mass loss of H_2SO_4 by nucleation is negligible compared with that from condensation on the aerosol particles because the nuclei formed have a diameter of the order of 0.001 μm and typical average nucleation rates expected in the MBL are of the order of 1000 cm^{-3} d^{-1} or less [*Hegg*, 1990; *Raes and Van Dingenen*, 1992; *Lin et al.*, 1992]. This assumption is also justified by the results of the present study, described in subsequent sections.

The condensation rate of H_2SO_4 to the aerosol particles is described using the modified form of the Fuchs-Sutugin equation [*Hegg*, 1990; *Kreidenweis et al.*, 1991]. The condensation rate J to a particle of diameter D_p is given by:

$$J = 2\pi DD_pF(Kn)A(P - P_o)$$

where D is the diffusivity of sulfuric acid in air (set to 0.1 cm^2 s^{-1}), Kn is the Knudsen number (that is the ratio of the air mean free path to the particle radius), $F(Kn)$ is a coefficient correcting for free molecular effects,

$$F(Kn) = \frac{1 + Kn}{1 + 1.71Kn + 1.33Kn^2}$$

and A a coefficient correcting for the interfacial mass transport limitations described by the accommodation coefficient a_c.

$$A = \left[1 + 1.33 Kn\, F(Kn)\left(\frac{1}{a_c} - 1\right)\right]^{-1}.$$

Finally, P is the bulk H_2SO_4 vapor partial pressure and P_O is its partial pressure at the particle surface. An accommodation coefficient of 0.02 for the condensation of H_2SO_4 on the aerosol particles is assumed [*Van Dingenen and Raes*, 1991]; the sensitivity of the model predictions to this parameter is examined later. The vapor pressure of H_2SO_4 at the aerosol surface can be estimated from the data of *Bolsaitis and Elliot* [1990]. A value of 10^{-5} ppt was calculated for a relative humidity of 90% and a temperature of 293 K and therefore the surface vapor pressure of H_2SO_4 in the mass transfer calculation can be assumed to be zero.

For the ith aerosol size section from $x_i = \log_{10}(D_i)$ to $x_{i+1} = \log_{10}(D_{i+1})$ and a particle number concentration N_i the H_2SO_4 condensation rate is given by

$$J_i = K^i_{mt} N_i (H_2SO_4)_g$$

where the sectional mass transfer coefficients K^i_{mt} are calculated by

$$K^i_{mt} = \frac{2\pi D}{x_{i+1} - x_i} \int_{x_i}^{x_{i+1}} 10^x F(x) A(x) dx.$$

A deposition velocity of 1 cm s^{-1} is assumed for H_2SO_4 corresponding to a dry deposition rate constant, $K^{H_2SO_4}_{dep}$, equal to 0.86 d^{-1} for a MBL height of 1000 m. During the processing of the air parcel by clouds, the particles in the accumulation mode grow to cloud droplets of an average diameter of 20 μm. Since their corresponding surface area increases by more than three orders of magnitude, one can assume that all the sulfuric acid vapor is scavenged by the droplets in a period much shorter than that which the air parcel spends inside the cloud. The average mass transfer rate of H_2SO_4 to cloud droplets, $R^{H_2SO_4}_{cloud}$, can therefore be approximated by $R^{H_2SO_4}_{cloud} = f_{cloud}(H_2SO_4)_g$.

The temporal variation of the sulfuric acid gas-phase concentration, $(H_2SO_4)_g$, is given by:

$$\frac{d(H_2SO_4)_g}{dt} = k_{SO_2}(OH)_g(SO_2)_g - L_{nucl} - (K^1_{mt}N_1 + K^2_{mt}N_2)(H_2SO_4)_g - K^{H_2SO_4}_{dep}(H_2SO_4)_g - R^{H_2SO_4}_{cloud}. \quad (3)$$

2.4. Nucleation Mode Aerosol

Aerosol particles in the nucleation mode are produced by sulfuric acid-water nucleation with a rate J_{nucl}. This nucleation rate is primarily a function of the H_2SO_4 concentration, the temperature, and the relative humidity. The results of Jaecker-*Voirol and Mirabel* [1989] from hydrate theory for homogeneous binary nucleation are multiplied by an experimentally determined nucleation factor, t_n, to produce the nucleation rate used [*Raes et al.*, 1992a]. For a temperature of 298 K, selecting a value of t_n equal to 10^7 [*Raes et al.*, 1992a], the nucleation rate, J_{nucl} in particles cm^{-3} s^{-1}, used in this study is:

$$\log_{10} J_{nucl} = 7 + [-(64.24 + 4.7RH) + (6.13 + 1.95RH)\log_{10}(H_2SO_4)_g] \quad (4)$$

with the relative humidity, RH, varying from zero to one and $(H_2SO_4)_g$ the concentration of sulfuric acid vapor in molec cm^{-3}.

The deposition velocity of the aerosol particles is calculated using the theory developed by *Hummelshoj et al.* [1992] for dry deposition of particles to the sea surface. A deposition velocity of 0.04 cm s^{-1} for wind speed of 8 m s^{-1} is appropriate for the nucleation mode aerosol.

The condensation of sulfuric acid and water to the nucleation mode aerosol particles causes them to grow to accumulation mode particles with a growth rate of J_{growth}. At 80% RH and 298 K the equilibrium composition of a sulfuric acid solution is 25% per mass H_2SO_4 [*Giauque*, 1960]. Thus, the total condensation rate is assumed to be 4 times the H_2SO_4 condensation rate. The growth rate is calculated according to the theory developed by *Warren and Seinfeld* [1985], based on aerosol number and mass conservation during condensation. The volume concentration of the particles in section i, V_i in μm^3 cm^{-3}, is given by [*Seinfeld*, 1986]

$$V_i = \int_{x_i}^{x_{i+1}} \frac{1}{6}\pi D_p^3 n(x) dx = 0.0758 N_i \frac{\exp(6.908\, x_{i+1}) - \exp(6.908 x_i)}{x_{i+1} - x_i}$$

where x_i, x_{i+1} are the sectional boundaries, and N_i the number concentration of particles in this section in cm^{-3}. Therefore, the volume concentrations for the two size sections used in this study are

$$V_1(\mu m^3 cm^{-3}) = 1.41 \times 10^{-4} N_1(cm^{-3})$$
$$V_2(\mu m^3 cm^{-3}) = 2.09 \times 10^{-2} N_2(cm^{-3}).$$

and the volume equivalent average diameters of the two sections are 0.06 and 0.34 μm correspondingly. When a volume dV of condensate (sulfuric acid and water) is added to the particles of the first section, it causes growth of dN particles to the second section. The diameter of these particles increases from D_p ($D_1 < D_p < D_a$), to $D_a = 0.1$ μm. The corresponding volume change is

$$dV(\mu m^3 cm^{-3}) = 3.8 \times 10^{-4}\, dN(cm^{-3}).$$

The total condensate (H_2SO_4 and H_2O) flux J_{cond} is

$$J_{cond} = \frac{dV}{dt} = \frac{K^1_{mt}}{r_{H_2SO_4}} N_1 (H_2SO_4)_g$$

where $r_{H_2SO_4}$ is the H_2SO_4 mass fraction in the aqueous solution in equilibrium with the atmosphere at 80% RH and 298 K [*Giauque*, 1960]. Combining the last two expressions one can show that the growth rate is

$$J_{growth} = \frac{dN}{dt} = 0.12 N_1 (H_2SO_4)_g$$

where the growth rate is expressed in particles cm^{-3} d^{-1}, N_1 is in particles cm^{-3} and $(H_2SO_4)_g$ is in ppt. The above method is equivalent to calculating the particle growth rate by dividing the total condensate flux (sulfuric acid and water) by the volume change of a particle growing from the volume average diameter of the first section (0.06 μm) to the minimum CCN diameter (0.1 μm). For a nucleation mode concentration of 100 cm^{-3} and a $(H_2SO_4)_g$ mixing ratio of 1 ppt, the growth rate is 12 particles cm^{-3} d^{-1}.

The particles in the nuclei mode coagulate with themselves, with particles in the accumulation mode, and with cloud droplets. *Lin et al.* [1992] demonstrated that the growth of nuclei by coagulation with other aerosol particles in the remote marine atmosphere is a relatively inefficient process over the time scales of interest and can be neglected when compared to other processes influencing their concentration. On the contrary, the removal of these particles by collisions with cloud droplets during the processing of the air parcel by clouds is significant [*Flossmann* et al., 1985]. The coagulation coefficient for the nucleation mode aerosol with 20 μm diameter cloud droplets is 2×10^{-3} cm^3 d^{-1} [*Seinfeld*, 1986]. The fact that the air parcel spends, on average, 2 h per day in a cloud environment [*Raes et al.*, 1992b], has been factored in the above value. The evolution of the number concentration of the nuclei mode aerosol, N_1, is therefore described by:

$$\frac{dN_1}{dt} = J_{nucl} - K^1_{dep} N_1 - J_{growth} - K_{coag} N_1 N_2 . \qquad (5)$$

2.5. Accumulation Mode Aerosol

Aerosol particles in the accumulation mode are either sea-salt particles that have been directly emitted to the MBL or nuclei mode particles that have grown by vapor condensation to this mode. The number emission rate (particles cm^{-3} d^{-1}) of sea salt particles is calculated after *Monahan et al.* [1983] to be

$$J_{salt} = \frac{2.5 U^{3.41}}{H_{mix}}$$

where the mixing height, H_{mix}, is in m, and U is the wind speed in m s^{-1}. The deposition velocity of the accumulation mode aerosol for a wind speed of 8 m s^{-1} is 0.06 cm s^{-1} [*Hummelshoj et al.*, 1992] and the corresponding deposition constant K^2_{dep} is 0.05 d^{-1}.

The periods that the air parcel spends in non-precipitating clouds are assumed not to affect directly the number of accumulation mode particles, but the processing of the air parcel by raining clouds depletes the MBL of these particles. If f_{precip} is the frequency of processing of the parcel by raining clouds (a value of 0.1 d^{-1} is assumed in the base case), e_p is the CCN rainout efficiency, and the rainout rate of these particles is equal to $f_{precip} e_p N_2$. The rainout efficiency is expected, in general, to depend on the number of CCN and the raindrop size distribution [*Pruppacher and Klett*, 1980]. Following *Raes et al.* [1992b] a rainout efficiency of 1.0 is assumed. This choice results effectively in the linearization of the nonlinear rainout process; the sensitivity of the model to this choice will be examined subsequently.

The number concentration of the accumulation mode particles is thus governed by:

$$\frac{dN_2}{dt} = J_{salt} + J_{growth} - K^2_{dep} N_2 - f_{precip} e_p N_2 . \qquad (6)$$

3. The System in Steady-State

Valuable insights about the interactions of the various components of the system can be gained by studying its steady-state behavior. While the system is characterized by a diurnal variation [*Raes et al.*, 1992b], a pseudo-steady state can be envisioned as a sufficiently long-term average. Such an approach is supported by the available experimental evidence suggesting that aerosol concentrations are remarkably constant in the remote marine boundary layer [*Baker and Charlson*, 1990].

The timescales for reaching such a pseudo-steady state for the system can be estimated from the corresponding equations. They are:

$$\tau_{DMS} = \left(k_{DMS}(OH)_g\right)^{-1} = 1 \text{ d}$$

$$\tau_{SO_2} = \left(K^{SO_2}_{dep} + k_{SO_2}(OH)_g + f_{cloud}\right)^{-1} = 1 \text{ d}$$

$$\tau_{H_2SO_4} = \left(K^1_{nu} N_1 + K^2_{nu} N_2 + K^{H_2SO_4}_{dep} + f_{cloud}\right)^{-1} < 1 \text{ d}$$

The timescales for the two modes of the aerosol distribution reaching their corresponding steady-states are approximately:

$$\tau_{N_1} = \left(K^1_{dep} + 0.12(H_2SO_4)_g + K_{coag} N_2\right)^{-1} = 3 \text{ d}$$

$$\tau_{N_2} = \left(K^2_{dep} + f_{precip}\right)^{-1} = 6 \text{ d}$$

where values of $(H_2SO_4)_g$=1 ppt, and N_2 = 100 cm^{-3} have been used (see results of base case simulation below). These calculations indicate that the gas-phase species are expected to reach their pseudo-steady state concentrations in around one day, while the aerosol distribution requires significantly more time. The six days necessary for the aerosol distribution to attain its pseudo-steady state are significantly less than the time that a typical air parcel spends in the marine atmosphere [*Hamrud and Rodhe*, 1986; *Savoie et al.*, 1992; *Ellis et al.*, 1993]. Hence, the pseudo-steady state is consistent with the time available for the trip of the air parcel in the marine atmosphere, before being influenced by anthropogenic sources. The time scales calculated above for approach to the pseudo-steady state are sensitive to a series of selected variables.

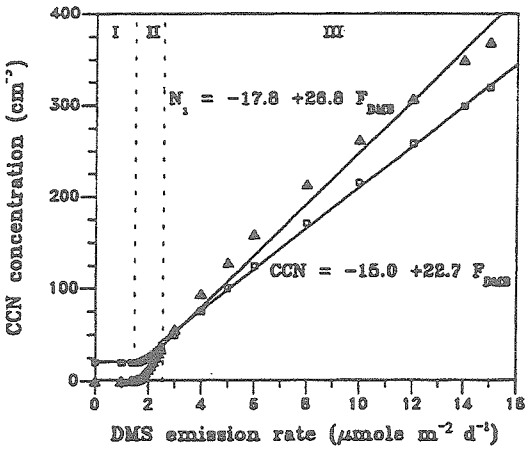

Figure 3. Predicted nuclei (N_1) and accumulation mode (CCN) concentration versus DMS emission flux for the base case meteorological conditions. The three DMS flux regimes are indicated.

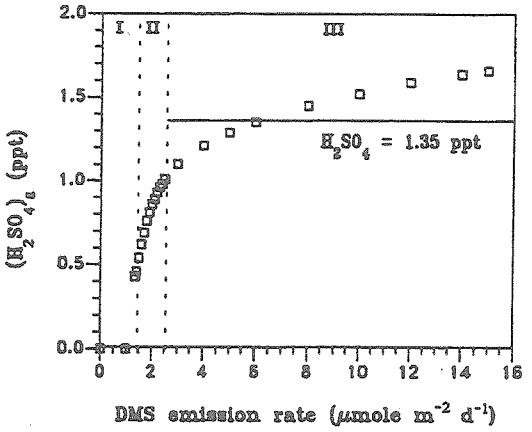

Figure 4. Predicted sulfuric acid vapor concentration versus DMS emission flux for the base case meteorological conditions. The three DMS flux regimes are indicated.

For example, increasing the rainout frequency from 0.1 d^{-1} to 0.3 d^{-1} results in a reduction of the τ_{N_2} timescale from six to three days.

The present steady-state model is obtained by setting the right hand sides of equations (1), (2), (3), (5) and (6) to zero. This model is expected to approximate the average conditions in the remote MBL, that is, after the air parcel has spent several days over the ocean and the aerosol distribution has relaxed to its pseudo-steady state form. This simplified approach provides valuable insights into the interdependencies among critical MBL processes.

4. The Dependence of CCN on DMS Flux

Erickson et al. [1990] have suggested that the DMS flux varies with time and latitude from 0-15 μmole m^{-2} d^{-1}. Varying the DMS flux and solving the above steady-state model produces the CCN (accumulation mode) number concentration variation shown in Figure 3. The predicted CCN number concentration varies between roughly 20 and 350 particles cm^{-3}. This figure suggests that there are three distinct regimes of functional dependence of CCN on DMS for the flux range shown. When the DMS emission flux is smaller than 1.3 μmole m^{-2} d^{-1}, the CCN concentration is predicted to be essentially constant at 20 particles cm^{-3}. In this regime all the SO_2 produced by the DMS oxidation is oxidized to sulfate in the available sea-salt aerosol particles and the concentration of H_2SO_4 vapor is effectively zero. The only available CCN source is the sea salt emitted by the ocean, and the steady-state CCN concentration is determined by a balance between the wind-dependent emission rate and the dry and wet deposition rates. In the second DMS emission regime, extending between 1.3 and 2.3 μmole m^{-2} d^{-1}, most of the SO_2, but not all, is consumed by heterogeneous reaction and only a few particles per day can grow and become CCN. The CCN concentration increases slowly (by 10 particles cm^{-3}) as the DMS emission rate increases in this regime. The third region corresponds to DMS emission fluxes larger than 2.3 μmole m^{-2} d^{-1}; despite the extreme nonlinearity of the system, the CCN concentration in this regime is a surprisingly linear function of the DMS flux.

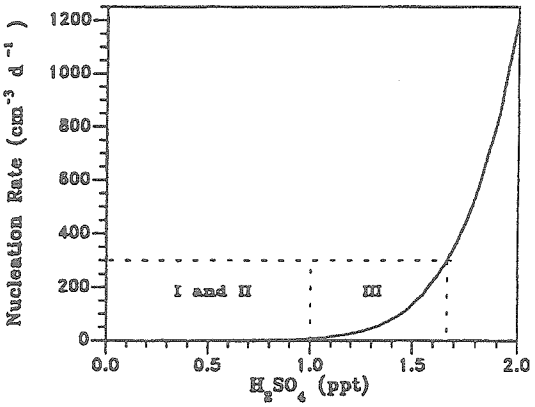

Figure 5. Nucleation rate as a function of the H_2SO_4 concentration for a relative humidity of 80% and a temperature of 298 K. The three DMS flux regimes are indicated.

The explanation of this unexpected behavior lies in the predicted sulfuric acid concentrations (Figure 4). In region I, as expected, the H_2SO_4 concentration is essentially zero. In the transition region II, the H_2SO_4 concentration rises sharply from zero to about 1 ppt as the DMS flux increases. However, the nucleation rate (Figure 5) is still practically zero in this region. The inability of the system to create any appreciable number of new nuclei in this region results in a very small increase of the CCN concentration. When the DMS flux exceeds 2.3 μmole

m^{-2} d^{-1}, sulfuric acid exceeds the threshold value of 1 ppt and appreciable nucleation commences. Interestingly enough, the H_2SO_4 does not need to change very much (from 1 to 1.6 ppt) to produce the relevant range of nucleation rates (Figure 5) for the system (from 0 to 300 particles cm^{-3} d^{-1}); furthermore, in region III, that concentration is nearly constant at about 1.35 ppt (within 30%). This small variation of the sulfuric acid vapor concentration is the key to the linear dependence of the CCN on DMS flux.

Equation (1) suggests that the DMS steady-state gas-phase concentration increases linearly with increasing DMS emission rate. Replacing $(DMS)_g$ with a linear function of the the DMS emission rate in equation (2), one can show that the SO_2 steady-state gas-phase concentration is also a linear function of the DMS emission rate. The linear dependence of the DMS and SO_2 concentrations on the DMS flux, F_{DMS}, is described by:

$$(DMS)_g = 17.7F_{DMS} \text{ (regions I, II \& III)}$$

$$(SO_2)_g = -12.2 + 13.7F_{DMS} \text{ (regions II \& III)}$$

Using this linearity together with the fact that $(H_2SO_4)_g$ is practically constant at 1.35 ppt in region III, equation (3) in steady-state can be rewritten as

$$k_{SO_2}(OH)_g(-12.2 + 13.7F_{DMS}) + 13K_{dep}^{H_2SO_4} + 1.35f_{cloud} = 1.35K_{nuc}^1N_1 + 1.35K_{nuc}^2N_2$$

Therefore, a linear combination of N_1 and N_2, corresponding to the H_2SO_4 condensation flux, is a linear function of the DMS emission rate. Similarly the steady-state form of equation (6) is equivalent to

$$J_{salt} = -0.12N_1 1.35 + K_{dep}^2N_2 + f_{precip}e_pN_2$$

suggesting that a linear combination of N_1 and N_2 is a constant independent of the DMS flux. These last two relationships show that indeed both N_1 and N_2 are expected to depend linearly on the DMS rate for DMS emission fluxes in region III. From a physical point of view, the requirement of a H_2SO_4 steady state results in a linear variation of the H_2SO_4 condensation flux to the marine aerosol with the DMS flux, or that for constant sectional boundaries the total number of aerosol particles should increase linearly with the DMS flux. The CCN steady state requires the nuclei mode particle concentration, that is the main CCN source, to vary similarly to the CCN concentration. These two requirements can only be satisfied if both aerosol mode particle concentrations vary linearly with the DMS flux.

5. Comparison With Available Measurements

Measured DMS gas-phase concentrations vary from 25 to 300 ppt [*Andreae*, 1985; *Andreae and Raemdock*, 1983; *Putaud et al.*, 1992; *Saltzman and Cooper*, 1988] with a mean concentration around 100 ppt [*Andreae*, 1985; *Berresheim*, 1987]. The predictions of the steady-state model vary from zero to 270 ppt with a value of 100 ppt corresponding to the reasonable average DMS flux of around 5 μmole m^{-2} d^{-1}. A wide variation of SO_2 gas-phase concentrations has been reported in the remote MBL varying from a few ppt to 100 ppt with averages around 40 ppt [*Andreae et al.*, 1988; *Berresheim et al.*, 1990; *Quinn et al.*, 1990; 1980; *Nguyen et al.*, 1983; *Bonsang et al.*, 1980; *Delmas and Servant*, 1980; *Putaud et al.*, 1992]. The range of the predicted steady state SO_2 concentrations is from zero to 190 ppt, in satisfactory agreement with the above measurements, although with a tendency of overprediction. For the average DMS flux of 5 μmole m^{-2} d^{-1} an SO_2 concentration of 57 ppt is predicted.

Eisele and Tanner [1993] recently reported gas-phase H_2SO_4 concentrations in relatively clean air masses varying from 0.01 to 1 ppt. These measurements are in qualitative agreement with 0 to 1.7 ppt predicted. The number concentration of aerosol particles in the nuclei mode in the remote marine boundary layer has been measured to be from around 50 to roughly 500 cm^{-3} [*Quinn et al.*, 1993; *Gras*, 1989; *Hegg et al.*, 1991; *Hoppel and Frick*, 1990]. We predict concentrations from zero to around 350 particles cm^{-3}, with a concentration of 120 particles corresponding to the average DMS flux.

As predicted here, all available studies point to the existence of nonzero minimum accumulation mode aerosol number concentration around 40 particles cm^{-3} [*Hegg et al.*, 1991]. Sea-salt particles emitted even when the DMS emission flux is too low to result in the production of any additional aerosol lead to a predicted concentration around 20 particles cm^{-3}. The highest accumulation mode aerosol concentrations measured in the clean MBL are around 250 particles cm^{-3} [*Quinn et al.*, 1993; *Hegg et al.*, 1991; *Hoppel and Frick*, 1990], in good agreement with the 300 particles cm^{-3} predicted in the present study.

The role of sea-salt particles as CCN has received little attention. *Charlson et al.* [1987] suggested that observed sea-salt particle concentrations at cloud height are typically of the order of 1 cm^{-3}, so the sea itself cannot be the main source of CCN. *Blanchard and Cipriano* [1987] argued that the actual sea-salt particle concentration is much higher, around 20cm^{-3} at cloud height. *Latham and Smith* [1990] calculated that for wind speeds around 8 m s^{-1} about 3 sea-salt particles cm^{-3} should be present, while the study of *Blanchard and Woodcock* [1980] had suggested 20-30 cm^{-3}. In the most recent study *O'Dowd and Smith* [1993] measured at ship level sea-salt particles at concentrations representing 20% of the accumulation mode number, and in high winds (17 m s^{-1}) the percentage increased to 75%. The present model suggests a sea-salt particle concentration of 20cm^{-3}, that, for low DMS fluxes, represents almost 100% of the accumulation mode aerosol number concentration and, for the average DMS flux of 5 μmoles m^{-2} d^{-1}, represents 20% of the total CCN accumulation mode number in agreement with the *O'Dowd and Smith* measurements [1993]. This model prediction is also in agreement with the conclusion of Ayers and Gras [1991] that at low DMS and MSA concentrations there was another source of CCN apart from DMS, probably sea-salt. These particles also indirectly influence the CCN number concentration by

providing the necessary alkalinity for the heterogeneous oxidation of SO_2.

A notable feature of the remote MBL is the constancy of the aerosol concentrations; in summer, the total particle concentration varies around 300-500 cm^{-3} with CCN being more than 20% of the total aerosol number concentration [*Raes et al.*, 1992b]. *Hoppel and Frick* [1990] reported 100-300 cm^{-3} in the trade wind region and 25-1000 cm^{-3} south of trade wind region. Other measurements have indicated concentrations from 60-450 cm^{-3} [*Hoppel et al.*, 1989; *Parungo et al.*, 1987; *Kim et al.*, 1990] The model predictions of total particle concentrations from 20-700 cm^{-3} are in good agreement with the above observations.

Raes et al. [1992b] suggest as a major test of MBL models that the predicted CCN concentrations should be more than 20% of the total aerosol number concentration. Measurements have indicated ratios of 40-60% [*Quinn et al.*, 1993; *Gras*, 1989] and 20% [*Hegg et al.*, 1991]. The model predicts for region III that accumulation mode particles represent from 40 to 50% of the total number concentration with this value increasing to almost 100% as the DMS flux approaches zero.

Bates et al. [1987] attempted to reconstruct the CN to DMS flux relationship using field measurements that unfortunately were not concurrent in space or time. The suggested relationship was $CN = -16.9 + 77\,F_{DMS}$, which agrees within 30% with that predicted here, $CN = -32.8 + 50\,F_{DMS}$. A similar set of relationships has been proposed by *Hegg et al.* [1991] between the CCN number concentration at various supersaturations and the DMS gas-phase concentration

$$CCN(1\%\ \text{supersaturation}) = 23 + 0.86(DMS)_g$$

$$CCN(0.3\%\ \text{supersaturation}) = 50 + 0.4(DMS)_g$$

The corresponding relationship predicted by the present model is CCN ($D_p > 0.1$ μm) = $15 + 1.28\,(DMS)_g$. Note that for an average DMS concentration of 100 ppt, the model predicts 143 cm^{-3}, while the two relationships by *Hegg at al.* [1991] predict 109 cm^{-3} and 90 cm^{-3}, respectively.

The above comparison indicates that the steady-state model reproduces the main features of gas/aerosol phenomena in the MBL.

6. Sensitivity Analysis

To investigate the effect of the choices of model parameters on the reported base case results, a detailed sensitivity analysis of the model has been performed (Table I). The change in CCN number has been calculated relative to a DMS flux of 5 μmoles m^{-2} d^{-1}.

6.1. Meteorological Conditions

The particle nucleation rate depends exponentially on the MBL relative humidity and changes of 10% in RH result in significant changes in the predicted CCN concentration. The relative humidity also influences the amount of water that condenses together with sulfuric acid vapor, enhancing the growth of small particles to CCN. An increase of the MBL height results in dilution of the DMS emission flux and to lower DMS, H_2SO_4, and sulfate concentrations. This results in a decrease of the CCN levels that is partially offset by smaller losses to the ocean surfaces of all species involved. Wind speed increases, under constant DMS flux, lead to two opposing effects, increase of the sea-salt particle production, but also higher heterogeneous oxidation rates for SO_2 in the same particles. Therefore, for higher wind speeds, the sea-salt number concentration increases, but the total CCN number concentration is predicted to decrease.

6.2. Cloud Processing

The period that the air parcel spends between consecutive cloud processing is one of the most important model parameters. When this time (equal to $1/f_{cloud}$) is 16 h the predicted CCN concentration is 69 cm^{-3}; for 24 h it increases to 100 cm^{-3} and for 48 h it reaches 153 cm^{-3}. Every time that the air parcel passes through such a system, all the available $(SO_2)_g$ is assumed to be lost because of heterogeneous reaction with H_2O_2 and the available $(H_2SO_4)_g$ condenses on the droplets. The processing of the air parcel by raining clouds is less important as, even if rainout were to deplete the MBL of CCN entirely, this event occurs relatively infrequently (only once in 10 days in the base case). Doubling the rainout frequency results in a 10% reduction of the predicted CCN concentration. If one assumes that the rainout efficiency is not unity, but just 50%, this is equivalent to doubling the time between rainout events (equation 6). Expressing this rainout efficiency as a function of the CCN number concentration has little qualitative effect on the predicted linearity of the DMS-CCN relationship for efficiency values ranging from 50% to 100%.

Processing of the air parcel by clouds and the consequent in-cloud oxidation of SO_2, scavenging of H_2SO_4 by cloud droplets, and CCN rainout have been treated as continuous processes in the present model. In reality, the air parcel spends most of the time outside the cloud layer and is processed by clouds for a limited time per day. This assumption of continuous cloud processing is expected to result in underestimation of the maximum H_2SO_4 vapor concentration and consequently of the nucleation rate. Hence, use of this assumption is expected to result in lower predicted concentrations of the nuclei and accumulation particle concentrations. In a series of sensitivity simulations the continuous cloud processing assumption has been relaxed and the corresponding variation of the system variables has been studied. Use of this assumption was indeed found to result in an underprediction of the CCN concentration by 50%, but did not change the linearity of the DMS/CCN relationship. These dynamic simulations will be discussed in detail in a forthcoming publication.

6.3. Gas Phase Chemistry

The parameters involved in the descriptions of the gas-phase reactions leading to the H_2SO_4 production influence significantly the model results. Reduction of the OH radical concentration to half its assumed base case value results in a 50% reduction of the predicted CCN concentration. The SO_2 yield during the DMS oxidation is

Table 1. Parameter Variation in Steady State DMS/CCN Model for MBL

	Base Case Value	Test Values	Percent Change in CCN Number
Relative humidity	0.8	0.7	-26
		0.9	+37
Mixing height (m)	1000	500	+40
		1500	-23
Wind speed (m s^{-1})	8	4	+15
		12	-21
Cloud frequency (d^{-1})	1	0.5	+53
		1.5	-31
Precipitation frequency (d^{-1})	0.1	0.05	+9
		0.20	-10
Coagulation coefficient ($cm^3 d^{-1}$)	0.002	0.001	+5
		0.00	-3
$(OH)_g$ (molec cm^{-3})	$2x10^6$	$1x10^6$	-50
		$3x10^6$	+43
DMS to SO_2 yield	0.9	0.7	-27
SO_2 deposition velocity (cm s^{-1})	0.5	0.25	+16
		1.00	-22
Sea salt mass flux (g $m^{-2} d^{-1}$)	0.06	0.03	+10
		0.12	-20
Sea salt number flux ($cm^{-3} d^{-1}$)	3	6	+4
Alkalinity flux (μg Ca $m^{-3} d^{-1}$)	0.03	0.015	+11
		0.060	-20
Accommodation coefficient	0.02	0.05	-45
D_1 (μm)	0.03	0.001	-12
D_2 (μm)	0.6	1.2	-72
D_{CCN} (μm)	0.1	0.05	+40
$(H_2SO_4)_g$ deposition velocity (cm s^{-1})	1.0	0.5	+6
		1.5	-5
Nuclei deposition velocity (cm s^{-1})	0.04	0.02	+1
		0.06	-1
CCN deposition velocity (cm s^{-1})	0.06	0.1	-4
H_2SO_4 condensate fraction	0.26	0.13	+8
Nucleation factor	$1x10^7$	$1x10^4$	-60

The effect of varying parameters in the steady-state DMS/CCN model of the marine boundary layer is calculated as percent change in predicted CCN number concentration relative to a base case DMS Flux of 5 μmole $m^{-2} d^{-1}$.

of similar importance. A reduction of this yield by 28% resulted in a 27% reduction of the CCN concentration. If H_2SO_4 is not the major final product of the DMS oxidation, the proposed DMS-CCN link will weaken considerably. Alternative pathways not involving SO_2 as an intermediate product (e.g. involving SO_3) could actually strengthen this link [*Lin and Chameides*, 1992].

6.4. MBL-Ocean Surface Interaction

The predicted CCN concentration changes corresponding to 50% changes in the selected deposition velocities for H_2SO_4 and the two aerosol modes is less than 10%, while for SO_2 the predicted CCN level increases to 20%. Changes of CCN concentrations around 20% are also the result of 50% variation of the sea-salt flux variables.

6.5. Aerosol Distribution

The selected sectional boundaries, D_1, D_2, and D_a are reasonable but by no means unique. If a much smaller lower boundary of the distribution is selected, e.g. 0.001 μm, the changes in predicted variables are not dramatic. The steady state CCN concentration is reduced by 12% mainly because the nucleation mode particles cannot compete as effectively for the condensing sulfuric acid vapor. In this case, however, the number of these particles increases by a factor of three. The model is more sensitive to the selection of the activation diameter. Selecting a diameter $D_a = 0.05$ μm, resulted in a 40% increase of the CCN concentration. The choice of the upper distribution boundary D_2 is also important because it determines the surface area of the accumulation mode particles. Selecting a rather extreme value of 1.2 μm resulted in a 71% decrease in the CCN concentration, because of the effectiveness of these CCN as H_2SO_4 condensation sites. Changes in the growth expression used can be expressed as equivalent changes in the sectional boundaries.

The above sensitivity analysis (Table I) indicates that the predicted CCN concentrations are sensitive to the meteorological conditions (especially the RH), to the OH concentration levels, to the SO_2 yield during DMS oxidation, to the H_2SO_4 mass transport accommodation coefficient, to the activation diameter, to the size of the particles in the accumulation mode, and to the nucleation rate. An independent variation of most model parameters by a factor of two or more resulted in CCN concentration changes of generally less than 50%. A similar surprisingly small change was observed during variations of the nucleation rate by 3 orders of magnitude. Variables like the precipitation frequency, coagulation coefficient, sea salt number flux, the size of the nuclei mode particles, the H_2SO_4 and aerosol dry deposition velocities, and the species (e.g. NH_3) that condense with H_2SO_4 appear to have a secondary effect on the CCN concentration levels for a typical DMS flux.

7. Discussion

The present study suggests that under constant meteorological conditions (temperature, relative humidity, wind speed and mixing height) the CCN number concentration is expected to vary almost linearly with the DMS emission flux. It is important to note the weaknesses of the system of equations (1), (2), (3), (5), and (6) as a representation of the remote marine boundary layer. The model assumes that the MBL remains homogeneous. *Hegg et al.* [1990] proposed, for example, that new particle production can occur in the vicinity of marine clouds, and, while temporally and spatially inhomogeneous, this source could be significant.

One of the main assumptions we have made is that the diameters of the two aerosol modes are fixed and do not change significantly for this region of the DMS fluxes. The diameter D_2 of the CCN particles seems to be the most important parameter. We have relaxed this assumption, adding to the set of equations the mass balances of the two aerosol modes, calculating explicitly the diameter D_2. This diameter indeed increases with increasing DMS flux but the change is small enough not to affect the presented conclusions beyond the sensitivity analysis values of Table I. Another problem of the specific representation of the aerosol distribution used is numerical diffusion. When a group of particles are created, the model automatically distributes them over the first section and artificially 'diffuses' them. This numerical artifact allows faster growth to the second section. When a similar group of particles grows to the second section the same numerical smearing occurs. In this case, this numerical error results in an increased condensation of H_2SO_4 in this section and prevents more CCN growing. Therefore, this numerical error from the one side accelerates and from the other decelerates the CCN growth.

Baker and Charlson [1990] proposed that two stable CCN concentration regimes exist, one corresponding to the low concentration observed over the oceans and the other to the higher continental concentrations. The first steady state results from the balancing of the CCN source by the rainout sink and corresponds to the steady-state discussed in this study. The second steady-state proposed by *Baker and Charlson* [1990] was the result of the interaction of the CCN concentration with the MBL structure in their model. This interaction between the aerosol concentration and the MBL structure has not been included in the present study and therefore only one steady state is predicted by the present model. *Baker and Charlson* [1990] proposed that at high CCN levels, the precipitation sink ceases and coagulation becomes the main sink, allowing a much higher CCN steady-state concentration.

Lin et al. [1992] and *Raes et al.* [1992b] have raised some questions about the ability of the MBL to sustain a reasonable CCN concentration and have suggested that new CCN can be produced only under special conditions (very low CCN levels) or in the free troposphere by oxidation of DMS that escapes the MBL. The above models have generally been initialized with zero nucleation mode particles and used for the simulation of one cloud cycle (usually a few days). The simulations were terminated long before a steady state was reached, thus precluding direct comparison with the results of this study.

Acknowledgments. This work was supported by National Science Foundation grant ATM-9307603.

References

Andreae, M. O., and H. Raemdock, Dimethyl sulfide in the surface ocean and the marine atmosphere- A global view, *Science*, *221*, 744-747, 1983.

Andreae, M. O., The emission of sulfur to the remote atmosphere, in *The Biogeochemical Cycles of Sulfur and Nitrogen in the Remote Atmosphere*, ed. N. J. Galloway et al., p. 5-25, Hingham, Mass., 1985.

Andreae, M. O., H. Berresheim, T. W. Andreae, M. A. Kritz, T. S. Bates, and J. T. Merrill, Vertical distribution of dimethylsulfide, sulfur dioxide, aerosol ions, and radon over the northeast Pacific ocean, *J. Atmos. Chem.*, *6*, 149-173, 1988.

Atkinson, R., and A. C. Lloyd, Evaluation of kinetic and mechanistic data for modeling of photochemical smog, *J. Phys. Chem. Ref. Data*, *13*, 315-444, 1984.

Atkinson, R., J. N. Pitts Jr., and S. M. Aschmann, Tropospheric reactions of dimethyl sulfide with NO_3 and OH radicals, *J. Phys. Chem*, *88*, 1584-1587, 1984.

Ayers, G. P., and J. L. Gras, Seasonal relationship between cloud condensation nuclei and aerosol methanesulfonate in marine air, *Nature*, *353*, 834-835, 1991.

Baker, M. B. and R. J. Charlson, Bistability of CCN concentrations and thermodynamics in the cloud-topped boundary layer, *Nature, 345*, 142-145, 1990.

Bandy, A. R., D. L. Scott, B. W. Blomquist, S. M. Chen, and D. C. Thornton, Low yields of SO_2 from dimethyl sulfide oxidation in the marine boundary layer, *Geophys. Res. Lett., 19*, 1125-1127, 1992.

Bates, T. S., R. J. Charlson, and R. H. Gammon, Evidence for the climatic role of marine biogenic sulfur, *Nature, 329*, 319-321, 1987.

Berresheim, H., Biogenic sulfur emissions from the subantarctic and antarctic oceans, *J. Geophys. Res., 92*, 13245-13262, 1987.

Berresheim, H., M. O. Andrae, G. P. Ayers, R. W. Gillett, J. T. Merrill, V. J. Davis, and W. L. Chameides, Airborne measurements of dimethylsulfide, sulfur dioxide, and aerosol ions over the southern-ocean south of Australia, *J. Atmos. Chem., 10*, 341-370, 1990.

Berresheim, H., F. L. Eisele, D. J. Tanner, L. M. McInnes, and D. C. Ramseybell, Atmospheric sulfur chemistry and cloud condensation nuclei (CCN) concentrations over the northeastern Pacific coast, *J. Geophys. Res., 98*, 12701-12711, 1993.

Blanchard, D. C., and R. J. Cipriano, Biological regulation of climate, Letter, *Nature, 330*, 526, 1987.

Blanchard, D. C., and A. H. Woodcock, The production, concentration, and vertical distribution of the sea-salt aerosol, Ann. *N. Y. Acad. Sci., 338*, 330-347, 1980.

Bolsaitis, P., and J. F. Elliott, Thermodynamic activities and equilibrium partial pressures for aqueous sulfuric-acid-solutions, *J. Chem. Eng. Data, 35*, 69, 1990.

Bonsang, B., B. C. Nguyen, A. Gaudry, and G. J. Lambert, Sulfate enrichment in marine aerosols owing to gaseous sulfur compounds, *J. Geophys. Res., 85*, 7410-7416, 1980.

Chameides, W. L. and A. W. Stelson, Aqueous-phase chemical processes in deliquescent sea salt aerosols: A mechanism that couples the atmospheric cycles of S and sea salt, *J. Geophys. Res., 97*, 20565-20580, 1992.

Charlson, R. J., J. E. Lovelock, M. O. Andreae, and S. G. Warren, Oceanic phytoplankton, atmospheric sulfur, cloud albedo and climate, *Nature, 326*, 655-661, 1987.

Crutzen, P. J., and P. H. Zimmermann, The changing photochemistry of the atmosphere, *Tellus, 43AB*, 136-151, 1991.

Daykin, E. P., and P. H. Wine, Rate of reaction of IO radicals with dimethylsulfide, *J. Geophys. Res., 95*, 18547-18553, 1990.

Delmas, R., and J. Servant, The origins of sulfur compounds in the atmosphere of a zone with high productivity, *J. Geophys. Res., 87*, 11019-11026, 1980.

Durkee, P. A., F. Pfeil, E. Frost, and R. Shema, Global analysis of aerosol-particle characteristics, *Atmos. Environ., 25A*, 2457-2471, 1991.

Eisele, F. L., and D. J. Tanner, Measurement of the gas-phase concentration of H_2SO_4 and methane sulfonic acid and estimates of H_2SO_4 production and loss in the atmosphere, *J. Geophys. Res., 98*, 9001-9010, 1993.

Ellis, W. G. Jr., R. Arimoto, D. L. Savoie, J. T. Merrill, R. A. Duce, and J. M. Prospero, Aerosol selenium at Bermuda and Barbados, *J. Geophys. Res., 98*, 12673-12686, 1993.

Erickson, D. J.III, S. J. Ghan, and J. E. Penner, Global ocean-to-atmosphere dimethyl sulfide flux, *J. Geophys. Res., 95*, 7543-7552, 1990.

Fitzgerald, J. W., Marine aerosols-A review, *Atmos. Environ., 25A*, 533-545, 1991.

Flossmann, A. I., W. D. Hall, and H. R. Pruppacher, A theoretical study of the wet removal of atmospheric pollutants I. The redistribution of aerosol particles captured through nucleation and impaction scavenging by growing cloud drops, *J. Atmos. Sci., 42*, 583-606, 1985.

Giauque, W. F., E. W. Hornung, J. E. Kunzler, and T. R. Rubin, The thermodynamic properties of aqueous sulfuric acid solutions and hydrates from 15 to 330°K, *J. Am. Chem. Soc., 82*, 62-70, 1960.

Gras, J. L., Baseline Atmospheric Program (Australia) 1987, ed. B. W. Forgan and P. J. Fraser, 47-48, *CSIRO*, Newcastle NSW, 1989.

Hamrud, M. and H. Rodhe, Lagrangian time scales connected with clouds and precipitation, *J. Geophys. Res., 91*, 14377-14383, 1986.

Hegg, D. A., Heterogeneous production of cloud condensation nuclei in the marine atmosphere, *Geophys. Res. Lett., 17*, 2165-2168, 1990.

Hegg, D. A., and P. V. Hobbs, *Nucleation and Atmospheric Aerosols*, ed. N. Fukuta and P. E. Wagner, p. 181-192, Deepak, Hampton, VA, 1992.

Hegg, D. A., L. F. Radke, and P. V. Hobbs, Particle production associated with marine clouds, *J. Geophys. Res., 96*, 13917-13926, 1990.

Hegg, D. A., L. F. Radke, and P. V. Hobbs, Measurement of aitken nuclei and cloud condensation nuclei in the marine atmosphere and their relation to the DMS-cloud-climate hypothesis, *J. Geophys. Res., 96*, 8727-8733, 1991.

Hoppel, W. A., The role of nonprecipitating cloud cycles and gas-to-particle conversion in the maintenance of the submicron aerosol size distribution over the tropical oceans, in *Aerosols and Climate*, ed. P. Hobbs and P. McCormick, p. 9-19, Deepak, Hampton, VA, 1988.

Hoppel, W. A. , J. W. Fitzgerald, G. M. Frick, R. E. Larson, and E. J. Mack, *Atmospheric Aerosol Size Distributions and Optical Properties in the Marine Boundary Layer over the Atlantic Ocean*, NRL Report 9188, 1989.

Hoppel, W. A., and G. M. Frick, Submicron aerosol size distributions measured over the tropical and south Pacific, *Atmos. Environ., 24A*, 645-659, 1990.

Hummlshoj, P., N. O. Jensen, and S. E. Larsen, Particle dry deposition to a sea surface, in *Precipitation Scavenging and Atmosphere Surface Exchange, ed. Schwartz*, S. E. and W. G. N. Slinn, p. 829-840, Hemishere Pub. Co., Washington, 1992.

Jaecker-Voirol, A., and P. Mirabel, Heteromolecular nucleation in the sulfuric acid-water system, *Atmos. Environ., 23*, 2053-2057, 1989.

Kim, Y., H. Sievering, and J. F. Boatman, Volume and surface area size distribution, water mass and model fitting of CASE-WATOX marine aerosols, *Global Biogeochem. Cycles, 4*, 165-178, 1990.

Kreidenweis, S. M. and Seinfeld, J. H. , Nucleation of sulfuric-acid water and methanesulfonic acid water solution particles. Implications for the atmospheric chemistry of organosulfur species, *Atmos. Environ., 22*, 283-296, 1988.

Kreidenweis, S. M., F. Yin, S. C. Wang, D. Grosjean, R. C. Flagan, and J. H. Seinfeld, Aerosol formation during photooxidation of organosulfur species, *Atmos. Environ., 25A*, 2491-2500, 1991.

Langner, J., and H. Rodhe, A global 3-dimensional model of the troposheric sulfur cycle, *J. Atmos. Chem., 13*, 225-263, 1991.

Latham, J. and M. H. Smith, Effect on global warming of wind dependent aerosol generation at the ocean surface, *Nature, 347*, 372-373, 1990.

Lin, X., W. L. Chameides, C. S. Kiang, A. W. Stelson, and H. J. Berresheim, A model study of the formation of cloud condensation nuclei in remore marine areas, *J. Geophys. Res., 97*, 18161-18171, 1992.

Lin, X. and W. L. Chameides, CCN formation from DMS oxidation without SO_2 acting as an intermediate, *Geophys. Res. Lett., 20*, 579-582, 1993.

Luria, M., C. C. Van Valin, R. L. Gunter, D. L. Wellman, W.

C. Keene, J. N. Galloway, H. Sievering, and J. F. Boatman, Sulfur dioxide over the western North Atlantic Ocean during GCE/CASE/WATOX, *Global Biochem. Cycles*, *4*, 381-394, 1990.

Monahan, E. C., C. W. Fairall, K. L. Davidson, and P. Jones Boyle, Observed interrelations between 10m winds, ocean whitecaps and marine aerosols, *Q. J. R. Meteorol. Soc.*, *109*, 379-392, 1983.

Nguyen, B. C., B. Bonsang, and A. Gaudry, The role of the ocean in the global atmospheric sulfur cycle, *J. Geophys. Res.*, *88*, 10903-10914, 1983.

O'Dowd, C. D., and M. H. Smith, Physicochemical properties of aerosols over the northeast Atlantic: evidence for wind speed related submicron sea-salt production, *J. Geophys. Res.*, *98*, 1137-1149, 1993.

Pandis, S. N., and J. H. Seinfeld, Sensitivity analysis of a chemical mechanism for aqueous-phase atmospheric chemistry, *J. Geophys. Res.*, *94*, 1105-1126, 1989.

Parungo, F. P., C. T. Nagamoto, R. Madel, J. Rosinski, and P. L. Haagenson, Marine aerosols in Pacific upwelling regions, *J. Aerosol Sci.*, *18*, 277-290, 1987.

Pruppacher, H. R., and J. D. Klett, *Microphysics of Cloud and Precipitation*, D. Reidel, Norwell, Mass., 1980.

Putaud, J. P., N. Mihalopoulos, B. C. Nguyen, J. M. Campin, and S. J. Belviso, Seasonal variations of atmospheric sulfur dioxide and dimethylsulfide concentrations at Amsterdam island in the southern Indian ocean, *J. Atmos. Chem.*, *15*, 117-131, 1992.

Quinn, P. K., T. Bates, J. Johnson, D. S. Covert, and R. J. Charlson, Interactions between the sulfur and reduced nitrogen cycles over the central Pacific ocean, *J. Geophys. Res.*, *95*, 16405-16416, 1990.

Quinn, P. K., D. S. Covert, T. S. Bates, V. N. Kapustin, D. C. Ramsey-Bell, and L. M. McInnes, Dimethylsulfide cloud condensation nuclei system relevant size-resolved measurements of the chemical and physical properties of atmospheric aerosol particles, *J. Geophys. Res.*, *98*, 10411-10428, 1993.

Raes, F., A. Saltelli, and R. Van Dingenen, Modeling formation and growth of H_2SO_4-H_2O aerosols-Uncertainty analysis and experimental evaluation, *J. Aerosol Sci.*, *23*, 759-771, 1992a.

Raes, F., R. Van Dingenen, J. Wilson and A. Saltelli, Cloud condensation nuclei from dimethyl sulphide in the natural marine boundary layer:remote vs. in-situ production, in *'Dimethylsulphide: Oceans, Atmosphere and Climate'* (eds. G. Restelli and G. Angeletti), Kluwer Academic Publishers, Dordrecht, 311-330, 1992b.

Raes, F., and R. Van Dingenen, Simulations of condensation and cloud condensation nuclei from biogenic SO_2 in the remote marine boundary layer, *J. Geophys. Res.*, *97*, 12901-12912, 1992.

Ray, J. D., C. C. Van Valin, M. Luria, and J. F. Boatman, Oxidants in the marine troposhere: H_2O_2 and O_3 over the western Atlantic Ocean, *Global Biochem. Cycles*, *4*, 201-214, 1990.

Riley, J. P., and R. Chester, *Introduction to Marine Chemistry*, Academic Press, San Diego, Calif., 1971.

Saltzman, E. S., and D. J. Cooper, Shipboard measurements of atmospheric dimethylsulfide and hydrogen sulfide in the Caribbean and Gulf of Mexico, *J. Atmos. Chem.*, *7*, 191-209, 1988.

Saltzman, E. S., D. L. Savoie, R. G. Zika, and J. M. Prospero, Methane sulfonic acid in the marine atmosphere, *J. Geophys. Res.*, *88*, 10897-10902, 1983.

Savoie, D. L., J. M. Prospero, S. J. Oltmans, W. C. Graustein, K. K. Turekian, J. T. Merrill, and H. Levy II, Sources of nitrate and ozone in the marine boundary layer of the tropical north Atlantic, *J. Geophys. Res.*, *97*, 11575-11589, 1992.

Seinfeld, J. H., *Atmospheric Chemistry and Physics of Air Pollution*, John Wiley, New York, 1986.

Sievering, H., J. Boatman, E. Gorman, Y. Kim, L. Anderson, G. Ennis, M. Luria, and S. Pandis, Removal of sulfur from the marine boundary layer by ozone oxidation in sea-salt aerosols, *Nature*, *360*, 571-573, 1992.

Van Dingenen, R. and F. Raes, Determination of the condensation accomodation coefficient of sulfuric acid on water-sulfuric acid aerosol, *Aeros. Sci. Technol.*, *15*, 93-106, 1991.

Warren, D. R. and J. H. Seinfeld, Simulation of aerosol size-distribution evolution in systems with simultaneous nucleation, condensation and coagulation, *Aerosol Sci. Technol.*, *4*, 31-43, 1985.

Wyslouzil, B. E., J. H. Seinfeld, R. C. Flagan and K. Okuyama, Binary nucleation in acid water systems. I. Methanesulfonic-acid water, *J. Chem. Phys.*, *94*, 6827-6841, 1991a.

Wyslouzil, B. E., J. H. Seinfeld, R. C. Flagan and K. Okuyama, Binary nucleation in acid water systems. II. Sulfuric acid-water and a comparison with methanesulfonic acid-water, *J. Chem. Phys.*, *94*, 6842-6850, 1991b.

S. N. Pandis, Department of Chemical Engineering, Carnegie Mellon University, Pittsburgh, PA 15213-3890. (e-mail: spyros@andrew.cmu.edu)

L. M. Russell and J. H. Seinfeld, Department of Chemical Engineering, California Institute of Technology, Pasadena, CA 91125.

(Received September 27, 1993; revised April 21, 1994; accepted April 21, 1994.)

Appendix B

Detailed Method for Online SFE/GC-MS Analysis

B.1 Connecting SFE.

1. Note GC temperatures then lower injector B to well below 100°C (this takes a while so you should do this first).

2. Make sure CO_2 inlet valve on SFE closed. Make sure CO_2 tank valve closed. Unscrew larger (gold) nut slowly. Put large cap over CO_2 tank.

3. Disconnect Accutrap gases (note if they are open or shut). Put tank on cart, fasten it, cart it to GC room. Unplug the four electrical connections. Check brakes on cart. Roll up inlet wire for the SFE; carefully transport to the GC room.

4. Unroll CO_2 inlet line on the SFE. Remove white Teflon tape from the CO_2 tank. Burp the tank, then replace Teflon tape; wrap it around in the same direction you are going to twist it. Fasten CO_2 inlet line from the SFE to the CO_2 tank.

5. Plug in the SFE, Accutrap, heated transfer line, and modifier pump. Make sure you're plumbed in correctly. Open CO_2 valve.

6. Purge the system of "dead air" in the SFE by running in dynamic mode for a while. Equilibrate and look for snow. Set power stat controlling heating tape on connecting tubing in Accutrap to 70; wait around 20 min for the temperature to reach "equilibrium."

7. Connect the heated transfer line: Make sure injector B temperature well below 100°C. Remove plastic lid from injectors. Unscrew green nut on injector; pressure should go to zero. Replace septum. Insert heated transfer line into the septum as close to the center as possible. Make sure not to scrape the injector. About 1 inch of the heated transfer line should be inside the GC. Screw green nut back on carefully, making sure not to tighten it too tightly. Pressure should come back up to about 5 psi.

B.2 In-line SFE-GC extraction.

1. Set the power stat controlling the heating tape on the connecting tubing in the Accutrap to 70. Wait for about 20 min for the temperature inside to reach equilibrium.

2. Turn on the SFE, Accutrap and Modifier pump. If you followed procedure for connecting correctly, you should get a red STOP and green pressure reading zero on the modifier pump.

3. Make sure modifier lead is in the methanol. If it is not, rinse it with methanol and put it in.

4. Remove air bubbles out of modifier:

   (a) make sure on/off valve is closed,

(b) attach syringe to the prime/purge valve and turn it counterclockwise about three turns,

(c) suck about 20 ml out,

(d) close the prime/purge valve.

5. If you are running a method that uses splitless mode, make sure Purge B is OFF on the front panel of the GC oven. Otherwise, make sure you're in split mode by making sure Purge B is ON.

6. Load the method, and let the GC get ready.

   (a) make sure vessel is on Static mode and on/off valve is closed,

   (b) open the vent/purge valve to purge the vessel,

   (c) take out vessel, load sample, put vessel back in,

   (d) make sure: on/off valve is ON, vent/purge valve is closed, and vessel is on Static mode,

   (e) introduce method on the method page (see Table B.1).

7. Check for leaks everyday; go to edit page and select 12.

8. Start the SFE method.

9. Notice: Keep your eye on the pressure gauge (green LED display on modifier pump). The pressure should not exceed 500 atm!

Table B.1: SFE Procedure.

Step	Pressure	Temperature	Period	Mode	Modifier	EPC Setting (GC)
Eq	300 atm	150°C		Static	0% by vol	
1	450 atm	150°C	10 min	Static	0% by vol	
2	450 atm	150°C	10 min	Dynamic	10% by vol	5 ml min^{-1}
3	450 atm	150°C	10 min	Static	0% by vol	5 ml min^{-1}
4	450 atm	150°C	20 min	Dynamic	10% by vol	5 ml min^{-1}
5	0 atm	50°C	20 min	Static	0% by vol	

10. The EPC settings in the SFE procedure refer to the flow control on the GC. A flow rate of 5 ml min^{-1} is used during dynamic transfers from the SFE to the GC.

11. The last step in the SFE procedure serves to reset the SFE and decrease the temperature of the vessel so that the sample may be removed. Thirty seconds after method reaches step 5, hit the start button on the GC oven front panel to start detecting. (The Chemstation GC/MS method should already be loaded and in standby mode.)

B.3 GC/MS Method.

The GC/MS method is controlled by the HP Chemstation software using specifications stored in method files. The operating temperatures and instrument specifications used to separate and detect species collected in the cryotrap are stored in these files specific for each operating method. The cryotrap and column are maintained at -45°C until the SFE method is com-

plete, then the procedures which follow provide the oven temperatures and prescribed heating rates. An Electronic Pressure Control unit (Hewlett-Packard) is used to maintain a constant flow rate of 1 ml min^{-1} during the run. Due to the different operating specifications of the two GC columns, the oven temperatures and ramping rates used for each of the two columns are different. Here we present both the method employed for runs with the HP5MS column and the DB1701 column (HP Unix Chemstation method archived as 5mscryramp320by2.m and 1701cryramp280hi2.m, respectively). Here we summarize the log of the operating specifications for both the MS engine temperature parameters and the GC oven operating rates, as given in the msacqmth.mac files of the ChemStation software. Note that in both cases the operating injector is Injector B and the operating detector is Detector B. The HP5MS method lasts 159.5 min, and the DB1701 method is 123 min since the maximum temperature is lower.

B.3.1 HP-5MS column method 5mscryramp320by2.m.

name msacqmth

CheckConfig 5970A, 5890, 7673

SetAcqInlet GC

SetInjSource MANUAL

if (MSPRESENT = 1) then

SetTuneName /chem/config/dvc/ms5989-1/lmrtune.u

SetEM 0, REL

SetAcqMode SCAN

SetScanParams 1, 50:300, 0, 2

SetScanParams 2, 10:600, 2000, 2

SetScanParams 3, 10:800, 3000, 2

if ((MSTYPE= "$HP5989$")or($MSTYPE$ = "HP5989x")) then

SetZone SOURCE, 250

SetMax SOURCE, 375

SetZone QUAD, 100

SetMax QUAD, 150

endif

SetRunTime 159.5

endif

if (GCPRESENT = 1) then

SetPressureUnits PSI

SetOvenTracking INJA, OFF

SetZone INJA, 100

SetRampInitValue INJA, 100

SetRampInitTime INJA, 10

SetRampRate INJA, 1, 0

SetRampFinalValue INJA, 1, 100

SetRampFinalTime INJA, 1, 0

SetRampRate INJA, 2, 0

SetRampFinalValue INJA, 2, 100

SetRampFinalTime INJA, 2, 0

SetRampRate INJA, 3, 0

SetRampFinalValue INJA, 3, 100

SetRampFinalTime INJA, 3, 0

SetConstantFlow INJA-EPP, OFF

SetRefTemp INJA-EPP, 50

SetRampInitValue INJA-EPP, 0

SetRampInitTime INJA-EPP, 10

SetRampRate INJA-EPP, 1, 0

SetRampFinalValue INJA-EPP, 1, 0

SetRampFinalTime INJA-EPP, 1, 0

SetRampRate INJA-EPP, 2, 0

SetRampFinalValue INJA-EPP, 2, 0

SetRampFinalTime INJA-EPP, 2, 0

SetRampRate INJA-EPP, 3, 0

SetRampFinalValue INJA-EPP, 3, 0

SetRampFinalTime INJA-EPP, 3, 0

SetOvenTracking INJB, OFF

SetZone INJB, 320

SetRampInitValue INJB, 320

SetRampInitTime INJB, 10

SetRampRate INJB, 1, 0

SetRampFinalValue INJB, 1, 100

SetRampFinalTime INJB, 1, 0

SetRampRate INJB, 2, 0

SetRampFinalValue INJB, 2, 100

SetRampFinalTime INJB, 2, 0

SetRampRate INJB, 3, 0

SetRampFinalValue INJB, 3, 100

SetRampFinalTime INJB, 3, 0

SetConstantFlow INJB-EPP, OFF

SetRefTemp INJB-EPP, 50

SetRampInitValue INJB-EPP, 0

SetRampInitTime INJB-EPP, 10

SetRampRate INJB-EPP, 1, 0

SetRampFinalValue INJB-EPP, 1, 0

SetRampFinalTime INJB-EPP, 1, 0

SetRampRate INJB-EPP, 2, 0

SetRampFinalValue INJB-EPP, 2, 0

SetRampFinalTime INJB-EPP, 2, 0

SetRampRate INJB-EPP, 3, 0

SetRampFinalValue INJB-EPP, 3, 0

SetRampFinalTime INJB-EPP, 3, 0

SetZone DETA, OFF

SetZone DETB, 320

SetZone AUX, 280

SetZone OVEN, -45

SetRampInitValue OVEN, -45

SetRampInitTime OVEN, 3

SetRampRate OVEN, 1, 20

SetRampFinalValue OVEN, 1, 35

SetRampFinalTime OVEN, 1, 5

SetRampRate OVEN, 2, 2

SetRampFinalValue OVEN, 2, 320

SetRampFinalTime OVEN, 2, 5

SetRampRate OVEN, 3, 0

SetRampFinalValue OVEN, 3, 0

SetRampFinalTime OVEN, 3, 0

SetMax OVEN, 325

SetEquibTime 0.5

SetCryo ON

SetCryoBlast OFF

SetCryoAmbient 25

SetPurge A, OFF

SetPurgeTime A, ON, 0

SetPurgeTime A, OFF, 0

SetPurge B, ON

SetPurgeTime B, ON, 0

SetPurgeTime B, OFF, 0

endif

SetUpPlot 3, 10, 3, ACTIVE

SetPlotParams 1, TIC, 10:800, 1.07983e+06

SetPlotParams 2, SPECTRUM, 10:110, 4096.02

SetPlotParams 3, EIC, 50:110, 1.12206e+06

ClrRunTable

AddRtEntry 0, GROUP, 1

AddRtEntry 2.5, STORAGE, ON

AddRtEntry 3, MSON

SetSolvDelay

return

An example of the extraction and identification of compounds with this method employing the HP5MS column is illustrated in Figure B.1.

B.3.2 DB-1701 column method 1701cryramp280hi2.m.

name msacqmth

CheckConfig 5970A, 5890, 7673

SetAcqInlet GC

SetInjSource MANUAL if (MSPRESENT = 1) then

SetTuneName /chem/config/dvc/ms5989-1/lmrtune.u

SetEM 0, REL

SetAcqMode SCAN

SetScanParams 1, 50:300, 0, 2

SetScanParams 2, 10:600, 2000, 2

SetScanParams 3, 10:800, 3000, 2

if ((MSTYPE= "$HP5989$")or($MSTYPE$ = "HP5989x")) then

SetZone SOURCE, 250

SetMax SOURCE, 375

SetZone QUAD, 100

SetMax QUAD, 150

endif

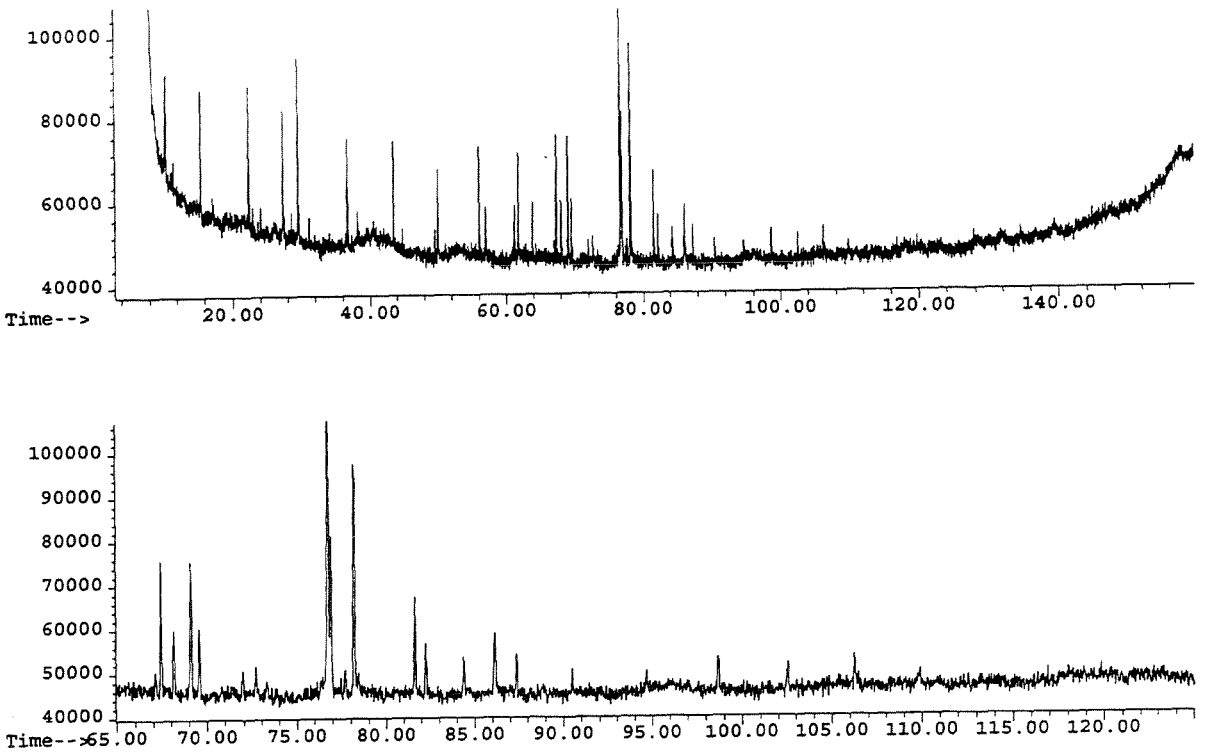

Figure B.1: Total ion chromatogram for HP5MS column method. The top diagram illustrates the complete chromatogram and the bottom diagram shows the detail where the PAHs studied elute. In both diagrams, the left axis is total ion abundance and the bottom axis is time in minutes. The PAHs included in this chromatogram may be identified from their retention times in Table C.3. For this analysis, 10 μl of diluted mixture of the standards listed in Table C.3 (obtained from Accustandard, Inc.) was placed on a quartz filter and extracted by SFE with the method described above.

SetRunTime 123

endif

if (GCPRESENT = 1) then

SetPressureUnits PSI

SetOvenTracking INJA, OFF

SetZone INJA, 100

SetRampInitValue INJA, 100

SetRampInitTime INJA, 10

SetRampRate INJA, 1, 0

SetRampFinalValue INJA, 1, 100

SetRampFinalTime INJA, 1, 0

SetRampRate INJA, 2, 0

SetRampFinalValue INJA, 2, 100

SetRampFinalTime INJA, 2, 0

SetRampRate INJA, 3, 0

SetRampFinalValue INJA, 3, 100

SetRampFinalTime INJA, 3, 0

SetConstantFlow INJA-EPP, OFF

SetRefTemp INJA-EPP, 50

SetRampInitValue INJA-EPP, 0

SetRampInitTime INJA-EPP, 10

SetRampRate INJA-EPP, 1, 0

SetRampFinalValue INJA-EPP, 1, 0

SetRampFinalTime INJA-EPP, 1, 0

SetRampRate INJA-EPP, 2, 0

SetRampFinalValue INJA-EPP, 2, 0

SetRampFinalTime INJA-EPP, 2, 0

SetRampRate INJA-EPP, 3, 0

SetRampFinalValue INJA-EPP, 3, 0

SetRampFinalTime INJA-EPP, 3, 0

SetOvenTracking INJB, OFF

SetZone INJB, 280

SetRampInitValue INJB, 280

SetRampInitTime INJB, 10

SetRampRate INJB, 1, 0

SetRampFinalValue INJB, 1, 100

SetRampFinalTime INJB, 1, 0

SetRampRate INJB, 2, 0

SetRampFinalValue INJB, 2, 100

SetRampFinalTime INJB, 2, 0

SetRampRate INJB, 3, 0

SetRampFinalValue INJB, 3, 100

SetRampFinalTime INJB, 3, 0

SetConstantFlow INJB-EPP, OFF

SetRefTemp INJB-EPP, 50

SetRampInitValue INJB-EPP, 0

SetRampInitTime INJB-EPP, 10

SetRampRate INJB-EPP, 1, 0

SetRampFinalValue INJB-EPP, 1, 0

SetRampFinalTime INJB-EPP, 1, 0

SetRampRate INJB-EPP, 2, 0

SetRampFinalValue INJB-EPP, 2, 0

SetRampFinalTime INJB-EPP, 2, 0

SetRampRate INJB-EPP, 3, 0

SetRampFinalValue INJB-EPP, 3, 0

SetRampFinalTime INJB-EPP, 3, 0

SetZone DETA, OFF

SetZone DETB, 280

SetZone AUX, 280

SetZone OVEN, -45

SetRampInitValue OVEN, -45

SetRampInitTime OVEN, 3

SetRampRate OVEN, 1, 20

SetRampFinalValue OVEN, 1, 105

SetRampFinalTime OVEN, 1, 5

SetRampRate OVEN, 2, 2

SetRampFinalValue OVEN, 2, 280

SetRampFinalTime OVEN, 2, 20

SetRampRate OVEN, 3, 0

SetRampFinalValue OVEN, 3, 0

SetRampFinalTime OVEN, 3, 0

SetMax OVEN, 280

SetEquibTime 0.5

SetCryo ON

SetCryoBlast OFF

```
SetCryoAmbient 25
SetPurge A, OFF
SetPurgeTime A, ON, 0
SetPurgeTime A, OFF, 0
SetPurge B, ON
SetPurgeTime B, ON, 0
SetPurgeTime B, OFF, 0
endif
SetUpPlot 3, 10, 3, ACTIVE
SetPlotParams 1, TIC, 10:800, 1.07983e+06
SetPlotParams 2, SPECTRUM, 10:110, 4096.02
SetPlotParams 3, EIC, 50:110, 1.12206e+06
ClrRunTable
AddRtEntry 0, GROUP, 1
AddRtEntry 2.5, STORAGE, ON
AddRtEntry 3, MSON
SetSolvDelay
return
```

An example of the extraction and identification of compounds with this method employing the DB1701 column is illustrated in Figure B.2.

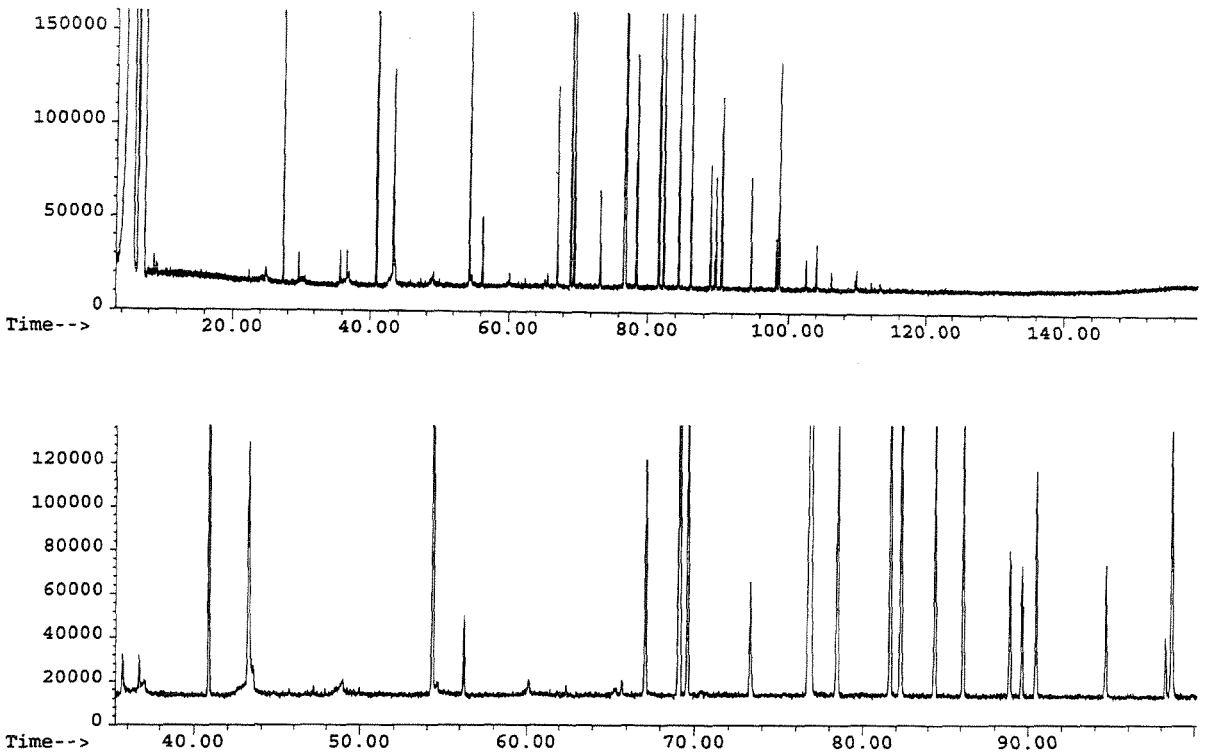

Figure B.2: Total ion chromatogram for DB1701 column method. The top diagram illustrates the complete chromatogram and the bottom diagram shows the detail where the PAHs studied elute. In both diagrams, the left axis is total ion abundance and the bottom axis is time in minutes. The PAHs included in this chromatogram may be identified from their retention times in Table C.3. For this analysis, 5 μl of diluted mixture of the standards listed in Table C.3 (obtained from Accustandard, Inc.) was placed on a quartz filter and extracted by SFE with the method described above.

B.4 Disconnecting SFE.

1. Cool Injector B to well below 100°C by using the keyboard on the GC front panel (it takes a while so you should do this first).

2. Purge system: close CO_2 inlet valve on the SFE, open vent purge valve until all CO_2 is out, and take your sample out of the SFE.

3. Disconnect all the plugs. Close CO_2 tank valve. Slowly unscrew smaller nut (silver), then unscrew larger nut (gold). Roll SFE inlet line up carefully; put it somewhere on the SFE so it's out of the way.

4. If injector temperature has dropped low enough to comfortably touch, unscrew green nut, pull heated transfer line out of septum, lay it carefully on SFE so that it's out of the way, then replace septum. Put green nut back on injector, and pressure should come back up to about 5 psi.

5. Carefully transport SFE to its place at the back of the lab; set the brakes.

6. Remove large cap from the CO_2 tank. Burp the tank. Replace Teflon tape (make sure to wrap it around in the same direction you are going to twist it). Screw on the large gold nut. Attach the smaller silver nut to the CO_2 tank.

7. Connect accutrap gases. Purge the SFE again to get all the "dead" air that may have developed when you were transporting it. Make sure to

prepare the GC for the next user:

(a) replace the septum,

(b) set oven temp to 200°C (if there is a chance water is in the column from your runs, you should only go up to 150°C),

(c) set Injector B and Detector B temperatures on GC oven front panel to 220°C,

(d) put the lid back on injectors.

Appendix C

Organic Analysis Logs, Standards, and MAST Experiment Data

Table C.1: Aerosol interstitial and out-of-cloud filter samples analysis log.

PC File	Disk	Unix File	Disk	JDT	Sample	Column	Analysis	CO_2	Flow	Last EM	Next EM	Run Obs	Comments
		S6001		151	stby-blank								
S6002~s1.d	3B	S6002B51.d	3B	151	ferry	HP5MS	01/03/95	B		1701	1701		Seattle/Monterey ferry
S6003~l3.d	3B	S6003C51.d	3B	151	flt-blank	HP5MS	01/03/95	B		1701	1701	17	
		S6004		151	flt-blank			B					
S6005~00.d	2B	S6005gba.d	2B	152	glv-blank	HP5MS	12/28/94	B		1654	1677	12	
S6005~4m.d	2B	S6005gbb.d	2B	152		HP5MS	12/28/94	B		1654	1677		
S6006~00.d	1B	S6006A52.d		152	bkgd-mbl	HP5MS	11/19/94	A'	2.05		1748	8,10	
S6006~v8.d	1B	S6006r2.d				HP5MS	11/20/94	A'		1748	1819	3,8	
S6007~c1.d	1B	S6007B52.d		152	plume-mbl	HP5MS	11/19/94	A'	2.24		1748	6,8,9	Mexicana Linea, few
S6007~00.d	1B	S6007r2.d				HP5MS	11/19/94	A'			1748	3,10	particles in DMPS
S6008~00.d	1B	S6008blk.d		152	flt-blank	HP5MS	11/19/94	A'			1748	7	
		S6009			flt-blank			A'					
S6010~6s.d	3B	S6010A59.d	3A	159	plume-mbl	HP5MS	12/31/94	B	2.54	1677	1677	10,17	sample lost
S6011~9p.d	3B	S6011B59.d	3A	159	bkgd-mbl	HP5MS	12/31/94	B	1.58	1677	1677		
S6012~cj.d	3B	S6012C59.d	3A	159	flt-blank	HP5MS	12/31/94	B		1677	1677	7,12,19	
S6013~fd.d	3B	S6013D59.d	3A	159	bkgd-mbl	HP5MS	12/31/94	B	0.945	1677	1677		
S6014~00.d	2B	S6014A60.d	2A	160	plume-mbl	DB1701	11/27/94	A	2.925	1724	1724		no clouds
S6015~nd.d	2B	S6015B60.d	2A	160	amb-inst	DB1701	11/27/94	A	0.983	1724	1724		
S6016~00.d	2B	S6016C60.d	2A	160	flt-blank	DB1701	11/27/94	A		1724	1724	4,11	
S6017~ui.d	2B	S6017A62.d	2A	162	track-inst	DB1701	11/28/94	A	2.23	1724	1772	4,5	
S6018~00.d	2B	S6018B62.d	2A	162	amb-inst	DB1701	11/28/94	A	2.04	1724	1772	4,9	
S6019~00.d	2B	S6019C62.d	2A	162	flt-blank	DB1701	11/28/94	A		1724	1772	4	
S6020~00.d	2B	S6020A63.d	2A	163	plume-mbl	DB1701	11/30/94	B	2.198	1748	1724	9	
S6021~00.d	2B	S6021B63.d	2A	163	bkgd-mbl	DB1701	11/30/94	B	1.65	1724	1795		
S6022~00.d	2B	S6022C63.d	2A	163	track-inst	DB1701	11/30/94	B	1.763	1724	1795		Safeguard, Glorita
S6023~00.d	2B	S6023D63.d	2A	163	flt-blank	DB1701	11/30/94	B		1748	1724	10	
S6024~pa.d	2B	S6024A66.d	2A	166	plume-mbl	DB1701	11/29/94	B	1.103	1772	1748	8,12,13,14	Abe Lincoln
S6025~gp.d	2B	S6025B66.d	2A	166	bkgd-mbl	DB1701	11/29/94	B	1.425	1772	1748	12	
S6026~8m.d	2B	S6026C66.d	2A	166	flt-blank	DB1701	11/29/94	B		1772	1748	12	
S6027~00.d	2B	S6027A72.d	2B	172	amb-inst	HP5MS	12/27/94	B	1.628	1724	1630	5	
S6028~yf.d	2B	S6028B72.d	2B	172	track-inst	HP5MS	12/27/94	B	2.175	1724	1630	1,5,7,12	
S6029~sx.d	2B	S6029C72.d	2B	172	plume-mbl	HP5MS	12/28/94	B	1.335	1630	1654	12	
S6030~hu.d	3A	S6030D72.d	2B	172	bkgd-mbl	HP5MS	12/28/94	B	1.560	1630	1654		
S6031~lj.d	3A	S6031E72.d	2B	172	flt-blank	HP5MS	12/27/94	B		1724	1630	5,7	
S6032~i7.d	3A	S6032F72.d	3A	172	flt-blank	HP5MS	12/28/94	B		1630	1654	12	
S6033~l6.d	3A	S6033A78.d	3A	178	track-inst	HP5MS	12/29/94	B	2.213	1677	1654	2,7	
S6034~38.d	3A	S6034B78.d	3A	178	amb-inst	HP5MS	12/29/94	B	2.010	1677	1654	17	
S6035~bt.d	3A	S6035C78.d	3A	178	track-inst	HP5MS	12/29/94	B	1.590	1677	1654		Costco
S6036~75.d	3A	S6036D78.d	3A	178	bkgd-mbl	HP5MS	12/29/94	B	1.673	1677	1654		
S6037~e7.d	3A	S6037E78.d	3A	178	plume-mbl	HP5MS	12/29/94	B	1.612	1677	1654		Mt. Vernon
S6038~jg.d	3A	S6038F78.d	3A	178	flt-blank	HP5MS	12/29/94	B		1677	1654	10,12	
S6039~op.d	3B	S6039A79.d	3B	179	amb-inst	HP5MS	01/01/95	B	1.748	1677	1654	18	
S6040~tp.d	3B	S6040B79.d	3B	179	track-inst	HP5MS	01/01/95	B	2.850	1677	1654	18	
S6041~xc.d	3B	S6041C79.d	3B	179	scuz-ft	HP5MS	01/01/95	B	0.893	1677	1654	18	
S6042~fx.d	3B	S6042D79.d	3B	179	flt-blank	HP5MS	01/01/95	B		1677	1654	18	
S6043~jn.d	3B	S6043A80.d	3B	180	amb-inst	HP5MS	01/02/95	B	1.950	1654	1701	18	dirty ambient
S6044~aw.d	4A	S6044B80.d	3B	180	track-inst	HP5MS	01/02/95	B	2.153	1654	1701	18	
S6045~1j.d	4A	S6045C80.d	3B	180	amb-inst	HP5MS	01/02/95	B	1.628	1654	1701	9,18	cleaner ambient
S6046~7q.d	4A	S6046D80.d	3B	180	plume-mbl	HP5MS	01/02/95	B	1.575	1654	1701	1,18	Star Livorno
S6047~yi.d	4A	S6047E80.d	3B	180	bkgd-mbl	HP5MS	01/02/95	B	1.598	1654	1701	18	
S6048~sk.d	4A	S6048F80.d	3B	180	flt-blank	HP5MS	01/02/95	B		1654	1701	18	
S6049~bo.d	3B	S6049A81.d	3A	181	amb-inst	HP5MS	12/30/94	B	2.018	1654	1677		
S6050~24.d	3B	S6050B81.d	3A	181	track-inst	HP5MS	12/30/94	B	1.875	1654	1677	1,17	clouds dissipating
S6051~bm.d	3B	S6051C81.d	3A	181	plume-mbl	HP5MS	12/30/94	B	1.358	1654	1677	12	NYK Sunrise
S6052~xa.d	3B	S6052D81.d	3A	181	bkgd-mbl	HP5MS	12/30/94	B	1.628	1654	1677		
S6053~54.d	3B	S6053E81.d	3A	181	plume-mbl	HP5MS	12/30/94	B		1654	1677		Copeland
S6054~bk.d	3B	S6054F81.d	3A	181	flt-blnk	HP5MS	12/30/94	B		1654	1677		

1 SPE pressured and vented due to leak in SPE vessel
2 SPE pressured and vented for other reason
3 Extraction repeated on pre-extracted sample
4 EPC did not maintain constant flow during run
5 EPC off during run
6 Bubble in SPE modifier line
7 Switched to dynamic mode early (during static phase) to avoid overpressure
8 GC warmed above -45 deg C during SPE run
9 GC run started more than 1 min after end of SPE cycle
10 GC run interrupted or shortened
11 Leak in GC noted, or bad air/water check
12 SPE pressure fluctuates between 437 and 442 atm or other signs of leak
13 Rupture disk blown during run
14 LN2 ran out during run and replaced
15 Filter packed with baked blank
16 Extended SPE static run to allow GC to cool to -45 deg C
17 EPC low during part or all of dynamic phase
18 Used vinyl gloves
19 Allowed upstream leak to release pressure
20 Sample jar seal broken during storage
21 Bad frit used in run
22 Standard method not used

Table C.2: Residual cloud droplet samples analysis log.

PC File	Disk	Unix File	Disk	JDT	Sample	Column	Analysis	CO_2	Flow	Last EM	Next EM	Run Obs	Comments
C2001-00.d	1B	C2001gb.d	1B	152	glv-blank	HP5MS	11/20/94	A'		1748	1819	8,11,15	
C2002-00.d	1B	C2002A52.d	1B	152	ambient	HP5MS	11/20/94	A'		1748	1819	7,11,15	
C2003-00.d	1B	C2003B52.d	1B	152	track	HP5MS	11/20/94	A'		1748	1819	2,11,15	Mexicana Linea
C2004-00d	1B	C2004A59.d	1B	159	ambient	HP5MS	11/21/94	A'	0.541	1819	1843	1	
C2004-tp.d	1B		1B					A'					
C2005-00.d	1B	C2005B59.d	1B	159	track	HP5MS	11/21/94	A'	0.142	1819	1843	10	
C2006-00.d	1B	C2006A60.d	2A	160	plume	DB1701	12/02/94	B	0.035	1795	1772	16	steaming north
C2007-00.d	1B	C2007B60.d	2A	160	plume	DB1701	12/02/94	B	0.049	1795	1772	16	steaming south
C2008-00.d	1B	C2008A62.d	2A	162	bkgd-mbl	DB1701	12/02/94	B	1.329	1795	1772	16,17	
C2009-61.d	1B	C2009B62.d	2A	162	plume	DB1701	12/02/94	B	0.171	1795	1772	8	
C2010-00.d	3A	C2010A63.d	2B	163	ambient	DB1701	12/03/94	B	0.254	1772	1819		
C2011-00.d	3A	C2011B63.d	2B	163	track	DB1701	12/03/94	B	0.091	1772	1819	7	
C2012-00.d	3A	C2012G59.d	2B	163	glv-blank	DB1701	12/03/94	B		1772	1819		
C2013-00.d	3A	C2013A59.d	2B	166	bkgd-mbl	DB1701	12/04/94	B	0.083	1819	1795		
C2014-2b.d	3A	C2014B60.d	2B	166	plume	DB1701	12/04/94	B	0.024	1819	1795	16	Abe Lincoln
C2015-p2.d	3A	C2015G60.d	2B	166	glv-blank	DB1701	12/04/94	B		1819	1795	1	
C2016-i9.d	3A	C2016A68.d	2B	168	ambient	DB1701	12/04/94	B	0.082	1819	1795	7	
C2017-iq.d	3A	C2017B68.d	2B	168	flt-blank	DB1701	12/04/94	B	0.000	1819	1795		
C2018-j9.d	4A	C2018A72.d	4A	172	ambient	HP5MS	01/07/95	C	0.665		1724		
C2019-hn.d	4A	C2019B72.d	4A	172	track	HP5MS	01/07/95	C	0.160		1724	8	
C2020-00.d	4A	C2020G72.d	4A	172	glv-blank	HP5MS	01/07/95	C			1724		
C2021-00.d	4A	C2021A78.d	4A	178	ambient	HP5MS	01/06/95	C	0.635	1866			
C2022-00.d	4A	C2022B78.d	4A	178	track	HP5MS	01/06/95	C	0.127	1866			Tai He
C2023-00.d	4A	C2023G78.d	4A	178	glv-blank	HP5MS	01/06/95	C		1724	1866		
C2024-00.d	4A	C2024G79.d	4A	179	glv-blank	HP5MS	01/03/95	C		1701	1724	2,12,21	
C2025-00.d	4A	C2025A79.d	4A	179	ambient	HP5MS	01/03/95	C	0.287	1701	1724		
C2026-00d	4B	C2026B79d	4A	179	track	HP5MS	01/03/95	C	0.085	1701	1724	20	Mt. Vernon
C2027-cw.d	4B	C2027G80.d	4A	180	glv-blank	HP5MS	01/03/95	B		1701	1701		
C2028-4ud	4B	C2028A80d	4A	180	ambient	HP5MS	01/03/95	B	0.835	1701	1701		
C2029-0a.d	4B	C2029B80.d	4A	180	track	HP5MS	01/03/95	B	0.109	1701	1701		Star Livorno
C2030-00.d	4A	C2030G81.d	4B	181	glv-blank	HP5MS	01/04/95	B		1701	1701	2,12	
C2031-00.d	4A	C2031A81.d	4B	181	ambient	HP5MS	01/04/95	B	0.630	1701	1701		
C2032-00.d	4A	C2032B81.d	4B	181	track	HP5MS	01/04/95	B	0.088	1701	1701		NYK Sunrise

1 SPE pressured and vented due to leak in SPE vessel
2 SPE pressured and vented for other reason
3 Extraction repeated on pre-extracted sample
4 EPC did not maintain constant flow during run
5 EPC off during run
6 Bubble in SPE modifier line
7 Switched to dynamic mode early (during static phase) to avoid overpressure
8 GC warmed above -45 deg C during SPE run
9 GC run started more than 1 run after end of SPE cycle
10 GC run interrupted or aborted
11 Leak in GC noted, or bad air/water check
12 SPE pressure fluctuates between 437 and 442 atm or other signs of leak
13 Rupture disk blown during run
14 LN2 ran out during run and replaced
15 Filter packed with baked blank
16 Extended SPE static run to allow GC to cool to -45 deg C
17 EPC low during part or all of dynamic phase
18 Used vinyl gloves
19 Allowed upstream leak to release pressure
20 Sample jar seal broken during storage
21 Bad frit used in run
22 Standard method not used

Table C.3: Primary standards and their retention times.

	Carbon Index	Molecular Weight amu	Major Mass Spectral Peaks M/Z	Retention Time DB-1701 min	Retention Time HP-5MS min	Detection Limit DB-1701 µg	Detection Limit HP-5MS µg
n-Alkanes							
nonadecane	C-19	268.3	57, 71, 85	39.57	77.02	1.11E-01	1.88E-02
eicosane	C-20	282.3	57, 71, 85	44.58	81.73	7.31E-02	2.44E-02
heneicosane	C-21	296.3	57, 71, 85	48.75	86.20	7.48E-02	3.34E-02
docosane	C-22	310.4	57, 71, 85	53.08	90.52	7.54E-02	5.13E-02
tricosane	C-23	324.4	57, 71, 85	57.21	94.38	7.12E-02	8.22E-02
tetracosane	C-24	338.4	57, 71, 85	61.18	98.36	3.01E-01	8.30E-02
pentacosane	C-25	352.4	57, 71, 85	65.03	102.30	2.58E-02	9.87E-02
hexacosane	C-26	366.4	57, 71, 85	68.75	106.24	1.43E-02	5.51E-02
heptacosane	C-27	380.4	57, 71, 85	72.33	109.45	1.05E-02	9.42E-02
octacosane	C-28	394.5	57, 71, 85	75.77	113.02	1.13E-02	1.08E-01
nonacosane	C-29	408.5	57, 71, 85	79.09	116.23	1.42E-02	1.19E-01
triacontane	C-30	422.5	57, 71, 85	82.31	119.88	2.41E-02	1.64E-01
hentriacontane	C-31	436.5	57, 71, 85	85.45	NR	3.62E-02	NR
n-Alkanoic Acids							
hexanoic acid	C-6	116.1	60, 27, 87	11.54	24.44	1.42E-01	1.05E+00
heptanoic acid	C-7	130.1	60, 27, 87	12.90	31.21	3.34E-01	1.30E+00
octanoic acid	C-8	144.1	60, 27, 87	15.10	37.93	6.84E+00	1.36E+00
nonanoic acid	C-9	158.1	60, 27, 87	18.95	43.78	9.07E-01	1.42E+00
decanoic acid	C-10	172.1	60, 27, 87	23.63	49.62	7.46E-01	1.40E+00
undecanoic acid	C-11	186.2	60, 27, 87	27.99	54.43	2.14E+00	1.13E+00
dodecanoic acid	C-12	200.2	60, 27, 87	32.88	60.60	1.42E+00	9.96E-01
tridecanoic acid	C-13	214.2	60, 27, 87	37.53	65.75	9.66E+00	9.71E-01
tetradecanoic acid	C-14	228.2	60, 27, 87	42.23	70.72	1.70E+01	1.41E+00
pentadecanoic acid	C-15	242.2	60, 27, 87	NR	75.51	NR	2.82E+00
Substituted Benzaldehydes and Benzoic Acid							
4-methylbenzaldehyde	C-8	120.1	119, 91, 65	12.12	26.16	9.62E-01	1.09E+00
3,4-dimethyloxybenzaldehyde	C-9	166.1	166, 95,151	28.86	54.43	2.80E-01	6.62E-01
4-methylbenzoic acid	C-8	136.1	91, 136, 65	NR	44.22	NR	1.17E+00
Polycyclic Aromatic Hydrocarbons							
anthracene	C-14	178.1	178, 89, 76	39.53	69.74	1.13E-01	2.29E-02
phenanthrene	C-14	178.1	178, 89, 76	39.53	69.30	NQ	2.77E-02
flouranthene	C-16	202.1	202, 101, 87	53.00	82.42	3.14E-02	2.31E-02
pyrene	C-16	202.1	202, 101, 88	54.97	84.54	3.30E-02	2.83E-02
benzo[a]flourene	C-17	216.1	216, 108, 187	59.24	88.99	6.78E-02	1.52E-01
benzo[b]flourene	C-17	216.1	216, 108,189	60.01	89.73	7.84E-02	1.80E-01
benz[a]anthracene	C-18	228.1	228, 114, 164	69.39	98.33	3.60E-02	3.93E-02
chrysene (1)	C-18	228.1	228, 114, 202	69.69	98.75	2.86E-02	7.26E-02
triphenylene (1)	C-18	228.1	228, 114, 202	69.69	98.75	NQ	NQ
benzo[a]pyrene (2)	C-20	252.1	252, 126, 113	81.38	109.61	5.76E-02	6.26E-02
benzo[k]fluoranthene (2)	C-20	252.1	252, 126, 112	81.05	109.61	NQ	NQ
benzo[e]pyrene	C-20	252.1	252, 126, 113	84.79	NR	7.04E-02	3.63E-01
perylene	C-20	252.1	252, 126, 113	83.42	111.99	2.87E-02	3.28E-01
indeno[1,2,3-cd]pyrene	C-22	276.1	276, 138, 125	94.21	122.32	3.37E-02	3.68E-01
benzo[ghi]perylene	C-22	276.1	276, 138, 125	95.93	124.14	3.22E-02	3.05E-01
dibenz[a,h]anthracene	C-22	276.1	278, 139, 125	95.03	122.98	3.42E-02	1.12E+00
Polycyclic Aromatic Ketones and Quinones							
9H-flouren-9-one (flourenone)	C-13	180.1	180, 152, 126	39.06	67.23	1.24E-01	4.56E-02
9,10-anthracenedione (anthraquinone)	C-14	208.1	180, 208, 152	50.34	78.26	3.06E-02	1.03E-01
9H-xanthen-9-one (xanthone)	C-13	196.1	196, 168, 139	44.84	73.37	7.23E-02	1.45E-01
7H-benz[de]anthracen-7-one	C-17	230.1	230, 202, 101	72.89	99.94	6.34E-02	4.12E-01
Other							
1-methyl-2-pyrrolidinone (m-pyrol)	C-5	99.1	99, 44	12.29	24.23	9.35E-02	2.96E-01
N,N-dibutylformamide	C-9	157.1	72, 114 , 30	18.92	42.72	7.58E-02	3.59E-02
2-(2-butoxyethoxy) ethanol	C-8	162.1	57, 75, 132	13.61	35.50	4.63E-01	8.02E-01
2,3-dihydroxyl-1H-indan-1-one (indanone) cholesterol	C-9	132.1	276, 138, 224	17.80	40.97	4.46E-01	3.23E-01
1,1'-sulfonylbis-benzene (reference time standard only)	C-12	218	125, 77, 218	52.36	76.73		

NR - compound not resolved
NQ - compound not quantified

(1) Since the chromatographic elution peaks of chrysene and triphenylene were not resolved, their concentrations are reported together.
(2) Since the chromatographic elution peaks of benz[a]pyrene and benzo[k]fluoranthene were not resolved, their concentrations are reported together.

Table C.4: Compound concentrations in all samples and blanks collected for MAST Experiment.

Mass Collected	S6002-S1.D	S6003-L3.D	S6005-00.D	S6005-4M.D	S6006-00.D	S6006-V8.D	S6007-C1.D
nonadecane	0.033572	0.033086	0.028744	0.058634	0	0.127073	1.721501
eicosane	2.740548	0.035796	0.098581	0.031313	0	3.138426	1.783455
heneicosane	4.863557	0.321099	0.128612	0.0361	0	4.449742	2.841134
docosane	4.026353	0.223063	0.206184	0.268417	0	4.389237	2.26135
tricosane	-1	2.683289	0.547008	2.500375	0	0.154871	-1
tetracosane	-1	1.815028	0.946732	-1	0	0.140212	-1
pentacosane	-1	0.722332	2.065208	-1	0	0.140782	-1
hexacosane	0.716592	0.055452	1.85932	0.121723	0	-1	8.284061
heptacosane	4.210562	0.578114	6.409239	-1	0	-1	-1
octacosane	0.446298	0.177458	-1	-1	0	-1	4.877595
nonacosane	0.160151	0.563846	-1	-1	0	-1	1.263605
triacontane	0.368749	0.323289	0.178207	0.240317	0	-1	0.402221
hexanoic acid	0	0	0	0	0	1.12432	0
heptanoic acid	0	0	0	0	0	1.331895	1.421212
octanoic acid	1.987573	0	0	0	0	0	0
nonanoic acid	0	0	0	0	0	11.93526	0
decanoic acid	0	0	0	0	0	0	0
undecanoic acid	0	1.144426	0	0	0	0	0
dodecanoic acid	3.695821	0	0	0	0	7.388805	4.165285
tridecanoic acid	1.398488	1.448322	0	0	0	1.915207	1.271422
tetradecanoic acid	0	0	0	0	0	1.550463	0
pentadecanoic acid	0	0	0	0	0	3.33235	0
4-methyl-benzoic acid	0	0	0	0	0	1.383227	0
4-methyl-benzaldehyde	0	1.184832	0	1.370081	0	0	1.847252
3,4-dimethoxybenzaldehyde	0	0	0	0	0	0	0.858001
anthracene	0	0	0.034039	0	0	0.0857	0.152398
phenanthrene	0.098032	0.203226	0.040928	0.052631	0	0.310804	0.372806
fluoranthene	0.093045	0.087121	0.096116	0	0	1.183356	0.832965
pyrene	0.167379	0.196122	0.120368	0.030921	0	1.582115	1.147344
11H-benzo[a]fluorene	0	0	0	0	0	2.877736	2.094567
11H-benzo[b]fluorene	0	0	0	0	0	2.943954	2.154985
benz[a]anthracene	0	0	0.466606	0.07918	0	1.473998	2.379162
chrysene	0	0	0.389161	0.201	0	2.804508	1.795813
triphenylene	0	0	0.460985	0.078226	0	1.456236	0.844478
benzo[a]pyrene	0	0	0.206995	0.095037	0	0.446685	0.181008
benzo[e]pyrene	0	0	0.68767	1.029603	0	3.670314	1.546573
benzo[k]fluoranthene	0	0	0.210828	0.096797	0	0.454956	0.184359
perylene	0	0	1.197804	0.668304	0	3.411038	1.612708
indeno[1,2,3-cd]pyrene	0	0	0	0.581003	0	0	0
benzo[ghi]perylene	0	0	1.000507	0.805405	0	0.707854	0
dibenz[a,h]anthracene	0	0	1.301171	2.231376	0	1.368558	0
9H-fluoren-9-one	0.062987	0.104144	0.055519	0	0	0.237106	0.215221
9,10-anthracenedione	0	0	0.221607	0	0	0.485648	0.547504
9H-xanthen-9-one	0	0.45646	0	0	0	0.434919	0.472639
7H-benz[de]anthracen-7-one	0	0	0	0.418742	0	1.405408	0
1-methyl-2-pyrrolidinone	0.879536	-1	0	0.644825	0.30959	0.461357	1.334542
N,N-dibutylformamide	-1	0	0	0	0	0.03752	0.041054
2-(2-butoxyethoxy)-ethanol	0	0	0	0	0	0	0
2,3-dihydro-1H-inden-1-one	0.539434	0	0	0	0	0.945213	0.746116
benz[a]anthracen-7,12-dione	0	0	0	0	0	0.265593	0
1,1'-sulfonylbisbenzene	1	1	1	1	0	1	1

Mass Collected	S6008~00.D	S6010~6S.D	S6011~9P.D	S6012~CJ.D	S6013~FD.D	S6014~00.D	S6015~ND.D
nonadecane	6.26323	0.23758	0.024136	0.027246	0.025185	0.0508516	0.5207009
eicosane	5.076562	0.048939	0.033116	0.10795	0.037745	1.0598328	0.3486696
heneicosane	4.57961	0.05679	4.461742	0.085982	4.200451	1.7533721	0.5889194
docosane	3.695795	0.225973	0.258224	0.070314	0.158596	0.0424043	0.3023772
tricosane	-1	0.083241	0.110251	-1	-1	0.0143349	0.4992572
tetracosane	-1	0.19689	-1	-1	-1	5.5554123	1.2126027
pentacosane	-1	0.137984	-1	-1	-1	0.1233126	1.3426428
hexacosane	-1	0.092705	-1	0.101892	-1	0.0917802	1.2688663
heptacosane	-1	0.863888	-1	-1	-1	0.0596111	1.1113177
octacosane	-1	0.736312	-1	-1	-1	0.0398128	1.0150147
nonacosane	2.404521	0.225072	-1	-1	-1	3.4657104	1.0013769
triacontane	0.641539	0.233655	-1	-1	-1	3.1049085	0.8863808
						2.3350708	0.6901855
hexanoic acid	1.141925	0	0	0	1.075461	0.037276	0.0155079
heptanoic acid	0	0	0	0	0	0.1213464	0
octanoic acid	0	0	1.941741	1.463647	0	19.446027	1.0850478
nonanoic acid	0	0	0	0	0	44.361955	2.1455921
decanoic acid	0	0	0	0	0	0.2015435	0.0959944
undecanoic acid	0	0	0	0	0	1.2506255	0
dodecanoic acid	1.105461	0	3.295842	3.023192	0	0.1516091	0.1504713
tridecanoic acid	2.747036	1.391311	0	1.160978	1.243028	0	0
tetradecanoic acid	0	2.423852	0	0	0	7.3380947	0
pentadecanoic acid	4.875394	10.51688	0	0	0	0	0
4-methyl-benzoic acid	0	0	0	0	0		
4-methyl-benzaldehyde	1.967948	0	1.320212	1.588688	0	0.3812868	0.2389295
3,4-dimethoxybenzaldehyde	0	0	0	0	0	0.0525826	0
anthracene	0.270672	0	0	0	0	0.0906759	0.0703399
phenanthrene	0.706006	0	0.094815	0.15825	0.121958	0.0479273	0.0371786
fluoranthene	1.200234	0	0.077152	0.10635	0.101845	0.0389589	0.0149755
pyrene	1.665645	0	0.109469	0.259608	0.143268	0.0403672	0.0177175
11H-benzo[a]fluorene	2.592685	0	0	0	0	0.0088879	0
11H-benzo[b]fluorene	2.614354	0	0	0.201411	0	0.0114172	0
benz[a]anthracene	3.292156	0	0	0	0	0.009267	0.0100735
chrysene	2.378154	0	0	0	0	0.005369	0.0040732
triphenylene	1.053679	0	0	0	0	0.0053761	0.0040786
benzo[a]pyrene	0.225647	0	0.097019	0	0.074125	0	0
benzo[e]pyrene	1.008639	0	0.781378	0	0.87445	0	0
benzo[k]fluoranthene	0.229826	0	0.098816	0	0.075497	0	0
perylene	1.984818	0	0	0	0	0	0.0028897
indeno[1,2,3-cd]pyrene	0	0	0	0	0	0	0
benzo[ghi]perylene	0	0	0	0	0	0.0155784	0.0097293
dibenz[a,h]anthracene	0	0	0	0	0	0	0
9H-fluoren-9-one	0.132124	0	0	0.094987	0	0.0555395	0.0188349
9,10-anthracenedione	0.703298	0	0	0	0	0	0
9H-xanthen-9-one	0.628012	0	0	0.163231	0	0.0091484	0
7H-benz[de]anthracen-7-one	0	0	0	0	0	0	0
1-methyl-2-pyrrolidinone	0.3447	0	0	0.813564	0.477928	0.1474302	0.0838772
N,N-dibutylformamide	0	0	0.154084	0.153266	0.044158	0.9238724	0.291352
2-(2-butoxyethoxy)-ethanol	0	0	0	0	0	11.65787	2.7362963
2,3-dihydro-1H-inden-1-one	0	0	0	0	0	0.486967	0.2262828
benz[a]anthracen-7,12-dione	0	0	0	0	0		
1,1'-sulfonylbisbenzene	1	1	1	1	1	0	0

Mass Collected	S6016-00.D	S6017-UI.D	S6018-00.D	S6019-00.D	S6020-00.D	S6021-00.D	S6022-00.D
nonadecane	0.022324	0	0.1699871	0.9915286	0.0822031	0.1643394	0.094588
eicosane	0.0178134	0.0091917	0.0114567	0.3601993	2.1827066	2.673679	5.6398692
heneicosane	0.5476539	0.0103949	0	1.0184455	2.5420829	5.7216794	0.0095573
docosane	0.4130533	0.0123158	0	0.8468792	1.5717764	0.0440926	0.0314904
tricosane	0.6969416	0.0073881	0.0213243	1.4160473	0.0535101	0.0563002	0.0688984
tetracosane	1.5852764	0.0410073	0	3.1737397	4.0991707	4.7142207	0.030064
pentacosane	1.7230437	0.0190585	0	3.7146656	4.4953359	5.0626998	0.0103702
hexacosane	1.6510365	0.0358801	0	3.6809942	3.6376765	0.010344	4.1887348
heptacosane	1.3868125	0.076768	0.0016546	3.2543348	3.0445434	0.0133823	0.0194536
octacosane	1.2073615	0.1843965	0	3.0913542	2.954499	3.3144975	3.3665152
nonacosane	1.0213371	0.4527272	0.0028466	3.1058315	3.1456781	3.2907376	0.0190446
triacontane	0.7949323	0.8344935	0.0039397	3.3087014	3.4616209	3.1489936	3.9928246
	0.5591802	1.1025139	2.0550212	3.1522312	3.4018613	2.831299	3.9923511
hexanoic acid	0.0235322	0	0.021142	0.0352841	0.033776	0.0436214	0.0326947
heptanoic acid	0	0	0.0536866	0.0427888	0.3044024	0.1418049	0.2459689
octanoic acid	0.7525552	0.6868777	0.8319156	1.1178866	6.2010551	7.8019453	1.8553907
nonanoic acid	0	0.1353583	0.1201169	0.109593	71.334361	67.200309	52.040906
decanoic acid	0.077333	0.0925607	0.1639221	0.0816625	0.3614347	0.2549899	0.4077151
undecanoic acid	0.2610113	0	0	0.2254383	0	0	0
dodecanoic acid	0	0	0.1644091	0.1604269	0	0.4650673	0.2605515
tridecanoic acid	0	0	1.6368162	1.3855929	0	0	0
tetradecanoic acid	0	0	1.8166632	2.0037727	2.2010882	2.1432544	3.0141641
pentadecanoic acid	0	0	0	0	0	0	0
4-methyl-benzoic acid							
4-methyl-benzaldehyde	0.2662467	0	0	0.1787162	0.8312514	0.5896287	0.6354139
3,4-dimethoxybenzaldehyde	0	0	0	0	0	0.0306545	0
anthracene	0.1016121	0.0282444	0	0.014077	0.0942911	0.1342626	0.1524972
phenanthrene	0.0537077	0.0149288	0	0.0074405	0.0498382	0.0709654	0.0806034
fluoranthene	0.018355	0.0075945	0.0039637	0.0626471	0.0272876	0.0300955	0.0388081
pyrene	0.0410332	0	0	0.1246028	0.0430772	0.0416793	0.1121142
11H-benzo[a]fluorene	0	0	0	0.0477775	0.0078024	0	0.0087522
11H-benzo[b]fluorene	0	0	0	0.0573528	0.0120446	0	0.0520676
benz[a]anthracene	0.009087	0.0066532	0	0.0315092	0.0101095	0.0084173	0.0115279
chrysene	0.0036098	0.002643	0	0.038581	0.0046682	0.006433	0.0050372
triphenylene	0.0036146	0.0026465	0	0.0386321	0.0046743	0.0064415	0.0050438
benzo[a]pyrene	0	0	0	0.0286073	0.0037882	0.0079564	0.0028901
benzo[e]pyrene	0	0	0.0343139	0.0518862	0	0.0090678	0
benzo[k]fluoranthene	0	0	0	0.0389613	0.0039963	0.0083935	0.0030489
perylene	0.0036523	0	0.0034631	0.0310357	0	0.004369	0.0038013
indeno[1,2,3-cd]pyrene	0	0	0	0.0142341	0	0	0
benzo[ghi]perylene	0.0128887	0.0075544	0.0033718	0.0092209	0	0.0047746	0
dibenz[a,h]anthracene	0	0	0	0.0152265	0	0	0
9H-fluoren-9-one	0.0243295	0	0	0	0.0429664	0.0575938	0.0479412
9,10-anthracenedione	0	0	0	0.0146206	0	0.0054911	0
9H-xanthen-9-one	0.0081512	0	0	0	0	0.0113019	0.0080789
7H-benz[de]anthracen-7-one	0	0	0	0.0150612	0	0	0
1-methyl-2-pyrrolidinone	0.0571958	0.0145093	0	0.0462016	0.0184919	0.0168839	0.0232971
N,N-dibutylformamide	0.0119995	0.048695	0.0095905	0.0113632	0.0259535	0.0099693	0.0217416
2-(2-butoxyethoxy)-ethanol	3.5086111	0	0.1937037	0.9772222	18.993704	23.15287	14.784074
2,3-dihydro-1H-inden-1-one	0	0	0	0	0.143666	0.1506175	0.1340407
benz[a]anthracen-7,12-dione							
1,1'-sulfonylbisbenzene	0	0	0	0	0	0	0

Mass Collected	S6023~00.D	S6024~PA.D	S6025~GP.D	S6026~8M.D	S6027~00.D	S6028~YF.D	S6029~SX.D
nonadecane	0	0.0850492	0.5009117	0.089385	0.106668	0.10152	0.020988
eicosane	0	0.7569462	0.3014399	3.2557935	1.768507	1.001865	0.048307
heneicosane	0	1.9101031	0.3366301	2.7639952	5.052258	6.429655	2.481787
docosane	0	0.7598849	0.1728279	1.2763938	14.5184	15.37337	0.179195
tricosane	0	1.5081918	0.2767467	1.2407977	0.167238	0.387411	2.776542
tetracosane	0	3.4220686	0.7937506	2.0552975	0.094804	0.229979	-1
pentacosane	0	3.8863776	1.499104	2.1233338	0.649792	0.673818	-1
hexacosane	0	3.6265359	2.0653895	1.970423	0.530438	0.105657	11.55698
heptacosane	0	3.2014517	2.2523599	1.6280189	-1	0.750375	-1
octacosane	0	3.0092076	2.2374802	1.4304573	0.273089	0.395845	-1
nonacosane	0	2.9098462	2.0239709	1.2612811	0.337834	-1	-1
triacontane	0	2.7177599	1.7197686	1.100863	0.233655	1.842029	-1
	0	2.2575023	1.2523614	0.8833035			
hexanoic acid	0.0692309	0.035654	0	0.0740682	1.188428	1.385711	0
heptanoic acid	0.1259596	0	0	0	0	0	0
octanoic acid	0.7977085	0.7443455	0	0	9.241105	10.20141	0
nonanoic acid	0	20.758627	0	0.1168509	2.255026	1.425867	0
decanoic acid	0	0.0749443	0	0	0	1.451096	0
undecanoic acid	0	0.2652972	0	0	1.258931	0	0
dodecanoic acid	0	0.1422224	0	0	1.050905	1.985635	2.451595
tridecanoic acid	0	0	0	1.0358128	1.188556	0	1.522476
tetradecanoic acid	0	0	0	1.7146035	1.707282	2.80824	0
pentadecanoic acid	0	0	0	0	2.982454	3.263014	0
4-methyl-benzoic acid					0	1.776095	0
4-methyl-benzaldehyde	0.1490905	0.1639033	0	0.4388069	1.100847	0	2.890414
3,4-dimethoxybenzaldehyde	0	0	0	0.0614209	0.820729	1.051551	0
anthracene	0	0.0807112	0.0450781	0.1914519	0	0.04273	0
phenanthrene	0	0.0426604	0.0238263	0.1011931	0	0.051235	0.116758
fluoranthene	0	0.0173939	0.0098434	0.0393107	0	0	0.031181
pyrene	0	0.0212782	0.0154031	0.1095954	0	0	0.181725
11H-benzo[a]fluorene	0	0	0	0.0101498	0	0	0
11H-benzo[b]fluorene	0	0	0	0.0482567	0	0	0
benz[a]anthracene	0	0.0047667	0.0094326	0.0061132	0	0	0
chrysene	0	0.0018936	0.0037471	0.0014931	0	0	0
triphenylene	0	0.0018961	0.0037521	0.0014951	0	0	0
benzo[a]pyrene	0	0	0.0067646	0	0	0	0
benzo[e]pyrene	0	0	0.010518	0	0	0	0
benzo[k]fluoranthene	0	0	0.0071363	0	0	0	0
perylene	0	0	0.0033828	0.0055615	0	0	0
indeno[1,2,3-cd]pyrene	0	0	0.0060369	0	0	0	0
benzo[ghi]perylene	0	0.0041053	0.0067951	0.0132748	0	0	0
dibenz[a,h]anthracene	0	0	0	0.003822	0	0	0
9H-fluoren-9-one	0	0.0196517	0.0209635	0.05351	0	0.053684	0.070726
9,10-anthracenedione	0	0	0	0.0075763	0	0	0
9H-xanthen-9-one	0	0	0	0.0265348	0	0	0
7H-benz[de]anthracen-7-one	0	0	0	0	0	0	0
1-methyl-2-pyrrolidinone	0.0611597	0.0838211	0.0104706	0.0849617	0.341609	2.904716	0.554647
N,N-dibutylformamide	0	0.4965863	0.0179387	0.042362	0.054283	0.07112	0.041992
2-(2-butoxyethoxy)-ethanol	1.142963	6.7412963	1.8257407	12.504259	0	0	0
2,3-dihydro-1H-inden-1-one	0	0.269953	0	0.0568604	0	0	0.485212
benz[a]anthracen-7,12-dione					0	0	0
1,1'-sulfonylbisbenzene	0	0	0	0	1	1	1

Mass Collected	S6030-HU.D	S6031-LJ.D	S6032-I7.D	S6033-L6.D	S6034-38.D	S6035-BT.D	S6036-75.D
nonadecane	0.021625	0.167004	0.023237	0.055912	0.046096	0.043817	0.081003
eicosane	1.489466	2.779506	0.090169	2.282294	0.029704	0.257413	0.027753
heneicosane	4.904592	0.202702	1.895832	4.704947	0.073122	7.941169	5.91977
docosane	0.159404	13.75547	2.05044	0.085309	0.067761	0.168093	0.086532
tricosane	0.119054	0.15437	0.133027	0.181469	0	-1	-1
tetracosane	-1	0.157036	-1	0.112366	0.256897	-1	-1
pentacosane	-1	0.125809	-1	-1	0.477559	-1	-1
hexacosane	-1	0.067824	-1	-1	0.325909	-1	-1
heptacosane	-1	-1	-1	-1	0.799274	-1	-1
octacosane	-1	0.133358	-1	-1	0.62489	-1	-1
nonacosane	-1	0.152918	-1	-1	0.639671	-1	-1
triacontane	-1	1.420708	-1	-1	0.446008	-1	-1
hexanoic acid	0	1.174698	0	0	0	0	0
heptanoic acid	0	0	0	0	0	0	0
octanoic acid	0	1.459593	0	2.12714	0	1.891044	1.934923
nonanoic acid	0	2.155026	0	0	0	0	0
decanoic acid	0	0	1.40872	0	0	0	0
undecanoic acid	0	0	0	0	0	0	0
dodecanoic acid	3.559435	0	0	1.103655	1.442189	3.802464	1.016185
tridecanoic acid	1.714044	1.358104	1.103544	1.883856	0	2.255521	1.305476
tetradecanoic acid	0	0	0	0	0	0	0
pentadecanoic acid	0	0	0	0	0	3.533626	0
4-methyl-benzoic acid	0	0	0	0	0	0	0
4-methyl-benzaldehyde	2.093153	1.935925	1.769693	1.574316	1.243683	2.334621	1.188136
3,4-dimethoxybenzaldehyde	0	0.662805	0	0	0	0	0
anthracene	0	0	0	0	0	0	0
phenanthrene	0.120736	0	0.135122	0.174449	0	0.143509	0.123382
fluoranthene	0.071794	0	0.070295	0.110805	0	0.104594	0.095213
pyrene	0.108145	0	0.111618	0.176048	0	0.270857	0.151831
11H-benzo[a]fluorene	0	0	0	0	0	0	0
11H-benzo[b]fluorene	0	0	0	0	0	0.269984	0
benz[a]anthracene	0	0	0.056375	0.052994	0	0.060543	0.115905
chrysene	0	0	0.0484	0.055052	0	0.051962	0.099077
triphenylene	0	0	0.055696	0.052356	0	0.059813	0.114509
benzo[a]pyrene	0.053867	0	0.050412	0.10712	0	0.076165	0.074125
benzo[e]pyrene	0.612998	0	0.473746	1.187915	0	0.590083	0.560573
benzo[k]fluoranthene	0.054864	0	0.051345	0.109103	0	0.077575	0.075497
perylene	0	0	0	0	0	0	0
indeno[1,2,3-cd]pyrene	0	0	0	0	0	0	0
benzo[ghi]perylene	0	0	0	0	0	0	0
dibenz[a,h]anthracene	0	0	0	0	0	0	0
9H-fluoren-9-one	0.05517	0	0.050879	0.13442	0	0.088239	0.087402
9,10-anthracenedione	0	0	0	0	0	0.106337	0
9H-xanthen-9-one	0	0	0	0.176066	0	0	0
7H-benz[de]anthracen-7-one	0	0	0	0	0	0	0
1-methyl-2-pyrrolidinone	0.710623	1.7468	2.106523	0.461993	0.695081	0.672888	0.871755
N,N-dibutylformamide	0.047193	0.064216	0	0.090153	0	0.699901	0.046398
2-(2-butoxyethoxy)-ethanol	0	0	0	0	0	0	0
2,3-dihydro-1H-inden-1-one	0	0	0	0.437093	0	0.334603	0.430224
benz[a]anthracen-7,12-dione	0	0	0	0	0	0	0
1,1'-sulfonylbisbenzene	1	1	1	1	1	1	1

Mass Collected	S6037-E7.D	S6038-00.D	S6039-OP.D	S6040-TP.D	S6041-XC.D	S6042-FX.D	S6043-JN.D
nonadecane	0.047328	0.0304284	0.028144	0.022487	0.019226	0.020388	0.020126
eicosane	0.130504	0.192714	0.063225	0.025558	0.06507	0.411367	0.02707
heneicosane	1.997015	0.9459373	1.439354	1.629329	0.078892	2.130434	0.971985
docosane	0.05468	0.0644928	0.060916	1.006019	0.055191	1.568947	0.073683
tricosane	-1	-1	0.916918	1.262119	2.234084	3.16188	0.880036
tetracosane	0.096642	-1	0.294024	0.3874	1.15285	-1	0.168835
pentacosane	-1	-1	1.240575	0.65965	0.944362	-1	0.200164
hexacosane	-1	-1	0.5468	0.433732	0.379622	-1	0.099124
heptacosane	-1	-1	0.573258	0.736496	0.551854	-1	0.099512
octacosane	-1	-1	0.199385	0.268433	0.402387	-1	0.122264
nonacosane	-1	-1	1.489536	0.188425	0.334377	-1	0
triacontane	-1	-1	1.084345	0	0	-1	0
hexanoic acid	0	0	0	0	0	1.228573	0
heptanoic acid	0	1.3673905	0	0	0	0	0
octanoic acid	2.212466	0	0	1.907353	1.642039	1.535779	0
nonanoic acid	0	0	0	0	0	0	0
decanoic acid	0	0	0	0	0	0	0
undecanoic acid	0	1.1339494	0	0	0	0	0
dodecanoic acid	4.364522	0	2.251961	2.900038	1.864784	0	1.840532
tridecanoic acid	1.473679	1.2684447	0	0	1.079963	0	0
tetradecanoic acid	0	0	0	1.468008	0	0	0
pentadecanoic acid	0	0	0	0	0	0	0
4-methyl-benzoic acid	1.213488	0	0	0	0	0	0
4-methyl-benzaldehyde	1.6314	0	0	1.237208	0	0	1.121253
3,4-dimethoxybenzaldehyde	0	0	0	0	0	0	0
anthracene	0	0	0	0	0	0	0
phenanthrene	0.108662	0.1341641	0.058522	0.040061	0.066564	0.117983	0.036695
fluoranthene	0.07452	0.0653367	0.032375	0	0	0.075291	0
pyrene	0.182752	0.1258596	0.034302	0.047849	0.093279	0.112775	0.038298
11H-benzo[a]fluorene	0	0	0	0	0	0	0
11H-benzo[b]fluorene	0	0	0	0	0	0	0
benz[a]anthracene	0	0.1393427	0	0	0	0	0
chrysene	0	0.1189085	0	0	0	0	0
triphenylene	0	0.137664	0	0	0	0	0
benzo[a]pyrene	0.079195	0.0541754	0	0	0	0	0
benzo[e]pyrene	1.0527	0	0	0	0	0	0
benzo[k]fluoranthene	0.080661	0.0551786	0	0	0	0	0
perylene	0		0	0	0	0	0
indeno[1,2,3-cd]pyrene	0		0	0	0	0	0
benzo[ghi]perylene	0	0	0	0	0	0	0
dibenz[a,h]anthracene	0	0	0	0	0	0	0
9H-fluoren-9-one	0.058741	0	0	0	0	0	0
9,10-anthracenedione	0		0	0	0	0	0
9H-xanthen-9-one	0	0.0771163	0	0	0	0	0
7H-benz[de]anthracen-7-one	0	0.1111678	0	0	0	0	0
1-methyl-2-pyrrolidinone	1.362931	0.1912766	0	0.448021	0.451827	2.220488	0.513206
N,N-dibutylformamide	0.668876	0	0.090299	0.3504	0.119217	0	0.125559
2-(2-butoxyethoxy)-ethanol	0	2.0488796	0	0	0	0	0
2,3-dihydro-1H-inden-1-one	0.398529	0	0	0	0	0	0
benz[a]anthracen-7,12-dione	0	0	0	0	0	0	0
1,1'-sulfonylbisbenzene	1	0	1	1	1	1	1

Mass Collected	S6044~AW.D	S6045~1J.D	S6046~7Q.D	S6047~YI.D	S6048~SK.D	S6049~BO.D	S6050~24.D
nonadecane	0.045311	0.045498	0.026497	0.026047	0.019826	0.070404	0.051621
eicosane	0.466334	0.031459	0.035114	0.034578	0.127327	0.694165	0.691429
heneicosane	1.472164	0.24409	1.630181	0.949091	0.716884	1.817941	2.096423
docosane	0.41524	2.03615	0.06817	0.877323	0.970759	0.061938	0.12223
tricosane	0.749869	1.96967	0.538028	0.845376	0.89169	5.162952	7.44668
tetracosane	0.258091	0.834504	0.503121	0.438994	0.625203	-1	-1
pentacosane	0.225584	0.867936	0.297262	0.308288	0.323629	-1	-1
hexacosane	0.171789	0.293517	0.15912	0.141244	0.246329	-1	-1
heptacosane	0.229613	0.910204	3.92647	0.314619	0.231929	-1	-1
octacosane	0.119005	0.148175	0.434729	0	0.311775	-1	-1
nonacosane	0.186246	0.373241	0.17053	0.161116	0.327467	-1	-1
triacontane	0	0	0	0	0.17258	-1	-1
hexanoic acid	0	0	0	0	0	0	0
heptanoic acid	0	0	0	0	0	0	0
octanoic acid	1.701405	0	1.80677	1.56061	0	0	1.534257
nonanoic acid	0	0	0	0	0	0	0
decanoic acid	0	0	0	0	0	0	0
undecanoic acid	0	0	0	0	0	0	0
dodecanoic acid	2.583733	2.43934	2.769983	2.120382	0	2.530204	2.82428
tridecanoic acid	0	0	0.987088	0	0	0	0
tetradecanoic acid	0	0	0	0	0	0	0
pentadecanoic acid	0	0	0	0	0	0	0
4-methyl-benzoic acid	0	0	0	0	0	0	0
4-methyl-benzaldehyde	1.435737	0	0	0	0	0	1.126329
3,4-dimethoxybenzaldehyde	0	0	0	0	0	0	0
anthracene	0	0	0	0	0	0	0
phenanthrene	0	0.039302	0.052148	0.040982	0.04989	0.049299	0.044121
fluoranthene	0	0	0	0	0	0	0
pyrene	0	0.066482	0.05183	0	0.04611	0.030188	0.037961
11H-benzo[a]fluorene	0	0	0	0	0	0	0
11H-benzo[b]fluorene	0	0	0	0	0	0	0
benz[a]anthracene	0	0	0	0	0	0	0
chrysene	0	0	0	0	0	0	0
triphenylene	0	0	0	0	0	0	0
benzo[a]pyrene	0	0	0	0	0	0	0
benzo[e]pyrene	0	0	0	0	0	0	0
benzo[k]fluoranthene	0	0	0	0	0	0	0
perylene	0	0	0	0	0	0	0
indeno[1,2,3-cd]pyrene	0	0	0	0	0	0	0
benzo[ghi]perylene	0	0	0	0	0	0	0
dibenz[a,h]anthracene	0	0	0	0	0	0	0
9H-fluoren-9-one	0	0	0	0	0	0	0
9,10-anthracenedione	0	0	0	0	0	0	0
9H-xanthen-9-one	0	0	0	0	0	0	0
7H-benz[de]anthracen-7-one	0	0	0	0	0	0	0
1-methyl-2-pyrrolidinone	0.395728	0.324953	0.323722	0.757631	1.257921	0.831696	0.30959
N,N-dibutylformamide	0.420724	0.349693	0.256057	0.190411	0	0.042281	0
2-(2-butoxyethoxy)-ethanol	0	0	0	0	0	0	0
2,3-dihydro-1H-inden-1-one	0.360531	0.38813	0	0	0	0	0
benz[a]anthracen-7,12-dione	0	0	0	0	0	0	0
1,1'-sulfonylbisbenzene	1	1	1	1	1	1	1

Mass Collected	S6051-BM.D	S6052-XA.D	S6053-54.D	S6054-BK.D
nonadecane	0.043556	0.019713	0.023837	0.030503
eicosane	0.046702	0.115861	0.030874	0.037647
heneicosane	0.07803	2.000808	1.471587	1.133331
docosane	2.494591	1.240547	2.489374	1.323934
tricosane	5.560832	4.403751	-1	4.39799
tetracosane	-1	-1	-1	-1
pentacosane	-1	-1	-1	-1
hexacosane	-1	-1	-1	0.072466
heptacosane	-1	-1	-1	-1
octacosane	-1	-1	-1	-1
nonacosane	-1	-1	-1	-1
triacontane	-1	-1	-1	-1
hexanoic acid	0	1.083079	0	0
heptanoic acid	0	0	0	0
octanoic acid	1.614526	1.749282	0	0
nonanoic acid	0	0	1.549474	0
decanoic acid	0	0	0	0
undecanoic acid	0	0	0	1.129887
dodecanoic acid	2.412988	2.431957	0	1.021077
tridecanoic acid	0	0	1.008147	0
tetradecanoic acid	0	0	0	0
pentadecanoic acid	0	0	0	0
4-methyl-benzoic acid	0	0	0	0
4-methyl-benzaldehyde	0	0	1.178211	0
3,4-dimethoxybenzaldehyde	0	0	0	0
anthracene	0	0	0	0
phenanthrene	0.050912	0	0.056918	0.089819
fluoranthene	0.026815	0	0.035038	0
pyrene	0.078349	0.060003	0.084628	0.044706
11H-benzo[a]fluorene	0	0	0	0
11H-benzo[b]fluorene	0	0	0	0
benz[a]anthracene	0	0	0	0
chrysene	0	0	0	0
triphenylene	0	0	0	0
benzo[a]pyrene	0	0	0	0
benzo[e]pyrene	0	0	0.479694	0
benzo[k]fluoranthene	0	0	0	0
perylene	0	0	0	0
indeno[1,2,3-cd]pyrene	0	0	0	0
benzo[ghi]perylene	0	0	0	0
dibenz[a,h]anthracene	0	0	0	0
9H-fluoren-9-one	0	0	0	0
9,10-anthracenedione	0	0	0	0
9H-xanthen-9-one	0	0	0	0
7H-benz[de]anthracen-7-one	0	0	0	0
1-methyl-2-pyrrolidinone	0	0.384474	0.911539	1.117321
N,N-dibutylformamide	0	0	0	0
2-(2-butoxyethoxy)-ethanol	0	0	0	0
2,3-dihydro-1H-inden-1-one	0	0	0	0
benz[a]anthracen-7,12-dione	0	0	0	0
1,1'-sulfonylbisbenzene	1	1	1	1

Mass Collected	C2001~00.D	C2002~00.D	C2003~00.D	C2004~00.D	C2004~TP.D	C2005~00.D
nonadecane	0.360304	0.025897	1.528436	0.419357	0.018926	0
eicosane	0.620751	0.038865	0.065604	0.941345	0.475827	0
heneicosane	0.819786	3.352378	2.886718	1.187092	0.75528	0
docosane	0.938441	4.985403	4.338068	1.683482	1.038391	0
tricosane	2.23316	0.105604	0.111745	0.084399	1.565646	0
tetracosane	6.79451	-1	0.103831	0.118229	0.100152	0
pentacosane	-1	-1	-1	-1	0.148779	0
hexacosane	6.785528	-1	-1	4.238471	1.810162	0
heptacosane	-1	0.109763	0.124403	0.098564	0.09534	0
octacosane	6.412968	0.107715	0.15363	0.195214	1.503006	0
nonacosane	1.525048	0.217534	0.232618	0.197873	0.132223	0
triacontane	0.630436	-1	1.496246	0.248983	0.237985	0
hexanoic acid	0	1.145883	1.641021	1.129153	1.20869	0
heptanoic acid	0	1.374394	1.559192	1.775949	1.868422	0
octanoic acid	0	1.64622	1.357437	1.562098	1.520475	0
nonanoic acid	1.559411	1.500673	1.463849	1.502745	1.644725	0
decanoic acid	0	1.461401	1.595638	1.56665	1.425775	0
undecanoic acid	0	1.246054	1.32502	1.170489	1.132327	0
dodecanoic acid	0	2.151709	1.718214	1.155732	1.270033	0
tridecanoic acid	0	4.01403	0	0	0	0
tetradecanoic acid	0	1.973258	1.418489	2.182092	0	0
pentadecanoic acid	0	0	0	0	0	0
4-methyl-benzoic acid	0	1.334054	0	1.229022	1.239011	0
4-methyl-benzaldehyde	0	1.841962	6.648312	1.575756	1.237208	0
3,4-dimethoxybenzaldehyde	0	0.668873	0.813417	0	0	0
anthracene	0.046953	0.248893	0.029114	0.060493	0.02345	0
phenanthrene	0.056222	0.281834	0.201738	0.072127	0.028294	0
fluoranthene	0.455205	2.114264	1.873524	0.930703	0.350333	0
pyrene	0.652695	2.868236	2.562133	1.280569	0.511815	0
11H-benzo[a]fluorene	1.40263	4.258838	3.938346	0.169111	1.182903	0
11H-benzo[b]fluorene	1.319998	4.058959	3.752737	1.773233	1.034737	0
benz[a]anthracene	1.878067	11.98539	2.203163	0.729961	0.385923	0
chrysene	1.452985	6.623993	5.890071	2.597491	1.490625	0
triphenylene	0.399158	2.387169	2.176613	0.721166	0.381273	0
benzo[a]pyrene	0.073877	0.589187	0.516869	0.107678	0.11543	0
benzo[e]pyrene	0.623134	2.269757	2.280829	0.541834	0.78621	0
benzo[k]fluoranthene	0.075245	0.600097	0.526441	0.109672	0.117567	0
perylene	0.889751	3.996847	0.489934	0.809497	1.284405	0
indeno[1,2,3-cd]pyrene	0	0.375554	0.639914	0	0	0
benzo[ghi]perylene	0	0.471293	0.451173	0	0	0
dibenz[a,h]anthracene	0	1.233848	0	0	0	0
9H-fluoren-9-one	0	0.254213	0.137656	0.191026	0	0
9,10-anthracenedione	0.360951	1.059429	1.048205	0.537903	0.205854	0
9H-xanthen-9-one	0.245725	0.927329	0.776557	0.488214	0	0
7H-benz[de]anthracen-7-one	0	0.439957	0.543703	0.566178	0	0
1-methyl-2-pyrrolidinone	0	0.323107	-1	0	0	0
N,N-dibutylformamide	0	0.051821	0.162945	0.064144	0.040477	0
2-(2-butoxyethoxy)-ethanol	0	0	0	0	0	0
2,3-dihydro-1H-inden-1-one	0	0.488638	0.830393	0	0	0
benz[a]anthracen-7,12-dione	0	0.359965	0	0.29888	0	0
1,1'-sulfonylbisbenzene	1	1	1	1	1	0

Mass Collected	C2006-00.D	C2007-00.D	C2008-00.D	C2009-61.D	C2010-00.D	C2011-00.D	C2012-00.D
nonadecane	0	0	0	0.022412	0.0166096	0.0288389	0.0314404
eicosane	0.117452	0	0.036478	0.062497	0.0524173	0.0628511	0.0236148
heneicosane	0	0	0.047216	0	0.0262191	0.0074933	0.0116213
docosane	0	0	0	0	0.2932119	0.2061875	0.2374367
tricosane	1.289205	0.812539	0.154537	0.157209	0.0866924	0.1081876	0.0613395
tetracosane	0	0	0	0	0.149298	0.2281259	0.1115977
pentacosane	0.11425	0	0	0	0.1934895	0.2939774	0.1849354
hexacosane	0	0	0	0	0.1831808	0.2686998	0.1876147
heptacosane	0	0.101789	0	0	0.012414	0.0021557	0.1697434
octacosane	0	0	0.11314	0.116398	0.1659476	0.2517627	0.1586716
nonacosane	0	0	0	0	0.1816983	0.2250086	0.1627419
triacontane	0	0	0	0.200748	0.1752783	0.1945326	0.1413852
					0.154037	0.1535522	0.0947681
hexanoic acid	0	1.109677	0	0	0	0	0.0159917
heptanoic acid	0	1.297027	0	0	0	0	0
octanoic acid	0	0	0	0	1.0125288	0	0
nonanoic acid	0	0	0	1.49652	0	0.1077786	0
decanoic acid	0	0	0	0	0	0	0.0830061
undecanoic acid	0	0	0	1.182096	0	0	0
dodecanoic acid	0	0	0	0	0	0	0
tridecanoic acid	0	0	0	0	0	0	0.9797707
tetradecanoic acid	0	0	0	0	0	0	0
pentadecanoic acid	0	0	0	0	0	0	0
4-methyl-benzoic acid	1.308543	4.839304	2.830089	2.170024			
4-methyl-benzaldehyde	0	0	0	0	0.1117697	0	0
3,4-dimethoxybenzaldehyde	0	0	0	0	0	0	0
anthracene	0	0	0	0	0.0179634	0	0.0154553
phenanthrene	0	0	0	0	0.0094947	0	0.008169
fluoranthene	0	0	0	0	0.0082227	0.0051258	0.0095984
pyrene	0	0	0	0	0.0095544	0.0057168	0.0069169
11H-benzo[a]fluorene	0	0	0	0	0	0	0
11H-benzo[b]fluorene	0	0	0	0	0	0	0
benz[a]anthracene	0	0	0	0	0.0047595	0	0.0110239
chrysene	0	0	0	0	0.0023026	0	0.0045452
triphenylene	0	0	0	0	0.0023057	0	0.0045512
benzo[a]pyrene	0	0	0	0	0.0029707	0	0
benzo[e]pyrene	0	0	0	0	0	0	0
benzo[k]fluoranthene	0	0	0	0	0.0031339	0	0
perylene	0	0	0	0	0	0	0
indeno[1,2,3-cd]pyrene	0	0	0	0	0	0	0
benzo[ghi]perylene	0	0	0	0	0.0073677	0	0.0050191
dibenz[a,h]anthracene	0	0	0	0	0	0	0
9H-fluoren-9-one	0	0	0	0	0	0	0
9,10-anthracenedione	0	0	0	0	0	0	0
9H-xanthen-9-one	0	0	0	0	0	0	0
7H-benz[de]anthracen-7-one	0	0	0	0	0	0	0
1-methyl-2-pyrrolidinone	0	0	0	0	0	0	0
N,N-dibutylformamide	0	0	0	0	0	0	0
2-(2-butoxyethoxy)-ethanol	0	0	0	0	0.077963	0.0544444	0
2,3-dihydro-1H-inden-1-one	0.435933	0.589907	0.32759	0	0	0	0
benz[a]anthracen-7,12-dione	0	0	0	0			
1,1'-sulfonylbisbenzene	0	0	0	0	0	0	0

Mass Collected	C2013~00.D	C2014~2B.D	C2015~P2.D	C2016~I9.D	C2017~IQ.D	C2018~J9.D	C2019~HN.D
nonadecane	0.0791791	0.05183	0.05959	0.050607	0.06735	0.120832	0.11196
eicosane	0.2583311	0.0311991	0.8017354	0.0719843	0.1730634	0.045875	0.036576
heneicosane	0.0585255	0.0086001	0.0529167	0.0255011	0.0085253	0.141659	0.069938
docosane	0.4176812	0.2239753	0.7022103	0.1647179	0.2824338	0.088672	0.081843
tricosane	0.1581105	0.0431327	0.2863412	0.1077748	0.0718736	0.19237	0
tetracosane	0.405203	0.1139427	0.9388396	0.2774309	0.0318679	0.198075	0
pentacosane	0.4630324	0.1651236	1.0607331	0.3916379	0.1345651	0.122219	0.136386
hexacosane	0.4647228	0.166387	0.9996412	0.3786527	0.1385326	0.150457	0.058324
heptacosane	0.5604312	0.0029009	0.9043935	0.3832104	0.1393178	0.134115	0.135068
octacosane	0.4904219	0.1725129	0.8906519	0.3584777	0.1299142	0.184906	0.262452
nonacosane	0.5898214	0.1844994	0.9231994	0.3704349	0.1323536	0.142082	0.168356
triacontane	0.6672877	0.1847365	0.8183774	0.3189665	0.1242649	0	0
	0.7052361	0.1936751	0.6412349	0.2450787	0.104797		
hexanoic acid	0	0.014825	0	0.0181827	0	0	0
heptanoic acid	0.0377077	0	0	0	0	0	0
octanoic acid	0	0	0.8059182	0	0.7717112	0	0
nonanoic acid	0.1025167	0	0	0	0.1108632	1.433562	0
decanoic acid	0	0	0.0931579	0.0824089	0	0	0
undecanoic acid	0	0.2228668	0	0.214295	0	0	0
dodecanoic acid	0	0.1865958	0	0	0	2.162359	0
tridecanoic acid	0	1.004893	1.0705976	1.0319479	0	0	0
tetradecanoic acid	0	0	0	0	0	0	0
pentadecanoic acid	0	0	0	0	0	0	0
4-methyl-benzoic acid						0	0
4-methyl-benzaldehyde	0.1319691	0	0.1000349	0	0	0	0
3,4-dimethoxybenzaldehyde	0	0	0	0	0	0	0
anthracene	0.0125179	0.0147323	0.0259397	0.0170822	0.0150938	0	0
phenanthrene	0.0066164	0.0077868	0.0137106	0.0090289	0.0079779	0	0
fluoranthene	0.0099125	0.0043595	0.0087127	0.0085933	0.007293	0	0
pyrene	0.0074114	0	0	0.0087961	0.005763	0	0
11H-benzo[a]fluorene	0	0	0	0	0	0	0
11H-benzo[b]fluorene	0	0	0	0	0	0	0
benz[a]anthracene	0.0066028	0.0051915	0.0087126	0.0082157	0.0062284	0	0
chrysene	0.002623	0.0020623	0.0034611	0.0067019	0.0024742	0	0
triphenylene	0.0026265	0.0020651	0.0034657	0.0067108	0.0024775	0	0
benzo[a]pyrene	0.0033737	0	0	0	0	0	0
benzo[e]pyrene	0	0	0	0	0	0	0
benzo[k]fluoranthene	0.0031035	0	0	0	0	0	0
perylene	0	0	0.0036752	0	0	0	0
indeno[1,2,3-cd]pyrene	0	0	0	0	0	0	0
benzo[ghi]perylene	0.0053923	0	0.0039831	0.0053215	0	0	0
dibenz[a,h]anthracene	0	0	0	0	0	0	0
9H-fluoren-9-one	0	0	0	0	0	0	0
9,10-anthracenedione	0	0	0	0	0	0	0
9H-xanthen-9-one	0	0	0	0	0	0	0
7H-benz[de]anthracen-7-one	0	0	0	0	0	0	0
1-methyl-2-pyrrolidinone	0	0.0229793	0	0	0	0	0
N,N-dibutylformamide	0	0.0090148	0	0	0.0098026	0	0
2-(2-butoxyethoxy)-ethanol	0.0573148	0.155	0.1	0.0728704	0	0	0
2,3-dihydro-1H-inden-1-one	0	0	0	0	0	0	0
benz[a]anthracen-7,12-dione						0	0
1,1'-sulfonylbisbenzene	0	0	0	0	0	1	1

Mass Collected	C2020-00.D	C2021-00.D	C2022-00.D	C2023-00.D	C2024-00.D	C2025-00.D	C2026-00.D
nonadecane	0.052853	0.030354	0.282336	0.612554	0.140458	0.135852	0.116323
eicosane	0.056426	0.029558	0.052781	0.227673	0.034335	0.044123	0.055843
heneicosane	0.059447	0.076439	0.064495	0.248649	0.534469	0.04961	0.135336
docosane	0.067455	0.131361	0.051509	0.151011	0	0.053555	0.053862
tricosane	0	0.408465	0.282193	0.824261	0	0.083737	0.136025
tetracosane	0	0.110524	0.122587	1.443396	0	0	0
pentacosane	0.412407	0.770093	0.115843	4.807066	0.328749	0.212662	0.135188
hexacosane	0	0.057661	0.056777	0.100453	0.061748	0.056557	0.154011
heptacosane	0.094202	0.658909	1.30799	1.665592	0.219199	0.269861	0.13869
octacosane	0.14992	0.586129	0.565788	0.845453	0	0.110102	0.139673
nonacosane	0	0.193753	0.283936	0.142323	0.256767	0.199812	0.149786
triacontane	0	0.984065	0.28272	0.192123	0	0	0
hexanoic acid	0	1.152968	1.079701	1.129153	0	0	1.145092
heptanoic acid	0	1.576615	1.379974	1.514861	0	0	0
octanoic acid	0	1.468492	1.625178	1.796828	0	0	0
nonanoic acid	1.524291	1.74949	1.811288	1.449882	0	0	0
decanoic acid	0	1.586595	1.510222	1.602504	0	0	0
undecanoic acid	0	0	0	1.282123	0	0	0
dodecanoic acid	0	1.309478	1.164328	0	0	2.006149	0
tridecanoic acid	0	0	0	0	0	0	0
tetradecanoic acid	0	1.674125	0	0	0	0	0
pentadecanoic acid	0	0	0	0	0	0	0
4-methyl-benzoic acid	0	1.241656	1.214849	0	0	0	0
4-methyl-benzaldehyde	0	0	0	0	0	0	0
3,4-dimethoxybenzaldehyde	0	0	0	0	0	0	0
anthracene	0	0	0	0	0	0	0
phenanthrene	0	0.049837	0	0	0	0	0
fluoranthene	0	0	0	0	0	0	0
pyrene	0	0	0	0	0	0	0
11H-benzo[a]fluorene	0	0	0	0	0	0	0
11H-benzo[b]fluorene	0	0	0	0	0	0	0
benz[a]anthracene	0	0	0	0	0	0	0
chrysene	0	0	0	0	0	0	0
triphenylene	0	0	0	0	0	0	0
benzo[a]pyrene	0	0	0	0	0	0	0
benzo[e]pyrene	0	0	0	0	0	0	0
benzo[k]fluoranthene	0	0	0	0	0	0	0
perylene	0	0	0	0	0	0	0
indeno[1,2,3-cd]pyrene	0	0	0	0	0	0	0
benzo[ghi]perylene	0	0	0	0	0	0	0
dibenz[a,h]anthracene	0	0	0	0	0	0	0
9H-fluoren-9-one	0	0	0	0	0	0	0
9,10-anthracenedione	0	0	0	0	0	0	0
9H-xanthen-9-one	0	0	0	0	0	0	0
7H-benz[de]anthracen-7-one	0	0	0	0	0	0	0
1-methyl-2-pyrrolidinone	0	0.990242	0	0.382601	0	0	1.503705
N,N-dibutylformamide	0	0	0.036943	0	0	0	0
2-(2-butoxyethoxy)-ethanol	0	0	0	0	0	0	0
2,3-dihydro-1H-inden-1-one	0	0	0	0	0	0	0
benz[a]anthracen-7,12-dione	0	0	0	0	0	0	0
1,1'-sulfonylbisbenzene	1	1	1	1	1	1	1

Mass Collected	C2027~00.D	C2028~XK.D	C2029~00.D	C2030~00.D	C2031~00.D	C2032~00.D
nonadecane	0.0361536	0.0342458	0.1080007	0.051024	0.473888	0.133639
eicosane	0.067593	0.0322876	0.0929257	0.044074	0.04388	0.031069
heneicosane	2.0471566	0.6814539	0.1054377	8.043294	1.280644	0.385946
docosane	0.0646971	0.0780698	0.0918298	7.542404	1.076071	0.12426
tricosane	1.3586207	0.832883	0	0.323758	1.379136	0.123376
tetracosane	0.7399199	0.1147104	0.1127008	0.955007	1.572654	0
pentacosane	0.9336469	0.4358617	0.2720054	-1	1.240108	0.264689
hexacosane	0.2343852	0.24130493	0	0.554532	0.117289	0.062079
heptacosane	1.6892567	0.6176844	0.2253685	0.139453	0.224211	-1
octacosane	0.4096116	0.1468664	0.1287881	0.147957	1.761974	-1
nonacosane	0.2226395	0.119497	0	0.182616	0.123817	0.166183
triacontane	0.3893597	0.2613286	0	0.269679	0.191792	0
hexanoic acid	0	0	0	1.058305	0	0
heptanoic acid	0	0	0	0	0	0
octanoic acid	0	1.4733168	0	0	1.368112	0
nonanoic acid	0	0	0	1.515102	0	1.457423
decanoic acid	0	0	0	0	1.449876	0
undecanoic acid	0	0	0	0	0	0
dodecanoic acid	0	1.6603004	0	0	0	0
tridecanoic acid	0	0	0	0	0	0
tetradecanoic acid	0	0	0	0	0	0
pentadecanoic acid	0	0	0	0	0	0
4-methyl-benzoic acid	0	0	0	0	0	0
4-methyl-benzaldehyde	0	0	0	0	0	0
3,4-dimethoxybenzaldehyde	0	0	0	0	0	0
anthracene	0	0	0	0	0	0
phenanthrene	0.0595902	0	0	0.091643	0	0
fluoranthene	0.0305382	0	0	0.110355	0	0
pyrene	0.0312024	0	0	0.155262	0.039761	0
11H-benzo[a]fluorene	0	0	0	0	0	0
11H-benzo[b]fluorene	0	0	0	0	0	0
benz[a]anthracene	0	0	0	0	0	0
chrysene	0	0	0	0	0	0
triphenylene	0	0	0	0	0	0
benzo[a]pyrene	0	0	0	0	0	0
benzo[e]pyrene	0	0	0	0	0	0
benzo[k]fluoranthene	0	0	0	0	0	0
perylene	0	0	0	0	0	0
indeno[1,2,3-cd]pyrene	0	0	0	0	0	0
benzo[ghi]perylene	0	0	0	0	0	0
dibenz[a,h]anthracene	0	0	0	0	0	0
9H-fluoren-9-one				0	0	0
9,10-anthracenedione	0	0	0	0	0	0
9H-xanthen-9-one	0	0	0	0	0	0
7H-benz[de]anthracen-7-one	0	0	0	0	0	0
	0	0	0			
1-methyl-2-pyrrolidinone	0	0	0	0.429675	0	0
N,N-dibutylformamide	0	0	0	0	0	0
2-(2-butoxyethoxy)-ethanol	0	0	0	0	0	0
2,3-dihydro-1H-inden-1-one	0	0	0	0	0	0
benz[a]anthracen-7,12-dione	0	0	0	0	0	0
1,1'-sulfonylbisbenzene	1	1	1	1	1	1